New Strategies for Detailed Visualisation and Analysis of Stem Cell-Material Interactions

Sahana Gopal

A thesis submitted in partial fulfilment of the requirements for the degree of Doctorate of Philosophy and the Diploma of Imperial College London

Primary supervisor: Professor Yuri Korchev

Secondary supervisor: Professor Molly M. Stevens

Secondary supervisor: Doctor Andrew Shevchuk

June 2018

Declaration of Originality

I, Sahana Gopal confirm that the work presented in this thesis is my own. Where information has been derived from other sources, I confirm that this has been indicated in the thesis.

Copyright Declaration

The copyright of this thesis rests with the author and is made available under a Creative Commons Attribution Non-Commercial No Derivatives licence. Researchers are free to copy, distribute or transmit the thesis on the condition that they attribute it, that they do not use it for commercial purposes and that they do not alter, transform or build upon it. For any reuse or redistribution, researchers must make clear to others the licence terms of this work.

Acknowledgements

While I claim that this body of work is my own, it would not have been possible without the help and support of several people in the last four years. I would like to thank my supervisors, Professor Yuri Korchev, Professor Molly Stevens and Dr. Andrew Shevchuk for giving me the opportunity to pursue this work. I consider myself extremely lucky to have mentorship from these distinguished scientists, who I have learnt so much from, while trying to develop myself as a good scientist over the last few years. I have spent my PhD in two widely different but fantastic groups: being part of Professor Molly Stevens' group provided me with the freedom to explore, collaborate and ideate, while the intimate environment and hands-on approach in the Nanomedicine laboratory of Prof. Korchev and Dr. Shevchuk, taught me how to apply new and existing methods to help solve complex biological questions.

Special thanks to Dr. Ciro Chiappini, who has provided me with expert guidance from the beginning to the end of my project, without whom many of the fruitful discussions that led to interesting experiments and ideas would not have occurred. I would also like to thank Dr. Stephen Rothery for always being available for help with macros and image analysis. Being part of the Stevens group has acquainted me with a number of brilliant people who I have not only had immense pleasure working with, but who have also become dear friends: Katie Hansel (who I shared majority of my lunch breaks with, discussing our love for microscopy, the gym and everything else!), Vincent Leonardo, Stephanie Maynard, Spencer Crowder, Jelle Penders, Bakul Gupta, Hyejeong Seong, Jane Chia-Chen, Sam Worrapong, Chunching Li, Ye Wang, and Kella Kapnisi who have made my time in the lab a whole lot more fun and fulfilling.

I would also like to thank my partner, Krishna, who has given me unconditional support in the last four years, while also keeping me well-fed and sane during my write-up days! My parents, Samta and Gopal who, although have thought of the lab as a place where I conduct experiments to grow little insects, have always encouraged me to do my best and complete what I started. My sister, Spandana and my cousin, Ananth who have always been so encouraging about the science that I do! Sandra, Xiang, Tanel and Abbie, my dear friends from UCL who have all embarked on PhDs and sharing all our ups and downs as we moved to completion!

Abstract

The success of stem cell therapy and regenerative medicine relies on providing biochemical and biophysical cues to safely and reliably control cell fate transitions. It has now been recognised that recapitulating the physical attributes of the stem cell microenvironment is a key feature in controlling cell behaviour. Of particular interest is the ability of the extracellular microenvironment to present surface topographical features that contribute to control of cell attachment and morphology, which have a direct impact on maintenance of cell phenotype and gene expression. This realisation has led to the development of materials with surface topography to probe and control the stem cell behaviour.

In this thesis, the influence of material topography on cell behaviour is investigated through the use of both microscale and nanoscale topography, with a particular focus on visualisation strategies to characterise the features of the cell-material interface. Firstly, microscale topography in the form of microgrooves, is used to study the impact of topography at the level of the nucleus in neural stem cells. Through the development of new visualisation methods, incorporating state-of-the-art focused-ion beam scanning electron microscopy and scanning ion conductance microscopy, the nuclei of cells cultured on microgrooved topography are shown to correlatively remodel their nuclear architecture, epigenetics and mechanical properties.

Secondly, using nanoscale topography in the form of high aspect ratio nanoneedle arrays, the cell-material interface is investigated at the level of the plasma membrane in human mesenchymal stem cells. Nanoneedles, typically used to deliver a variety of therapeutically relevant payloads, are shown to create a tight interface with the cell membrane, while triggering changes in plasma membrane architecture and inducing the activation of endocytosis pathways, which contributes significantly to payload delivery at the interface.

Contents

List of Figures **10**

List of Tables **13**

Abbreviations **14**

1 Introduction **20**

1.1 Stem Cell Therapy: Possibilities and Challenges 20

1.2 Engineering the Stem Cell Microenvironment 24

1.2.1 Biochemical Cues 24

1.2.2 Biophysical Cues 25

1.3 Probing the Cell Response to Topographical Cues 40

1.3.1 Impact of Topography on Focal Adhesions and the Cytoskeleton 40

1.3.2 Impact of Topography on the Plasma Membrane 43

1.3.3 Impact of Topography on the Nucleus 48

2 Optimisation of Visualisation Methods to Study Cell-Material Interactions **54**

2.1 Overview of Available Techniques for Visualising Cell-Material Interactions 55

2.1.1 Light Microscopy 55

2.1.2 Electron Microscopy 57

2.1.3 Raman Spectroscopy 61

2.1.4 Scanning Probe Microscopy 62

2.2 Chapter Aims 68

2.3 Materials and Methods 69

2.3.1 Cell Culture 69

2.3.2 Nanoneedle Array Preparation 69

2.3.3 FIB-SEM Sample Preparation . . . 69
2.3.4 FIB-SEM Operation . . . 70
2.3.5 SICM Sample Preparation and Imaging . . . 71
2.3.6 Laurdan Imaging Optimisation . . . 72
2.4 Results and Discussion . . . 74
2.4.1 Optimisation of Sample Preparation for FIB-SEM . . . 74
2.4.2 Optimisation of Image Acquisition by SICM . . . 76
2.4.3 Optimisation of Laurdan Staining for Membrane Order Imaging by Two Photon Microscopy . . . 79
2.5 Conclusion . . . 82

3 New Microscopy Methods to Study the Influence of Microgrooved Substrates on Nuclear Remodelling 83

3.1 Introduction . . . 85
3.1.1 Nuclear Architecture and Gene Regulation . . . 85
3.1.2 The Epigenome and Gene Regulation . . . 88
3.1.3 Heterochromatin and the Nuclear Envelope . . . 90
3.1.4 Using Material Cues to Induce Nuclear Remodelling . . . 92
3.1.5 Developing New Techniques for Studying Nuclear Response to Material Topography . . . 94
3.2 Chapter Aims . . . 97
3.3 Materials and Methods . . . 99
3.3.1 Antibodies . . . 99
3.3.2 PDMS substrate fabrication . . . 99
3.3.3 Cell culture and Seeding . . . 99
3.3.4 Immunolabelling for Flourescence Microscopy . . . 100
3.3.5 Immunolabelling for FIB-SEM . . . 100
3.3.6 Gold Enhancement . . . 101
3.3.7 Electron Microscopy Preparation . . . 101
3.3.8 FIB-SEM Operation . . . 101
3.3.9 Energy Dispersive X-ray (EDX) Spectroscopy . . . 102
3.3.10 Image Analysis . . . 102

3.3.11 SICM Stiffness Mapping . . . 103
3.3.12 Statistical Analysis . . . 104
3.4 Results . . . 105
3.4.1 Characterising Nuclear Morphology with FIB-SEM . . . 105
3.4.2 Optimisation of Pre-embedding Immunolabelling for Fluorescence Microscopy and FIB-SEM . . . 105
3.4.3 The Epigenetic Mark H3K9me3 Increases in Response to Microgrooved Topography . . . 109
3.4.4 The Epigenetic Mark H3K9me3 is Enhanced at the Nuclear Periphery in Response to Microgrooved Topography . . . 110
3.4.5 SICM Reveals that Microgrooved Topography Stimulates Changes in Nuclear Stiffness . . . 112
3.5 Discussion . . . 114
3.6 Conclusion . . . 119

4 Investigating the Cell Membrane Response to Nanoneedle Arrays for Delivering Biological Payloads 120

4.1 Introduction . . . 121
4.1.1 The Need for Intracellular Access . . . 121
4.1.2 Current Methods for Intracellular Delivery . . . 121
4.1.3 Nanoneedle Arrays for Biomolecule Delivery . . . 132
4.1.4 Nanoneedle Properties for Intracellular Delivery . . . 135
4.1.5 Gaining Intracellular Access with Nanoneedles . . . 138
4.1.6 Properties that Influence Nanoneedle Penetration . . . 140
4.1.7 Potential Mechanisms of Nanoneedle-Mediated Delivery . . . 143
4.1.8 Porous Silicon Nanoneedle Arrays for Biomolecule Delivery . . . 145
4.2 Chapter Aims . . . 147
4.3 Materials and Methods . . . 148
4.3.1 Antibodies and Reagents . . . 148
4.3.2 Preparation of Nanoneedle Arrays . . . 148
4.3.3 Cell Culture . . . 148
4.3.4 SICM Operation . . . 149

4.3.5 Electron Microscopy Sample Preparation 150
4.3.6 Electron Microscopy Imaging 151
4.3.7 Laurdan Staining, Multiphoton Imaging and Analysis 152
4.3.8 Immunolabelling, confocal fluorescence imaging and analysis . . 154
4.3.9 Nanoneedle-Mediated Biomolecule Loading and Delivery 155
4.3.10 Flow Cytometry 155
4.3.11 Quantitative Real Time Polymerase Chain Reaction (qRT-PCR) 156
4.3.12 Statistical Analysis 157
4.4 Results 158
4.4.1 Cell Viability 158
4.4.2 Membrane Morphology on Nanoneedle Arrays 158
4.4.3 Membrane Integrity at the Cell-Nanoneedle Interface 162
4.4.4 Nanoneedle Interfacing Triggers Endocytosis 163
4.4.5 Pathway-Specific Endocytosis Accounts for Cytosolic Delivery . . 167
4.4.6 Nucleic Acid Fate Following Nanoneedle-Mediated Delivery . . . 172
4.4.7 Effect of Changing Surface Chemistry on Cell-Nanoneedle Interfacing 175
4.5 Discussion 179
4.6 Conclusion 186
4.7 Future Work 187
4.8 Limitations of the Study 188

5 Concluding Remarks and Future Directions 189

5.1 Optimisation of Visualisation Methods to Study Cell-Material Interactions 191
5.2 New Microscopy Methods to Study the Influence of Microgrooved Substrates on Nuclear Remodelling 192
5.2.1 Future Directions 192
5.3 Investigating the Cell Membrane Response to Nanoneedle Arrays for Delivering Biological Payloads 195
5.3.1 Future Directions 196
5.4 Conclusion 198

References 199

Appendix **245**

List of Publications 245

Rights and Permissions 247

List of Figures

1.1 Current stem cell types 22
1.2 Biochemical and biophysical cues in the cell microenvironment 26
1.3 The three pillars of tissue engineering: cells, biomaterials and biochemical agents 27
1.4 Material control of cell fate 34
1.5 Previous and current models of the plasma membrane 44
1.6 Mechanisms of membrane curvature generation 46
1.7 Linkage of the nucleus to the cytoskeleton 49

2.1 Schematic of FIB-SEM for biological sample imaging 59
2.2 Schematic of SICM 64
2.3 Set-up and schematic for angle scanning ion conductance microscopy (ASICM). 72
2.4 Optimisation of sample preparation for ultrastructural visualisation under FIB-SEM 75
2.5 Zoomed-in images of optimisation of sample preparation for ultrastructural visualisation under FIB-SEM 76
2.6 HPICM optimisation for scanning cells on nanoneedle arrays 77
2.7 SICM imaging of hMSCs using the angled approach 79
2.8 Schematic and optimisation of Laurdan staining for two photon microscopy 80

3.1 Schematic of nuclear architecture 86
3.2 Schematic illustration of the nucleoplasmic reticulum 87
3.3 Schematic of epigenetic modifications responsible for gene activation and silencing 89
3.4 Using microgrooved topography to stimulate epigenetic remodelling . . . 93

3.5 Schematic of the potential influence of microgrooved topography to stimulate epigenetic modifications. 97
3.6 A schematic of pre-embedding immunogold sample preparation for FIB-SEM 102
3.7 Process flow of FIB-SEM data processing and analysis 103
3.8 Characterisation of nuclear morphology on microgrooves with FIB-SEM 106
3.9 Fluorescence Microscopy of NSCs with different permeabilisation agents 107
3.10 Optimisation of immunogold FIB-SEM sample preparation 108
3.11 Microgrooves stimulate an increase in H3K9me3 density 110
3.12 H3K9 is enhanced at the nuclear periphery 111
3.13 Cell stiffness increases in response to microgrooved topography 112

4.1 Potential applications of gaining intracellular access 122
4.2 Overview of Physical and biochemical methods of intracellular delivery . 123
4.3 Schematic of formation of clathrin coated pits during clathrin mediated endocytosis 126
4.4 Schematic of structural composition of caveolae 127
4.5 Methods of nanoneedle fabrication 135
4.6 Microscopy of the cell-nanoneedle interface 139
4.7 Schematic of methods to gain intracellular access using nanoneedles . . 142
4.8 Fabrication, structure and degradation of vertical arrays of porous silicon nanoneedles 146
4.9 Schematic and process flow of FIB-SEM lift-out sample preparation for TEM 153
4.10 Fluorescence microscopy images of same species double immunostaining controls 155
4.11 LIVE/DEAD^{TM} labelling of hMSCs cultured on nanoneedle arrays . . . 159
4.12 The apical membrane response to nanoneedle interfacing 160
4.13 Nanoneedle stimulate changes in membrane order in hMSCs 161
4.14 FIB-SEM characterisation of hMSCs on nanoneedle arrays 163
4.15 STEM and TEM characterisation of hMSCs on nanoneedle arrays . . . 164

4.16 Clathrin light chain and caveolin-1 localisation to sites of nanoneedle interfacing . . . 165
4.17 FIB-SEM characterisation of endocytotic vesicle localisation at sites of nanoneedle interfacing . . . 166
4.18 Quantification of payload loading on nanoneedle and FSW substrates . 168
4.19 Delivery of Transferrin via nanoneedle arrays . . . 169
4.20 Delivery of CavME specific albumin and CTxB via nanoneedle arrays . 170
4.21 Delivery of dextrans via nanoneedle arrays . . . 171
4.22 Co-localisation analysis of delivered endocytotic cargo via nanoneedle arrays . . . 172
4.23 Fate of nucleic acids delivered via nanoneedles . . . 174
4.24 Effect of APTES functionalisation of nanoneedles on the membrane morphology . . . 176
4.25 Basal membrane morphology at the AP-nanoneedle-membrane interface 177
4.26 Effect of APTES surface functionalisation of nanoneedles on endocytotic protein localisation . . . 178
4.27 Schematic of possible mechanism of increasing membrane lipid order by nanoneedle interfacing . . . 181
4.28 Schematic of mechanisms of nanoneedle-mediated delivery related to endocytosis . . . 184

List of Tables

1.1 Summary of adhesion and cytoskeleton mediated responses induced by various substrate topographies. 42
1.2 Summary of plasma membrane responses induced by substrate topography. 48
1.3 Summary of nuclear envelope response to surface topography. 51

2.1 Summary of current visualisation methods for investigating cell-material interactions 67
2.2 Cell staining protocols for visualisation under FIB-SEM 70

4.1 Table of pathways of endocytosis, their key coat components, scission mechanisms, sizes and cargoes 128
4.2 qRT-PCR Primer Sequences 157

Abbreviations

- ESC = embryonic stem cell
- iPSC = induced pluripotent stem cell
- BM-MSC = bone marrow mesenchymal stromal cell
- MSC = mesenchymal stem cell
- HSC = haematopoeitic stem cell
- hMSC = human mesenchymal stem cell
- ECM = extracellular matrix
- AFM = atomic force microscopy
- PA = polyacrylamide
- PDMS = polydimethylsiloxane
- PEG = polyethyleneglycol
- HA = hyaluronic acid
- MEF = mouse embryonic fibroblast
- PMMA = polymethyl methacrylate
- PS = polystyrene
- CHO = chinese hamster ovary
- ROCK = Rho-associated protein kinase
- EBL = electron beam lithography
- GPI-AP = glycosylphosphatidyinositol anchored proteins

- Cav-1 = caveolin-1
- BAR = bin/amphiphysin/Rvs
- CLC = clathrin light chain
- LINC = linker of nucleoskeleton and cytoskeleton complex
- NPC = nuclear pore complex
- IF = intermediate filament
- MT = microtubules
- ONM = outer nuclear membrane
- INM = inner nuclear membrane
- mRNA = messenger ribonucleic acid
- LBR = lamin B receptor
- NUPs = nucleoporins
- TAZ = transcriptional coactivator with PDZ-binding motif
- LM = light microscopy
- SRM = super-resolution microscopy
- SIM = structured illumination microscopy
- LLSM = lattice light sheet microscopy
- STED = stimulated emission depletion microscopy
- STORM = stochastic optical reconstruction microscopy
- PALM = photoactivated localisation microscopy
- EM = electron microscopy
- TEM = transmission electron microscopy
- SEM = scanning electron microscopy

- FIB-SEM = focused ion beam scanning electron microscopy
- SBF-SEM = serial block face scanning electron microscopy
- STEM = scanning transmission electro microscopy
- CLEM = correlative light and electron microscopy
- HRP = horse radish peroxidase
- DAB = diaminobenzidine
- APEX = ascorbate peroxidase
- GFP = green fluorescent protein
- RS = Raman spectroscopy
- SICM = scanning ion conductance microscopy
- MERF = mouse ear fibroblasts
- FBS = foetal bovine serum
- HPICM = hopping probe ion conductance microscopy
- ASICM = angle scanning ion conductance microscopy
- WGA = wheat germ agglutinin
- APTES = 3-aminopropyl triethoxysilane
- NR = nucleoplasmic reticulum
- DNMT = DNA methyltranferases
- M-CpG = methyl-CpG recognising proteins
- FRET = fluorescence resonance energy transfer
- HDAC = histone deacetylase
- HP1 = heterochromatin protein 1
- LBR = lamin B receptor

- LAP2β= lamina-associated polypeptide-2-β
- ROI = region of interest
- DAPI = 4', 6-diamidino-2-phenylindole
- FNG = fluoronanogold
- NSC = neural stem cell
- GA = glutaraldehyde
- EDX = energy dispersive X-ray spectroscopy
- TALEN = transcription-activator like effector nuclease
- miRNA = microRNA
- ZFN = zinc finger nuclease
- EE = early endosome
- LE = late endosome
- PDGF = platelet derived growth factor
- CSF-1 = macrophage colony stimulating factor-1
- EGF = epidermal growth factor
- PIP3 = phosphatidylinositol-triphosphate
- CME = clathrin mediated endocytosis
- Tfn = transferrin
- LDL = low density lipoprotein
- AP = adaptor protein
- HSP70 = heat shock cognate 70
- FBN17 = formin binding protein 17
- CavME = caveolae mediated endocytosis

- CTx = cholera toxin
- SV40 = simian virus 40
- CLIC = clathrin independent carrier
- GEEC = GPI-AP enriched early endosome
- TGN = trans-golgi network
- ILV = intralumenal vesicles
- MVB = multivesicular body
- ESCRT = endosomal sorting complex required for transport
- siRNA = small interfering RNA
- MACE = metal assisted electrochemical etching
- DRIE = deep reactive ion etching
- FIB = focused ion beam
- EEA-1 = early endosome antigen-1
- LAMP-1 = lysosome associated membrane protein-1
- CTxB = cholera toxin β subunit
- Alb = albumin
- Dex = dextran
- nN = nanoneedle
- FSW = flat silicon wafer
- MSCGM = mesenchymal stem cell growth media
- ∝-MEM = minimum essential media alpha
- PFA = paraformaldehyde
- PBS = phosphate buffered saline

- HMDS = hexamethyldisilazane
- DMSO = dimethyl sulphoxide
- BSA = bovine serum albumin
- qRT-PCR = quantitative real time polymerase chain reaction
- HUVEC = human umbilical vein endothelial cells
- GP = general polarisation
- MP = macropinocytosis
- FFT = fast fourier transform
- Cy3 = cyanine 3
- GAPDH = glyceraldehyde 3-phosphate dehydrogenase

1. Introduction

1.1 Stem Cell Therapy: Possibilities and Challenges

A stem cell is a cell that has the capacity to self-renew and differentiate into other cell types. From the very early stages of the embryo, to the end of an organism's lifetime, stem cells have the unique ability to proliferate, giving rise to more specialised cells, while also replenishing aged tissue through an adult organism's lifetime. The discovery of stem cells' ability to self-renew and differentiate into multiple cell types has led to several promising applications in regenerative medicine, where the hope is to replace tissues that are degenerated through the processes of ageing, disease or trauma. In the current state of affairs, the type of stem cell selected for a particular regenerative application is based on a number of factors including the risks surrounding their implantation or administration, their availability from host or other sources and their differentiation capability into the desired cell type[1](Fig 1.1).

Stem cells can be classified based on their potential for self-renewal and differentiation. Stem cells with the greatest proliferative and differentiation potential, being able to generate all other cell types, come from the 8-cell stage embryo, better known as blastomeres or embryonic stem cells (ESCs)[2]. More recently, pluripotent potential was induced in somatic cells using a cocktail of transcription factors[3]. These induced pluripotent stem cells (iPSCs) provide a patient-specific source of stem cells with unparalleled differentiation potential and overcoming ethical challenges surrounding ESCs, thereby providing immense opportunity for regenerative medicine. Despite these advances, the number of clinical trials using iPSCs are few in number, mostly due to the potential risk of forming tumours from uncontrolled proliferation after *in-vivo* transplantation[4]. However, the most successful trials have been conducted for ocular disases[5] due the tissue's immunoprivileged trait. In addition, new methods of repro-

gramming somatic cells to iPSCs using non-integrative viruses that do not cause the overexpression of oncogenic genes have only recently been established, which can now potentially overcome the tumorigenecity barrier[5].

Somatic stem cells are heterogeneous populations of stem cells that are found in different tissues in an adult organism. They are defined by their ability to self-renew under certain conditions and differentiate into cell types of that specific tissue[6]. For example, mesenchymal stromal cells can be derived from adipose, bone marrow, endometrium or placental tissue[7]. Given their relative ease of extraction and expansion from bone marrow, and safety for transplantation, bone-marrow derived stromal cells (BM-MSCs), more commonly known as mesenchymal stem cells (MSCs) have been at the forefront of stem cell therapy for decades. MSCs can differentiate into cell types of skeletal tissue, namely chondrocytes, adipocytes, osteocytes, and fibroblasts[8]. Moreover, BM-MSCs are responsible for establishment, organisation and maintenance of haematopoietic niches, where stem cells of the blood or haematopoietic stem cells (HSCs) are generated on a scale of billions per day[6]. Harnessing the abilities of HSCs has led to clinically successful HSC therapies such as bone marrow transplantations, blood cancers[9], inherited severe combined immunodeficiency[10], and benign haematopoietic conditions such as sickle cell anaemia[11].

The notion that MSCs are a population of cells that can establish cell niches and regulate turnover have led to numerous studies to induce differentiation into non-skeletal cell types. A considerable number of clinical trials involving systemic delivery of MSCs for a variety of non-skeletal conditions including myocardial infarction, neurodegeneration and Duchenne muscular dystrophy have been conducted with limited success[12]. The results are not surprising as there is no evidence that MSCs can establish these tissues *in-vivo*[7]. Moreover, there is no universal MSC as MSCs extracted from different tissues are heterogeneous in nature and exhibit unique differentiation and proliferative potentials[6]. The most successful clinical applications of MSCs are those which pertain to treatment of tissues they are extracted from. For example, BM-MSCs are more successful in repairing bone or cartilage defects that those from adipose-derived tissue or placental tissue. The initial evidence that MSCs can differentiate into only skeletal cell types has been challenged by numerous attempts to induce MSCs to undergo differentiation into cells of other germ layers such as hepatocytes or neurons, and also

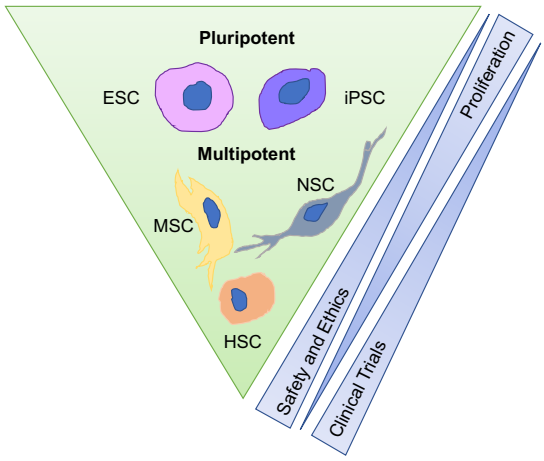


Figure 1.1: A basic overview of current stem cell types classified on the basis of their potential to differentiate (green triangle) and their corresponding properties and clinical use (blue triangles). Broadest to narrowest regions of the triangles indicate high to low. Pluripotent cells such as embryonic stem cells (ESCs) and induced pluripotent stem cells (iPSCs) exhibit the highest potential to differentiate by their capacity to give rise to all three germ layers. They have highest renewal and proliferative potential but are currently limited in clinical trials due to safety and ethical concerns. Multipotent stem cells are normally adult stem cells found in various tissues of an adult organism and are able to give rise to the tissue of their origin from being pre-committed to differentiation. Of particular interest are mesenchymal stem cells (MSCs) that can be derived from a number of tissues including bone marrow and adipose tissue as well as neural stem cells that are found in nerve tissue. Haematopoietic stem cells (HSCs) from the blood are currently most extensively used in clinical trials.

other cells of the mesoderm including smooth muscle cells and cardiomyocytes. However, the establishment of these functional cell types *in-vivo* is yet to be observed, as most indications for inducing differentiation are *in-vitro*, and exhibit poor correlation to *in-vivo* results. With respect to differentiation potential, MSCs can therefore be considered a cell type that can be 'reprogrammed' under chemical factors *in-vitro* rather than differentiated to non-skeletal cell types *in-vivo*. The current consensus on systemic injections of heterogeneous stem cells to achieve localised and specific regeneration of injured or diseased tissue is hence an unrealistic strategy for stem cell therapy, and calls for more robust methods to characterise, monitor and engineer these cell types prior to engraftment or transplantation.

The failure of trials of systemic injections of stem cells has created a shift in paradigm, whereby chemical and or genetic manipulation of cultured stem cells can be performed *in-vitro*, to induce their differentiation into desired cell types that can then be

delivered to the patient. *In-vitro* culture, expansion and differentiation of stem cells (of iPSCs in particular) has led to great advances such as providing a patient-specific cell source, establishment of new genotype to phenotype relationships, platforms of individualised drug screening and genetic repair for cell replacement therapy. By identifying the series of biochemical factors that enables a stem cell to adopt a specific lineage, it is now possible to differentiate stem cells successfully to a variety of cell types *in-vitro*. In addition, the identification of transcription factors to facilitate reprogramming is now paving the way towards *in-vivo* reprogramming[13]. However, the major hurdle in stem cell differentiation and somatic cell reprogramming is the low efficiency with which unlimited pure populations of genetically matched and differentiated cells can be obtained. Moreover, the cost of maintaining these cultures for months at a time, and the variability they can exhibit between donors is considerably high. At the end of the differentiation process, even the most successful protocols produce only immature cell types and are often unable to prove adult state functionality *in-vitro* or *in-vivo*. For example, iPSC derived cardiomyocytes are unable to develop mature t-tubules[14] and iPSC derived beta-islet cells are only weakly responsive to glucose[15]. Although in-vivo reprogramming could potentially circumvent these issues, the processes governing the lineage transformation must be better understood. Thus careful considerations of the cues required in the stem cell microenvironment during the differentiation process must be made to improve efficiency of these protocols and precisely control their behaviour.

1.2 Engineering the Stem Cell Microenvironment

The ability to self-divide or differentiate into specific and mature cell lineages *in-vivo* is dependent on the intrinsic and extrinsic signals experienced by stem cells in their microenvironment. Typically, stem cells are resident in 'niches', or anatomical locations that experience highly specialised signals from surrounding stromal cells and the extracellular matrix (ECM)[16]. The ECM that makes up this microenvironment is a hydrated proteinaceous surrounding naturally secreted by resident cells. Initially thought to have the sole purpose of providing structure to tissue, it is now well established that the ECM provides specific physical as well as chemical cues, that are generated and sensed by the surrounding cellular population. This establishes a bidirectional and dynamic dialogue through which the ECM is under constant remodelling, while the cells themselves receive cues from the ECM in a reciprocal fashion[17]. Although the ECM may be envisioned as relatively homogenous structure across tissues being composed of water, fibrous proteins and polysaccharides, the actual biochemical and physical properties of ECM are highly tissue-specific and support the mechanical and chemical functions of that tissue. For example, the combinations and type of fibrous proteins and polysaccharides[18], cell adhesion sites, growth factors and ligands available[19], topography[20], mechanical properties[21] or influence of enzymes such as proteases[22] can all dictate the activity of resident cells of that tissue, ultimately influencing the cell response.

1.2.1 Biochemical Cues

From a biochemical stand point, signalling to stem cells takes place through a variety of mechanisms (Fig. 1.2). The adhesion of cells to their ECM is based on the arrangement, density, conformation and combination of molecules present in the matrix. Cell-ECM contacts are formed mainly by integrins, a family of heterodimeric transmembrane proteins that can bind to the ECM directly via their extracellular domains. In addition to this, integrins act as cell membrane receptors that can also bind different ligands, cytokines and growth factors. Combinations of α and β subunits are able to bind to protein domains of the ECM such as fibronectin, laminin or collagen, providing signals for cells to stay within their niches. For example, the presence of integrin $\beta 1$ on HSCs

and spermatogenic stem cells promotes their homing activity within their respective niches[23, 24]. In contrast, satellite cells or stem cells of skeletal muscle are bound to the niche via α7β1[25] while skin stem cells express high levels of α6, β4 and β1[26]. Moreoever, the type of integrin subunits present, the degree of clustering, and binding kinetics can trigger a host of intracellular signalling pathways, via focal adhesion kinases (FAKs) and phosphoinositide-3-kinases. The activation of these signalling cascades ultimately triggers changes in cell morphology, renewal, proliferation, migration and homing[27]. Conversely, inside-out signalling also occurs, whereby intracellular signals can change the expression and consequent binding capabilities of surface integrins[28].

Secondly, signalling in the stem cell microenvironment can also exist through secreted factors. Exposure to cytokines, chemokines, matrix remodelling enzymes, growth factors and small molecules can also occur from local cell secretions, nearby circulation and distant nerve impulses[29]. For example, a protein Sonic Hedgehog originally thought to influence local stem cell populations, has recently been shown to travel great distances via axons to reach astrocytes of a completely different niche[30]. Signalling molecules bind to specific receptors on the cell surface, triggering a host of intracellular signalling cascades.

Thirdly, cell-cell communication that occurs through proteins that form gap junctions enables chemical exchange of small molecules between stromal support cells and stem cells they support. For example, Connexin43, a gap junction protein, plays a key role in secreting stromal cell derived factor-1 or CXCL12 that is required for HSC self-renewal[31]. In addition, cell-cell communication can promote niche maintenance through binding of two transmembrane proteins on adjacent cells, Notch and Delta[32]. Binding of the ligands initiates an intracellular signalling cascade in the two neighbouring somatic cells resulting in their recruitment to the niche and expression of stem cell-like markers.

1.2.2 Biophysical Cues

Due to the immense progress in identification of various biochemical cues in stem cell differentiation and their ease of administration, sequential supplementation of chemical effectors in growth media has been the gold standard for cell reprogramming and differentiation protocols. For instance, direct conversion (transdifferentiation) of somatic

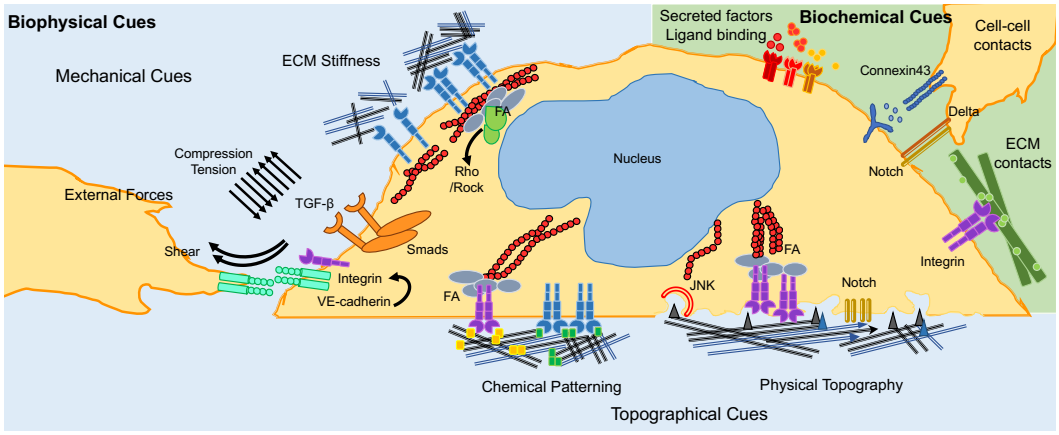


Figure 1.2: The cell microenvironment: cues for cell signalling in the microenvironment can be broadly classified as biophysical or biochemical. It is important to note that both types of cues lead to signal transduction via overlapping receptors, protein effectors and cytoskeletal components. Biochemical cues include cell-ECM (integrins) and cell-cell interactions (via cell-cell receptors including connexins, notch and delta) and signalling by secreted factors such as chemokines, cytokines and growth factors that are found in the local environment. Biophysical cues be classified into mechanical cues and topographical cues. Mechanical forces arising from extracellular matrix (ECM) stiffness can influence focal adhesion (FA) density and cytoskeletal tension triggering signalling pathways such as Rho/ROCK that have downstream effects on gene expression. In addition, a number of external forces: tension, compression and shear influence ligand receptor binding. Clustering and activation TGF-β receptors occurs in high compression environments such as in cartilage. Under conditions of shear stress VE-cadherin at cell-cell junctions can facilitate activation of integrins. Topographical cues act by presenting chemical or physical patterns that leads to differences in ligand presentation and binding by cell receptors or physical micro- or nanotopography and spacing of the ECM itself that organises receptor binding. This can result in signalling pathways by Notch, JNK and changes in cytoskeletal tension via FA. More details of these mechanisms can be found in the main text.

cells into cardiomyocytes is achieved through overexpression of key transcription factors delivered as an exogenous cocktail[33]. However, the efficiency of conversion using these protocols remains extremely low and there is difficulty in generating cardiomyocytes of mature phenotype. A potential reason for low efficiencies of conversion is the presentation of biochemical cues, typically controlled by the physical, chemical and mechanical properties of the ECM *in-vivo*, that ultimately impacts cell attachment and spreading. For instance, the topography of the matrix in the form of ligand availability, density, roughness and surface chemistry can dictate the specificities of adhesion, ligand binding and receptor clustering which have downstream effects on gene expression[34]. The ECM is also presented with external mechanical forces such as twisting, shear force or stretch, which can change ligand conformation and binding sites for cells. In many cases, the physicochemical changes in the ECM occur with great spatiotemporal detail, and often, gradients of biophysical cues can be found within a single tissue or microenvironment (Fig 1.2). Thus, understanding the ECM and its contributions to

directing cell fate has led to improvements in field of tissue engineering, where it is hoped that biomaterial scaffolds can recapitulate key features of tissue-specific ECM, by not only supporting the supplementation of biochemical factors but also providing an attachment area for isolated stem cells or progenitors[35](Fig 1.3).

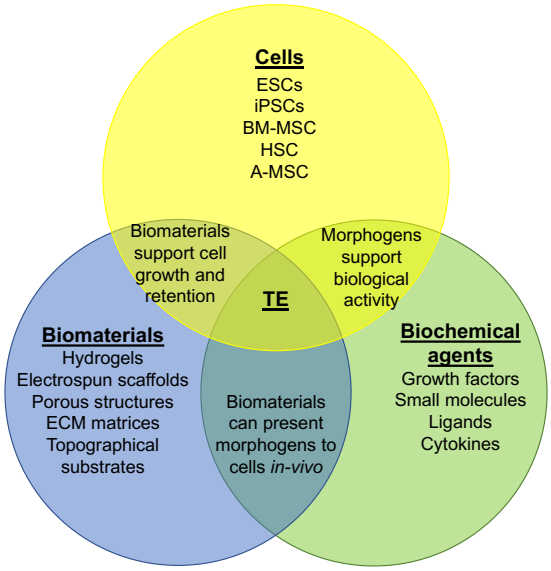


Figure 1.3: The three pillars of tissue engineering: cells, biomaterials and biochemical agents. Since the early days of differentiating cells and attempting to construct tissues in culture, cells and biochemical agents have been best characterised. It is now evident that a scaffold or biomaterial is essential in providing the physical cues present in tissue-specific ECM that can help govern the cell response, while also aiding in cell attachment, growth and survival. Adapted from [36].

Direct coupling of the ECM to the intracellular environment occurs via integrins, enabling cells to transduce mechanical information to the nucleus, by a process known as mechanotransduction[37]. Integrins themselves are linked to the actin cytoskeleton and associated myosin in a highly organised signalling complex consisting of over 160 possible components[38]. At these focal adhesion sites, most components are constitutional while some become transiently associated with the focal adhesion complex based on the activation of the signalling pathway. The focal adhesion complex and its associated signalling molecules such as kinases, phosphatases and GTP binding proteins have a direct impact on the structure and conformation of the actin cytoskeleton[39]. These proteins play a regulatory role in actin assembly and disassembly by phosphorylating myosin or other actin binding proteins, triggering changes in cell shape[40] motility[41], proliferation[42], uptake[43] or adhesion[44]. Through this process, the

physical attributes of the cell environment can dictate how cells respond to or internalise administered biochemical agents such as nucleic acids and therapeutic proteins.

Mechanotransduction thus enables cells to constantly sense their external environment, and unsurprisingly, the specialised nature of ECM that exists for each tissue makes resident cells highly sensitive to any changes in their physical or chemical properties. This is not only essential for homeostatic maintenance, but also critical in understanding ECM changes that occur during ageing, disease or trauma. Insight into how specific biophysical cues can exert control over biochemical signalling pathways is hence fundamental to developing platforms to control cell fate and function. The complex mechanisms by which physical forces are exerted on cells within the matrix has led to the creation of synthetic material systems to study and control various aspects of cell behaviour. Since the influence of biophysical cues is a much more recent realisation compared to biochemical strategies, a great deal of research is currently spent in not only recapitulating the mechanical and topographical environment, but developing biomaterials and culturing systems to study the mechanisms by which stem cells respond to individual cues. Although various biophysical cues can be identified, it is important to note that mechanotransduction enables cells to respond to each cue in an overlapping fashion i.e. each biophysical cue may influence the same collection of mechanosensing elements of the cell membrane in additive or opposing ways to trigger the same biochemical signalling pathways.

1.2.2.1 Mechanical Cues

Substrate stiffness

The stiffness of a tissue is dictated by the composition of its ECM. Typically it is composed of fibrous proteins such as collagens, laminin, fibronectin and elastin, as well as tissue specific proteoglycans which act as mechanical buffers and induce hydration[45]. Fibrous proteins, particularly collagens are the most abundant proteins of the ECM and provide the structural backbone through their ability to form sheets, cables, fibrils or meshes, ultimately giving rise to tissue organisation[46]. The ability of fibrous proteins to assemble together in different conformations and undergo post-translational modifications results in a range of tissue specific stiffnesses[45].

The stiffness of the ECM can range from a few hundred pascals in soft tissues such

as brain and adipose tissue to tens of kilopascals for cartilage and non-mineralised bone[47, 48]. Tissue specific stiffnesses are also known to change during disease and have adverse effects on cell function. For example, normal liver tissue has a stiffness of 300-600 Pa, but liver cirrhosis is accompanied by the tissue stiffening up to 20 kPa[49]. Considering the gigapascal values of glass and tissue culture plastic, cells of even the hardest tissues are cultured routinely in non-physiological stiffness substrates, which alters their intrinsic functions resulting in dedifferentiation and an unfavourable change in phenotype.

The cytoskeleton of resident cells within ECM is also known to reflect the stiffness of the ECM that surrounds them. For instance, as substrate stiffness increases, cytoskeletal tension increases and stress fibres are established in mechanosensitive cell types[50]. Atomic force microscopy (AFM) measurements of cell stiffness support this finding as stiffness was found to increase with increase substrate stiffness, saturating at 20 kPa substrates[51]. Although measuring cell stiffness through compressive methods such as AFM has been essential in highlighting the ability of ECM stiffness to modulate cytoskeletal tension, since cells sense ECM stiffness by pulling rather than pushing on their ECM, there is considerable debate as to whether compressive measurements are reflective of the true degree of stiffness. Indeed, surface tension exerted by cells pulling on a substrate has been shown to affect AFM indentation measurements, resulting in overestimation of elastic moduli of cells[52]. Nevertheless, newly developed models taking into account the effect of surface tension, as well as the development of other methods such optical stretching, magnetic twisting and micropipette aspiration can help to delineate true cell stiffness[52, 53, 54, 55].

The first indication for control of stem cell fate by substrate stiffness was demonstrated by Engler et al., where in hMSCs cultured on polyacrylamide (PA) gels functionalised with collagen of stiffnesses resembling that of brain, muscle and bone tissue lead to the expression of neurogenic, myogenic and osteogenic-specific genes respectively[56]. Since then, in addition to PA, synthetic substrates such as polydimethylsiloxane (PDMS), hyaluronic acid, polyethylene glycol (PEG) have been used to generate a range of substrate stiffnesses. In addition, another study showed that that varying conjugations of PA result in different porosities which can also contribute to cross-linking capacity of collagen and its spacing, affecting its mechanical properties

and the anchoring behaviour of cells[57]. This was confirmed by the observation that PDMS of varying stiffnesses with covalently linked collagen did not have an effect on hMSC differentiation, because collagen cross linking remained the same across different PDMS stiffness[57]. However, more recent data show that PDMS stiffness values may be underestimated and that they do not support protein tethering, therefore making PDMS an inapplicable substrate to study cell-substrate stiffness sensing[58]. Future studies that focus on decoupling the aspects of stiffness sensing, porosity and adhesion in other synthetic materials that do not require covalent linkage of ECM molecules will likely shed light on the extent of stiffness-mediated mechanisms affecting cell fate transitions.

Tailoring stiffnesses to initiate lineage decisions in the presence of soluble factors can be a simple yet effective platform for stem cell culture systems. Relatively stiff PA substrates in the order of 1-10 kPa have been shown to promote glial differentiation versus softer substrates of 100-500 Pa that induce neuronal differentiation in adult neural stem cells in the presence of neuronal growth factors[59]. 2D systems with dynamically tuneable stiffness are becoming important cell culture platforms for studying changes that occur in tissues overtime or promoting certain types of lineage specification. Hyaluronic acid (HA) gels subject to sequential cross-linking and increasing stiffness have been used to induce increased spreading and traction forces in the short-term and increased osteogenesis in the long-term for hMSCs[60]. In 2D culture systems, substrate stiffness has been useful in improving the ability of cells to internalise therapeutic material such as DNA complexes for gene therapy, likely via increasing the density of adhesion ligands and membrane tension that occurs via increasing substrate stiffness[61].

Since resolving these effects can be complex in 2D system, it is unsurprising that 3D hydrogel systems are even more elaborate to characterise. Nevertheless, by synthesis of versatile methacrylated dextran fibrous scaffolds that mimic collagen matrices, the effect of ECM fibre stiffness on cell behaviour has been investigated to find that stiff fibres can suppress cell proliferation and spreading[62]. Another consideration is that ECM stiffness is most often measured by the elastic/Young's modulus E, while in reality, naturally occurring matrices are viscoelastic rather than elastic in nature. In order to address this, alginate polymers have recently been used to generate matrices

with adequate stiffness and viscoelastic properties, that allow cells to sense and remodel their matrix. This has enabled MSCs incorporated within these matrices to promote bone tissue repair and matrix integration[63]. Additionally, the ability of alginate matrices to have tuneable and fast relaxation and stiffening properties were shown to promote bone-formation *in-vivo*[64]. The next generation of materials to probe the effects of matrix stiffness by incorporating other such dynamically tuneable viscoelastic materials to other tissue applications such as cartilage, cardiac or neuronal, will provide more answers of the role of ECM stiffness on cell behaviour.

External Forces

Throughout development of the embryo, the cell microenvironment is under constant influence of external mechanical forces. For example, the build up of shear forces by surrounding fluid drive the formation of gradients of biochemical factors that lead to left-right symmetry determination[65]. As development progresses and ECM is deposited, the type and degree of force experienced becomes more specific in nature, contributing to tissue level organisation and cell-lineage specification. Smooth muscle develops in lungs under the influence of tensile forces during breathing[66], compressive forces and fluid flow lead to skeletal tissue formation and fluid shear stress and cyclic strain stimulate the development of the cardiovascular system[67]. Moreover, the ability of external forces to control cell behaviour is emphasised by the fact that changes in the magnitude, frequency or type of external force lead to the loss of homeostasis or disease. For example, atherosclerotic plaques are normally found in regions of extremely turbulent fluid shear stress, where the vascular endothelium is abnormally activated and unable to downregulate biochemical signalling pathways[68]. Similar trends are seen with other mechanically sensitive tissues such as bone where mechanical loading is imperative for maintenance, as it has been shown that in conditions of microgravity, normally experienced by astronauts, a significant loss in bone mass is observed[69].

Extrinsically applied forces are typically sensed via mechanically-gated ion channels which open or close in response to stretch for example, or transmembrane receptors such as G-protein coupled receptors or cell adhesion proteins such as cadherins, which change in physical conformation in response to external forces. In addition, each type of force whether shear, compression or tensile can be sensed by the appropriate cellular machinery. For instance, endothelial cells that are under constant influence of fluid shear stress

transmit these forces primarily via cell-adhesion ligands including vascular-endothelial cadherin (VE-cad), that signal activation of integrins[70], whereas compressive forces typically experienced in mechanically loaded tissues such as cartilage trigger intracellular signalling cascades to maintain chondrogenic phenotype via activation of otherwise latent transforming growth factor-β and Smads[71]. In other studies, it has been shown that applying 0.5 MPa of hydrostatic pressure on chondrocytes resulted in two-fold increase in intracellular calcium ion concentration, which was reduced by the inhibition of stretch-activated ion channels[72]. The different types of forces cells experience also create changes in cell shape and orientation, primarily driven by the response mounted by the cytoskeleton, giving rise to specialised cell shapes, characteristic of that tissue. For example, cell types under the influence of fluid shear stress such as vascular endothelial cells are oriented with their long axis and stress fibres in the direction of the flow[73]. In other cases, the influence of hydrostatic pressure on chondrocytes allows them to maintain their rounded shape, which is vital to the maintenance of their phenotype[74], while tensile strain is critically important in the establishment of muscle cell orientation into myotubes for efficient force transfer[75]. These mechanically triggered cell shape changes and movement occur primarily by the control of Rho-family of GTPases and downstream effectors such as Rho-associated protein kinase (ROCK), which establish stress fibre formation and actin-myosin contractility[76].

The heavy reliance of certain tissue types on external forces for their homeostasis, has fuelled an interest in studying the effects of individual external forces in controlling stem cell fate. In the simplest of cases, forces that act statically and cyclically have been applied via ECM-like 2D and 3D substrates, inducing shear stress through flow in a culture system or applying forces to cells via magnetic beads. The type of force applied on stem cells has an effect on their lineage specification. For example, applying cyclic uniaxial mechanical strain on MSCs has been shown to promote their lineage specification into vascular smooth muscle cells[77] while applying hydrostatic pressure to MSCs encapsulated in alginate hydrogels was seen to promote chondrogenesis in the presence of TGF-β[78]. The degree of tensile stress applied to MSCs can also dictate whether MSCs adopt myogenic or chondrogenic phenotypes, where high tensile stress was shown to promote myogenic behaviour[79]. The application of fluid shear stress is widely used to promote features of the endothelium. Shear stress mimicking the

beating heart has been shown to aid in the differentiation of ESCs into endothelial cells to create organised vascular tubules via the shear stress activation of a tyrosine kinase pathway[80]. In other instances, laminar shear stress was found to improve the cardiac commitment of mouse ESCs, in the presence of epigenetic effectors[81].

Using physiologically relevant forces within 3D scaffolds, however has limitations in terms of quantifying the magnitude and the uniformity of the applied forces at the cellular level, not to mention the effect of movement of biochemical factors or gases. It must be taken into account how efficient the scaffold is in transmitting forces. Due to this reason, the application of remote forces such as electromagnetic and acoustic waves have not only been used to study individual effects on cells through their uniform application but also to control cell-cell organisation, alignment and orientation which are useful especially in cases where these parameters are physiologically important such as in developing myogenic, cardiac or neuronal tissue[82]. For example, specification into cardiac mesoderm was recently achieved in ESCs using a cyclic magnetic stretcher controlled remotely through internalised magnetic nanoparticles[83].

Overall, the data suggest that external mechanical forces play an important role in influencing stem cell behaviour through their convergence on specific biochemical signalling pathways, not only from a developmental standpoint but also from a tissue engineering perspective. The success of using external forces in controlling cell fate transitions relies on characterising mechanisms of force-sensing, and the development of unified material systems to apply measurable forces.

1.2.2.2 Topographical Cues

Chemical Patterning

Traditionally, biomaterials and engineered scaffolds have been created based on macroscale tissue properties. However, it is now evident that the ECM of each tissue is structurally and biochemically heterogeneous at the nanoscale, which stresses the importance of engineering material interfaces at this level. Besides specific signalling that takes place from a reservoir of ligands in matrix[84], controlled and coordinated biochemical signalling within the microenvironment occurs via key motifs or amino acid sequences present within ECM proteins. These amino acid sequences can then be recognised by cell surface receptors such as integrins, which establish focal adhesions and

subsequent signalling pathways. Arginine-Glycine-Aspartic acid or commonly known as RGD was the first motif to be discovered in a number of different ECM proteins including fibronectin and collagen, and a key binding site for cell adhesion via integrins[85]. Through this process, different types of integrin partners recognise one or many RGD sequences present within one or more ECM proteins, resulting in an intracellular signal for migration, polarisation, differentiation or survival. If specific responses can be mounted based on the type, pattern and density of ECM motifs, artificial patterning of surfaces can then be used to manipulate cell behaviour. In most cases, it is a combination of different binding motifs that will dictate the precise cell attachment and behaviour, or act to regulate activity of other agonists. For example, the 4Å spacing between RGD and another amino acid 'synergy site' was shown to be important for enhancing attachment, proliferation and osteogenic gene expression[86]. Since then, there have been more efforts to characterise stem cell responses to various ECM molecules, and combinations of them[87, 88, 89].

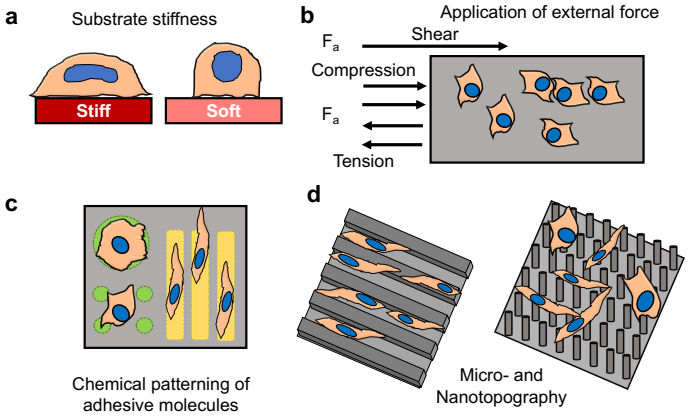


Figure 1.4: Material control of cell fate: The assessment of various physical parameters of the ECM has led to the engineering of materials to mimic specific aspects of the extracellular environment that are relevant for directing their fate into specific cell types. a) Matrices of varying stiffness have been used to promote lineage specificity in stem cells such as stiffer matrices for bone, and softer ones for adipogenesis[56]. b) External mechanical forces (F_a) applied across a material have been used to produce desirable responses in stem cells to support their differentiation into endothelial cells or chondrocytes[80, 78]. c) Chemical patterning of adhesive proteins and ligands can help to control cell fate by not only controlling cell shape and spreading[90] but also by presentation of ligands in the correct conformation[91]. d) Micro- and nanotopography of materials can be used to direct cell alignment and shape, while also triggering specific cell responses based on the separation of features available for adhesion[92].

The developments in chemistry and surface engineering have led to the ability to tether growth factors, chemically functional and/or adhesive groups on biomaterials to control cell fate. Growth factors tethered to surfaces can promote desirable cell re-

sponses by participating in continuous signalling or by inducing cell receptor clustering as their density on the surface can be controlled. For example, immobilising ligands such as Jagged-1 on polystyrene culture plates has been shown to enhance differentiation of epithelial cells via membrane receptor Notch signalling, when compared to delivery of Jagged-1 in solution[91]. Organising TGF-β on a surface prior to culturing cells was shown to enhance TGF-β signalling activities through coordinating membrane receptor dimerisation[93]. Patterning of motifs can be conducted rapidly in PEG hydrogel systems as ECM proteins do not adsorb easily to these substrates, allowing the effect of individual motifs to be assessed in a high-throughput manner, and new discoveries of matrix protein-stem cell interactions to be made[94]. Indeed these decoupling experiments are particularly important as the cross-linking capacity of the ECM protein in question can impact not only the stiffness of the matrix but also the availability of adhesion sites[57]. In addition, the ability to tether small functional groups such as phosphate groups to induce ostegenesis and hydrophobic t-butyl groups to induce adipogenesis in MSCs encapsulated in PEG hydrogels was demonstrated without altering other properties such as stiffness[95].

Depending on the microstructure of the tissue-specific ECM its adhesion sites, cells begin to define their shape during development and maintain this phenotype usually through adulthood. Cell shape can be an important predictor of phenotype. For example, cells undergoing epithelial-to-mesenchymal transition (EMT) are recognised by their change in cell shape, where epithelial cells that are more rounded become elongated and stretched[96]. Attempts have been made to directly influence stem cell fate by controlling cell shape via micropatterning of ECM proteins in various shapes and areas. By controlling cell shape and spreading area through microcontact printing, MSCs cultured on small round fibronectin islands underwent adipogenesis while culturing them on large square islands induced ostegenesis[97]. This type of differentiation occurred on the basis of focal adhesion signalling axis. Microcontact printing of laminin containing ECM of different sizes is demonstrated to be essential for the maintenance of ESCs, wherein small dense clusters of ESCs were shown to maintain ESC marker Oct4 expression, while larger clusters differentiated[98]. In other instances, surface patterning platforms for forming gradients of molecules responsible for providing axonal guidance have been created to promote growth cone directionality, which can poten-

tially be applied to many applications in which controlled cell migration is an essential requirement[99]. The development of chemical patterning technologies has shed light on mechanisms that may well exist in the 3D complexity of stem cell microenvironments, potentially driving new discoveries and incorporation of key components into more complex 3D systems.

Physical Topography

The heterogeneity that arises from different matrix proteins and their assembly gives rise to structural differences, resulting in micro- and nanotopographies. Much like chemical patterning, physical topography in the form of roughness, fibre direction or size and porosity play a fundamental role in the maintenance and differentiation of stem cells[100, 92]. By the process of contact guidance, cells adhere and respond to the features of the substrate they are grown on, giving rise to tissue specific cell alignment, morphology and polarity. For instance, native ECM of cardiac tissue consists of aligned 100 nm collagen fibrils that guide cardiomyocyte alignment, which is critical for effective transmission of action potentials[101]. Indeed, the loss of topographical cues within the ECM can lead to disruption of cell function. The extraction and culture of cardiomyocytes *in-vitro* results in the loss of a number of physiological functions and phenotype. Moreover, biomaterials implanted *in-vivo* may have micro- or nanoscale topography that can impact the cell response from the surrounding matrix[102].

The importance of topography in maintaining cell function has driven the development of biomaterials to maintain stemness, promote differentiation or study cell behaviour. Creating materials with topographies within the range for cell sensing could enable the production of scalable and reproducible cultured platforms for regenerative medicine. Fabrication techniques such as photolithography[103], electron beam lithography (EBL)[104], chemical etching[105], replica mould-casting[106] have been used to design biomaterials with a varying range of surface features from the order of nanometers to microns.

A deeper understanding of the effect of topographical cues in-vivo has been made possible using 2D culture systems. Moreover, these systems have shown promise in terms of enhancing differentiation in the presence of biochemical agents. In situations where recapitulation of the microenvironment requires cell alignment, substrate topography in the form of grooves, ridges and fibres at different length scales have been

utilised. By studying the dimensions and topography of the fibres of native cardiac ECM, PEG hydrogels were used to fabricate constructs similar to native tissue with nanoscale feature sizes, which aided in the propagation of anisotropic action potentials[101]. A number of studies have shown improved differentiation of neural progenitor cells and aligned neurites cultured in the presence of grooved topographies[107, 108, 109, 110]. Moreover, cells are also responsive to different length scales as neural stem cells were seen to differentiate and proliferate in accordance with nanometer changes in electrospun fibre diameters[111]. Ordered fibres and grooves are efficient in promoting cell elongation and increased intracellular tension, thereby enhancing lineage transformations into cell types that function in high-force environments. For instance, coating surfaces with aligned carbon nanotubes have been shown to promote myogenic differentiation of adipose derived stem cells[112] while using titanium nanotubes to promote cell alignment have been shown to promote osteogenesis of MSCs[113]. In order to mimic the structural periodicity of collagen *in-vivo*, twisted silica nanoribbons have been used to differentiate MSCs into osteoblasts, given that collagen is a major constituent of bone[114]. The influence of topography on differentiation of ESC and iPSC colonies is only beginning to be uncovered. Recent evidence indicates that colonies are sensitive to the depth and width of nanogrooves, while impacting the distribution of pluripotency markers Oct4 and Nanog that were shown to be highly expressed at the colony periphery[115]. Moreover, ESCs cultured on grooves and ridges with 600 nm gratings show reduced proliferation potential and increased alignment, effects that were disrupted in the presence of cytoskeletal disruptive agents indicating an essential role of the cytoskeleton in the proliferative activity of ESCs[116]. This is consistent with data from another study that indicates ESC culture on nanogrooves in the absence of feeder cells triggers differentiation spontaneously[117].

Although the physiological relevance of surface features such as nano-sized pits or troughs within stem cell niches *in-vivo* are less well characterised, changing geometries and order of surface features exhibits profound effects on different stem cell types *in-vitro*. In the absence of biochemical supplements to induce osteogenesis, 120 nm sized pits in a slightly disordered array (with a maximum displacement of 50 nm) were shown to promote osteogenesis in MSCs significantly compared to ordered arrays which had little to no effect on differentiation[92]. Moreover, this osteogenic effect was similar

to what occurs in the presence of biochemical factors such as ascorbic acid or dexamethasone. Subsequently, ordered pitted arrays have been used to maintain MSC multipotency markers and stemness, while permitting proliferation in a cell-cycle dependent manner[100, 118]. The ability of nanotopography to induce osteogenesis of MSCs has key implications for the development of implantable materials that have improved osseointegration. Nanoscale surface modifications of titanium implants can be used to trigger desirable osteogenic differentiation of MSCs *in-vivo*[119]. Differentiation of ESCs is impacted when cultured on ion-etched glass surfaces with nanoscale roughness as the expression of Oct4, a key pluripotency marker in ESCs was seen to decrease, hence promoting differentiation[120]. The importance of the type of geometry and biochemical supplementation for inducing changes in Oct4 expression has also been highlighted, as culturing ESCs on nanopillar substrates induced an increase of Oct4 in cells on one type of geometry and a decrease in another, which was also dependent on the presence or absence of a growth factor[121].

While there is compelling evidence to show that differentiation of stem cells can be introduced by micro- and nanotopography, the impact of topography on enhancing their reprogramming capacity has also been investigated[122]. The generation of iPSCs was improved by culturing cells on 10 μm grooves as demonstrated by a four-fold increase in Nanog-positive colonies. Additionally, an attempt to directly reprogram mouse embryonic fibroblasts into neurons in the presence of various microtopographies indicated that 5 μm gratings were most influential in improving the reprogramming process[123]. In another instance, culture on microgrooves demonstrated potential for improving direct programming and maturation of cardiac progenitor cells into cardiomyocytes[124]. Following this study, a comparative analysis of mechanical stretching, substrate stiffness and microgrooved topography showed that topography alone could aid in direct reprogramming of fibroblasts into cardiomyocytes, and in the presence of biochemical factors expressed mature cardiac markers such as cardiac troponin and improved contractility[125].

Overall, the ability of biophysical cues to control multiple aspects of cell behaviour make them promising, if not an essential feature of stem cell and tissue engineering applications. Engineering successful biomaterials now relies on elucidating the intracellular mechanisms involved in promoting desired cellular responses, which do not act

separately, but converge on the same molecular machinery that drives an overall cell response. At the same time, due to the many aspects of material-cell interactions yet to be identified, biomaterials themselves can be used to probe cell behaviour. Advances in material fabrication and new techniques to study cell-material interactions will allow this interdisciplinary field to answer biological questions of crucial importance.

1.3 Probing the Cell Response to Topographical Cues

Since the first demonstration of contact guidance in 1911[126], modulating surface topography has proved to be a simple yet effective strategy of manipulating stem cell behaviour. As mentioned in the previous section, current data suggest that these materials have profound impact on modifying intracellular pathways that lead to changes in gene expression and phenotype. In addition, other studies have shown that various types of topographies can exert effects by directly modifying the shape and structure of the cell membrane[127] or nucleus[128]. Although there are vast numbers of studies demonstrating the impact of topography on cell behaviour, the underlying mechanisms that lead to these changes are less well studied. Due to the complexity of the interplay between material cues, cell components and intracellular signalling mechanisms, studies investigating cell-material interactions are limited in defining precise mechanisms and pathways responsible for observations, and they remain largely phenomenon based. Moreover, the cell response to topography can be transient in nature, leading to material cues being modified over time as cells begin to adapt to the surface, secrete biomolecules as well as ECM proteins leading to confounding observations. More investigations into the mechanisms of cell-topography sensing are hence essential to developing new and improved materials for controlling stem cell behaviour. Concurrently, scalable and reproducible topographical substrates consisting of features at the length scales and geometries relevant for subcellular components to be activated, provide biologists with novel tools to optimise, probe and potentially control stem cell behaviour.

1.3.1 Impact of Topography on Focal Adhesions and the Cytoskeleton

Considering all aspects of the cell response to topography, the effects of topography on integrin binding, focal adhesion assembly and cytoskeletal rearrangements is the most widely characterised (Table 1.1). This is unsurprising as the the adhesion of a cell to a material is carried out by integrins that in turn assembles focal adhesions and the cytoskeletal rearrangement based on the underlying topography. As integrins cluster together, focal adhesions can change in size and number, triggering different cell

behaviours. While large focal adhesions promote high tension and adherence, small adhesions can drive cell movement. Moreover, the nanometer spacing of ligands such as RGD have been shown to either promote or inhibit focal adhesion formation, with ligand spacing less than 70 nm favouring large focal adhesion formation[129, 130]. This observation is particularly important when generating materials with topographies varying height and pitch, as increasing the pitch could increase the distance between integrin binding sites reducing the cell's ability to form adhesion complexes. In addition, the feature size itself plays a role in the establishment cytoskeletal tension, as clusters of five integrins covering approximately 50 nm in size were shown to be the minimum for the establishment of actin bundles[131]. Thirdly, it has been shown that the size of focal adhesions can be reduced by increasing the height or depth of the features; assuming that serum and matrix proteins account for approximately 30 nm of surface coating, heights and depths in excess of this can increase the separation of focal contacts[132]. Indeed, this finding is consistent with other reports, where increasing pit depth to 100 nm while maintaining the pitch was found to reduce focal adhesion formation[133, 134]. In the case of grooved topography, the ability of focal adhesions to form along the direction of grooves, results in cytoskeletal alignment, which is disrupted in the presence of inhibitor of G-protein Rho, but not Cdc42 or Rac, outlining the involvement of Rho in stress fibre formation[136]. The molecular mechanisms by which focal adhesions themselves align in response to grooved topography however are only beginning to emerge. The involvement of actin rich protrusions or filopodia can explain focal adhesion alignment, as time-lapse microscopy of cells cultured on nano-grooved substrates indicated that cells retract their filopodia when their direction is perpendicular to the direction of the grooves[144]. Moreover, perpendicular protrusions only consisted of immature focal adhesions perhaps due to the unfavourable force imposed on the cytoskeleton. The role of filopodia in sensing nanotopography has been further outlined in their ability to exert traction forces independent of focal adhesions, which is based on the contact angle created between the substrate and the filopodium[145]. The threshold height at which focal adhesions and the cytoskeleton can realign according to attachment by filopodia is currently estimated at 35 nm[141]. More recently, even smaller membrane protrusions termed as 'nanopodia' originating from filopodia were found to attach to 8 nm features, suggesting that cell sensing of topography occurs at

Focal Adhesions and Cytoskeleton					
Micro-topography	Material	Feature size	Cell type	Cell response	Ref
Microgrooves	Polyimide	5 μm deep, 4 μm wide	Osteoblasts	Nuclear and focal adhesion alignment	[135]
Microgrooves	Quartz	1, 2 or 4 μm wide, 1 μm deep	Corneal epithelial cells	FA alignment and stress fibre activation by Rho	[136]
Microposts	PDMS	1 μm high, 3 μm wide , 2 μm pitch	Mouse MSCs	Increased integrin recruitment, FA formation and RhoA at microposts	[137]
Micro-projections	PDMS	15 μm high	Mouse ESCs	Reduction of proliferation and Rho kinase activation	[138]
Micropillars	PDMS	5 μm high, 2 μm diameter, 2 μm pitch	MEFs	Increased FA anchorage and tension generated by vinculin	[139]
Nanoposts	PMMA	45 nm high, 2.2 μm diameter	Human MSCs	Increased cytoskeletal tension, vimentin, tubulin expression	[140]
Nanogrooves	PDMS	600 nm deep, 600 nm wide	Human ESCs	Cytoskeletal dependent cell organisation drives proliferation	[116]
Nanopits	PMMA	100 nm deep, 120 nm diameter, 300 nm pitch	Fibroblasts	Reduced FA formation, disorganised actin	[134]
Nanogrooves	PS	5-350 nm deep, 20-1000 nm wide	Fibroblasts	No alignments for depths above 35nm and width above 100 nm	[141]
Nanopillars	PS	200-700 nm diameter, 1 μm height	CHO cells	Decreased FA formation with decreasing nanopillar size, except increase with 200 nm pillar	[142]
Nanopillars	PS	200-280 nm diameter	Mouse ESCs	Increased vinculin, p-Cofilin dependent cytoskeletal organisation	[143]

Table 1.1: Summary of adhesion and cytoskeleton mediated responses induced by various substrate topographies. FA = focal adhesion, MEF = mouse embryonic fibroblasts, PMMA = polymethyl methacrylate, PS = polystyrene, CHO = chinese hamster ovary.

the scale of single integrins[146].

1.3.2 Impact of Topography on the Plasma Membrane

1.3.2.1 The Plasma Membrane: Composition, Structure and Function

In order to understand how the plasma membrane can regulate the cell response to topography, the various components of the plasma membrane must be outlined. Cell membrane receptors, integrins and other functional molecules may be anchored within or associated with the plasma membrane, a lipid bilayer mainly comprised of phospholipids (phosphatidylcholine and sphingomyelin in the outer leaflet and phosphatidylethanolamine, phosphatidylinositol and phosphatidylserine in the inner leaflet) as well as cholesterol which imparts mechanical stiffness[147]. Although initially envisaged as a two dimensional fluid structure with a few membrane proteins randomly placed within it[148], it is becoming more evident that the cell membrane contains a much greater proportion of membrane associated proteins(Fig 1.5)[149]. Membrane (associated or transmembrane) proteins are now known to interact with the membrane in a wide variety of conformations - being partially embedded into the outer or inner leaflet, oriented parallel to the plane of the membrane or in different angles, or traverse the membrane only at specific locations[150]. Due to their inherent interaction capabilities, it is now believed that membranes are comprised of preferentially segregated protein-protein, protein-lipid and lipid-lipid microdomains that behave as signalling platforms[151, 152, 149, 153]. Indeed, the evidence supporting the strength of protein-protein interactions along with the realisation that majority of proteins in the membrane are oligomeric complexes rather than single entities makes us support the idea of protein 'patches' within the membrane[149, 154].

Much in the same way, lipids in the membrane assemble together asymmetrically to give rise to different degrees of ordering, which also influences membrane fluidity. The outer leaflet of the plasma membrane, primarily comprised of sphingolipids and cholesterol have the capacity to form ordered domains, due to the close packing that is possible with cholesterol and the saturated acyl chains of sphingolipids[155]. As a result, unsaturated lipids in the membrane form disordered and naturally more fluid domains around them due to their inability to pack as tightly. Thus, by a dual process, the structuring of membrane lipids in ordered and disordered domains combined with membrane protein assemblies enable membrane proteins to oligomerise and par-

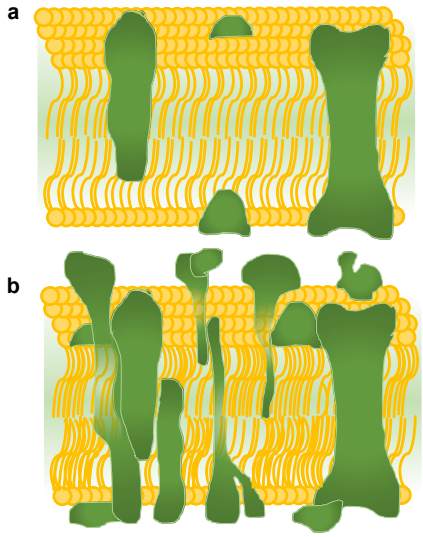


Figure 1.5: a) The initial mosaic model of the plasma membrane by [148] depicting a few proteins randomly floating within the fluid lipid bilayer. b) An updated schematic of the lipid bilayer by [149] showing that the membrane contains many more proteins than initially anticipated that may be transiently associated with membrane domains and have different membrane spanning capacities. These membrane proteins are also known to segregate through specific interactions[150]. Membrane lipids may also cluster together giving rise to differentially ordered lipid domains. Figure adapted from [149].

ticipate in signal transduction[156]. The association between membrane proteins and lipids can be important for their localisation and clustering within the membrane. For example, signalling proteins that bind to glycosylphosphatidyinositol commonly called GPI-anchored proteins (GPI-APs), are key signal transduction proteins that are closely associated with ordered domains due to their anchoring via saturated acyl chains[157]. Other membrane proteins that are myristated or palmitoylated such as G-proteins, Src kinases and Hedgehog proteins also rely on association with lipid ordered domains and clustering to initiate their signalling cascades[158]. Hence, rather than a passive system that encompasses individually functional membrane proteins, the lipids and proteins of the cell membrane exert direct control over membrane protein function through spatial segregation and patterning[159].

Since lipids in the membrane contribute to membrane fluidity, they ultimately play a key role in membrane shape, spontaneous curvature and bending stiffness[160]. If we imagine that the segregation of lipids and proteins between bilayer leaflets occurs,

the membrane shape can change from flat to curved[161]. Studies of biological membranes indicate that along with the heterogenous membrane protein population, the specific composition of lipid domains is fundamental in establishing the degree of curvature[162]. For instance, lipid ordered phases and lipid disordered phases can readily phase-separate and establish phase-dominant curvature in synthetic membranes[163]. Moreover, experimental and modelling experiments have shown that by externally controlling the degree of curvature using 100 nm patterned quartz substrates, lipid ordered domains were shown to preferentially associate with areas of low curvature, indicating that topography could have a great impact on membrane reorganisation and function as multiple cellular membranous structures exist at this length scale[164, 165, 166]. This has led to the idea that lipid ordered domains separate to form lipid rafts in the membrane, that accumulate proteins within them, a heavily controversial idea that is an area of intense research. Although the existence of lipid rafts is now clear[167], the debate as to whether lipids themselves or proteins are responsible for their formation is yet ongoing. Since phase separation has not been directly observed *in-vivo*[168], and protein-lipid interactions and protein heterogeneity exert a substantial influence over the formation of domains within the membrane, it is more likely that individual protein-lipid, protein-protein interactions within the heterogenous membrane pool leads to the formation of phase separated domains that impart membrane bending properties[160]. For example, the degree of insertion of amphipathic helices of proteins into lipid membranes can heavily influence the formation and stability of membrane curvature[169, 170](Fig 1.6). Moreover, a subset of clustered lipid raft domains that contain palmitoylated hairpin-shaped protein Caveolin-1 (Cav-1), appear as inwardly invaginating 60-80 nm structures that are reliant on Cav-1 oligomerisation within rafts[171]. Nevertheless, whether it is protein or lipid-driven organisation of the membrane, the resulting effect is that the transient and dynamic micro- or nanodomains of lipids created can ultimately influence cell function. For instance, polyunsaturated phospholipids can facilitate cell uptake mechanisms that rely on deformation, invagination and scission of the membrane such clathrin-mediated endocytosis in living cells suggests that formation of differential lipid domains in the membrane is important for carrying out a variety of cellular processes[172].

1.3.2.2 The Plasma Membrane as a Curvature Sensor

The notion that the plasma membrane is a highly active and dynamic encompassment of lipid and proteins, with bending capabilities (imparted by constituent lipids) that form tubules, vesicles or buds calls into question how the plasma membrane responds to topography. Topography of a surface ultimately induces formation of protein and lipid assemblies, and through their molecular stabilisation, trigger changes in cell behaviour. For instance, creating synthetic immunological synapses by incorporating GPI-proteins such as ICAM-1 and major histocompatibility (MHC) proteins in a lipid bilayer sup-

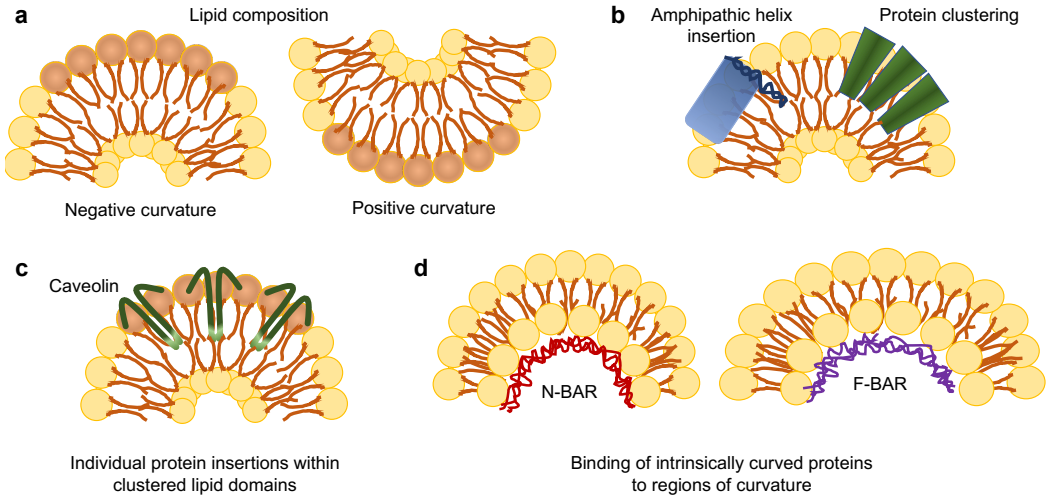


Figure 1.6: Mechanisms of membrane curvature generation a) The lipid bilayer itself can give rise to spontaneous curvature based on the type of lipids present. b) Membranes can bend when proteins segregate and form clusters or when transmembrane proteins with amphipathic helices are inserted. c) Membrane curvature is induced with the insertion of oligomerised proteins that interact with specific lipid domains such as caveolin-1. d) Membrane curvature can be developed through the binding of curved proteins, or those containing BAR domains that insert amphipathic helices. F-BAR containing proteins recognise shallower curvature than N-BAR containing proteins. Lipids shown not to scale. Figure adapted from [173, 161].

ported by a silica substrate with topographical features, resulted in specific activation of T-cells based on the spatial constraints imposed by the nanoscale surface features[174]. It can be envisaged that topography induces changes in membrane curvature, whose degree and orientation, stabilises molecular assemblies and scaffolds for signalling. The ability of cells to recognise concave (nanopits) or convex (nanopillars) and respond to them differently suggest that the membrane is equipped with machinery for curvature sensing[175, 176] (Table 1.2).

Following the bending of the plasma membrane, curvature is recognised and sta-

bilised by family of proteins that contain a crescent-shaped bin/amphiphysin/Rvs (BAR) domain. Preferential binding to curved membranes occurs primarily through electrostatic interactions between the curved amphiphysin portion of the domain. Moreover, BAR proteins can be associated with amphipathic α-helices (N-BAR) to form curved structures, Fer/Cip4 (F-BAR) forming shallow and long stuctures, or shaped inversely to F-BAR to form I-BAR domains[177, 178]. The curvature and orientation of different BARs make them capable of sensing specific degrees of curvature that relate to the function of the protein. For example, N-BARs containing proteins such as amphiphysin, nadrin and endophilin have important functions of stabilising membrane tubulation due to their propensity to bind to areas of similar positive curvature[178]. The recognition of curvature by N-BARs can initiate many cell functions. It has been shown that in nerve terminals, the recognition of the positive curvature of a budding clathrin coated pit is recognised by amphiphysin, whose binding partner dynamin is localised in the process, enabling vesicle scission[179]. Another N-BAR protein endophilin was found to control its own route of endocytosis that was independent of clathrin and other adaptor proteins that are normally necessary to facilitate cell uptake[180]. Inherently formed of shallow curvature, F-BARs are usually observed at the sites of clathrin endocytosis in its earliest stages and aid in clathrin pit nucleation[181]. Given their inverse shape, I-BARs found in protein IPSp53, is capable of recognising negative (protruding) membrane curvature are recruited to areas of filopodia formation, while interacting with small GTPases such as Cdc42[182].

Because BAR domains can recruit a host of cell signalling proteins such as GTPases, inducing BAR domain accumulation by providing topographical cues can have far reaching implications for cell signalling. Additionally, surface topography can be used to study the many unknown mechanisms of BAR domain recruitment. Cells cultured on tin oxide nanostructures (nanocones) used to induce cell membrane curvature, showed recruitment of nadrin-2, an N-BAR containing protein to the sites of nanostructure interfacing[183]. Moreover, N-BAR recruitment resulted in actin-myosin contraction and clathrin pit stabilisation. Another recent study has shown that by nanopillar topography, N-BAR containing proteins epsin, amphiphysin had a strong localisation to sites of high membrane deformation by nanopillars, while F-BAR protein FCHo1 localised to a lesser extent[127]. Proteins involved in CME such as dynamin-2

and clathrin light chain (CLC) were also seen to localise suggesting that topography induced membrane deformation can reduce the energy required to initiate endocytosis. Overall, these studies highlight that external mechanical deformations can change create changes in cell behaviour such as migration and endocytosis.

Plasma Membrane and Curvature Sensing					
Micro-topography	Material	Feature size	Cell type	Cell response	Ref
Nanocones	Tin Oxide	200 nm and 600 nm high	Fibroblasts	Localisation of BAR proteins and clathrin pit stabilisation	[183]
Nanocolumns	PMMA	160 nm high, 200 nm diameter	Fibroblasts	Some nascent vesicles, dynamin, clathrin localisation	[184]
Nanopillars	Quartz	50-500 nm radii, 700 nm height	Human melanoma cells	N-bar proteins recruited to areas of high membrane curvature	[127]
Micropillars	Titanium	5 μm high, 5 μm wide	Osteoblasts	Caveolin-1 localisation to sites of pillars	[185]
Microfibres	PMMA	1.6 μm diameter	Osteo sarcoma cells	Reduced membrane tension and cell uptake on fibres	[186]

Table 1.2: Summary of plasma membrane responses induced by substrate topography.

1.3.3 Impact of Topography on the Nucleus

1.3.3.1 Physical Linkage of the Nucleus with the External Environment

The nucleus is physically coupled with the extracellular space via the plasma membrane and cytoskeleton enabling it to respond to biophysical stimuli, including topography. Rearrangements of cytoskeletal elements can induce changes within the nucleus given their direct attachment to the nuclear envelope (a double lipid bilayer) at different locations: the Linker of Nucleoskeleton and Cytoskeleton Complex (LINC)[187] and its associated nuclear lamina[188], as well as nuclear pore complexes (NPCs)[189]. The LINC is composed of a number of proteins and their isoforms including emerin, sun proteins and nesprins. Depending on the isoform, the proteins of LINC can bind to different components of the cytoskeleton through their specific binding domains. For example, nesprin-1 and -2 link to F-actin via calponin homology domains, nesprin-3 links with intermediate filaments (IF) via its plectin binding domain and nesprin-4 links with microtubules (MT) via subunits of MT motors such as kinesin-1[190]. Nesprins

are localised primarily in the outer nuclear membrane (ONM) and the SUN proteins are integral membrane proteins of the inner nuclear membrane (INM) that extend to engage with nesprins in the lumen of the nuclear membrane[190]. Sun proteins of LINC can indirectly influence intranuclear changes through the nuclear lamina, composed of Lamins A/C and B1/2 that are a type of IF which are physically linked to chromatin. In contrast, NPCs that are found in association with MTs, offer direct channel of transport for biomolecules including messenger RNA (mRNA) sequences across the nuclear membrane based on their conformation[189](Fig. 1.7)

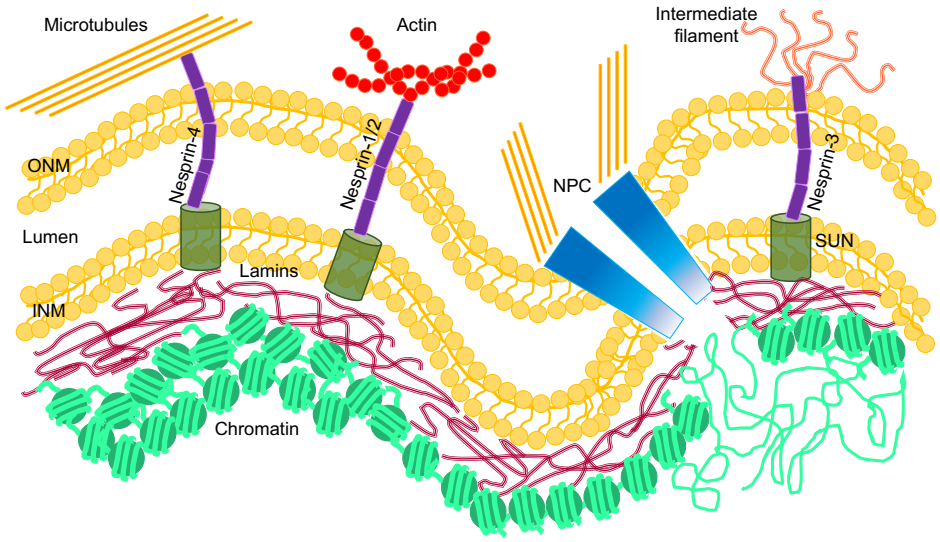


Figure 1.7: The nucleus is linked to various components of the cytoskeleton via proteins of LINC. Actin, microtubules and intermediate filaments bind to respective nesprin proteins in the outer nuclear membrane (ONM) that link with SUN in the inner nuclear membrane (INM) proteins across the lumen of the nucleus. SUN proteins are anchored to nuclear Lamins within the INM that organise the chromatin framework by associating with chromatin binding proteins[187]. In addition, the nuclear pore complex (NPC) can also bind to the cytoskeleton (microtubules) via kinesin and dynein motor proteins. The NPC plays in important role in gene expression as it modulates entry and exit of messenger RNAs as well as a host of other molecular regulatory platforms[191].

1.3.3.2 The Nucleus as a Topography Sensor

The nucleus is the stiffest organelle in the cell. Nevertheless its attachment to the cytoskeleton enables it to undergo a corresponding deformation in response to topography having profound effects on chromatin remodelling and gene expression. Movement of chromatin within the nucleus leads to gene activation and silencing based on their reorganisation and localisation[192]. It is therefore not surprising that incorporating 2D and 3D topographical cues to control of nuclear morphology have shown dramatic

effects at the level of the genome as well as the epigenome[193, 194].

The nuclear lamina has for long been known as the structural framework of the nucleus. It is responsible for the maintenance of nuclear architecture and nuclear shape, which includes nanoscale and microscale peripheral invaginations, as well as intranuclear tubulations and channels[195, 196]. While lamin A/C imparts nuclear stiffness, lamin B contributes to nuclear elasticity[197]. Lamin proteins are type V IFs that can be post-translationally modified to form a meshwork within the INM, that enables them to bind to a host of intranuclear and INM transmembrane proteins including soluble factors, Lamin B receptor (LBR), DNA/RNA complexes and histones and many others, making them critical in establishing structural organisation within the nucleus[198]. Moreover, post-translational modifications of the lamin proteins themselves can influence the shape of the nuclear envelope, as evidenced by expression of farnesylated C-terminal motifs that were sufficient to induce nuclear folding[199]. Due to their attachment to LINC, chromatin and histones, the lamina plays a role in organising peripheral chromatin, which contains majority of a cell's transcriptionally silent chromatin, otherwise known as heterochromatin. Modifications of the lamina can hence result in the loss or activation of silencing of specific genes. For instance, the importance of the nuclear lamina in maintaining nuclear architecture is exemplified in the case of cancer cells and laminopathies, where in nuclear deformations in the form of invaginations, are accompanied by a reduction in lamin levels as well as modifications in chromatin organisation and gene silencing[200, 201]. Moreover, reduced levels of lamins in neutrophils are thought to be linked to their lobed and deformable nuclei[202]. In ESCs, the initial lack of lamin A/C and high deformability eventually leads to a 6-fold increase in stiffness driven by Lamin A/C expression during terminal differentiation[203]. This feature is further emphasised by the finding that inherent ECM stiffness scales with lamin A/C expression[204]. The evidence highlights a role for lamins in providing stiffness that makes the nucleus more resistant to deformation given the downstream effects on chromatin modifications. Indeed, nuclei of cells overexpressing lamin A showed less deformation compared to non-transfected controls when cultured on nanopillar arrays[128]. In addition, an investigation of the nuclear lamina in cells confined by microgrooves showed that there were fewer lamin B1 tagged intranuclear tubules as well as invaginations, and that these changes were accompanied

by repositioning of chromosome 1 to the nuclear periphery[205].

While lamins control the structural response of the nucleus to topography, NPCs act as curvature sensors within the nuclear envelope. Similar to BAR proteins that sense plasma membrane curvature, nuclear pore complex proteins can possess similar amphipathic helices that allow them to sense nuclear membrane deformation[206, 169]. The NPC is equipped with approximately 30 different nucleoporins (NUPs), that have different roles in NPC assembly and structure[207]. The fact that nuclear deformation during interphase is accompanied by amphipathic helix containing NUP localisation such as NUP153 or NUP53 indicates a stabilising if not active role for NUPs in nuclear membrane bending[208, 209]. Moreover, through fluorescence microscopy, NUPs have been shown to localise to sites of nuclear invaginations, possibly to promote better access into the central portion of the nuclear containing highly active euchromatin[210, 211]. In this manner, it is evident that NPCs can control nuclear membrane curvature or bending and provide cytosolic-nuclear cross from various locations in the nucleus.

Nuclear Envelope and Chromatin					
Micro-topography	Material	Feature size	Cell type	Cell response	Ref
Nanopillars	Quartz	50-350 nm radius, 2-10 μm pitch, 0.7-2 μm height	Fibroblasts	Nuclear deformation highly dependent on pitch, less deformation with Lamin A overexpression	[128]
Microgrooves	Quartz	12.5 μm wide, 2 μm deep	Fibroblasts	Fewer lamin B1 invaginations, chromosome 1 at nuclear periphery	[205]
Nanogrooves	Polyimide	650 nm width, 200 nm depth	iPSCs	Nuclear elongation and alignment, transcriptional factor (TAZ) activation	[115]
Microgrooves	PDMS	10 μm wide and deep	Fibroblasts	Cytoskeletal mediated epigenetic changes that promote reprogramming	[122]
Microgrooves	PDMS	10 μm wide and deep	hMSCs	Lamin A/C knockdown does not change nuclear shape on grooves	[212]
Microgrooves	PDMS	10 μm wide, 3 μm deep	Cardiac progenitors	Nuclear elongation and epigenetic changes that promote reprogramming	[124]

Table 1.3: Summary of nuclear envelope response to surface topography. TAZ = transcriptional coactivator with PDZ-binding motif.

NPCs composition can vary with cell type as well as differentiation state. NUP210

has been shown to be highly expressed when myoblasts differentiate into myotubes, however the reasons for this in relation to the changes in nuclear morphology that occur during myoblast differentiation remain unknown[213]. Nevertheless, the ability of NPC to regulate gene expression has recently become an area of intense research, as various promoter sequences have been shown to localise with NPCs, enabling reorganisation to the nuclear periphery[214]. Moreover, the fact that NPCs are typically surrounded by euchromatin[215] and that different cell types rely on differential expression patterns of NUPs indicate that NPCs exert direct control over chromatin domains by their ability to link to different genes at different locations. Despite the recent and extensive literature on NPC function, the ability of NPCs to respond to externally induced curvature such as topography is yet to be studied. Considering these roles of the NPCs and since substrate topography influences nuclear deformation, chromatin positioning and nuclear lamina reorganisation, it is likely that these processes are heavily interrelated.

Taken together, the advances in material fabrication and high-resolution methods have allowed us to study and better characterise structure-function relationship between cells and materials. We can now attempt to tailor material properties to suit the requirements of specific cell fate transitions. In particular, material topography proves to be a valuable tool in directly influencing individual components of the cell including the nucleus and the cell membrane, which will have a significant impact on future strategies to understand and control cell behaviour.

Scope of the Thesis

This body of work aims to develop new analytical methods to assess the cell-material interface and use them to investigate the stem cell response to topographical cues.

In chapter 2, optimisation procedures of conventional and state-of-the-art techniques are discussed in relation to their applicability to studying the cell response to material topography. The chapter provides the basis for which specific protocols are selected and developed for following chapters.

In chapter 3, the nuclear response to material topography in the form of microgrooves is described using a combination of novel immunogold FIB-SEM technique alongside SICM, providing insight into nuclear remodelling, its associated localisation of epigenetic marks and nuclear stiffness that accompany cell differentiation. It is proposed that methods developed in this study can contribute to the effort of the wider research community, particularly those who study complex stem cell-material systems.

In chapter 4, the influence of nanotopography in the form of porous nanoneedle arrays on the plasma membrane and its associated components are studied in relation to endocytosis and intracellular delivery. By perturbing the plasma membrane using nanoneedles, the mechanisms of inducing biomolecule delivery via nanoneedles into stem cells is investigated, which has important findings for designing stem cell manipulation strategies.

In chapter 5, concluding remarks and avenues for future work are described, while highlighting the contribution of the body of work to the field of biomaterials and tissue engineering.

2. Optimisation of Visualisation Methods to Study Cell-Material Interactions

Advancements in material science and cell manipulation technologies have created more complex systems to study, requiring methods with accuracy, high spatial and temporal resolution, and ideally non-destructive. Along with standard molecular biology techniques, new visualisation methods and adaptations of currently existing methods is necessary. Monitoring cell phenomena in response to material cues is an important parameter for the continued development and optimisation of biomaterials to control cell behaviour. Studying sub-cellular changes as opposed to whole cells or entire tissue provides a mechanistic understanding of cellular processes responsible for the observed outcome. This task has become particularly more challenging with respect to cells cultured on biomaterials which constitute non-standard substrates that can be extremely soft, opaque, thick, or patterned. Techniques must then be adapted if possible to suit the constraints of the cell-material system. Here, a number of promising methods as well as the challenges that accompany them in studying cell-material interactions are highlighted, following which the optimisation procedures of a selection of these techniques are demonstrated with respect to the materials used for cell interfacing.

2.1 Overview of Available Techniques for Visualising Cell-Material Interactions

2.1.1 Light Microscopy

Light microscopy (LM) has been fundamental in improving our understanding of the cell response to material cues. Labelling specific cellular targets through the use of antibodies, genetic probes and membrane binding dyes, fluorescence microscopy has enabled high throughput analysis of protein expression and localisation, and is the gold standard for identifying the key aspects of cell-material interactions. In addition, because intracellular antigens and membrane components can be labelled live, the technique has revolutionised the understanding of dynamic intracellular interactions and membrane behaviour. In particular, the development of novel fluorescent probes that can specifically bind to cell membrane components in their living state is an important tool in studying how cell membrane organise themselves on new materials. For instance, the development and characterisation of polarity sensitive membrane dyes such as Laurdan and di-4-ANEPPDHQ enables their use in visualising and quantifying the degree of membrane order, when it undergoes dynamic reorganisation[216].

In the case of imaging cells on thick and/or opaque substrates exhibiting surface topography, confocal reflection microscopy has been combined with standard widefield fluorescence microscopy using an upright microscope. In this way, imaging of glial cells interacting with opaque micropillar substrates has been conducted[217]. For higher resolution confocal imaging, equipment mostly consists of inverted instruments as opposed to upright, for a number of reasons including prevention of clashing the objective into the sample[218]. Using such inverted microscopes to study of cells on opaque substrates is normally conducted by inverting the sample often along with labelling the substrate, particularly in the case of studying the cell-material interface[219]. Despite its advantages and widespread use in biology, confocal fluorescence microscopy is limited to the diffraction limit of light (200-300 nm in the lateral direction, and 500-700 nm in the axial direction at best) and often results in high background fluorescence due to reflected light from the substrate[220]. This significantly impacts the study of interactions between cells and their supporting substrate which typically occur on the

nanoscale, in the order of tens of nanometres.

Super-resolution microscopy (SRM) techniques have revolutionised the field of fluorescence microscopy as they have broken the diffraction limit. A variety of methods exist, including structured illumination microscopy (SIM), lattice light sheet microscopy (LLSM), stimulated emission depletion microscopy (STED), stochastic optical reconstruction microscopy (STORM) and photoactivated localisation microscopy (PALM). Although the principles of operation are different, SRM techniques have axial resolution of 10-300 nm and a lateral resolution of 10-130 nm[221], which can provide structural information on molecular assemblies. SRM has been used to resolve a host of intracellular and surface structures including membrane raft domains[222], NPCs[223], cytoskeletal components[224], endocytotic vesicles[225] and many more organelles and sub cellular structures[226].

The ability of SRM to study cell-material interactions has only started being explored. For instance, SIM showed that by restricting endothelial cell spreading using microcontact printing increased LINC protein density by two fold at sites of nuclear deformation[227]. Using STORM, it was found that focal adhesion protein vinculin was spaced 50 nm apart within the focal adhesion assembly, irrespective of the size of the nanopatterned adhesion island, and that vinculin became more dense on smaller fibronectin islands[228]. In addition to focal adhesions and cytoskeletal elements, the combination of 3D-SIM and fluorescence *in-situ* hybridisation enable specific chromosome territories and DNA sequences to be imaged with a resolution down to 100 nm[229]. Extending 3D-SIM to studying the structure of nuclei under the influence of material cues could provide great insight into mechanisms of material directed nuclear remodelling.

SRM techniques exhibit certain limitations. For instance, studying live cells and dynamics is difficult, mainly due to cell damage induced by laser light[230]. Moreover, the SRM techniques with highest resolution such as STORM often cannot be conducted on samples which have high depth or thickness as they work best only near the glass surface, while STED and PALM use high laser powers that can cause rapid photobleaching, damaging the cell as well as the substrate[230, 231, 232]. Moreover, although super resolution techniques provide highly specific localisation, they do not provide information about the position of the labels in relation to the ultrastructure.

2.1.2 Electron Microscopy

Electron microscopy (EM) is an indispensable tool for studying the ultrastructure of cellular components at nanometre resolution, that is mainly based on the scattering or transmission of electrons from a beam on a sample. Currently EM provides the highest resolution possible (down to 2 nm[233]) for imaging biological samples and has defined our visual perception of all organelles and subcellular structures. Techniques such as transmission EM (TEM), scanning EM (SEM), focused-ion beam SEM (FIB-SEM), and serial block face SEM (SBF-SEM) have revolutionised our understanding of biology.

The interactions between cells and materials has been studied extensively by SEM. SEM has been fundamental in our understanding of cell morphology and spreading behaviour. The majority of studies of cell-material systems use SEM to visualise cell extensions such as filopodia and lamellipodia and their interactions with materials[234, 235]. SEM imaging of cells on silicon nanowire arrays has also been used to gain quantitative information such as the force applied by cells on each wire based on the deflection angles of the wires[236].

TEM is normally the method of choice for visualisation of the plasma membrane components as well as the cell interior owing to its high lateral resolution. Samples are contrasted and block embedded in resin after which thin-sections (<100 nm) are generated using a diamond knife. In order to obtain sufficient contrast of intracellular components, a variety of staining protocols have been developed over the years. In most cases, EM preparation includes treatment of the sample with osmium tetroxide, that heavily stains lipids, improving the contrast of membraneous structures within the cell[237]. However, lipid staining is often not sufficient for visualisation of structures with high protein or nucleic acid content, such as chromatin and protein complexes, requiring the use of other contrast agents such as uranyl acetate (UA), that can enhance contrast by binding to nucleic acids, glycoproteins and lipids[238]. In addition, the contrast imparted by osmium tetroxide can be enhanced by uranyl acetate staining, via the use of mordants such as tannic acid or by the reduction of osmium tetroxide by potassium ferricyanide or lead citrate[239, 240, 241]. Other chemical agents such as Pt-Blue have also been used to generate intranuclear contrast, or stain chromosomes[242].

Investigation of the cell-material interface by TEM has been conducted on a variety of substrates including hydrogels[243], implant materials[244], biosensing apparatus[245], nanopillars[246] and electrical devices[247]. For instance, it was found by TEM that changing the surface roughness was shown to improve cell adherence to titanium substrates used for dental implants[244], tight engulfment of microelectrodes was sufficient to record action potentials[247] and membrane deformation by nanostructures induced few endocytotic events[184]. However, the use of an ultra-microtome to generate thin sections can often create artefacts in the sample during mechanical sectioning of samples consisting of different densities (biological and substrate) while studying the cell-material interface *in-situ*. Alternatively, hard substrates are removed prior to mechanical sectioning, which can also introduce artefacts while tearing off the substrate[246], or ultra-thin sections can be generated by focused ion beam (FIB) lift-out, albeit a time-consuming laborious process that is yet to be attempted.

Since sections of samples are <100 nm thick, TEM is largely considered a 2D microscopy technique. However, 3D images of nanoscale biological structures can be obtained by electron tomography, where in the beam direction is fixed and the thin section is rotated through various angles, painting a 3D picture. The various images can then be reconstructed to obtain an electron tomograph. The method usually requires sections up to a thickness of 300 nm[248]. Scanning TEM (STEM), wherein scattered electrons and their angles of scattering are detected, offers a significant advantage over standard TEM tomography as sections up to 1 μm can be analysed[249]. Although useful for specific regions of interest, gaining whole cell information is still lacking as cells are generally larger than this size.

High-resolution 3D information of whole cells can be obtained using an alternative electron microscopy technique FIB-SEM (Fig. 2.1)[250]. A focused gallium ion beam in combination with a scanning electron microscope enables imaging of biological samples *in-situ* with section thickness as low as 5-10 nm and can approach TEM-like resolution[251]. Serial cross-sections obtained via milling the front face of the sample and imaging via SEM, commonly called slice and view, allows observation of sub-cellular structures over hundreds of sections per cell to generate a complete 3D picture of its ultrastructural composition, a feature which is considerably more difficult with TEM. 3D reconstruction can be generated by segmenting the area of interest, from which

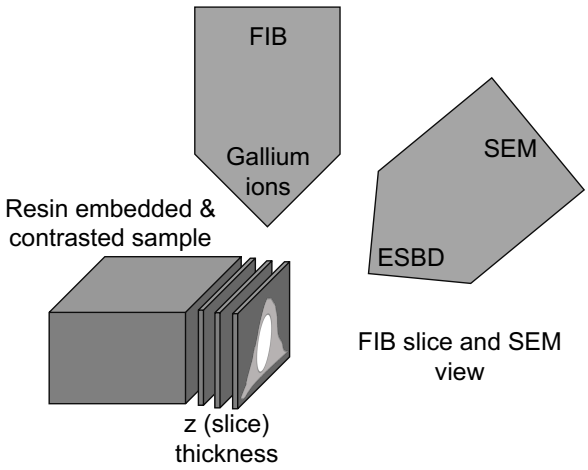


Figure 2.1: Schematic of FIB-SEM for biological sample imaging. Contrasted resin embedded samples are subject to a focused Gallium ion beam that mills the sample orthogonally. As the front face of the sample is exposed, simultaneous imaging is conducted using an angled SEM equipped with an energy selective backscatter (ESB) detector. Serial milling at slice thicknesses determined by the milling current enables newly milled front face of the sample to be imaged by SEM in a simultaneous fashion.

precise volume calculations and analyses are possible. Moreover, milling the sample *in-situ* avoids the complications of mechanical sectioning due to difference in densities between the substrate and biological material, thereby reducing the probability of artefacts at the interface. Imaging intracellular architecture by FIB-SEM to achieve TEM-like resolution is a relatively recent method, which has been achieved through similar sample contrasting methods used for TEM sample preparation, including osmium tetroxide post-fixation and staining, as well as resin embedding. Instead of mechanical sectioning, resin embedded samples are directly introduced under the FIB. Recently, FIB-SEM has been used to study cell interactions with biomaterials in the form of pillars[252], wires[253] and needles[254] as well as 3D gel systems[255]. Through FIB-SEM, a number of first instance observations have been made including the ability of cells to break nanowires off a surface and engulf them[253], undergo severe nuclear deformation at multiple locations[254, 253] or exhibit DNA damage by direct penetration of long nanowires[256]. These findings have provided insight on the many interactions that occur at the cell-material interface. However, ultrastructural information alone is often inadequate to determine the precise nature and localisation of intracellular proteins, vesicular bodies, or nuclear components.

The last decade has seen great progress in correlative light and electron microscopy

(CLEM). Localisation of proteins of interest labelled with fluorophores combined with ultrastructural information has the potential to create a complete picture of the structure-function relationship of antigens of interest. Conventional LM and SRM have been combined with SEM, TEM and more recently FIB-SEM in a number of instances to study viral-cell interactions[257] focal adhesion assembly[258], NPCs[259] and endocytosis[260]. Extending CLEM to studying cell-material platforms is currently limited by the fact that integrated microscopes as cannot image by LM or EM simultaneously due to sample opacity and thickness, and image integrating using different microscopes requires considerable technical expertise and equipment set up.

While the combination of antigen labelling and ultrastructure visualisation in the same sample represents one of the most powerful imaging techniques, introducing labels within EM samples can be done in multiple ways, each of which are highlighted in the following section.

2.1.2.1 Considerations for Labelling Proteins of Interest in EM Preparations

It is possible to combine electron microscopy with intracellular labelling. This not only allows the precise localisation of cellular targets but also provides quantitative and structural information[261, 262]. Since fluorescent probes are not visible in the electron microscope, antibodies conjugated to colloidal gold particles (immunogold) have been used to visualise labeled structures with TEM, and represents the gold standard for labelling structures of interest in EM. Depending on whether labelling is conducted before heavy metal staining and resin embedding or after ultra-thin section preparation, labelling can be classified as pre- or post-embedding. While pre-embedding has the advantages of achieving greater specificity and labelling densities than post-embedding[263], it often requires permeabilisation of the cells for efficient penetration of immunogold, resulting in damage to ultrastructure[264]. Generally, the more gentle the permeabilisation, the less the penetrability of the antibody. The use of extremely small gold particles conjugated to antibodies has circumvented some of these issues, as their small size (1.4 nm) easily penetrates cells, after which their size can be increased using silver or gold enhancement reagents to be observed under EM. As the enhancement process is highly controlled, by using different enhancement times, it has been possible

to detect multiple antigens in the same samples distinguished by gold particle size[265].

The need for permeabilisation can also be circumvented through the use of genetic probes. This occurs through expression of genetically encoded EM tags that produce horseradish peroxidase (HRP) fused to proteins of interest. Contrast is enhanced at the protein location through oxidation of diaminobenzidine (DAB) that forms a precipitate in the presence of HRP and osmium tetroxide during sample preparation[266]. However, there is difficulty in expressing HRP in the cytosol of mammalian cells as HRP requires high intracellular calcium concentrations for binding, which is not the case for mammalian cells and limits their use[267]. The use of light to generate oxygen that precipitates DAB has also been shown, although the process is limited to thin samples due to inadequate penetration by light[268]. More recent probes that incorporating ascorbate peroxidase (APEX) are currently the most advanced as they are are smaller, light-independent and can potentially be tagged to any protein of interest in mammalian cells[269, 270].

Several considerations when using genetic tags such as APEX for EM remain. The introduction of EM tags, like other genetic tags such as Green Fluorescent Protein (GFP) has the risks of affecting endogenous protein function and localisation, and controls involving antibody detection are required to assess this possibility. They also carry the risk of being cytotoxic to primary and sensitive cell types[266]. Since EM tags produce enhanced contrast via DAB, the fixation and incubation with DAB reagents must be carefully controlled in order to prevent 'spread' of the DAB product. Because the contrast of EM tags must be higher than the background, it can potentially mask the ultrastructure of nearby structures if too high, or be insufficient to detect if too low[270].

2.1.3 Raman Spectroscopy

A technique that is capable of non-invasive label free imaging is Raman spectroscopy (RS). RS is based on the principle of inelastic scattering of an incident monochromatic laser beam through its interactions with molecules of a sample. Thus RS can provide biochemical information and a spatial map of lipids, nucleic acids or protein present in a sample. This enables studying differences in the biochemical signature between cell populations, tissue samples or ECM. For instance, RS was able to distinguish between

the quality of mineral content in engineered bone tissue derived from MSCs and ESCs compared to native bone, showing that mineral from MSC derived bone was more similar to native tissue[271]. RS can also distinguish between biochemical signatures of cancerous and non-cancerous cell types[272] and ESCs and their derived cardiac progenitors[273]. Because RS can identify metabolites, RS has far reaching applications in disease diagnosis both *in-vitro* and *in-vivo*[274]. A more recent advancement of RS is 3D RS confocal imaging of various cell systems including MSCs within hydrogels, highlighting the great potential for high resolution biochemical characterisation of cells in different microenvironments[275].

Although RS non-destructively provides biochemical signatures information, some limitations remain. One of the most challenging aspects of RS is the detection of differences in chemical signatures itself, that requires high signal to background ratios, in order to decouple effects. For instance, the type of fixative and substrate can affect the Raman signal, or autoflourescence of the sample may create high background signal[276]. When these signals are low, it can also lead to high acquisition times. Moreover, for thick and opaque samples, without the use of labels with confocal, the z-axis resolution and substrate background levels remain high, complicating the analysis due to spectral signature overlap. The spatial resolution of Raman is theoretically the diffraction limit of light, but in reality because of scattering at the sample interface this is rarely achieved, and is limited to about 0.5 μm when intracellular signatures are required for localisation analysis.

2.1.4 Scanning Probe Microscopy

2.1.4.1 Atomic Force Microscopy

The basic working principle of atomic force microscropy (AFM) is that a controlled force is applied through a cantilever which deflects when it comes in contact with the sample surface, enabling topographical maps and other physical measurements to be made[277]. AFM is a technique that can be used to image surface features at the nanoscale as well as measure several functional attributes such as stiffness, binding kinetics between receptors and ligands, and membrane/protein architecture[278]. This is particularly important for studying biointerfaces, as a great deal of physicochemical attributes of biointerfaces can be measured at the length scales they occur in their native

state. Through its various imaging modes and resolution that is typically dependent on the probe tip size, AFM has been successful in imaging molecular machinery and their dynamics involved in cell-material interactions. For instance, the force of integrin-ECM adhesion and unbinding[279] and focal adhesion structure and organisation[280] can been measured using AFM. Moreover, the ability to combine AFM with other imaging or analytical tools such as confocal fluorescence or Raman spectroscopy makes it a potentially powerful non-destructive tool in characterising complex biointerfaces[281].

Since only surface features and interactions can be recorded, it constitutes a significant drawback for AFM, in terms of studying basal surface of a cell in contact with the substrate. Moreover, because all standard AFM cantilevers come into contact with the cell surface during imaging and stiffness mapping modes, they have been shown to cause cell damage in some instances[282, 283]. This is particularly important in stiffness mapping and dynamic imaging as cell viability must be maintained through physical probing throughout the experiment. Moreover, it has been shown that accurate imaging by AFM is highly sensitive to the imaging set-point used, and the most accurate images are obtained only at cell surface height, making it difficult to obtain both deformation measurements and accurate high-resolution topographical images simultaneously[284]. Cell imaging by AFM likely represents not only the surface but also the underlying cytoskeleton, as it can indent the surface by 200-400 nm at the cell periphery and close to 800 nm at the highest part of the cell[285]. A more recently developed technique, fluidic force microscopy (Fluidic FM), that uses hollow cantilevers to deliver biomolecules to individual cells as well as monitor their interactions at the cell surface[286], potentially enabling functional cell studies along with topographical imaging and force mapping[287, 288].

2.1.4.2 Scanning Ion Conductance Microscopy (SICM)

Another type of scanning probe microscopy technique, relatively less well known is scanning ion conductance microscopy (SICM). Initially developed by Hansma et al[289], SICM relies on a fluid-filled nanopipette in ionic solution to scan over biological samples without making contact with the sample surface[289, 290, 291](Fig. 2.2). The probe-sample separation is maintained by a distance control feedback hardware and software system. Voltage that is applied across an Ag/AgCl electrode in the nanopipette and a

reference electrode in the sample bath results in the ion current flow through the opening of the nanopipette. As the probe approaches the sample, resistance to current flow is built up and the ion current drops. A piezoelectric stage is used to move the nanopipette in the z-direction to keep the current at a constant value and in this manner, the z-position of the nanopipette is recorded at each point, generating a topographical map that can potentially reach a resolution of 10 nm (Fig. 2.2) [290, 292]. The resolution of the SICM image is determined by the pipette diameter and is estimated to provide a resolution of 3 times the inner diameter[293]. Typically, the set-up of SICM allows scans of a maximum size of 100 μm by 100 μm, but has more recently been developed to image 25 mm by 25 mm areas[294].

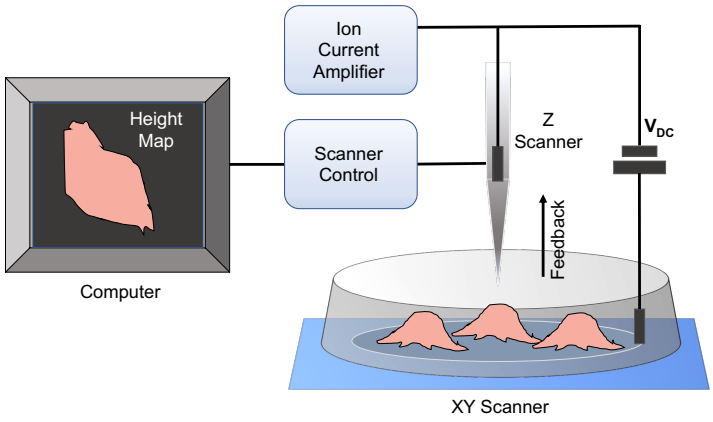


Figure 2.2: Schematic of SICM and its applications for investigating cell morphology. The sample is placed in a petri dish in ionic solution (physiological media). Voltage is applied between the silver electrodes in the pipette probe and in the bath and results in an ion current. At every pixel the pipette approaches the sample until the drop in current is achieved is between 0.25-1%. At this point the height (Z) is recorded and stored in a topographical map. The pipette is then retracted and moved to the next imaging location. In hopping mode of the probe approaches the sample from a much greater height above the sample preventing collision into tall structures[291].

SICM has been able to image clathrin coated pits at the cell surface[295], hair cell cilia[296], microvilli[297] and ion channels[298], without the need for labels or contact with the cell surface in its hydrated state. In addition, SICM has been used to map membrane contours and correlatively determine their surface charge and density, as well as study dynamic membrane events such as clathrin mediated endocytosis[295]. Due to the fact that the pipette probe can be fabricated with multiple inner channels

as well as different tip sizes and functionalisation, the SICM probe is well suited to conducting biomolecule delivery and sensing. For instance, along with obtaining nanoscale topographical information, it is possible to locate single ion channels and obtain electrophysiological recordings simultaneously[299, 300]. This multiple functionality of the SICM probe has enabled functional studies of t-tubules[301, 302] and synapses[303] as well as monitoring the release of secretory proteins[304]. Fabricating the SICM probe as a carbon double barrel electrode functionalised with poly pyroll to conduct measurements of extracellular pH[305]. SICM has also been combined with other techniques including AFM[306], shear force microscopy[307] and confocal microscopy[308], making it a powerful complementary, if not stand-alone technique.

Like AFM, SICM can be used to obtain stiffness measurements. Application of hydrostatic pressure through the pipette tip, induces membrane deformation as the tip approaches the cell surface[309, 310]. The resulting degree of deformation results in a greater distance travelled by the probe controlled by the set-point. A deformation height map is then obtained allowing calculation of the cell stiffness based on the stress applied by the probe and degree of strain of the membrane at each position[310]. Another more recent method of acquiring local cell stiffness data is by modulating the distance control feedback, without the application of external pressure[311]. This is based on the idea that as the pipette probe approaches the cell surface, the current drop is much slower for soft surface than a stiff substrate, thereby allowing multiple set-points to be used over the soft sample, inducing more deformation. This slow decrease in current can be modelled by the probe-surface interaction, where it was shown that as the pipette approaches the soft surface, it is pushed away by the glass tip by 10 times the distance than a stiff surface would be[312]. Again, because the probe does not come into contact with the sample, and because much smaller pipette probes can be used, it enables mechanical properties of biological samples to be mapped with similar lateral and vertical resolution to topographical imaging by SICM[311].

Due to the fact that imaging and mechanical mapping by SICM do not make contact with the sample surface, it is possible to study changes in cell morphology and function without the complication of probe-sample interactions, which is a considerable advantage over AFM. It has been shown that topographical imaging of cells by AFM is underestimated by 25% when measuring height, 15% when measuring the width,

compared to SICM[285]. Moreover, small features on the cell surface were also shown to be 70% smaller with AFM[285].

Like AFM, SICM is limited in terms of studying surface level behaviour of cells. In addition, the vertical system is limited in the sense that it is fitted with an inverted microscope to locate cells prior to imaging, making it less applicable to opaque or thick samples, or inaccessible surface structures. However, recently developments have been made where in SICM was combined with an upright microscope, to enable patch clamping of intercalated discs of cardiomyocytes, and visualisation of the arrangement and organisation of individual stereocilia as well as surface features of cells on opaque nanostructured arrays which was previously a challenge with the vertical scanning system[296].

A summary of the possibilities and challenges of currently available techniques is highlighted in 2.1.

Possibilities and Challenges of Existing Visualisation Techniques		
Technique	Possibilities	Challenges
LM/SRM	-SRM resolution can reach 10 nm -Multicolour labelling of antigens -Straightforward sample preparation -High-throughput compared to other techniques	-Standard LM has an upper resolution limit of 200 nm -No ultrastructural information -Applying SRM to non-standard substrates is limited by sample thickness, opacity
TEM	-Highest resolution (2 nm) -Labelling with immunogold or genetic reporters along with ultrastructure -Less time consuming (imaging) -Semi-3D up to 1.5 μm thick	-Complete 3D reconstruction is not possible -Requires lift-out or substrate removal if using biomaterials -Usually chemically fixed and dehydrated samples, cannot be conducted live
FIB-SEM	-Approaches TEM-like resolution (10 nm) -Complete 3D reconstruction of cells in-situ -No need for substrate removal -Can potentially be combined with labels -Can select and mill any region of interest at any location	-Physical destruction of the sample after milling -Artefacts from milling possible -Chemically fixed and dehydrated samples, cannot be conducted live -Time-consuming sample preparation, imaging and processing times
RS	-Chemical information from sample -Label free and live -3D imaging possible -Large depth of penetration	-Lower resolution (typically 500 nm) compared to other techniques -High signal to noise ratio required -Background autofluorescence can complicate analysis
AFM	-Fast scan time compared to SICM -Minimum sample preparation -Can be conducted live and hydrated samples -3D images obtainable -Temporal imaging possible	-Overestimates feature dimensions -Comes into contact with sample during imaging and stiffness measurements
SICM	-Non-contact, does not touch the cell surface -Resolution up to 50 nm -Live and hydrated state -3D images obtainable -Temporal events can be mapped	-Surface features only -Challenging for opaque samples

Table 2.1: Summary of current visualisation methods for investigating cell-material interactions

2.2 Chapter Aims

In light of the current techniques available for studying cell-material interactions, the aim of this chapter is to demonstrate the challenges and optimisation of visualisation techniques, prior to their use in addressing specific biological questions. In particular, this chapter highlights the optimisation procedures for sample preparation as well as microscope operation and data analysis through visualisation of subcellular features by FIB-SEM, SICM and fluorescence based two-photon microscopy.

Visualisation of intracellular features by FIB-SEM requires a sufficient amount of contrast between intracellular structures. This is usually achievable by the application of osmium tetroxide, an electron dense fixation and contrast agent. However, the degree of contrast achievable with osmium tetroxide fixation is limited as it primarily enhances contrast of lipid-dense structures. Thus in this study, staining protocols incorporating osmium tetroxide along with other contrast agents are tested with the aim to identify optimum staining parameters in a universal protocol that enable visualisation of cell ultrastructure with FIB-SEM.

Visualisation of surface features of cells on material substrates using SICM has previously not been conducted. Two methods of SICM operation, a vertical approach as well as an angled approach are described, with the aim to optimise imaging parameters to study cell behaviour on non-standard substrates. Indeed, the development of these scanning systems to study cells on opaque high-aspect biomaterial substrates demonstrated in this chapter provided the basis for its inclusion in the publication 'Angular Approach Scanning Ion Conductance Microscopy' published in 2016 by Dr. Andrew Shevchuk[296].

Lastly, the generation of novel probes for fluorescence microscopy has enabled high throughput analysis of membrane dynamics and lipid order. However, relatively little is known about using such probes (concentrations, propensity to adhere to non-standard substrates) while studying the cell-material interface, therefore requiring optimisation of probe labelling and microscope set up.

2.3 Materials and Methods

2.3.1 Cell Culture

Mouse ear fibroblasts (MERFs) from C57B/6 mice (P0) were kindly isolated and provided by Constant Morez (Imperial College London). MERFs were expanded and maintained in Dulbecco's Minimum Essential Media (DMEM, Invitrogen) along with 10% (v/v) Fetal Bovine Serum (FBS) and 1% (w/v) Antibiotic-Antimycotic (A/A, Life Technologies). For FIB-SEM experiments, cells were expanded for 1-2 passages after which they were seeded onto flat PDMS membranes (see chapter 3, methods) coated with 2% (w/v) gelatin at 10,000 cells/cm^2.

HMSCs were purchased from Lonza, expanded and cultured in Alpha Minimum Essential Medium (Invitrogen) supplemented with 16% (v/v) FBS and 1% A/A (w/v). HUVECs were cultured in endothelial basal medium supplemented with EGM2 SingleQuot Kit supplement and growth factors (Lonza). All cells were cultured in a humidified atmosphere at 37^{o}C containing 5% CO_2. HUVECs and hMSCs were subsequently cultured on nanoneedle arrays or glass coverslips at 30,000 and 20,000 cells per cm^2 as indicated for 6 hours.

2.3.2 Nanoneedle Array Preparation

Nanoneedle arrays were fabricated by Dr. Ciro Chiappini (King's College London) according to [296]. Nanoneedle arrays were functionalised with 3-aminopropyl triethoxysilane (APTES) by liquid phase conjugation (for details see chapter 4, methods).

2.3.3 FIB-SEM Sample Preparation

Media was aspirated and MERFs were washed in PBS. Prior to fixing, cells were washed in 0.1 M sodium cacodylate buffer (Electron Microscopy Sciences) for 5 minutes. Cells were fixed in 2.5% (v/v) glutaraldehyde (GA, Sigma) in 0.1 M sodium cacodylate buffer for 1 hour at room temperature. Samples were washed twice for thirty minutes in 0.1 M sodium cacodylate buffer.

For staining, cells were stained with a number of different agents (Table 2.2). All samples were stained with 1% (v/v) OsO_4 with or without 1% (w/v) potassium ferricyanide (EM Sciences) in 0.1 M sodium cacodylate buffer and rinsed with Milli-Q twice

for 5-10 minutes. Samples were subsequently processed for dehydration, or further incubated with 1% (v/v) Platinum Blue (Pt-Blue, TAAB Laboratories) in distilled water for 30 minutes, or stained with 1% (w/v) tannic acid for one hour. Samples stained with tannic acid were washed twice in Milli-Q water for 10 minutes and further stained with 1% (w/v) Uranyl acetate (UA, Sigma) in Milli-Q water for at least 2.5 hours in the dark.

FIB-SEM Sample Staining Optimisation		
Stain 1	Stain 2	Stain 3
1% OsO_4, $K_3[Fe(CN)_6]$	-	-
1% OsO_4	1% Platinum Blue	-
1% OsO_4	1% Tannic Acid	1% Uranyl Acetate

Table 2.2: Cell staining protocols for visualisation under FIB-SEM. $K_3[Fe(CN)_6]$ = Potassium ferricyanide.

All samples were dehydrated in graded series of ethanol at concentrations of 20, 30, 50, 70, 80, 90 and 100% twice for 5 minutes at each concentration of ethanol. Complete dehydration was achieved by treatment with 100% ethanol 4 times for 5 minutes. Samples were infiltrated with resin made according to the manufacturer's instructions (Epoxy resin embedding medium kit, Sigma) in resin to ethanol (v/v) ratios of 1:3, 1:2, 2:1 for 3 hours each. Pure resin was allowed to infiltrate overnight. Pure resin was replaced once and then again after 6 hours. Excess resin over the sample was removed with ethanol using a spray bottle, dipping membranes in ethanol, dabbing the membrane face down on paper towel or allowing the resin to drip off. Membranes were allowed to polymerize in an oven over 48 hours at 60^{o}C. Samples were mounted and coated with 20 nm of chromium in a sputter coater (Q150T S Quorum).

2.3.4 FIB-SEM Operation

Samples were imaged using a FIB-SEM (Cross Beam Workstation Auriga, Zeiss) with the help of Dr. Ciro Chiappini. Cells of interest were located from above under standard SEM by using an accelerating voltage of 5 kV. Once located, a region of interest was selected and a milling current of 1 nA was used, with an accelerating voltage of 1.6 kV and 5 mm working distance.

2.3.5 SICM Sample Preparation and Imaging

For experiments carried out on fixed samples, media was aspirated and samples were washed with phosphate buffered saline (PBS, Invitrogen) and fixed with 4% (v/v) paraformaldehyde solution (PFA, Sigma) following 6 hours of culture on nanoneedle arrays (For nanoneedle substrate preparation, see chapter 4). For live experiments, cells were washed in PBS, imaged in Leibovitz' media (Invitrogen) at 37^{o}C. All samples were transferred to a 35 mm dish prior to imaging.

Borosilicate glass (Outer diameter = 1 mm, inner diameter = 0.5 mm, Intracel, Cambridge, UK) was used to pull pipettes of inner diameters of approximately 100 nm using a P-2000 laser puller (Sutter Instruments, Novato, CA). Ion current measurements were obtained using Axopatch 200B amplifiers (Molecular Devices, Wokingham, UK). Prior to imaging, pipettes were filled with sterile filtered PBS. Pulling parameters for temperature and velocity of pull were optimised for each experiment to yield pipettes of roughly 100 nm and ion currents of 1 nA. A bias potential of 200 mV was applied prior to imaging and current traces were analysed using pClamp 10 (Molecular Devices).

2.3.5.1 Hopping Probe Ion Conductance Microscopy (HPICM) Operation

HPICM consisted of an upright pipette that vertically approaches the sample and an inverted microscope. After the pipette was immersed, a current of approximately 1 nA was detected, and the piezo controller was used to approach the sample. The pipette approached the sample until there was a 0.3%-0.6% drop in current due to proximity to the sample surface. Due to the opacity of the substrate, HUVECs and hMSCs were located by observing the sudden withdrawal of the piezo (by its feedback mechanism) in the z-direction when the pipette was moved in x and y directions. A quick low-resolution scan was conducted to confirm the presence of the cell. The area containing the cell was selected and scanned at high resolution. Due to the high aspect ratio of the surface features of the nanoneedles substrate, a pre-scan hop size of 10 μm was used when imaging cells in these instances.

2.3.5.2 Angle Scanning Ion Conductance Microscopy (ASICM)

The HPICM set up was adapted around an upright optical microscope (Fig. 2.3). In order to achieve this, a micromanipulator (Patchstar, Scientifica, UK) was used to coarsely position the pipette probe that allowed 20 mm of movement in the x, y and z directions, whose angle could also be changed between 0 and 90^o. Live or fixed samples were incubated with 0.5 μg/ml of Wheat Germ Agglutinin (WGA) Alexafluor 488 Conjugate (Life Technologies) for 10 minutes in the dark and washed in PBS prior to imaging with ASICM. Cells on nanoneedle arrays were located by fluorescence using an upright microscope. The pipette was immersed and approached manually with the same set-point range and current values as standard HPICM. The approach angle was set between 30-40^o. The pipette probe was then positioned accurately alongside the cell of interest to initiate scanning.

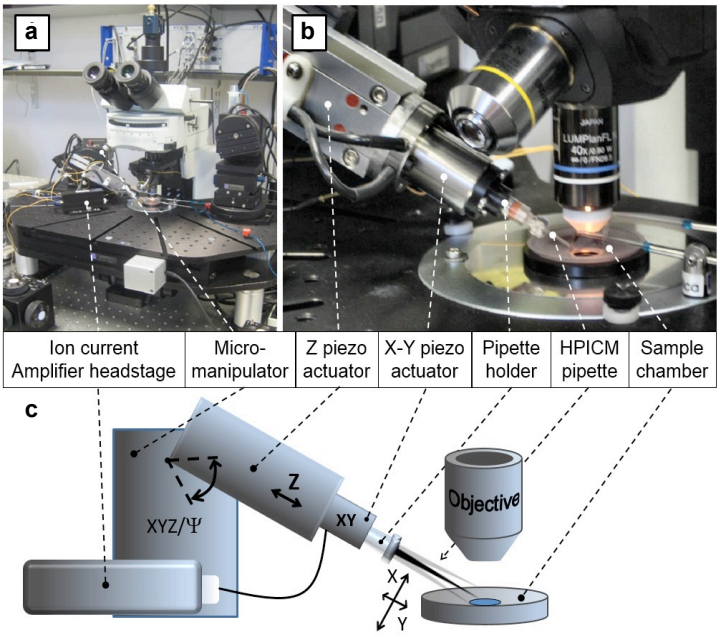


Figure 2.3: Set-up and schematic for angle scanning ion conductance microscopy (ASICM). a) SICM mounted on an upright microscope. b) View of the piezo in conjunction with the optical microscope objective. c) Schematic of the components of the angle set-up. Image reproduced from [296] with permission under the Creative Commons Attribution License.

2.3.6 Laurdan Imaging Optimisation

HMSCs cultured on glass coverslips, nanoneedle arrays or flat silicon wafers were washed with serum free media and treated with different concentrations (10, 30, 50 μM) of

fluorescent membrane probe 6-Dodecanoyl-2-Dimethylaminonaphthalene or Laurdan (Thermofisher Scientific) thirty minutes prior to washing with PBS and fixation with 4% (v/v) PFA. HMSCs on nanoneedle arrays and FSW were incubated with Laurdan containing media at 37^{o}C for 20 or 40 minutes.

Imaging of Laurdan stained samples was conducted using a Leica SP5 upright confocal microscope or Leica SP5 inverted confocal microscope equipped with a Spectra-physics Mai-Tai 690-1020 multiphoton laser and a 63x oil immersion objective. Multiphoton imaging was set up according to [216]. Laurdan was excited at 800 nm and intensity images were detected by photomultiplier tubes (PMT) at 400-460 nm and 470-530 nm.

2.4 Results and Discussion

2.4.1 Optimisation of Sample Preparation for FIB-SEM

Unlike TEM, in which cells are resin embedded in blocks and mechanically sectioned prior to imaging, FIB-SEM proceeds with direct milling of the resin embedded sample *in-situ*. Although this is advantageous for observing the cell-material interface, it does require the ability to recognise the cell surface under SEM, as blindly milling through micrometer depths of resin blocks to find a cell is time consuming. Thus, in order to identify cells on the substrate, excess resin must be removed after embedding and prior to polymerisation. For this process, a number of different approaches were tested (Table 2.2), including washing with ethanol, spraying the sample with ethanol and drying it under air intermittently, as well as allowing excess resin to drain by gravity. It was found that the excess resin was best removed by spraying with ethanol and intermittent drying. Repeating this process twice was the most effective way to retain a thin-layer of resin over the sample, allowing cells to be distinguished on the substrate (Fig. 2.4a). This method to remove excess resin is consistent with another report where rinsing with small volumes of ethanol was found to retain a layer of resin over the cells[313]. Milling the sample in this manner ensured sufficiently infiltrated sample along with a protective layer of resin above the cells, which is particularly advantageous for FIB milling (Fig. 2.4b).

Observing the intracellular architecture of cells using FIB-SEM is a relatively new technique, that has mostly been achieved through the application of heavy metal staining, as in cell preparations for TEM. In order to prepare samples with adequate intracellular contrast and ultrastructural preservation for visualisation under FIB-SEM, adaptations of different EM staining protocols that have previously been used in the literature were tested (Table 2.2). Three staining protocols were tested in which samples were always treated with osmium tetroxide, the gold standard for post-fixation and lipid staining in electron microscopy. In addition, the effect of using potassium ferricyanide, uranyl acetate and Platinum-Blue in conjunction with osmium tetroxide staining was investigated according to protocols in a number of recent papers published(Fig. 2.4c-e)[256, 314].

In order to ascertain which staining parameters were optimal for visualisation of

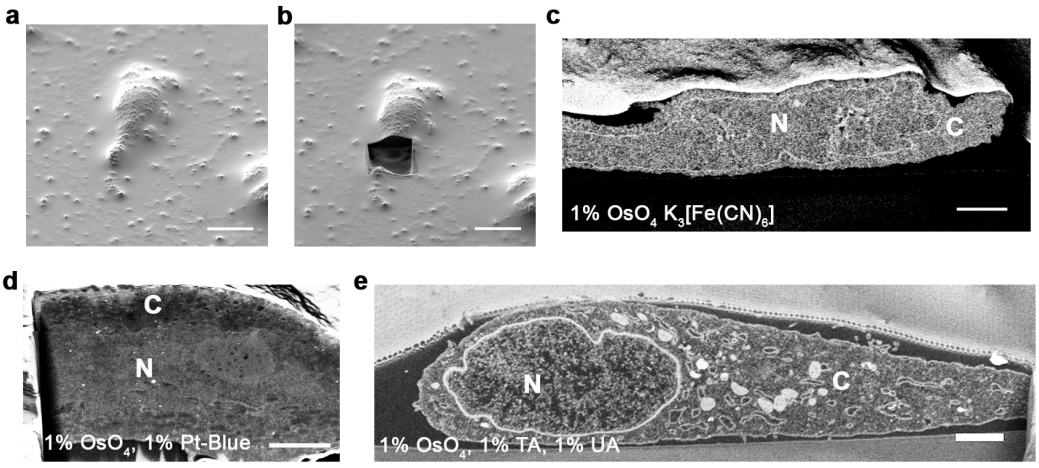


Figure 2.4: Optimisation of sample preparation for ultrastructural visualisation under FIB-SEM. a) SEM image of a MERF embedded in resin with excess resin removed by washing with ethanol. Scale bar 20 μm. b) SEM image of a MERF being milled by the FIB, exposing the cross-sectional face. Scale bar = 20 μm. c) SEM image of the milled cross-section of a cell stained with a combination of 1% OsO_4 and $K_3[Fe(CN)_6]$. Scale bar = 2 μm. d) SEM image of the milled cross-section of a cell stained with 1% OsO_4 and Pt-Blue. Scale bar = 2 μm. e) SEM image of the milled cross-section of a cell stained with 1% OsO_4, 1% tannic acid (TA) and 1% UA. Scale bar = 2 μm. N = nucleus, C = cytoplasm.

ultrastructure by FIB-SEM, milled samples were imaged using an ESB detector. SEM images of cross-sections of cells revealed vast differences in intracellular contrast. For all preparation protocols however, the nuclear membrane could be observed, perhaps due to osmium post-fixation and staining. Post-fixation and staining of cells conducted with osmium tetroxide and potassium ferricyanide showed the nuclear membrane faintly contrasted with the cytosol. However, no other intracellular structures were detected using this staining protocol (Fig. 2.4c, Fig. 2.5a). Similarly, cells post-fixed and stained with osmium tetroxide and further stained with Platinum Blue, similar to that used in [314] resulted in low contrast within the cells, although nuclear components could be faintly distinguished (Fig. 2.4d, Fig. 2.5b). Remarkably, the addition of tannic acid and uranyl acetate in the staining protocol in a sequential manner provided the best contrast and ultrastructural visualisation (Fig. 2.4e, Fig. 2.5c, d). A variety of organelles within the cytoplasm, including golgi bodies, mitochondria, lysosomes, endoplasmic reticulum as well as chromatin domains such as heterochromatin and euchromatin were observed within a highly contrasted nuclear membrane (Fig. 2.5c, d). The results indicate that the post-fixation and staining with osmium, followed by the use of tannic acid as a mordant, and uranyl acetate for further staining offers sufficient contrast to distinguish various intracellular components when imaged under FIB-SEM. This staining protocol,

was an adaptation from [256] and [252], wherein FIB-SEM was demonstrated as a valuable technique to study the cell response to surface topography in the form of high-aspect nanostructure arrays.

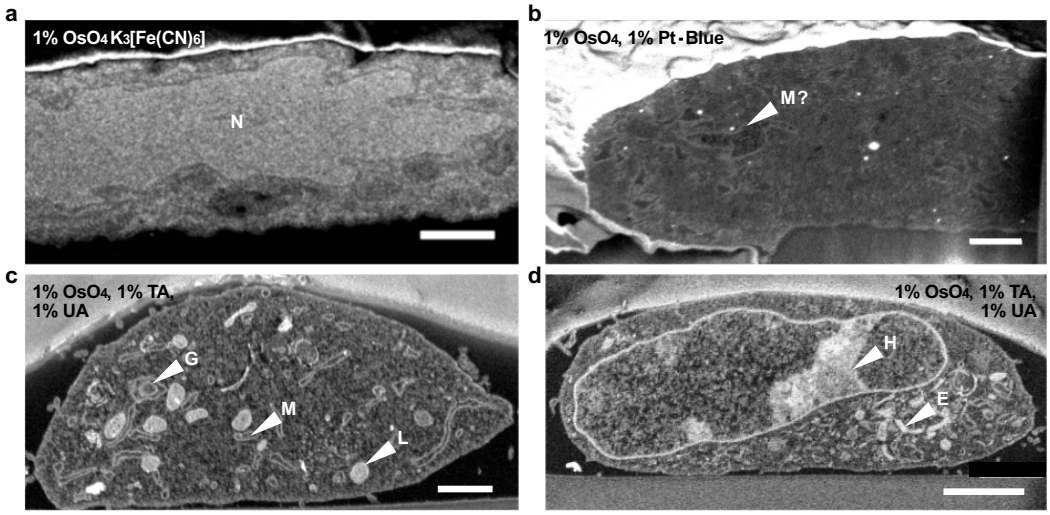


Figure 2.5: Zoomed-in SEM cross-sections of cells prepared with a) 1% OsO_4 and $K_3[Fe(CN)_6]$ indicating nuclear membrane but no other organelles. b) 1% OsO_4 and Pt-Blue indicating cytoplasmic region and potentially a mitochondrion. c) and d) 1% OsO_4, 1% TA and 1% UA indicating stained organelles and condensed chromatin. G = Golgi Body, M = mitochondrion, L = lysosome, E = endoplasmic reticulum, H = heterochromatin. Scale bars = 1 μm.

2.4.2 Optimisation of Image Acquisition by SICM

In this section, some images are reproduced from the publication 'Angular Approach Scanning Ion Conductance Microscopy' authored by Andrew Shevchuk, Sergiy Tokar, Sahana Gopal, Jose L. Sanchez-Alonso, Andrei I. Tarasov, A. Catalina Velez-Ortega, Ciro Chiappini, Patrik Rorsman, Molly M. Stevens, Julia Gorelik, Gregory I. Frolenkov, David Klenerman and Yuri Korchev. Biophysical Journal, Volume 110, Issue 10, 2016, Pages 2252-2265, DOI: 10.1016/j.bpj.2016.04.017 under the Creative Commons Attribution License. Data collection in this section are my own, and images have been adapted for publication by Dr. Shevchuk, unless otherwise specified.

For SICM imaging, two scanning approaches were used, including a vertical approach where the pipette scans the top of the cell (HPICM), and an angled approach (ASICM), where the pipette is designed to scan the top as well as side of the cell, in contact with substrate. Since the vertical approach system is equipped with with an inverted optical microscope, scanning cells cultured on opaque samples must be conducted without optical guidance. To demonstrate that it was possible to scan the surface of

cells cultured on opaque substrates, hMSCs and HUVECs cultured on nanoneedle arrays, were scanned using the vertical approach. By culturing cells at high enough densities on these substrates, a low resolution pre-scan of a 100 μm by 100 μm area was used to identify and relocate the pipette to the region of interest containing a cell (Fig. 2.6a). By scanning such a region, the area containing a cell was selected and scanned at a higher resolution.

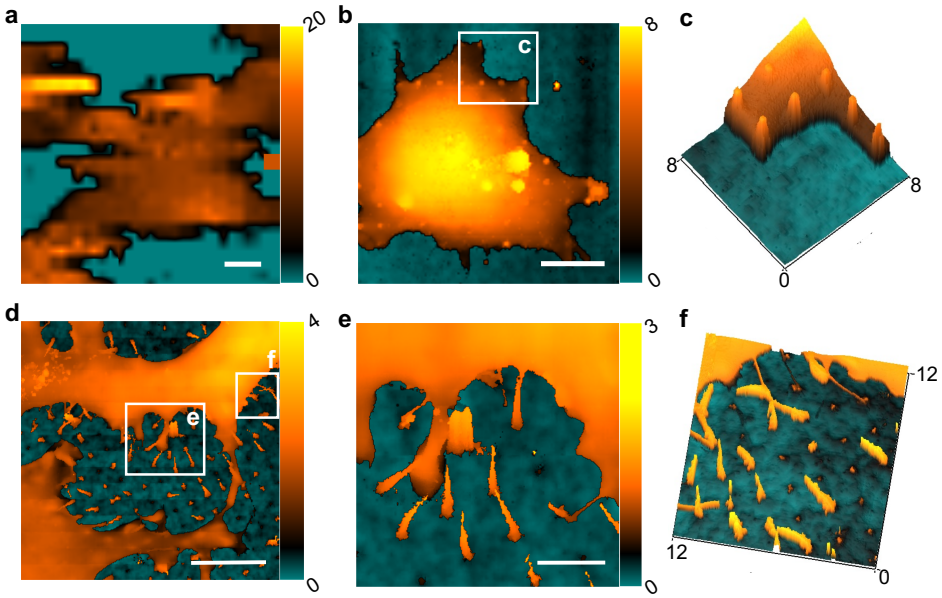


Figure 2.6: HPICM optimisation for scanning cells on nanoneedle arrays. a) Quick 100 μm x 100 μm pre-scan of cells on nanoneedle arrays used to locate cells using upright HPICM. Low resolution height map indicates presence of cell(s) (in orange, contrasted against the substrate in blue. Scale bar = 20 μm. Scan height indicated adjacently in microns. b) 2D SICM image of a HUVEC cultured on nanoneedle arrays after 6 hours. Scale bar = 5 μm. Scan height indicated adjacently in microns. Image reproduced from [296] under the Creative Commons Attribution License, copyright 2016. c) Zoomed-in 3D SICM projected of area highlighted in b) indicating edge of HUVEC following the grid-like pattern of the nanoneedles. Scan scale indicated in microns. d) 2D SICM image of HUVECs cultured on nanoneedle arrays for 48 hours. Scale bar = 10 μm. Height indicated adjacently in microns. e) 2D image of zoomed-in area indicated in d). Scale bar = 4 μm. e) 3D SICM scan of zoomed-in area indicated in d). Scan dimensions indicated in microns. Images in (b, d, e) reproduced from [296] under the Creative Commons Attribution License, copyright 2016.

Moreover, using a low set-point and high pre-scan position (10 μm) allowed the pipette to retract to a height above the sample that prevented collision when it moved laterally. In this manner HUVECs cultured on nanoneedles and could be scanned using the vertical approach (Fig. 2.6b-f). At this resolution of scanning (200 nm per pixel), nanoneedles surrounding the cell were often not detected, due to their small tip size (50-100 nm) and high aspect ratio, while the feedback control often reached the base of the

nanoneedle substrate. Nevertheless, these scanning parameters allowed for entire cells to be scanned on nanoneedle arrays, and portions of the apical cell membrane could be seen enveloping the nanoneedle arrays (Fig. 2.6b). Moreover, regions of interest such as the edges of cells interacting with the nanoneedle array could be selectively scanned and visualised as 3D maps, as indicated by the edge of the HUVEC following the grid like pattern of the array after 6 hours of culture (Fig. 2.6c). The nanoneedle arrays used in this study are biodegradable, and although little degradation is expected by 6 hours, they have been shown to remain as short stubs after 48 hours[315]. HUVECs on nanoneedles were subsequently scanned after 48 hours of culture (Fig. 2.6d-f). In this instance, images were acquired at two scanning resolutions (110 and 220 nm per pixel) to find that HUVECs appeared more spread, and confirmed that nanoneedles remained as short stumps (Fig. 2.6 d). On closer observation, the edge of the HUVECs could be observed pulling the remaining stumps of nanoneedles towards them (Fig. 2.6e). However since the pipette approaches vertically, 3D images of these regions could not be resolved as they are projected as cliffs (Fig. 2.6e). Nevertheless, the vertical approach of SICM was able to provide information not only of the apical cell surface interacting with nanoneedle arrays but also cytoplasmic extensions that seemed to cause bending of nanoneedles towards the cell (Fig. 2.6f)[296, 145].

The construction of SICM around an upright microscope enabled identification of cell location on opaque substrates prior to beginning a scan, so long as the cell was labelled using conventional membrane dyes. In this instance, WGA was used to label cells on nanoneedles prior to imaging (Fig. 2.7a). The scanning pipette was angled at 33^o to the sample surface prior to imaging. This allowed the pipette to scan the sample without obstructing the 40x objective of the upright microscope.

Due to the angled position of the pipette, raw topography images of the cells on nanoneedles causes the nanoneedles to be observed as steps (Fig. 2.7b). However, by correcting the slope, the image can be rotated to yield a visual representation of the side of the cell interacting with nanoneedles (Fig. 2.7c). 3D projections of ASICM images provided better visualisation of the edge of the cell interacting with the nanoneedles (Fig. 2.7d, e), however could not resolve details at this interface (For example, nanoneedles under the edge of the cell could not be imaged). Moreover, the maximum scan area that could be imaged by ASICM was 15 x 15 μm due to the fact that cells on nanonee-

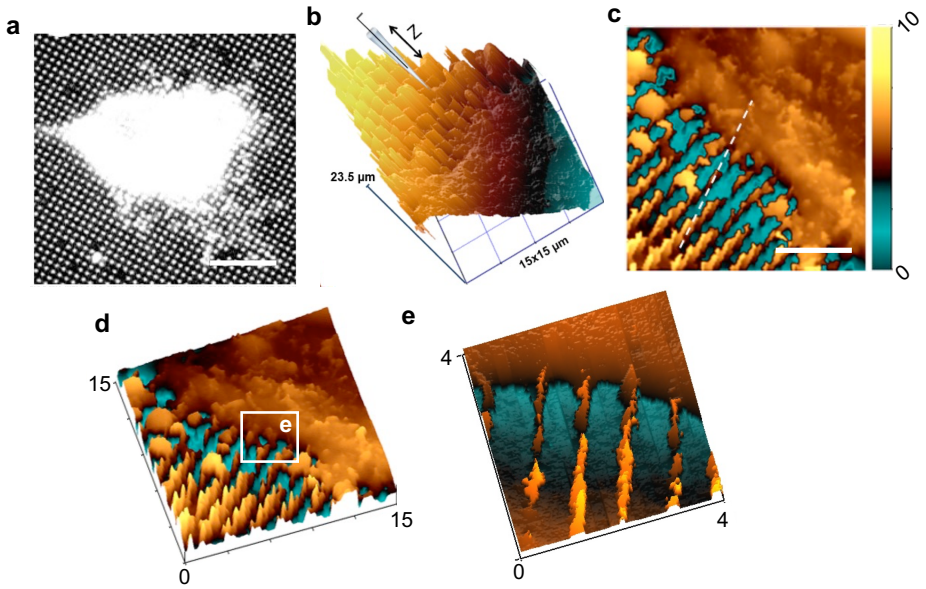


Figure 2.7: SICM imaging of hMSCs using the angled approach. a) Fluorescent image of hMSC labelled with WGA. Scale bar = 20 μm. b) 3D projected raw topographical image of hMSC on nanoneedle after 6 hours of interfacing. Schematic of pipette indicates angle of scanning. c) 2D ASICM image of hMSC cultured on nanoneedles with corrected slope from b) indicated by dashed line. Scale bar = 5 μm. d) 3D projected image of c). Scan scale indicated in microns. e) 3D Zoomed-in high-resolution image of region indicated in d) showing the angled slope corrected view of the cell-nanoneedle interface. Scan scale indicated in microns. Images (a-d) reproduced from [296] under the Creative Commons Attribution License, copyright 2016.

dles are relatively tall samples, causing inability to withdraw the pipette sufficiently for regions further away from the pipette. For these reasons, vertical scanning approach was used to assess the behaviour of the apical membrane of cells on nanoneedle arrays, which is highlighted in chapter 4.

2.4.3 Optimisation of Laurdan Staining for Membrane Order Imaging by Two Photon Microscopy

The membrane dye Laurdan was recently characterised for imaging and quantitative analysis of membrane order, which is a measure of the degree of packing of lipids in the bilayer[216]. Laurdan is a polarity sensitive dye. When Laurdan binds to a membrane in a less polar (hydrophobic and lipid dense) environment, a 50 nm negative shift in its emission spectrum results, which corresponds to a higher degree of lipid packing, often considered to be accumulation sites of lipid rafts (Fig. 2.8a). Thus, observing the spectral shift in different regions of the membrane provides information on membrane order by calculating proportions of fluorescence in two separate channels[316].

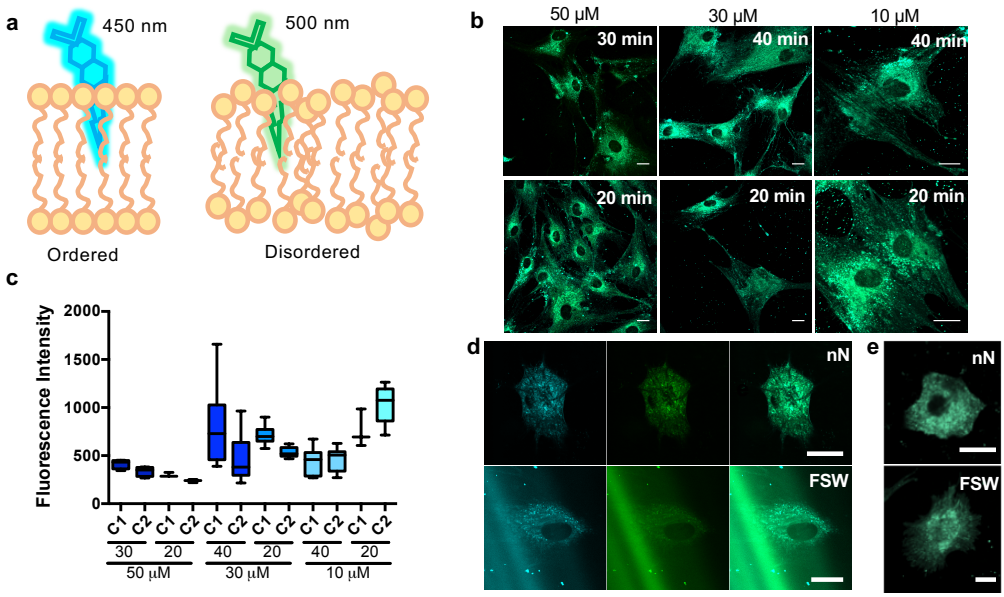


Figure 2.8: Schematic and Optimisation of Laurdan Staining for Two Photon Microscopy. a) Schematic of polarity-sensitive Laurdan dye intercalating with the membrane. Emission of Laurdan is 450 nm (cyan) when it binds to ordered regions in the membrane, whereas it fluoresces at 500 nm (green) when bound to polar or disordered regions in the membrane. b) Optimisation of Laurdan concentrations and incubation times. Merged (ordered and disordered) channel images of Laurdan labelled hMSCs at indicated concentrations and times. Scale bar = 20 μm. c) Fluorescence images of ordered, disordered and merged (L-R) of Laurdan labelled hMSCs on nanoneedle arrays (nN, top) and flat silicon wafers (FSW, bottom) after 6 hours of culture imaged on an inverted microscope. Reflection is observed for images on FSW. Scale bars = 20 μm. d) Mean fluorescence intensity measurements of Laurdan in channel 1 (C1) and channel 2 (C2) at 50, 30 and 10 μM concentrations for incubated for indicated times (in minutes) in hMSCs. Data from 5-15 cells in each condition and plotted as box and whisker diagrams. e) Merged single plane fluorescence images of the membrane region above the nanoneedles and basal membrane of hMSC on FSW labelled with 50 μM Laurdan for 30 minutes imaged with an upright microscope. Scale bar = 20 μm.

Labelling cells with Laurdan is a relatively straight forward process, that proceeds with incubating live cells with the dye for approximately 30 minutes. In order to test the labelling of membrane of hMSCs with Laurdan, different times of incubation and concentrations were tested (Fig. 2.8b). Laurdan concentrations of 50 μM, 30 μM and 10 μM were incubated with cells between 20 and 40 minutes. These concentration were selected based on Laurdan concentrations recommended in the literature[216] and that Laurdan should typically label the plasma membrane alone, and not be internalised. In addition, the intensity of the ordered and disordered channels should be similar for quantification and analysis. Thus the quantity of ordered and disordered domains can be calculated irrespective of intensity, as long as the channel intensities are similar. Incubation times for Laurdan generally range from 30 to 40 minutes. Incubation of hMSCs with Laurdan at all three concentrations and two different time points showed

similar staining distributions indicating that these parameters did not change whether Laurdan was present in the cytosol. Recently, a new variant of Laurdan, called C-Laurdan has been shown to be more specific than Laudran in labelling the plasma membrane alone, but has not been investigated here[317]. 50 μM concentrations of Laurdan incubated for 30 and 20 minutes respectively demonstrated the least difference between the two channels (Fig. 2.8c). Moreover, the variation in intensity profiles for 50 μM concentrations was much less than for other concentrations (Fig. 2.8c). Previous data of Laurdan analysis have only used single sections for quantitative analysis[318, 319]. This becomes an important consideration, particularly as the membrane of cells cultured on topographical substrates may be present in different planes. Thus for the analysis in this study, Z-stacks were obtained for membrane order quantification.

In order to image cells labelled with Laurdan, a suitable microscope set up is required. Since Laurdan is excited at 400 nm, it can be imaged easily through excitation by a multi-photon laser at 800 nm. In addition, in order to study the changes in membrane order in cells cultured on topographical substrates, hMSCs cultured on nanoneedle arrays as well as flat silicon wafer (FSW) controls and labelled with Laurdan after 6 hours. Subsequently, cells were imaged by placing the opaque substrates upside down to be imaged by an inverted microscope equipped with a multiphoton laser. Although imaging of cells on nanoneedle arrays was easily achieved, images of cells cultured on flat silicon chips contained high background perhaps due to an alignment issue of the microscope (Fig. 2.8d). To overcome this, Laurdan imaging for cells on nanoneedles and flat silicon wafers were conducted using an upright microscope which did not show any alignment artefacts (Fig. 2.8e).

2.5 Conclusion

In this chapter, the optimisation of three important techniques: FIB-SEM, SICM and Laurdan labelling for two photon microscopy was demonstrated with a view to apply them to studying cell-material interactions. An optimisation of the sample preparation method identified the optimal staining parameters for visualising cell ultrastructure by FIB-SEM. An investigation into the scanning approach and operation of SICM for imaging cells on high-aspect nanostructures was conducted to find that the membrane of cells and surface structures could be imaged with nanometre resolution on such materials, without the need for extensive sample preparation. Lastly, the optimisation of Laurdan labelling time and concentrations as well as microscope selection for quantitative analysis and visualisation of membrane order of cells cultured on opaque substrates was successfully highlighted. These optimised methods are hence incorporated into chapter 3 and 4, with a focus to elucidating key features of the cell response to material cues.

3. New Microscopy Methods to Study the Influence of Microgrooved Substrates on Nuclear Remodelling

It has previously been shown that grooved topography can induce changes in the epigenome by controlling nuclear morphology[212, 122, 124]. Moreover, nuclear elongation can induce large scale chromatin silencing as DNA staining showed that it appeared to be more dense[320]. These epigenetic and chromatin modifications are accompanied by changes in gene expression and a corresponding change in cell differentiation state. The fact that microgrooved topography promotes differentiation to cell types that intrinsically possess elongated and aligned morphology in their mature state, suggests that there is a corresponding level of nuclear restructuring that is modulated by the epigenome[124].

In consideration of the current difficulties in extending available state-of-the-art techniques such as CLEM to complex cell-biomaterial systems, and that SRM does not provide ultrastructural information, few attempts to visualise the relationship between nuclear shape and histone modifications have been made. Moreover, the vast number of studies incorporating LM are unable to provide information on the precise localisation of specific histone modifications which is important in understanding genome organisation. Moreover, there is limited application of techniques such as scanning probe microscopy, that can measure physical response of the cell to its environment.

In this chapter, a newly developed technique incorporating immunolabelling with FIB-SEM was developed to study the influence of microgrooved topography on nuclear architecture and epigenetic remodelling. Through acquisition of serial sections at nanometre resolution, entire nuclei were reconstructed in 3D. By FIB-SEM, it was demonstrated that microgrooves induced deep nuclear invaginations, while also increas-

ing density of epigenetic marks. Moreover, by immunolabelling FIB-SEM, epigenetic marks were re-located to the nuclear periphery for cells cultured on microgrooves. This data is corroborated with the finding that cells on microgrooves increase their nuclear stiffness as measured by applying a scanning probe microscopy technique, SICM.

Immunogold FIB-SEM technique can potentially be used to acquire multiple sections of cells on any biomaterial or system, as long as it fits in the constraints of the primary antibody penetration, cell membrane permeabilisation and FIB-SEM sample preparation. This allows high-resolution mapping of proteins of interest in 3D within cells in-situ, along with ultrastructural information, and without the need for separate fluorescence and FIB-SEM microscopes, which complies with the current restrictions of most cell-biomaterial systems.

3.1 Introduction

3.1.1 Nuclear Architecture and Gene Regulation

3.1.1.1 Internal Nuclear Architecture

The nucleus of eukaryotic cells is a highly organised structure comprised of compartmentalised and regulated domains, required for reliable replication, repair, gene expression[321]. The loss of genomic organisation and nuclear architecture that often accompanies infection, cancer and genetic disorders supports this idea[322]. The compartmentalised framework of the nucleus is based on the non-random positioning of its components namely chromosome territories, proteinaceous bodies (namely Cajal and PML bodies), IF rich nuclear lamina, and ribosomal RNA rich nucleoli (Fig. 3.1)[192]. that can also dynamically interact with each other to influence gene expression[323, 324]. For instance, chromosome territories are separated from one another by distinct channels called interchromosomal domains[325]. These provide conduits for RNA processing, supplied by gene active regions, typically found at the peripheral region of the chromosomes[321]. Although there is separation of the territories, significant intermingling of different chromosome territories occurs in these regions, as chromatin from different territories can loop into these regions[326, 327].

Gene active regions can also be visualised ultrastructurally in the nucleus. Located centrally, these regions are recognised by low degrees of chromatin compaction termed as euchromatin. In contrast, gene inactive or gene poor regions are visualised as dense heterochromatin normally located at the nuclear periphery[328].Gene active regions are comprised of multiple chromosome territories. For instance, outward looping of chromatin consisting of transcriptionally active genes Hox1 and Hox9 into central domains has been shown in differentiating ESCs[329], while repositioning of various genes to the heterochromatin containing nuclear periphery is a hallmark of cell differentiation[330]. These effects are also seen microscopically. TEM images of undifferentiated ESC nuclei showed a de-condensed granular appearance, while retinoic acid induced differentiation of ESCs stimulated their nuclei to form heterochromatin domains[331]. It has also been found that genes within heterochromatin may not always be inactive, as their proximity to open regions could influence their activity, and it is the density of genes,

rather than expression that is different between euchromatin and heterochromatin domains[332]. Moreover, because of the sponge-like structure of chromosomal territories, and the looping of interchromosomal domains into heterochromatin compartments, nuclear transcription factors can still access these regions[327, 333]. Nevertheless, the function of heterochromatin as a repository for inactive genes represents an important feature for maintaining nuclear function and gene expression[334].

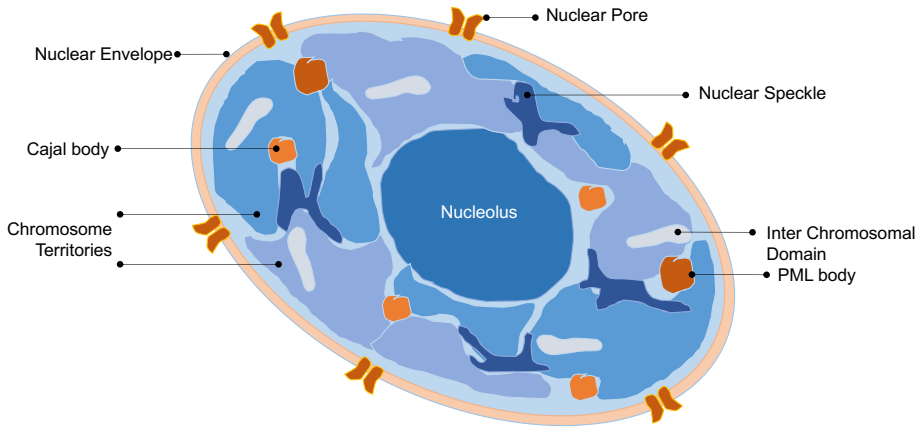


Figure 3.1: Schematic of nuclear architecture. The nucleus is organised into distinct domains as its constitutive components occupy non-random positions. Chromosome territories form the major distinct compartments which are separated by interchromosomal domains. Other substructures of the nucleus include the nucleoli, Cajal bodies and PML bodies, as well as nuclear speckles. The nuclear envelope is also punctured with nuclear pore complexes.

3.1.1.2 Nuclear Shape

In addition to internal nuclear architecture, nuclear shape plays an important role in cell function. Not only does nuclear shape vary with cell type, but also with differentiation or disease state[335]. It has been suggested that nuclear shape and morphology is regulated by the actin cytoskeleton and microtubules through their direct links with the nucleus[336, 337, 338] while the nuclear lamina is responsible for the maintenance of nuclear shape based on the dramatic changes observed in nuclear morphology in various laminopathies[199]. The nuclear envelope is composed of a double lipid-bilayer, perforated by nuclear pore complexes (NPCs) that span both membranes. While its outer membrane forms a continuous structure with the endoplasmic reticulum, its inner

membrane is in contact with the nuclear lamina and chromatin. Together they form a complex and tubulated organelle within the cell, referred to as the nucleoplasmic reticulum (NR)[339]. Although the inner and outer membranes often follow the same path and are found to invaginate deep within the nucleus (type II NR), the inner nuclear membrane has also been found to invaginate on its own (type I NR). Although they may be present in many cell types, the precise functions of type I and type II NRs are only beginning to be understood (Fig. 3.2)[339, 340, 211]. Currently, it is thought that type II NR provide access to the central nucleoplasm, where majority of active genes are transcribed. In addition, NPCs have been found to localise at these sites, facilitating import and export from the centre of the nucleus[210, 341]. NR invaginations have also been linked to calcium signalling as specific calcium release receptors have been found at NR locations, that can also lead to spatial control of calcium dependent transcription[342]. Yet another function of the NR is highlighted by its proximity to nucleoli, that are rich in ribosomal RNA, possibly facilitating the export of such molecules via NPCs[343].

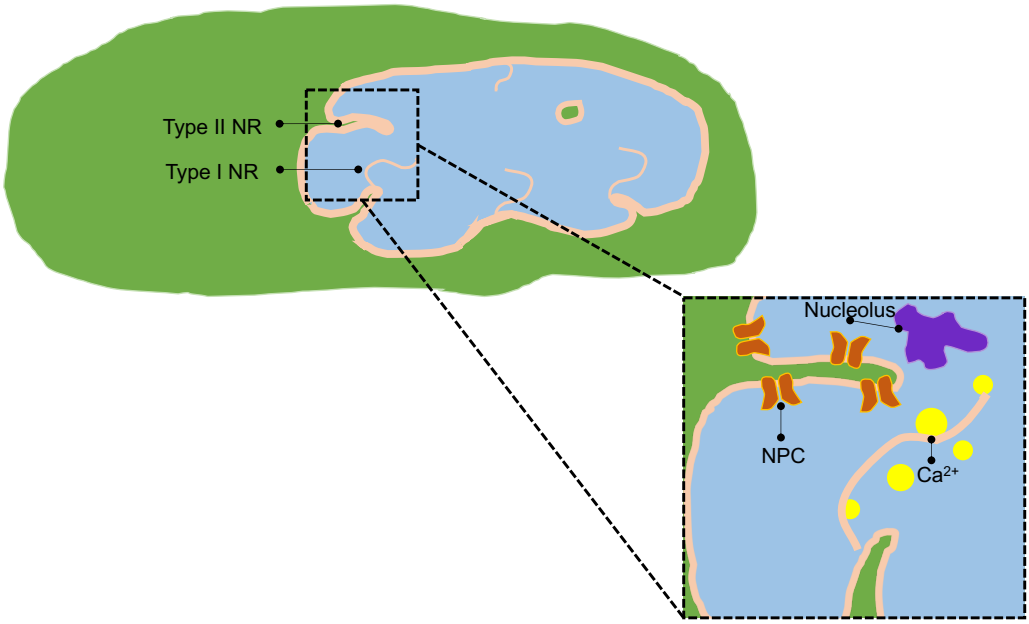


Figure 3.2: Schematic illustration of the nucleoplasmic reticulum (NR). Invagination of the INM called type I NR, or the ONM and INM called type II NR can regulate external architecture of the nucleus and provide channels of functions to the inner nuclear area. Type II NR may be studded with NPCs and have been found in close proximity to nucleoli, while type I NR have been found to consist of calcium receptors and kinases that regulate calcium signalling.

3.1.2 The Epigenome and Gene Regulation

The division of the eukaryotic nucleus into organised compartments provides sites for transcriptional activation and silencing, and the organisation of these compartments is dictated by their chemical modifications and resulting structural framework. Chemical modifications of the DNA backbone itself such as methylation of DNA on cytosine residues of CpG dinucleotides present in repetitive sequences and promoter regions is an epigenetic modification that directly regulates gene expression[344]. The methylation of cytosine, orchestrated by a family of enzymatic proteins, DNA methyltransferases (DNMTs) typically results in transcriptional silencing, that is normally mediated by recruitment of methyl-CpG recognising proteins (M-CpG) that bind to these sites[345, 346]. The methylation of DNA at CpG islands is often associated with heterochromatin at the periphery as distinct foci in interphase nuclei[347]. However, it is debated whether methylation itself can induce chromatin compaction. While a single molecule approach based on fluorescence resonance energy transfer (FRET) in an isolated system showed that chromatin compaction and rigidity increased with methylation of DNA, another study demonstrated by nucleosome digestion of nuclei of ES cells that DNA methylation had no effect on compaction, reflecting the complex interplay between multiple regulatory components[348, 349]

In addition to DNA methylation, chemical modifications of histone proteins constitute another form of epigenetic modification. An octamer of histone proteins encompassed by 146 base pairs of DNA constitute a nucleosome. Nucleosomes are linked together much like beads on a string, giving rise to the basic structure of chromatin[350]. Higher order chromatin structure is established through interactions of nucleosomes, and subsequent compaction of fibres that is mainly stabilised by histone linkers[351]. Histone proteins H2A, H2B, H3 and H4 can be chemically modified on their N-terminal tails that protrude outwards from chromatin fibres. Covalent modifications such as methylation, acetylation, sumoylation, ubiquitination and phosphorylation can take place at site-specific residues lysine, arginine, serine and threonines (Fig. 3.3). These modifications are carried out by families of enzymes that may act to specifically target a particular residue or act on more than one residue[352]. For instance, histone lysine methyl transferases can methylate H3 lysine 9 (H3K9) or H3K4 residues depending

on their enzymatic SET domain[353]. In contrast, histone deacetylases (HDACs) that are responsible for removing acetyl groups from histones are relatively non-specific and have been shown to act on multiple residues on histones[352]. Like DNA methylation, the resulting modifications have profound implications for gene expression and silencing. For instance, acetylation of lysine residues on histones can lead to neutralisation of the positive charge that otherwise attracts the negative charge of the DNA backbone, allowing DNA to be more accessible at the nucleosome, a case for directly modifying chromatin structure[354]. Majority of the histone modifications are found on lysine residues, while other residues such as serines and threonines can be phosphorylated, and arginine could be methylated. The different types of histone modifications can result in changes in the biochemical environment disrupting or promoting the localisation and interaction of various proteins involved in chromatin remodelling[355].

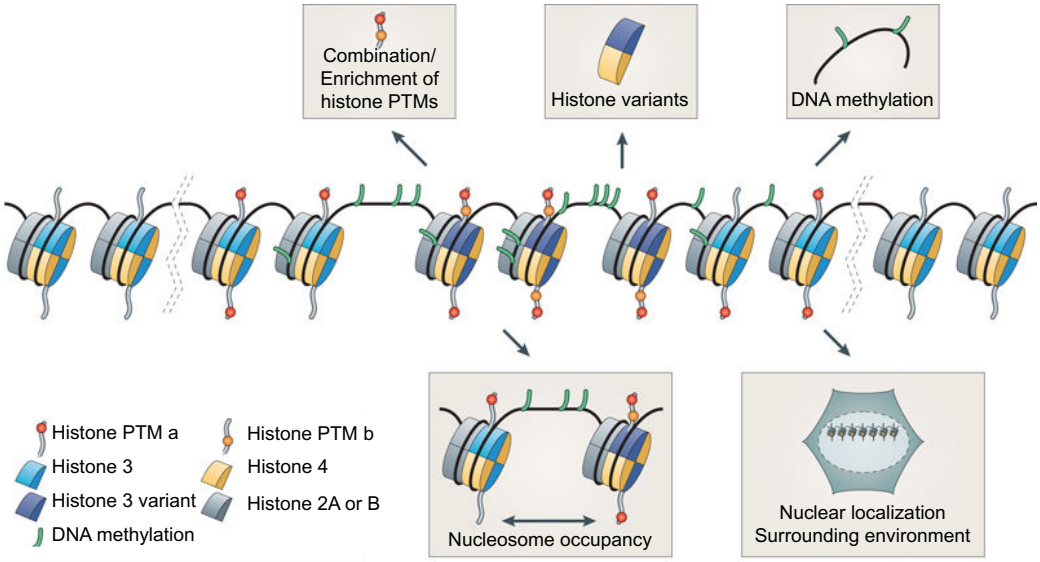


Figure 3.3: Schematic of epigenetic modifications responsible for gene activation and silencing. Epigenetic modifications are present on the DNA backbone itself as DNA methylation and as post-translational modifications of histone proteins that bind and package DNA. Depending on the type of modification on the DNA or histone, chromatin may be segregated into different domains (dashed line). Moreover, the enrichment of specific combinations of epigenetic modifications can also contribute to the nature of the chromatin order or landscape. Nucleosomes can also occupy specified regions that may be dictated by methylation patterns of DNA. Figure reproduced from [356] with permission from Springer Nature, copyright 2010.

Moreover, DNA methylation and histone epigenetic modifications exhibit significant interdependence. For instance, DNMTs and M-CpG proteins are known to facilitate recruitment of histone repressor complexes consisting of HDACs[357], while histone methylation of lysine residues recruits HP1 that in turn facilitates DNMTs to methylate

CpG islands. This in turn attracts M-CpG proteins that recruit HDACs resulting in a positive feedback loop for maintenance of repression[358].

While there is some evidence that histone modifications can directly impact chromosome structure, an alternative model is that histone modifications regulate chromatin structure via their ability to recruit specific proteins based on the histone code[359, 360, 361]. Methylation of specific lysine residues including tri-methylation of H3K4 (termed as H3K4me3) and acetylation of lysine residues on histones 3 and 4 have been found in majority of gene active regions. Normally, these histone marks are associated with chromatin decondensation, and are found on chromosome loops that can extend out of chromosome territories[329, 362]. In contrast, the epigenetic mark H3K9me3 (tri-methylation of lysine 9 on histone 3) acts as a repressive mark shielding transcription factors from accessing genomic regions when present at promoter sites[363]. H3K9me3 in turn can recruit chromatin remodelling complexes heterochromatin protein 1 (HP1) that result in heterochromatin nucleation and gene silencing[364, 352]. The loss of methylation of H3K9 also leads to genomic instability and heterochromatin disorganisation[365]. However, when H3K9me3 modifications are located within the gene sequence, it can behave as as an active mark[366]. This highlights that site-specificity in the histone code, particularly for H3K9me3, accounts for transcriptional control. Modifications of histones may also contribute to the positioning of chromosomes as it has been shown that inhibiting HDACs results in large-scale relocation of chromatin to the nuclear periphery[367].

3.1.3 Heterochromatin and the Nuclear Envelope

The presence of condensed heterochromatin at the nuclear periphery has led to investigating this region as a gene silencing compartment. In mammalian cells, multiple gene loci have been found to re-locate to the nuclear periphery and associate with peripheral heterochromatin[368]. However, considering the non-random positioning of chromosomes, and that some genes can remain active or inactive irrespective of their positioning[369], accumulation of peripheral heterochromatin is considered an effect rather than a cause of silencing. Moreover, silencing at heterochromatin regions is not considered to be an accessibility issue, due to the sponge-like structure of these domains, as well as their ability to loop inwards, as mentioned previously. To this end,

it is important to understand how peripheral heterochromatin is regulated to control and silence particular gene loci.

Peripheral heterochromatin is tethered to the nuclear lamina, a meshwork of intermediate filament proteins called lamins (see section 1.3.3.1). The lamin proteins including A-type (Lamin A/C) and B-type (Lamin B1 and B2) anchor to the INM by associating with integral SUN proteins. The importance of the nuclear lamina in regulating peripheral heterochromatin is based on the findings from the loss of peripheral heterochromatin that occurs during structural integrity of the nuclear lamina in ageing, laminopathies, and cancer[370, 201]. Moreover, unfavourable changes in nuclear shape are frequently observed in laminopathies, highlighting the interdependency of chromatin structure, nuclear shape and lamina integrity[199, 371]. In addition, the lack of lamin A/C and lamin B receptor (LBR) proteins in rod photoreceptors is accompanied by an inversion of global chromatin positioning, where heterochromatin is located in the nuclear interior[372]. The fact that this can be reversed by ectopic expression of LBR highlights the role of the nuclear lamina in tethering heterochromatin to the nuclear periphery[372].

The nuclear lamina and its binding partners can exert control over peripheral heterochromatin by their ability to bind to transcriptional repressors[373]. Transcriptional repressors such as HDACs can bind to lamin binding proteins that are present in the INM such as emerin and lamina-associated polypeptide-2-β (LAP2β), thereby stimulating deacetylation[374, 375]. Deacetylation via HDACs facilitates both CpG methylation and HP1 mediated H3K9me3 accumulation. LAP2β, emerin, and another INM protein MAN1 (collectively termed as LEM), have been shown to bind directly to chromatin at the nuclear periphery via BAF, a chromatin binding protein[373]. In contrast, LBR can bind to heterochromatin via HP1, which in turn binds and accumulates H3K9me3, thereby enriching and maintaining the peripheral heterochromatin with this repressive histone mark[202].

The interactions of heterochromatin and the nuclear lamina at the nuclear envelope are key to modulating gene expression, and as a consequence, cell differentiation. In undifferentiated states, the nuclear lamina is devoid of lamin A and cells display very few heterochromatin foci[376]. As cells differentiate and lose their pluripotency, the expression of lamin A commences, initiating peripheral heterochromatin tethering, while

also increasing nuclear rigidity and large scale gene silencing[377]. This is accompanied by an increased coverage of H3K9me3[378, 363]. The finding is supported by the fact that the use of biochemical inhibitors of H3K9me3 and HDACs in differentiated cell types can aid in maintenance of stem cell plasticity through their ability to control heterochromatin dynamics[378, 379]. In addition, H3K9me3 is considered to be a barrier to cell reprogramming[363]. Thus both the nuclear lamina and heterochromatin contribute significantly to structural as well as biochemical alterations of the nucleus, which has implications for stem cell differentiation as well as reprogramming.

3.1.4 Using Material Cues to Induce Nuclear Remodelling

Nuclear lamins play a significant role in imparting mechanical stiffness to the nucleus as it has been highlighted that lamin A/C increases with increasing tissue rigidity, substrate stiffness as well as cytoskeletal tension[204, 380, 197]. Moreover, external forces such as shear, compression and tension have all been shown to reorganise lamin A/C[381]. These studies provide evidence that nuclear lamins can directly sense and transduce mechanical forces from the extracellular environment, potentially leading to adaptations in chromatin structure and epigenetic modifications through their close association with heterochromatin.

Biophysical cues can control cell and nuclear morphology to induce dramatic alterations in chromatin organisation as well as in transcription[320]. Nuclear deformation induced by micropatterning of endothelial cells stimulated chromatin condensation and a subsequent reduction in cell proliferation[320]. This is consistent with another study in which increasing tensile stress on rectangular micropatterns was also shown to induce nuclear indentations in the lamina along with regions of condensed chromatin[227]. The effect of substrate topography on nuclear architecture has also been investigated. MSCs and fibroblasts cultured on 140 nm diameter nanocolumns show reduced nuclear area, and also stimulated chromosomal repositioning[382]. In other instances, substrate topography in the form of microgrooves reported similar changes in chromosome positioning in addition to silencing at telomeric regions which occurred in a lamin-dependent manner[205].

Unsurprisingly, the alterations in nuclear shape and chromatin condensation induced by material cues are often accompanied by changes at the epigenetic level

(Fig. 3.4). An increase in chromatin condensation and decrease in global gene expression is accompanied by decreases in histone 3 and 4 acetylation in epithelial cells forced to adopt a rounded morphology by circular micropatterns and 3D culture systems[383]. Opposite results have been observed in another study using MSCs on 10 μm microgrooves, indicating that nuclear elongation and increased tension are more favourable for increasing H3 histone acetylation and decreasing HDAC activity[212]. As an increase in histone acetylation is reflective of more accessible chromatin structure, the epigenetic signature of fibroblasts was altered to facilitate cell reprogramming using microgrooves (Fig. 3.4c, d). Along with global increases in active marks such as H3K4me3 and histone acetylation, topography in the form of microgrooves was seen to eliminate the need for biochemical epigenetic modifiers such as valproic acid[122]. More recently, microgrooved topography facilitated the generation of cardiomyocytes from cardiac progenitor cells, while suggesting that global acetylation mediated by microgrooves elicits a favourable epigenetic response that promotes forward reprogramming[124].

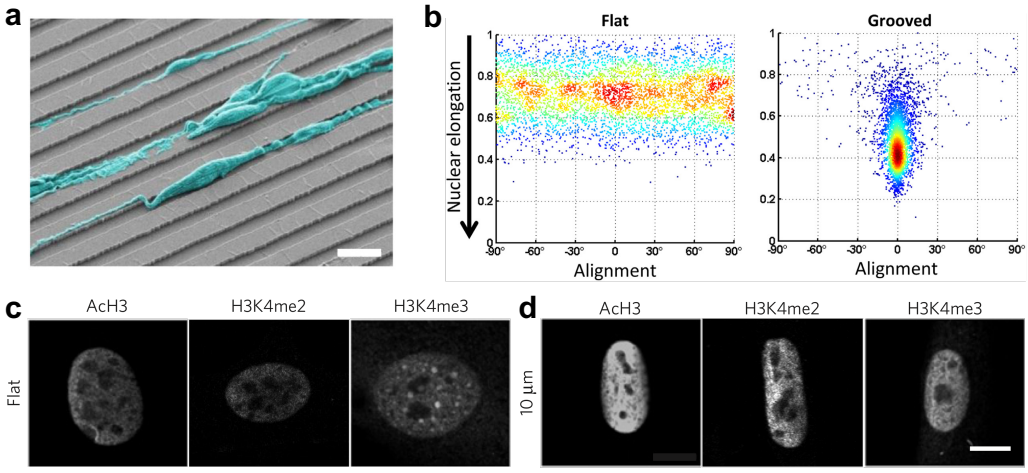


Figure 3.4: Using microgrooved topography to stimulate epigenetic remodelling. a) False-coloured SEM image of cells on microgrooves indicating elongated cell morphology and b) corresponding analysis of nuclear shape as a result of culturing cells on microgrooves indicating significant nuclear alignment. Scale bar = 20 μm. Images reproduced from [124] under the Creative Commons Attribution License. Confocal micrographs of fibroblasts cultured on c) flat and d) microgrooves labelled with indicated epigenetic modifications showing intensity of acetylation and histone marks. Scale bar = 10 μm. Images reproduced from [122] with permission from Springer Nature, copyright 2013.

3.1.5 Developing New Techniques for Studying Nuclear Response to Material Topography

3.1.5.1 Immunogold labelling with FIB-SEM

The potential of simple material cues to modulate changes in the epigenome that regulate differentiation provides immense opportunity for stem cell differentiation and reprogramming platforms. However, in order to develop such platforms towards clinical integration or into cell culture systems, it is necessary to characterise and understand the mechanisms of these precise interactions.

3D confocal microscopy has been instrumental in enabling the visualisation of not only the gross distribution of histone labels, but also the morphology of the nucleus. For instance, high magnification Z-stack projections of nuclei labelled with different histone marks have indicated the typical staining pattern of H3K4me3 which is seen to be present in the central portion of the nucleus[384], while H3K9me3 typically adopts a similar pattern of distribution to DAPI, co-localising with individual heterochromatin foci[385]. Moreover, the ability to label two different antigens in the same sample enables the distribution of histone marks within the nucleus to be studied in relation to its envelope morphology[384].

It has thus been possible to extend 3D confocal microscopy to characterising the influence of surface topography on histone distribution, nuclear morphology and architecture in separate instances[122, 124, 205, 128]. Although each of these studies investigates histone marks and nuclear architecture separately, a recent report incorporating SRM technique SIM was used to image the nuclear lamina, along with the actin cytoskeleton and DAPI-stained chromatin. This study highlighted the increase chromatin compaction as well as the ability of the actin cytoskeleton to localise to sites of high nuclear deformation that occurred in response to culturing cells on long rectangular micropatterns[227]. Because the nuclear lamina is continuous with the nuclear membrane, immunolabelling of lamin proteins allows detection of the contour of the nuclear membrane, which has enabled the detection of type II NR (deep nuclear invaginations) in a number of cell types[384, 386], as well as proposed to be influenced by microgrooved topography[205]. In addition to 3D confocal microscopy, a report investigating the nuclear response to cell interfacing with nanopillar arrays showed by

TEM that the nuclear membrane heavily deformed around the nanopillars, although no conclusions about internal nuclear architecture were made[128].

Thus most studies investigations of nuclear remodelling in response to material topography have utilised either 3D confocal microscopy that provides localisation information or TEM for structural information, limiting the ability to provide insight into structure-function relationships. For instance, elucidating how histone modifications are influenced alongside nuclear ultrastructure can shed light on the mechanisms involves in nuclear remodelling in response to material cues.

Of the number of current techniques (reviewed in section 2.1) that have the potential to study nuclear and epigenetic changes in response to material topography, FIB-SEM is ideally suited to visualising cell-material interactions, as it allows imaging of the cell in cross-section, *in-situ* at any desired location[252]. For instance, FIB-SEM enables particular regions of interest (ROI) to be imaged as the sample can be milled till the ROI appears during slice-and-view. In this way, the distance of the deforming nuclear membrane from nanopillars could be studied[252]. Moreover, samples can be milled in different directions that allows freedom to observe and orient the slices for 3D visualisation. Along with ultrastructural information, it is necessary to obtain information about specific proteins and their modifications that otherwise cannot be distinguished by ultrastructure. Immunogold labelling, routinely used in conjunction with TEM offers a straightforward readout of labelled antigen along with ultrastructural information. Moreover, the ease of detection of gold particles at the site of interest offers robust analysis compared with more ambiguous genetic probes that work by enhancing regional contrast alone.

Thus, given the advantages of using FIB-SEM for obtaining 3D ultrastructural information of cell-material interactions, its combination with immunogold labelling can potentially provide correlative information required to discern the nature of these complex biointerfaces, a method that is yet to be developed.

3.1.5.2 SICM in Stiffness Mapping Mode

Given the intimate link between nuclear shape, architecture and its mechanical properties, material topography can induce modifications of nuclear stiffness based on its ability to stimulate changes in nuclear morphology[387, 128, 388]. AFM has contributed

significantly to the study of mechanical properties of cells on various topographical substrates. For instance, culturing cells on 400 nm wide microgrooves compared to 2 μm wide microgrooves resulted in a decrease in the elastic modulus of nuclei measured by AFM, that was accompanied by a decrease in nuclear volume[387]. The ability to measure nuclear stiffness alongside obtaining fluorescence microscopy information, provides insight into how cells remodel their nuclei in response to substrate topography. For instance, using micropillar topography, AFM measurements showed unexpectedly that cell types that exhibited the highest deformability also demonstrate great cell stiffness, perhaps owing to the thick actin stress fibres observed correlatively by confocal microscopy[389].

SICM has recently demonstrated enormous potential for mapping the topography and elastic modulus of cells with higher lateral resolution than AFM[311, 285, 284]. Moreover, because the technique maps stiffness without coming into contact with the sample, it can potentially be used to gain stiffness measurements without inducing damage and minimally impacting cell physiology. Stiffness measurements using SICM are obtained alongside topographical imaging, thereby allowing correlations between nuclear topography and stiffness measurements to be made. A relatively new technique, low stress stiffness mapping is yet to be attempted on cells cultured on topographical substrates, and could provide an additional powerful tool in characterising the cell response to material topography.

3.2 Chapter Aims

Substrate topography in the form of microgrooves has previously been shown to facilitate cell reprogramming and differentiation via adaptations in nuclear architecture and downstream modifications in the epigenome. However, the specific nuclear adaptations that occur in response to microgroove topography in triggering epigenetic changes are yet to be elucidated (Fig. 3.5). Moreover, the close relationship between the 3D nuclear architecture and its mechanical properties warrant further characterisation to establish that microgrooved topography can induce changes in nuclear stiffness via modifications in nuclear architecture. In order to study these phenomena, new techniques must be

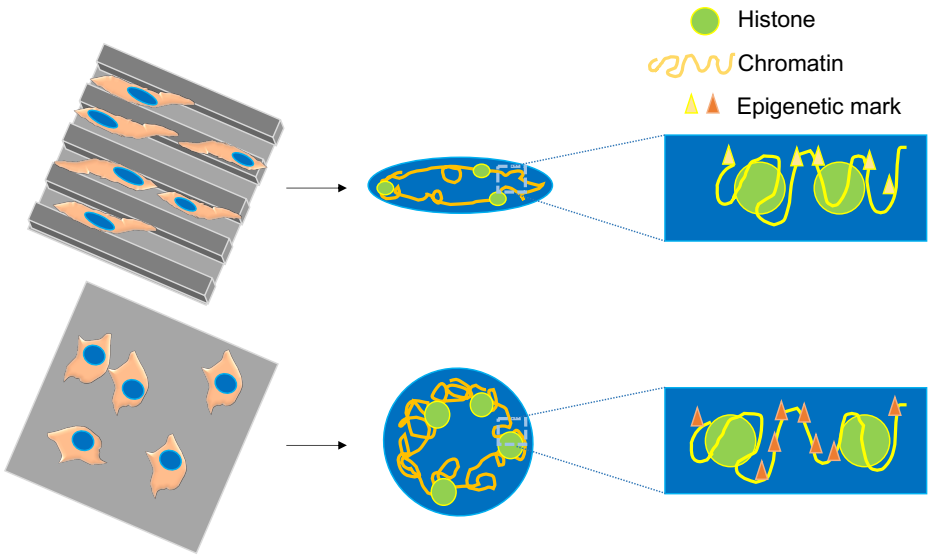


Figure 3.5: Schematic of the potential influence of microgrooved topography to stimulate epigenetic modifications. Cells cultured on microgrooved may adopt elongated morphologies which result in altered cytoskeletal organisation, resulting in nuclear shape changes. Nuclear shape changes can in turn exert effects on the internal chromatin structure and organisation in terms of its compaction and epigenetic modification through direct links to the cytoskeleton. Specific epigenetic marks may be reduced, increased or relocated.

developed and applied. While FIB-SEM has shown particular promise in revealing the cell-material interface at nanometre resolution, the combination of ultrastructural information with specific protein targeting using a robust immunogold labelling method has not been conducted previously. In this chapter, a technique using immunogold labelling and FIB-SEM is developed to elucidate the structural aspects of the relationship between the material-initiated stimulus and epigenetic response, that has the potential

to provide unprecedented resolution and spatial awareness. In order to demonstrate proof-of-concept of this method, a previously characterised microgrooves system used to influence the epigenetic state of neural stem cells was selected. Through this system it was previously found that the histone methylation mark H3K9me3 was markedly upregulated in response to microgrooves of 10 μm width and 10 μm height. For this reason, neural stem cells cultured on these grooves were selected to assess the localisation of H3K9me3 in relation to the ultrastructure of the nucleus in 3D. Second, by applying recently developed low-stress SICM, the mechanical properties of cells in response to microgrooved topography are measured. Through the application of these methods, the effect of biophysical cues induced by topography on nuclear ultrastructure is highlighted, potentially allowing these methods to be extended to a wide variety of cell-material systems.

3.3 Materials and Methods

3.3.1 Antibodies

Anti-H3K9me3 was purchased from Abcam. Anti-rabbit fluoronanogold-Alexa488 (FNG) was purchased from Nanoprobes. Donkey anti-rabbit secondary antibodies were purchased from Invitrogen.

3.3.2 PDMS substrate fabrication

Silicon wafer moulds of parallel microgrooves (10 μm wide and 3 μm deep) were prepared and provided by Dr Ciro Chiappini using established soft lithography techniques. For PDMS production, silicone elastomer and curing agent (Sylgard 182 Kit, Dow Corning) were mixed in a ratio of 10:1 (v/v) and placed in a vacuum chamber for 30 minutes. Silicon wafer moulds were subsequently spin-coated with PDMS at 500 rpm for 40 seconds. For curing, spin-coated moulds were placed on a hot plate for 15 minutes at 140^{o}C. Membranes were peeled off the masters, cut to appropriate dimensions with a blade or hole punch (depending on the application). They were then were sonicated in 70% (v/v) ethanol for 20 minutes (VWR, 150T sonicator) following which they were dried and oxygen-plasma treated for 1 minute (PlasmaPrep II, Gala Instrumente) to increase hydrophilicity and binding of protein coatings. Membranes were subsequently washed in 70% (v/v) ethanol and transferred to a culture plate under sterile conditions after which they were UV-sterilized for 1 hour and coated with 2% (w/v) gelatin and 1% (w/v) laminin in an incubator for at least 30 minutes prior to cell seeding.

3.3.3 Cell culture and Seeding

Neural stem cells (NSCs) were cultured and seeded on substrates by Chia-Chen Hsu (Department of Materials, Imperial College London). NSCs derived from hESCs and hiPSCs were detached with Accutase (Stemcell Technologies, UK) when the cells were 80 to 100% confluent. The dissociated cells were suspended in PBS, pelleted at 300 x g for 5 minutes and were resuspended in NSCR Neuron medium into the single-cell level and counted. Cells were plated on substrates placed within a 48-well plate at a density of 6.6 x 10^4 cells per cm^2 for immunostaining assays.

3.3.4 Immunolabelling for Flourescence Microscopy

Immunolabelling for standard fluorescence microscopy was performed by Chia-Chen Hsu. Immunolabelling for standard fluorescence microscopy were performed using the following protocol. Cells were fixed with 4% (v/v) PFA for 15 minutes, permeabilised with 0.2% (v/v) Triton X-100 for 10 minutes at room temperature, and then blocked in 3% (v/v) goat serum for at least 30 minutes. Primary antibody against histone 3 lysine 9 tri-methylation (H3K9me3) was then incubated with the sample for 1 hour in PBS, and washed three times in PBS followed by secondary antibody incubation for 30 minutes. The nuclei were counterstained with DAPI along with the secondary antibodies. The samples were mounted on slides with FluorSave^{TM} Reagent (Millipore, UK) and the cells fixed on the culture plates were preserved in PBS, and were both stored at 4^{o}C in the dark. Images were acquired with an epifluorescent microscope (EVOS FL Cell Imaging System; Life Technologies) or a SP5 MP/FLIM inverted confocal microscope (Leica).

3.3.5 Immunolabelling for FIB-SEM

HiPSC-derived NSCs were fixed with 4% (v/v) PFA for 15 minutes, permeabilised with 0.1% (w/v) Saponin (Sigma-Aldrich) or 0.1% (v/v) Triton X-100 for 5 minutes at room temperature, and then blocked in 3% (v/v) goat serum (with 0.1% (w/v) saponin for saponin-treated samples) in PBS for 30 minutes. The H3K9me3 primary antibody was then incubated for 1 hour in 1.5% (v/v) goat serum (and 0.1% (w/v) saponin for saponin-treated samples) in PBS. For pre-embedding fluorescence-immunogold labelling, samples were washed in 5% (w/v) skimmed milk in PBS 6 times for 5 minutes and then incubated with FNG for 1.5 hours in 1% (w/v) skimmed milk (and 0.1% (w/v) saponin for saponin-treated samples) in PBS in the dark at RT. Finally, samples were washed 4 times for 10 minutes in PBS and fixed with 2.5% (v/v) glutaraldehyde (GA, EM Sciences) in PBS for 10 minutes, rinsed 3-4 times in PBS and mounted in Vectashield (Vector Labs) for fluorescence imaging, prior to immunogold enhancement.

3.3.6 Gold Enhancement

For enhancement of FNG, Gold Enhance EM Plus (Nanoprobes) was used. Samples were washed extensively in double distilled water to remove any salts remaining. All reagents were prepared according to the manufacturer's instructions. Gold enhance solution was applied on samples for strict 5 minutes and washed in double distilled water twice for 5 minutes.

3.3.7 Electron Microscopy Preparation

Staining Samples were incubated in 0.1 M sodium cacodylate buffer twice for 5 minutes. Samples were then treated with 1% (v/v) OsO_4 solution in 0.1 M sodium cacodylate buffer for 1 hour at room temperature. Samples were washed in Milli-Q water twice for 5 minutes and incubated with 1% (w/v) tannic acid solution in water for 1 hour. Samples were washed in Milli-Q water twice for 5 minutes and incubated with 1% (w/v) filtered UA solution in water for at least 2.5 hours in the dark.

Dehydration Samples were taken through a series of dehydration steps (20, 30, 50, 70, 80, 90%) with each concentration of ethanol applied twice for 5 minutes. Samples were transferred to 100% ethanol four times for 5 minutes.

Resin embedding For resin embedding, Epon resin embedding kit was used to infiltrate the samples as described previously (Chapter 2). Excess resin was rinsed off with ethanol until a thin layer of resin was remaining on the samples. Infiltrated samples were polymerised at 60^oC for 24-48 hours. A schematic of the entire sample preparation process can be found in Figure 3.6.

3.3.8 FIB-SEM Operation

Samples were sputtered with 10 nm chromium (Quorum Q150T S) prior to FIB-SEM imaging. Samples were imaged using a FIB-SEM (Cross Beam Working Station, Auriga, Zeiss). Cells of interest were located using secondary ion beam at accelerating voltage of 5 kV and a standard aperture of 30 μm. The stage was tilted to 54^o, the acceleration voltage dropped to 1.6 kV and the cell was milled with a current of 1 nA at a working distance of 5 mm. Sections of 30 nm were milled and imaged at an interval of 3 resulting in a section thickness of 90 nm using an ESB detector.

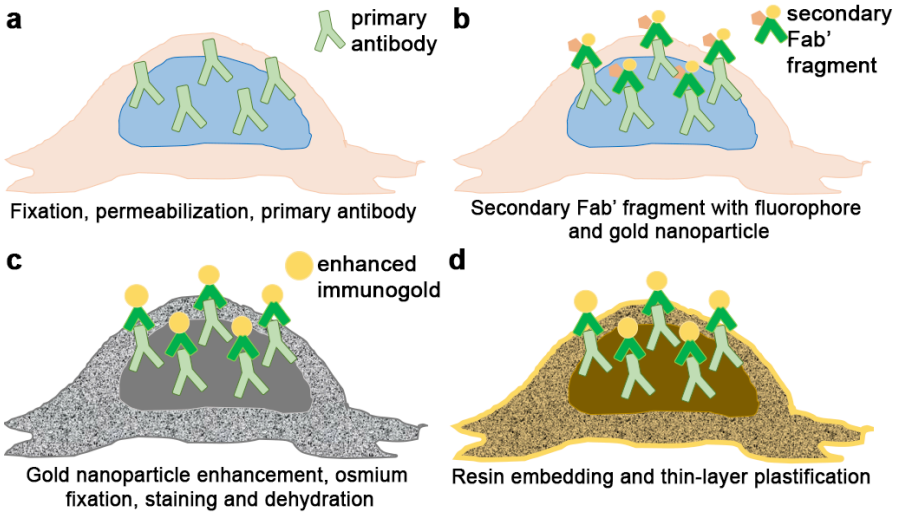


Figure 3.6: A schematic of pre-embedding immunogold sample preparation for FIB-SEM. a) Cells are labelled with primary antibody along with permeabilisation agents. b) Cells are labelled with a secondary antibody comprised of a Fab' fragment conjugated to a 1.4 nm gold particle and AlexaFluor molecules after which they can be observed with standard confocal or widefield fluorescence microscopy. c) The gold particle size on the Fab' fragment is enhanced up to 40 nm to enable clear detection under FIB-SEM. d) Samples are prepared for FIB-SEM by a standard protocol of fixation, staining, dehydration and embedding after which samples are milled with FIB-SEM for immunogold localisation of the protein of interest.

3.3.9 Energy Dispersive X-ray (EDX) Spectroscopy

EDX spectroscopy was conducted with Dr. Ciro Chiappini. EDX spectra were obtained with AZtec Energy system and INCA software (Oxford instruments) equipped within the FIB-SEM instrument. Point wise spectra were collected by dwelling the electron beam at the desired spot. Spots with high electron scattering putatively associated with gold nanoparticles were analysed, alongside control spots. The incident electron beam energy was set at 20 keV and the emitted X-ray collected over the 0-10 keV energy range, integrating for 60 seconds for every point. The INCA software analysed the relative atomic and weight composition of the selected elements within the analysis area.

3.3.10 Image Analysis

FIB-SEM images in .tiff formats were aligned in Amira (FEI) using a combination of manual and automatic alignment. Regions of interest such as the nucleus or immunogold labels were segmented manually. Segmented label files were converted into 3D tiffs which were then imported into ImageJ or Volocity (Perkin Elmer) for further analysis

(Fig. 3.7).

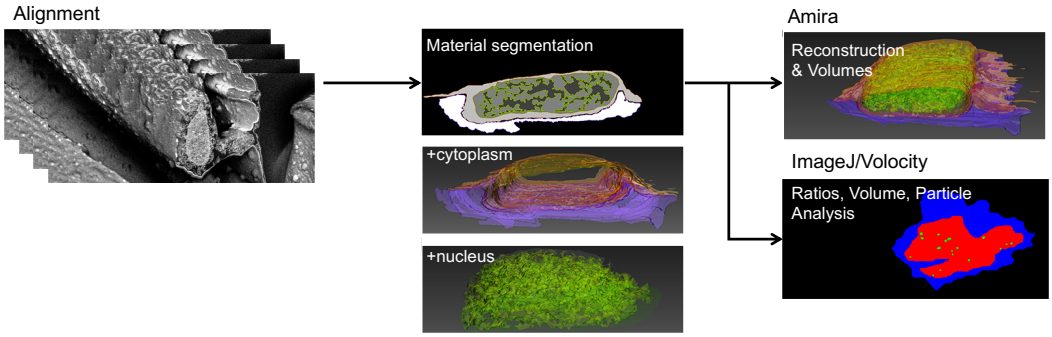


Figure 3.7: Process flow of FIB-SEM data processing and analysis. After the acquisition of serial cross-sections of complete cell nuclei, sequential images are aligned with a combination of manual and least squares aligning methods in Amira. The region(s) of interest are segmented in each slice manually using the lasso or paint tool resulting in different materials such as the cytoplasm, nucleus, immunogold, etc. Segmented regions from serial cross-sections are reconstructed in Amira to obtain volume and surface measurements. Materials segmented can be imported to ImageJ as multi-channel images to enable distance, particle and volumetric measurements of individual materials.

3.3.11 SICM Stiffness Mapping

hiPSC-derived NSCs were plated by Chia-Chen Hsu onto a 35 mm dish at 9.5 x 10^4 cells per cm^2, and the stiffness of the live NSCs was measured 48 hours after cell seeding using SICM. Borosilicate glass (Outer diameter = 1 mm, inner diameter = 0.5 mm, Intracel, Cambridge, UK) was used to pull pipettes of inner diameters of approximately 100 nm using a P-2000 laser puller (Sutter Instruments, Novato, CA). Ion current measurements were obtained using Axopatch 200B amplifiers (Molecular Devices, Wokingham, UK). Prior to imaging, pipettes were filled with sterile filtered PBS. A bias potential of 200 mV was applied prior to imaging and current traces were analyzed using pClamp 10 (Molecular Devices). Samples were placed in 35 mm dishes (Corning) and media was changed to warm Leibovitz-15 (Invitrogen) for the duration of the experiment. Stiffness maps were generated by simultaneously recording three topographical images at progressively increased set points using approach speed of 30 nm $ms^{-}1$ as described previously[311]. The topographical measurement (Z height) was acquired at set point of 0.3%-0.4% of ion current drop compared to the reference (maximum) current[291]. At this set point only minimal stress in the range of 0.1 Pa to 10 Pa is exerted by the nanopipette on the cell membrane. Then, the nanopipette was further lowered to two consecutive set points of 0.6% and 3% and corresponding heights were stored as separate

readings before the pipette moved to the next horizontal location. Eventually each image had recorded height maps representing height differences, effectively representing sample strain as the pipette deformed the sample at two higher, compressive stresses. Cell stiffness measurements were obtained for each height map on the basis of stress and strain using SICM image viewer software written by Dr. Pavel Novak, Queen Mary University of London.

3.3.12 Statistical Analysis

Statistical analysis was performed using GraphPad Prism 6.0. In the case where data was not normally distributed the non-parametric unpaired Wilcoxon-Mann-Whitney test was used. For analysis involving immunogold labelling, the paired Wilcoxon matched pairs signed rank test was used due to variations in immunogold labelling and enhancement between experiments. Significant differences were reported for p-values <0.05.

3.4 Results

3.4.1 Characterising Nuclear Morphology with FIB-SEM

In order assess the effect of microgrooved topography on nuclear morphology with FIB-SEM, serial cross-sections of complete nuclei of NSCs on microgrooves and flat PDMS substrates were acquired at a section thickness of 90 nm. Cells present within the grooves were selected for imaging and analysis. 3D reconstructions of nuclei on grooves appeared more elongated while displaying multiple folds on their surface (Fig. 3.8a, top). In contrast, nuclei on flat substrates appeared more rounded and did not exhibit folds on their surface (Fig. 3.8a, bottom). However, there was no significant reduction in nuclear volume for cells on grooves compared to flat substrates (Fig. 3.8b). Interestingly, cells on microgrooves exhibited a significant increase in surface area to volume ratios, consistent with what was observed in the 3D reconstructions (Fig. 3.8c). In addition, individual cross-sections revealed a high degree of nuclear invaginations in cells cultured on microgrooves compared to cells cultured on flat substrates (Fig. 3.8d). These invaginations could often be observed along multiple serial sections (often over a micron in length, and several hundred micrometres in width). Moreover, the number of nuclear invaginations was quantified in 3D reconstructions of nuclei on microgrooves and flat surfaces by segmenting the invagination in each image. This indicated a significantly higher degree of nuclear folding (over a two-fold increase) for nuclei on grooves compared to flat substrates (Fig. 3.8e, f).

3.4.2 Optimisation of Pre-embedding Immunolabelling for Fluorescence Microscopy and FIB-SEM

In order to investigate the effect of permeabilisation agents on immunolabelling for fluorescence microscopy, cells cultured on microgrooves and flat PDMS substrates were fixed in 4% PFA and permeabilised prior to immunostaining with 0.1% Triton X-100 or 0.1% Saponin. For cells cultured on microgrooves or flat substrates and permeabilised with Saponin or Triton X-100, both treatments resulted in detectable fluorescence of the H3K9me3 signal indicating that both Saponin and Triton effectively permeabilise the cell for entry and localisation of the primary antibody (Fig. 3.9). Moreover, the signal of histone mark H3K9me3, typically present in the nucleus overlapped with DAPI

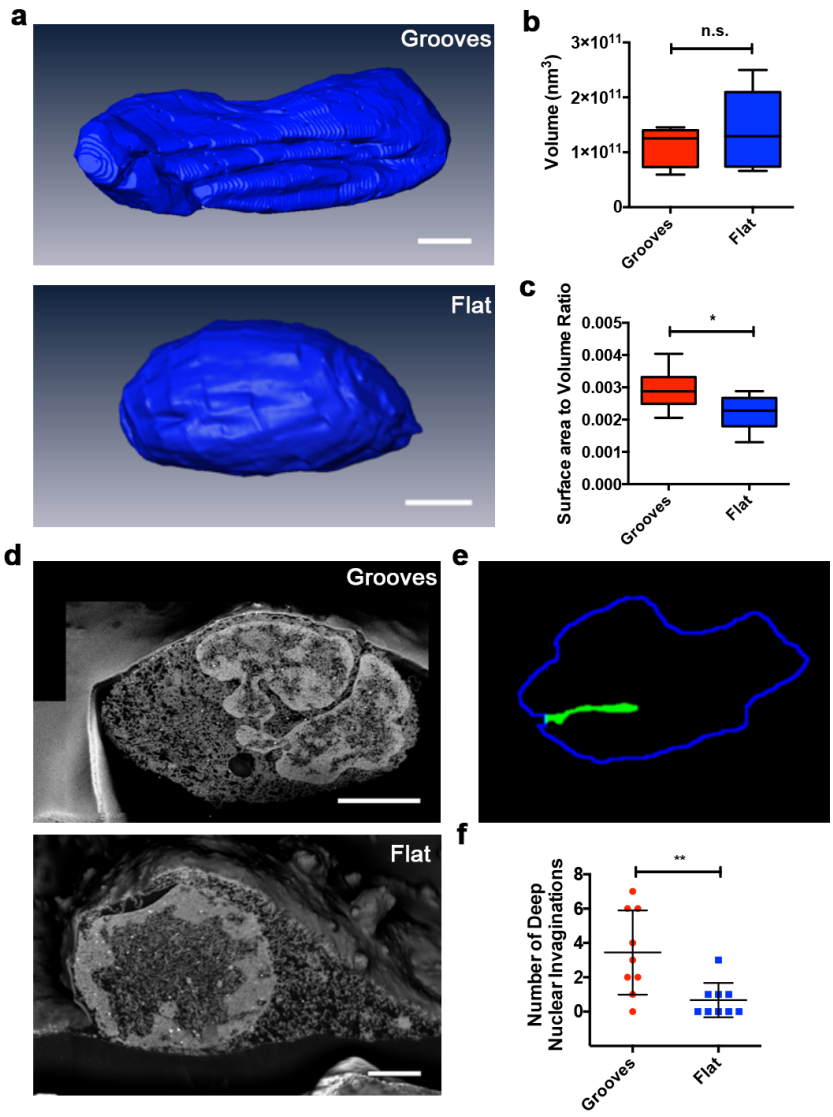


Figure 3.8: Characterisation of nuclear morphology on microgrooves with FIB-SEM. a) Representative 3D reconstruction of NSC cultured on microgrooves (top) and flat (bottom) displaying surface folds and elongation. Scale bars = 2 μm. b) Quantification of nuclear volume of NSCs on microgrooves compared to flat substrates. Data represented as scatter plots with lines representing mean ± s.d. N = 3, n = 3. c) Quantification of surface area to volume ratio of NSCs on microgrooves compared to FSW. Data represented as scatter plots with lines representing mean ± s.d. N = 3, n = 3 *p<0.05. d) 2D FIB-SEM cross-section of NSC on microgrooves (top) indicating deep nuclear invaginations and on flat substrate (bottom) showing no invaginations. Scale bars = 2 μm. e) 2D segmented FIB slice indicating nuclear membrane (blue) and nuclear invagination of the membrane (green). f) Quantification of number of nuclear invaginations per 3D reconstructed nucleus on microgrooves compared to flat substrates. Data represented at scatter plot with lines representing mean ± s.d. N = 3, n = 3, *p<0.05.

for immunostained cells with Triton X-100 and Saponin permeabilisation. Finally, the nuclei of cells on microgrooves were elongated in the direction of the grooves compared to nuclei on flat substrates that adopted random orientations.

Samples were subsequently prepared for visualisation under FIB-SEM by gold en-

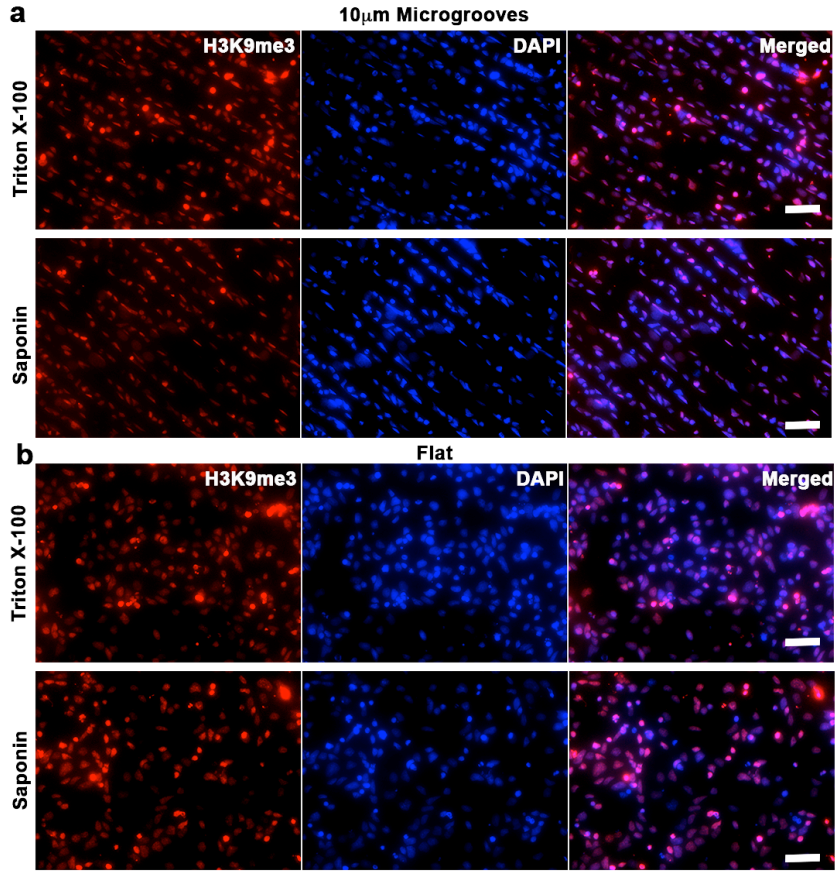


Figure 3.9: Fluorescence microscopy of NSCs on a) microgrooves or b) flat substrates treated with 0.1% Triton X-100 or 0.1% Saponin and immunolabelled with H3K9me3 and DAPI. Scale bar = 20 μm.

hancement followed by staining, dehydrating and embedding using thin-layer plastification (See chapter 2, methods). SEM of embedded samples showed that only a thin layer of resin was present on the surface of the cells on the substrate, and cells within microgrooves or flat surfaces could easily be identified (Fig 3.10a, top and bottom respectively). Visualisation under SEM was consistent in that cells spread along the direction of the microgrooves, with most cells being present within the grooves and few were spread in the direction of the ridges (Fig 3.10a, top). Cells on flat substrates once again adopted random orientations on the surface (Fig. 3.10a, bottom). In most cases, cells appeared smaller than the 10 μm width of the grooves and were not mechanically constrained, but were still elongated along the grooves.

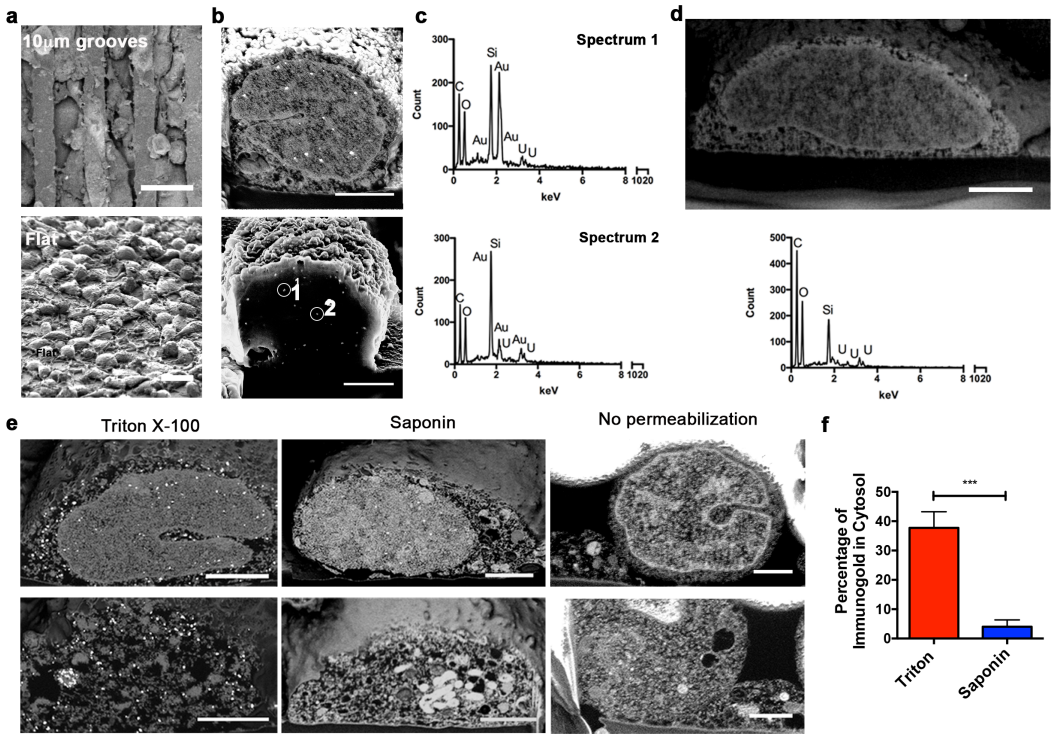


Figure 3.10: Optimisation of immunogold FIB-SEM sample preparation. a) SEM of FNG-probed and embedded NSCs on microgrooves (top) and flat PDMS substrates (bottom) after thin layer plastification showing easily identifiable cells after the preparation process. Scale bars = 10 μm. b) FIB-SEM cross-section under backscatter detector indicating bright puncta and corresponding image under secondary ion detector at 10 keV to obtain EDX spectra. Circled regions 1 and 2 containing bright spots correspond to spectrums in c) indicating presence of gold at these locations. Scale bar = 10 μm. EDX spectra obtained with Dr. Ciro Chiappini. d) FIB-SEM cross-section of a cell probed with FNG secondary but not H3K9me3 primary antibody (negative control) and corresponding spectrum (below) of the area indicating no gold was present. Scale bar = 10 μm. EDX spectra obtained with Dr. Ciro Chiappini. e) FIB-SEM cross-sections of regions containing the nucleus (top) and regions containing the cytosol (bottom) of cells treated with Triton X-100, Saponin or no permeabilisation agent prior to immunolabelling. Scale bars = 2 μm. f) Quantification of H3K9me3 immunogold labels in the cytosol in cells permeabilised by Triton X-100 or Saponin. Data presented as mean ± s.d. N = 3 cells, at least 60 cross-sections per cell containing the nucleus. ***$p<0.001$.

Using the FNG gold enhancement kit, the FNG was enhanced to a size detectable by FIB-SEM. Five minutes of incubation with the Gold enhancement kit resulted in detectable puncta within the nucleus as revealed by SEM imaging of milled cross-sections revealed bright spots on the order of 20 - 30 nm within the nuclei of cells (Fig. 3.10b). In order to confirm that the bright punctate spots were immunogold-labelled H3K9me3, energy dispersive x-ray (EDX) spectroscopy was used. Elemental analysis of point selected spectra at the sites of the puncta confirmed the presence of gold (Fig 3.10b, c). In the negative control sample of FNG incubated without the primary H3K9me3 antibody, no puncta or spectrum for gold was observed indicating

the specificity of FNG in binding target antigens within the sample (Fig. 3.10d).

Triton X-100 induced widespread damage to cell ultrastructure in comparison to Saponin-treated and non-permeabilised samples (Fig. 3.10e). Triton X-100 permeabilised cells showed a lack of identifiable organelles in the cytoplasm, with only the nuclear membrane intact. Moreover, there was considerably more non-specific FNG immunogold labelling of H3K9me3 in the cytosol as punctate spots were seen in these regions (Fig. 3.10e,f). Cell permeabilisation with 0.1% Saponin showed relatively better preservation of cell ultrastructure and was comparable to non-permeabilised cells (Fig. 3.10e). Vesicular structures, endosomes, vacuoles and mitochondria were visible in the cytosol, while the nucleoplasm also appeared to be conserved with an intact nuclear membrane. In addition, bright punctate spots were localised within the nucleus. In addition, only 3-6% of nuclear H3K9me3 labels were found in the cytosol compared with Triton permeabilised cells where approximately 40% were localised in the cytosol (Fig. 3.10f). 0.1% Saponin treatment was selected for further experiments due to these reasons.

3.4.3 The Epigenetic Mark H3K9me3 Increases in Response to Microgrooved Topography

In order to assess whether the epigenetic mark H3K9me3 in NSCs is affected by microgrooved topography, the numbers and density of H3K9me3 labelled particles within nuclei on microgrooves and flat substrates was assessed. 3D reconstructions of cell nuclei demonstrated a dramatic increase in the number of immunogold H3K9me3 labels between those cells cultured on microgrooves and flat surfaces, however there was no observable difference in their distribution within the nucleoplasm (Fig. 3.11a, b). Quantification of these particles confirmed this as cells on microgrooves exhibited a significant increase in H3K9me3 labels (Fig. 3.11c). Moreover, as the nuclear volume was not seen to change significantly on microgrooves, the increase in total H3K9 labels also resulted in approximately 2-fold increase in H3K9me3 density within nuclei (Fig. 3.11d).

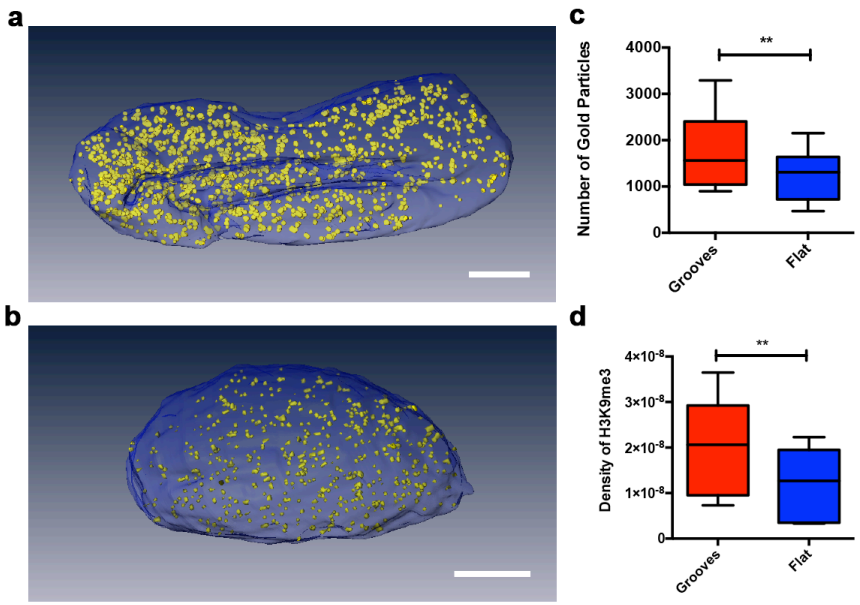


Figure 3.11: Microgrooves stimulate an increase in H3K9me3 density. a) 3D reconstruction of NSC nucleus on microgrooves showing H3K9me3 distribution labelled with immunogold. Scale bar = 2 μm. b) 3D reconstruction of NSC nucleus on flat PDMS showing H3K9me3 distribution labelled with immunogold. Scale bar = 2 μm. c) Quantification of number of H3K9me3 labels within NSC nuclei on microgrooves and flat PDMS. Data are represented as box and whisker plots from N = 3, n = 9, **p<0.01. d) Quantification of density of H3K9me3 labels within NSC nuclei on microgrooves or flat substrates (H3K9me3 labels per nuclear volume). Data are represented as box and whisker plots from N = 3, n = 9 cells per condition, **p<0.01.

3.4.4 The Epigenetic Mark H3K9me3 is Enhanced at the Nuclear Periphery in Response to Microgrooved Topography

Since immunogold labelling in FIB-SEM allows precise localisation analysis, the distribution of H3K9me3 within the nuclei of cells cultured on microgrooves and flat substrates was investigated. In order to do this, 3D stacks of segmented sections containing the nuclear membrane were used to obtain a mask of the central and peripheral regions of the nuclei (Fig. 3.12a). Since the nuclear membrane is approximately 50 nm thick, and the lamina along with peripheral heterochromatin is estimated to lie within 200 nm of the nuclear membrane, the peripheral mask was set as 150 nm while the central region corresponded to the volume within it (Fig. 3.12b). Next, the number of H3K9me3 particles within the central region and the peripheral region were counted within 3D projected mask, to obtain the number of particles in each domain. Quantification of particles in each domain indicated that the number of particles in peripheral region of nuclei on microgrooves was significantly increased compared to flat, while

there was no significant change in centrally located particles between microgrooves and flat substrates (Fig. 3.12c). In addition, comparing the ratio of peripheral particles to central particles for nuclei on microgrooves and flat substrates showed that the ratio was significantly higher for nuclei on microgrooves, supporting the result that there was a preferential shift in H3K9me3 localisation to the nuclear periphery (Fig. 3.12d).

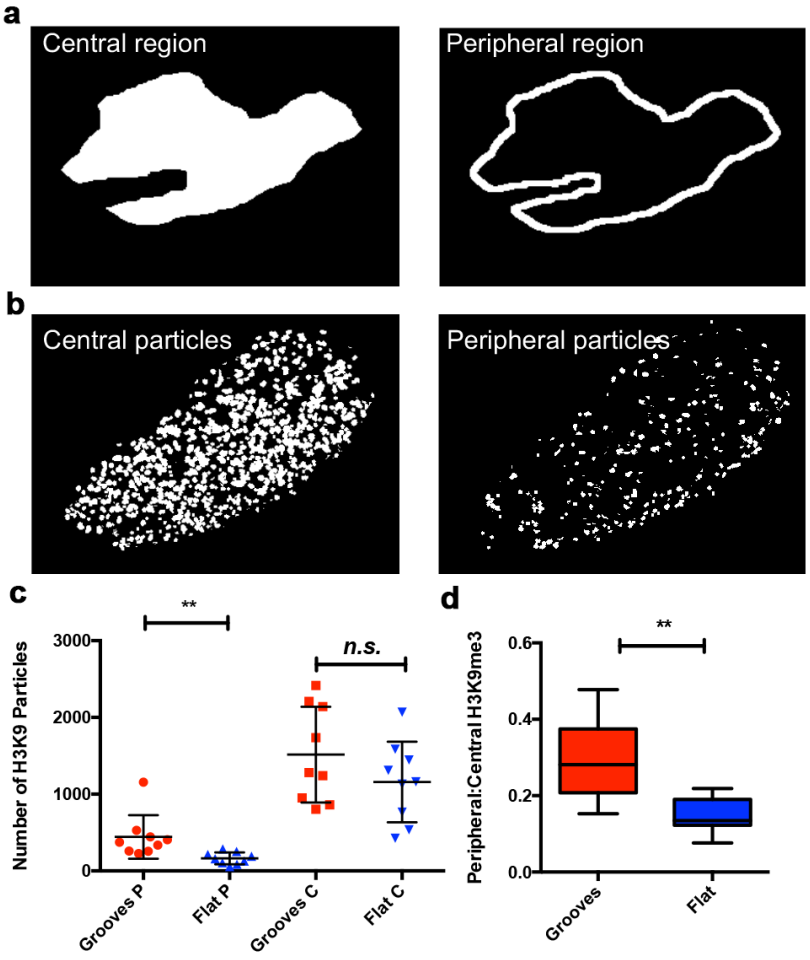


Figure 3.12: H3K9 is enhanced at the nuclear periphery. a) Representative 2D mask of central region (white) created from subtracting 150 nm from the nuclear centre. b) Representative 2D mask of peripheral region (white) created from adding 150 nm inwards from the nuclear membrane. c) 3D projected image of particles present in the central region obtained from stack of (a). d) 3D projected image of particles present in the central region obtained from stack of (b). e) Quantification of particles in central and peripheral locations for nuclei on microgrooves and flat substrates. Data represented as scatter plots with lines indicating mean ± s.d. N = 3, n = 9 cells for each condition, **p<0.01. f) Ratio of number of peripheral particles to central particles on microgrooves and flat substrates. Data represented as box and whisker plots, N = 3, n = 9 cells for each condition.

3.4.5 SICM Reveals that Microgrooved Topography Stimulates Changes in Nuclear Stiffness

Since microgrooved topography stimulates the accumulation of H3K9me3, a heterochromatin mark at the nuclear periphery, it was hypothesised whether it could contribute to an increase in nuclear stiffness. In order to assess this, a newly developed stiffness mapping mode of SICM was applied[311]. Topographical images obtained along with deformation maps enabled visualisation of cell morphology and location (within grooves or on ridges) to be correlated with stiffness measurements (Fig. 3.13a, c). Scanning with

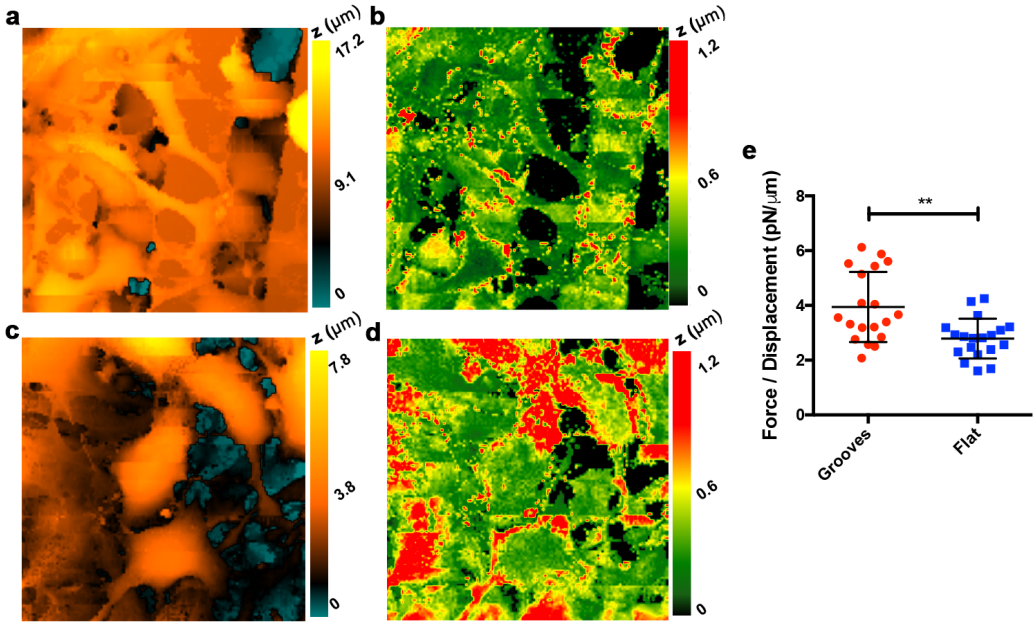


Figure 3.13: Cell stiffness increases in response to microgrooved topography. a) 50 μm x 50 μm SICM topographical map and corresponding b) deformation map of NSCs on microgrooves. c) 50 μm x 50 μm SICM topographical map and corresponding d) deformation map of NSCs on flat PDMS. e) Quantification of cell stiffness calculated from the ratio of force applied through the SICM probe (stress) to the degree of deformation (strain) detected by the deformation map. Data are represented as scatter plots with lines representing mean ± s.d. stiffness values reported in pN/μm. N = 4, n = 3 with 5-20 1 μm^2 diameter circular ROIs per 50 μm x 50 μm image **p<0.01.

multiple set-points enabled deformation maps to be obtained, which consisted of the increased distance travelled by the probe at each point, constituting the degree of strain or deformation at each point on the cell (Fig. 3.13b, d). Thus in deformation maps, the hard PDMS substrate could be visualised with little to no deformation (black regions) while the regions containing cells exhibited a degree of deformation (represented by change in height or effectively, the strain) dependent on their stiffness. Values of higher

compressive force applied through the SICM probe from higher set-points at each location, enabled the stiffness at each point in the image to be calculated[311]. Since NSC nuclei occupy the majority of the cell volume, central parts of the cells within grooves were selected as regions of interest (ROIs) for analysis. This enabled precise measurements of multiple areas within each image to be obtained. Quantification of cell stiffness in this manner revealed that culturing NSCs on microgrooves contributed to a significant increase in cell stiffness when compared to cells cultured on flat PDMS membranes (Fig. 3.13e).

3.5 Discussion

Currently, there is a great need to develop new methods to visualise cell-material interactions at the sub-cellular scale. Studying these complex interfaces can aid in identification of key sub-cellular components that are responsible for macroscopic changes in cell behaviour and function in response to material stimuli. This is particularly important due to the fact that biomaterials can then be optimised and improved to induce a specific biological outcome. Moreover, such material cues can be used not only to probe the many unknowns of cell interactions in changing environments but also for deciphering cell structure-function relationships stimulated by single physical cues. Thus in this chapter, the characterisation and application of new methods to visualise such cell-material interactions was investigated.

Through the use of simple microgrooved topography, which has already been proposed to stimulate physical changes in nuclear morphology and chemical modifications at the level of the epigenome[122, 390, 124], a protocol for immunogold labelling of epigenetic marks and their visualisation by FIB-SEM *in-situ* was successfully developed and applied to this system, with the view of corroborating changes nuclear architecture with epigenetic modifications. With the unique advantages FIB-SEM has to offer in terms of examining large volumes of single cells with TEM-like resolution as well as milling through the cell-substrate interface without the need for substrate removal, the additional ability to incorporate labels of specific targets in image analysis enables 3D localisation analysis of those targets alongside an ultrastructural backdrop. This feature of the technique can thereby help to reveal new characteristics of cells in response to material systems, that is particularly important for characterisation of cell response to implantable materials, biosensing apparatus and in this case, substrate topography to modulate nuclear organisation.

The utility of FIB-SEM in characterising the cell-material interface has been highlighted in several recent studies[252, 253, 254]. Typically, FIB-SEM imaging is used as an end point analysis of the plasma membrane and nuclear morphology, typically presented as single images or reconstructed sections of nuclei or cytoplasmic regions, but not whole-cell or whole-nuclei reconstructions. This is perhaps due to lengthy data acquisition and processing times compared to other microscopy techniques, which may

provide lower resolution, but similar quality of information.

In this study however, using FIB-SEM to reconstruct whole nuclei was vital in demonstrating how nuclear structure and topology are affected in response to substrate topography. Segmenting the highly contrasted nuclear membrane from each cross-sectional image yielded reconstructions and quantifications of the surface contours and volume, highlighting for the first time that while grooved topography induces nuclear elongation, it is also accompanied by a significant degree of deep nuclear infolding, otherwise known as type II NR, as opposed to a reduction in nuclear volume (Fig. 3.8). This result is consistent with another study that indicated tubulations and involuted regions of the nuclear envelope labelled with Lamin B1, that appeared to be in close proximity to nucleoli in response to microgrooved topography[205]. Type II NR of similar size range (300 nm) have previously been observed by FIB-SEM and TEM in mammary epithelial cells grown in 3D culture[341]. Since the formation of type II NR (membrane bending) is an energy dense process, it is speculated that grooved topography aids in overcoming the energy required to curve the nuclear membrane, potentially via reorganisation of the cytoskeletal framework, that further results in the aggregation of protein machinery that may stabilise the curvature[173, 161]. Thus, while nuclear elongation has been the main focus of majority of the studies incorporating microgrooved topography to influence nuclear function, these data reveal that creating an environment conducive to the formation of type II NR may be the key drivers of stimulating intranuclear modifications.

For image processing and analysis of FIB-SEM, the preparation of samples follows a strict protocol of fixation, staining, dehydration and embedding. The introduction of antibodies within the FIB-SEM samples complicates this preparation process as antibody penetration by immunolabelling becomes as important as ultrastructural preservation. Rather than visualisation of the fluorescence signal alone, the structural integrity of the surrounding components is vital for robust data acquisition and analysis by immunogold FIB-SEM. Thus in order to incorporate immunolabels effectively, with minimal impact on cell ultrastructure, different permeabilisation agents were tested to find that saponin best preserved cell ultrastructure, while allowing immunogold labels of intranuclear antigens to be detected, with minimal background (Fig. 3.10). This result was surprising as saponin permeabilisation, often considered as a reversible and

relatively gentle permeabilisation method has previously been shown not to allow penetration of antibodies into the nucleus[391]. Moreover, permeabilisation using ionic detergent Triton X-100 that is normally conducted for immunofluorescence staining, demonstrated the widespread damage it causes to ultrastructure, despite the initial fixation step with PFA. Organic solvents such as methanol and acetone were not tested in the optimisation process as they have been shown to negatively impact ultrastructure, even more so than Triton X-100[392]. Overall, the results from the permeabilisation optimisation indicate that if permeabilisation is necessary for antibody penetration, saponin induces the least amount of ultrastructural destruction.

The relationship between biophysical cues, nuclear architecture and epigenetic modifications remains greatly unexplored. Thus the epigenetic modification H3K9me3 was selected in order to assess its movement and density in response to topographical cues. The successful immunogold labelling of epigenetic mark H3K9me3 within NSC nuclei cultured on microgrooved substrates allowed the characterisation of their distribution in response to topography. Since the histone methylation mark H3K9me3 has previously been shown to modulate peripheral gene silencing and increase during differentiation[363], the ability of microgrooved topography to trigger changes in H3K9me3 was tested in NSC nuclei. NSCs, that are capable of differentiating into a range of neural cell types (such as astrocytes, oligodendrocytes and neurons), have previously been cultured on grooved topography, to demonstrate that providing organisational cues such as microgrooves can aid in NSC differentiation[393]. The results from this study are consistent with this idea, as microgrooved topography was shown to stimulate an increase in H3K9me3 histone marks (Fig. 3.11). Moreover, the finding that the increase in H3K9me3 in nuclei on microgrooves occurred primary at the nuclear periphery is indicative of the increasingly accepted notion that H3K9me3 is responsible for peripheral gene silencing and corresponding heterochromatin accumulation and anchoring to the nuclear lamina[378].

The accumulation of H3K9me3 epigenetic marks at the nuclear periphery was accompanied by an increase in cell stiffness as measured by SICM (Fig. 3.13). Since nuclei occupy a large proportion of the volume of these cells, it is likely that nuclear stiffness also contributes to the measured cell stiffness. Due to the fact that microgrooved topography exhibits differences in substrate height (grooves and ridges), and that SICM

stiffness maps are obtained using feature height thresholding, strain maps rather than elasticity (E) maps were displayed in order to make accurate calculations by excluding the ridge regions of the substrate. In addition, high spatial resolution permitted the analysis of only cells attached within the grooves rather than on ridges or that were not aligned. The method was hence adapted to stiffness mapping of cells on such topographical substrates, potentially allowing cells on different topographies to be distinguished and analysed within the same sample. Moreover, the SICM probe did not make contact with the sample at any point, which has not been possible with AFM.

The fact that increased cell stiffness accompanies a high degree of nuclear deformation may seem surprising, however these results are consistent with another report of cells cultured on micropillar arrays, where increased stiffness was observed in cells with highest deformable nuclei, possibly owing to the existence of thick actin fibres at the apical surface, above the nucleus[389].

In this study, the observed increase in cell stiffness is thought to arise from increased chromatin condensation at the nuclear periphery in response to microgrooved topography. Although we did not observe any obvious increase in heterochromatin accumulation at the nuclear periphery with FIB-SEM imaging, this may be due to lack of contrast within the nucleus as observed in another study[341]. As microgrooved topography triggers global rearrangements of the nuclear envelope, it is accompanied by a redistribution of chromatin domains and epigenetic marks, which can directly impact the mechanical properties of the nucleus. Indeed, two recent studies have highlighted that physical stretching of the chromatin results in chromatin decondensation as well as the loss of the H3K9me3 mark[394, 395], indicating that the density of chromatin at these regions can contribute to the mechanical stiffness of the nucleus. Moreover, the ability of the epigenome to modulate stiffness has also been shown through application of HDAC inhibitors that induced a reduction in nuclear viscosity[396]. Lastly, reorganisation of the nuclear envelope particularly with respect to increasing type II NR has been shown to increase with HDAC inhibition[397]. Although this corresponds to a greater level of chromatin decondensation and is contrary to what is observed for nuclei on microgrooves, type II NR are also found closely associated with repressive complexes such as polycomb group proteins and nuclear lamina anchor HP1[343], thereby highlighting the possible dual role and complexity of type II NRs in modulating

gene expression.

3.6 Conclusion

In conclusion, the influence of microgrooved topography on external nuclear architecture as well as internal epigenetic modifications were studied through the application of novel visualisation techniques immunogold FIB-SEM as well as low stress mechanical mapping by SICM.

Using FIB-SEM, serial sections of the cell-material cross-sectional interface enabled the production of 3D renders of nuclei on microgrooves. 3D rendering and analysis of nuclei on microgrooves were shown to undergo significant amount of nuclear infolding, reminiscent of nuclear invaginations recognised as type II NR. In order to advance FIB-SEM technique further, particularly for studying cell-material interactions, immunogold labelling was optimised and combined with FIB-SEM imaging for the first time. This technique offers a straight forward read-out that does not require superimposition and correlative analysis that is usually needed for CLEM. Successful immunogold labelling of epigenetic modification H3K9me3, enabled visualisation of this histone mark with surrounding nuclear architecture, that permitted robust analysis of its localisation and density within the nucleus in response to material topography.

The novel application of SICM in low stress mapping mode showed that it was possible to map the deformability of the nuclei with high lateral resolution on grooved substrates without making contact with the sample, which is a current difficulty with AFM. Since microgrooved topography was shown to stimulate an increase in nuclear stiffness, it is concluded that the increase in peripheral H3K9 methylation which is closely associated with compacted heterochromatin may contribute towards this finding.

Overall, this study provides insight on the ability of material topography in the form of microgrooves to stimulate coordinated changes in nuclear properties, achieved by the application of new visualisation techniques and analyses. The development of techniques described in this study are broadly applicable to investigating a variety of cell-material interactions and are particularly relevant to those cell-material systems that require *in-situ* nanoscale 3D localisation analysis.

4. Investigating the Cell Membrane Response to Nanoneedle Arrays for Delivering Biological Payloads

Arrays of high-aspect ratio nanostructures or nanoneedles are promising materials for intracellular delivery and sensing. Through mechanisms yet to be identified, nanoneedles of different geometries have been able to deliver a wide range of therapeutics including nucleic acids, proteins and cell-impermeable cargoes, without negatively impacting cell viability. In particular, whether nanoneedles can traverse the cell membrane, modulate membrane permeability or facilitate endocytosis for efficient intracellular delivery is yet to be elucidated. In this chapter, the interactions between human mesenchymal stem cells (hMSCs) and porous silicon nanoneedle arrays are investigated to identify the features of the plasma membrane responsible for modulating payload transfer that occurs across the membrane-nanoneedle interface. HMSCs interfaced with nanoneedles display significant modifications to plasma membrane architecture in the form of apical membrane ruffling and increase in membrane lipid order as demonstrated by SICM. Using electron microscopy techniques, we show that the basal membrane in contact with the nanoneedles has an intact lipid bilayer that is accompanied by an accumulation of clathrin pits and caveolae. Moreover, nanoneedle stimulated an increase in uptake of endocytotic cargo across the nanoneedle interface. Lastly, we show that this concurrent activation of endocytotic pathways by nanoneedle arrays contributes to nucleic acid payload entry into hMSCs and its distribution across the endolysosomal system. The data provide insight into the biological processes that arise from interfacing with nanoneedles and other such nanotopographical substrates, which has implications for development of next generation stem cell manipulation technologies, drug delivery platforms and achieving intracellular access for sensing applications.

4.1 Introduction

4.1.1 The Need for Intracellular Access

Currently, there is a great need for methods to access the cytosol to (i) assess the biochemical constitution and activity of cells and (ii) deliver biomolecules efficiently to manipulate cell function. These two aspects cover a myriad of applications such as monitoring electrical recordings, enabling efficient delivery of membrane-impermeable molecules (including nucleic acids), on demand disease diagnostics, sensing of nucleic acids and lipids, monitoring intracellular activities, amongst others (Fig 4.1).

While our understanding of biology has been fundamental in developing a multitude of intracellular delivery[398] and sensing probes[399], the success of their utilisation is highly dependent on their ability to gain cytosolic access. Obtaining intracellular access is dependent on designing strategies that are able to overcome the protective cell membrane barrier, enabling favourable interfacing with intracellular components while minimally impacting cell function. This is a formidable task, particularly in clinical applications, which involve the use of primary cell types. Even in basic research, transfection remains a considerable challenge in primary and stem cell types due to their high sensitivity to stress (ESCs, iPSCs and neurons)[400], lack of adherence (immune cells)[401] or inefficient cell uptake[402]. Of the many applications capable of achieving intracellular access, it is not surprising that the greatest focus has been on intracellular delivery of genetic material. New capabilities in gene editing technologies such as Crispr-Cas9, Zinc finger nucleases, transcription-activator like effector nucleases (TALEN) offer unparalleled potential to correct or remove deleterious sequences, or insert therapeutically relevant ones[403]. In other instances, different types of nucleic acids such as mRNAs[404] and micro-RNAs (miRNAs)[405] as well as proteins[406] have shown promise in their ability to generate iPSCs while avoiding the risks surrounding genomic integration. The success of these promising cargoes relies on designing next-generation platforms for safe and efficient intracellular delivery.

4.1.2 Current Methods for Intracellular Delivery

The plasma membrane is a key barrier to external molecules. Its physical and chemical properties are tightly regulated to allow the exchange of exogenous and endogenous fac-

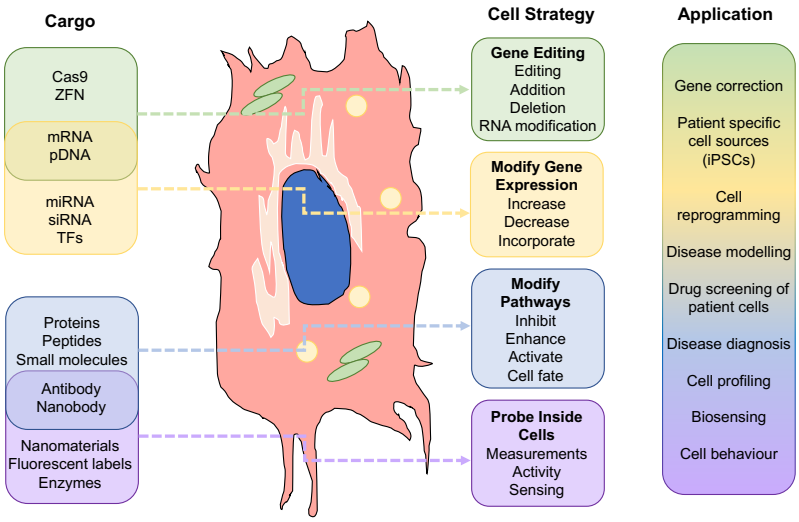


Figure 4.1: Potential applications of gaining intracellular access. Schematic illustration of different types of deliverable cargo and their associated ability to modify the cell response (cell strategy). Novel delivery apparatus such as Cas9 or Zinc finger nucleases (ZFN) currently exhibit the greatest ability to specifically edit genes of interest. Additionally, some conventional cargo such as plasmid DNA may act by exerting overlapping effects on gene expression. Protein cargoes are most suited to influencing intracellular signalling pathways. The success of intracellular delivery can be applied in a number of different respects listed in the schematic. Figure adapted from [407].

tors, particularly large and charged molecules. The plasma membrane is a selectively permeable entity and is segregated into inhomogeneous domains, providing a platform for specific biomolecules to enter and exit through their respective domains[408]. Internalisation of exogenous material proceeds via specific pathways at targeted regions within the membrane that often require receptor binding and recycling, enabling only required amounts of material to be internalised[409]. Thus, disturbing homeostatic regulation of the cell membrane through chemical or physical manipulation bears the risk of impeding cell function ultimately resulting in cell death. Bearing this in mind, methods to induce non-destructive interfacing at the nanoscale, that can act symbiotically with the cell response can increase the probability of successful delivery across the plasma membrane.

4.1.2.1 Biochemical Methods

In order to achieve intracellular delivery, a number of chemical and physical methods have been employed (Fig 4.2). Chemical platforms typically involve carriers to achieve intracellular delivery by relying on the inherent capabilities of cells to internalise ex-

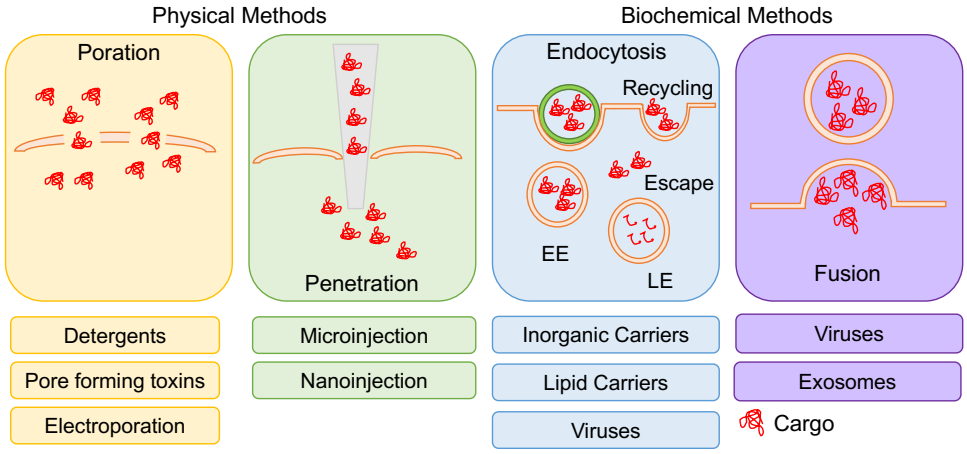


Figure 4.2: Physical and biochemical methods of intracellular delivery. Physical methods to disrupt the membrane include those that introduce pores in the membrane through the use of detergents, pore forming toxins or electroporation techniques. The use of high-aspect ratio structures such as microneedles or nanoneedles can be used to penetrate the membrane and introduce cargo into the cytosol. On the other hand, biochemical methods rely on endocytosis of carriers containing payload to enter cells. Inorganic carriers, lipid carriers and some viruses use endocytosis to enter cells after which they may be recycled to the surface, entrapped within early endosomes (EE) and late endosomes (LE) or escape these components altogether. Direct fusion of carriers such as extracellular vesicles or certain viruses can also enable release of cargo into the cytosol.

ogenous material. In particular, delivery of genetic material into cells has largely been achieved through the use of viral vectors due to their high efficiency of internalisation. Moreover, post-internalisation, viral vectors possess the capabilities to manipulate intracellular trafficking mechanisms and achieve genomic integration. This has led to their clinical success, and their testing in numerous clinical trials[410]. However, due to their immunogenicity, low loading capacity and tumorigenicity, they remain heavily restricted for the majority of clinical applications[411]. The slow progress in overcoming the limitations of viral vectors has fuelled the development of numerous non-viral carriers, including lipid-based vectors, polymers, inorganic particles and peptides in various sizes and conformations[412]. These non-viral vectors are typically designed to have better loading capacities, and more importantly, are safer and less immunogenic[412, 413]. Although many non-viral vectors possess these attributes, synthetic carriers are faced with the added challenge of overcoming multiple intracellular barriers they are confronted with before reaching their intracellular target site[414]. In order for a synthetic carrier to be successful in its delivery of exogenous cargo, it must (a) protect its cargo from degradative enzymes (b) be internalised effectively (c) escape harsh conditions in the intracellular environment and (d) find its way to its target site

of action i.e. the nucleus or specific protein complex in the cytosol. Each of these instances consist of a barrier established by cellular machinery.

Cells can actively exchange exogenous and endogenous molecules that cannot be transferred across the membrane by passive diffusion through the processes of endocytosis and exocytosis. Endocytosis is a natural mechanism practised by cells that involves active internalisation of exogenous molecules. It is initiated through binding of cargo to specific cell receptors or the membrane, followed by membrane deformation, invagination and scission of an incoming 'sac' or vesicle by specific proteins at the membrane interface. Internalisation of exogenous material by endocytosis not only represents the major mechanism of entry of pathogens into cells, but also delivery vectors[415]. Depending on the cargo properties and protein machinery recruited during vesicle formation, different types of endocytotic pathways can be activated (Summarised in Table 4.1). Properties such as size, charge, shape or stiffness of the carrier can influence the type and efficiency of internalisation through specific physicochemical interactions at the plasma membrane. This has resulted in the development and optimisation of hundreds of different organic and synthetic carriers for intracellular delivery (reviewed extensively in [416, 417, 418]). It is therefore important to understand the workings of different endocytotic pathways for controlling fate of delivered cargo. It is worth noting that some of these pathways are not fully understood due to the non-specific nature of inhibitors as well as lack of specific biomarkers. Moreover, carriers may be internalised by one or more routes simultaneously.

Macropinocytosis can be observed as cell surface ruffles engulfing and internalising exogenous material[419]. Normally, macropinocytosis is stimulated by the presence of growth factors such as platelet derived growth factor (PDGF), macrophage colony stimulating factor-1 (CSF-1) or epidermal growth factor (EGF) amongst others[420]. The formation of the macropinosome is coordinated by small GTPases such as Ras and signalling lipid phosphatidylinositol-triphosphate (PIP3)[421]. In the presence of these factors or in antigen presenting cells that are constitutively macropinocytotic, actin polymerisation drives the formation of membrane ruffles, that fold back on the plasma membrane to form large vesicles or macropinosomes encapsulating nearby cargo[421]. In this way, large amounts of exogenous material can be internalised by immune cells that can be processed for antigen presentation. Macropinosomes can range from 200

nm upto 5 μm in diameter, and do not exhibit any specific coat proteins, however due to the large size of vesicles, fluid phase markers such as Dextrans or Lucifer yellow are typically used to assess uptake[422]. Considering the relative non-specificity of internalisation by macropinocytosis, they have been investigated for delivery of a wide range of cargoes[423]. Lipoprotein and lipid vectors carrying nucleic acids have been shown to internalise via macropinocytosis, however their recycling to the cell surface was shown to be the reason for their inefficiency[424, 425]. Additionally it has been difficult to predict the trafficking route between cell types. While some cell types promote macropinosome maturation and direct trafficking to late endosomes and lysosomes[426], others fuse with early endosomes after which they may be recycled to the surface without entering lysosomes[427].

Clathrin-mediated endocytosis (CME) is the best characterised endocytotic pathway and plays a key role in multiple cellular processes. This includes the uptake of specific nutrients such as iron binding protein Transferrin (Tfn) or low density lipoprotein (LDL) via ligand-stimulated receptor mediated endocytosis, regulation of signal transduction pathways via modulating the distribution of cell membrane receptors at the cell surface, and synaptic vesicle recycling for neurotransmission[428]. Endocytosis via CME, occurs via the inward plasma membrane invagination of spherical vesicular structures coated with clathrin proteins that resemble lattice-like basket structures with sizes ranging from 70-200 nm in diameter depending on the cargo and cell type. Although clathrin itself does not bind to the plasma membrane, its ability to recognise shallow curvatures in the membrane (such as F-BAR domains) is believed to trigger its nucleation (Fig. 4.3)[181]. Assembly of clathrin pits occurs when clathrin triskelia (three-legged structures composed of three clathrin heavy chain proteins brought together by three light chains) assemble in polygonal lattices[428]. Cargo selection for CME mainly occurs through the combination of its adaptor proteins (AP), with AP2 typically recruiting other adaptors. Through this selective mechanism for cargoes, viral pathogens and consequently viral vectors, are known to exclusively enter cells via CME[429]. Moreover, viral proteins can increase the size of clathrin pits to accommodate them as cargo, with the upper limit currently thought to be 200-300 nm[430]. Because cargo interactions with the membrane can induce local deformation and curvature, it is also possible that nanoscale surface modifications, shape or charge of cargo

can have a profound impact on the generation of clathrin coated pits[431]. Eventually, cargo-containing clathrin coated vesicles undergo scission by GTPase dynamin, followed by uncoating of clathrin by ATPase heat shock cognate 70 (HSC70), resulting in an early endosome.

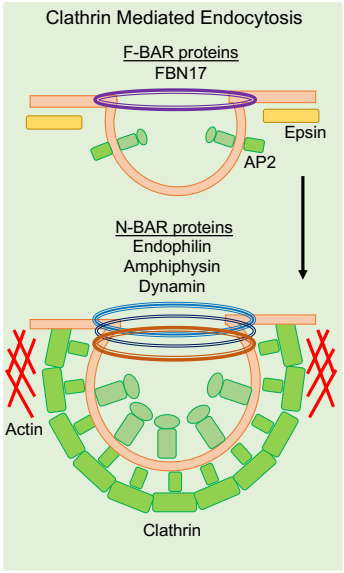


Figure 4.3: Formation of clathrin pit during CME. The formation of a clathrin coated pit is initiated by F-BAR proteins such as formin binding protein 17 (FBN17) that recognise low curvature and recruit Epsin, which in turn recruits adaptor protein 2 (AP2). AP2 is responsible for the recruitment of cargo specific receptors. AP2 participates in clathrin triskelion recruitment that polymerise to form a stable lattice. N-BAR proteins that sense higher curvatures such as endophilin and amphiphysin are recruited to the evolving neck of the clathrin pit, which results in further recruitment of dynamin to initiate clathrin pit scission with the help of actin pulling[428, 432].

Caveolae-mediated endocytosis (CavME) is perhaps the most widely recognised internalisation mechanism after CME. Caveolae are 50-100 nm flask shaped invaginations in the plasma membrane that contain oligomers of Caveolin-1 (Cav-1) protein within regions of the plasma membrane rich in cholesterol and sphingolipids (Fig. 4.4)[433]. Along with Cav-1, other sets of proteins such as Cavins, F-BAR-domain protein PACSIN-2 and ATPase EDH2 (similar to GTPase dynamins) are considered to be involved in caveolae formation[434]. Additionally there are large variations in presence of caveolae in different cell types. For instance, endothelial and smooth muscle cells can have over 50% of their cell surface covered in caveolae[435] while they are not found in certain kidney cells[436]. This has highlighted a potential role of caveolae for carrying out specific cell function. Endothelial cells can adapt their distribution of caveolae based on shear force they experience[437] and flattening out of caveolae has

been observed during high membrane tension, indicating that caveolae can act as tension regulators and mechanosensors[438]. By their ability to anchor within the plasma membrane and bind to cholesterol, caveolae participate in the regulation of lipids by increasing levels of cholesterol and uptake of fatty acids. How caveolae select their cargo and facilitate internalisation is less well understood. Caveolae are relatively immobile compared to clathrin pits. Caveolar endocytosis of integrins and fibronectin is thought to be involved during loss of cell adhesion[439, 440]. Moreover, caveolae are capable of removing glycosphingolipids such as GM1 from the membrane which can in turn modulate the presence and absence of raft associated membrane proteins, highlighting its role in membrane organisation[441]. Caveolae can also internalise pathogenic cargo. The internalisation of Cholera toxin (CTx) and Simian virus 40 (SV40) proceeds with CavME, although some evidence for SV40 points out that internalisation can occur independent of caveolae but dependent on cholesterol[442]. However since caveolae undergo similar dynamin dependent scission, and fusion with an endosome, and recycling this pathway represents an important mechanism of endocytosis[443].

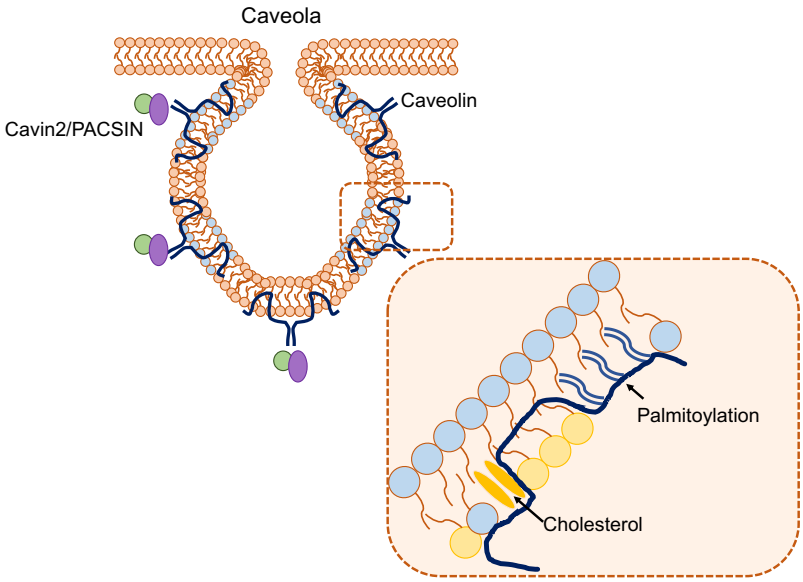


Figure 4.4: Structural composition of caveolae. Caveolae are recognised as 50-100 nm flask shaped invaginations of the plasma membrane. Caveola formation is stabilised by cavin and PACSIN (F-BAR protein). The major component of caveolae, Cav-1 is present in hairpin like structures inserts directly to the lipid membrane via palmotyl groups, while the other end of the caveolin interacts with cholesterol rich regions. Figure adapted from[433, 435].

Clathrin and Caveolin-Independent Endocytosis (CLIC) include a number of pathways that can be classified as dynamin dependent or independent[444]. Other

dynamin dependent pathways include small GTPase RhoA-mediated endocytosis responsible for internalisation of specific interleukin receptors in Chinese hamster ovary (CHO) cells that proceeds with 50-100 nm invaginations, whose constitution is yet to be determined[445, 446]. Dynamin independent pathways that are also devoid of any specific coat proteins include those which account for large scale fluid uptake and endocytose GPI-APs termed as the clathrin independent carrier- GPI-AP enriched early endosome (CLIC-GEEC) pathway and a cholesterol dependent pathway mediated by Arf6[447]. Flotillin-mediated endocytosis is an additional mechanism that is analogous in many ways to CavME[448], however its dependence on dynamin and caveolin itself is still controversial[449]. More details on CLIC pathways can be found in table 4.1.

Type	Coat	Size	Scission	Cargo	Ref
Clathrin-mediated	Clathrin	70-200 nm	Dynamin	Transferrin, LDL, EGF	[428]
Caveolae-mediated	Caveolins, Cavins	50-100 nm	Dynamin	Albumin, SV40, CTx, GPI-APs	[435]
RhoA-mediated	Unknown	50-100 nm	Dynamin	IL-2 receptor	[445]
CLIC-GEEC mediated	No coat, Stabilised by Arf1, GRAF1	50-80 nm	GRAF1	Fluid phase uptake (constitutive)	[450]
Flotillin-mediated	Flotillins 1, 2	50-100 nm	Dynamin (some instances)	CD59	[451]
Arf6-mediated	Actin	60-200 nm	Rac1	MHC Class 1, Glut1, E-cadherin	[452, 453]
Macropinocytosis	No coat	0.2-5μm	None	Dextran, LuciferYellow	[420]

Table 4.1: Pathways of internalisation, their key coat components, sizes, scission mechanisms and selected cargoes. Some endocytosis pathways such as RhoA have no identified coat proteins. In the CLIC-GEEC pathway no coat proteins are present however invaginations are stabilised by adenosine diphosphate-ribosylation factor-1 (Arf1) and GTPase regulator associated with focal adhesion kinase-1 (GRAF1) and while dynamin is not required for scission. The role of dynamin in flotillin-mediated uptake is also not clear as some cell types have shown dynamin dependence, while others do not. Arf6 mediated endocytotic vesicles are mostly found within the cytoplasm as recycling tubular structures, while scission is mediated by Rac1 rather than dynamins.

The many different mechanisms of endocytosis presented here demonstrate that the cell membrane is biochemically equipped for providing entry to exogenous biomolecules required for cell metabolism and function. Regulation of internalisation by endocytosis allows internalised biomolecules to be utilised and trafficked appropriately to target

locations within the cell. Following internalisation by endocytosis and scission of the incoming vesicle, pinosomes from macropinocytosis or incoming vesicles from other endocytotic routes are trafficked into the cytosol as early endosomes (EEs). EEs mature into late endosomes and lysosomes. Rather than being distinct entities, EEs undergo maturation as their contents, pH, surface markers and morphology are gradually altered by fusion with other vesicles, kiss-and-run events and connections to other vesicles via tubules that result in the formation of intermediates between lysosomes[454]. Moreover, during the maturation process EEs can generate branched tubulations and sort cargo within these domains for recycling or recruitment to the trans-golgi network (TGN)[455]. In other instances, the vacuolar portion of the EE can bud inwards and form intralumenal vesicles (ILVs) that are normally targeted for lysosomal degradation[456]. Often, many ILVs can be visualised within late endosomes or multi-vesicular bodies (MVBs), that have increased levels of lysosomal hydrolases and low levels of cargo to be recycled[454].

Since endocytosis is a tightly regulated process, internalised molecules are automatically recruited, destroyed or recycled to sites of their function mainly via signalling by the endosomal sorting complex required for transport (ESCRT) that cleaves off cargo labelled with ubiquitin for degradation[457]. Thus, for cargo which are not natural to the cell, internalisation normally results in rapid acidification of the endosomal environment and lysosomal degradation contributing to low efficiencies. For instance it has been estimated that even the most advanced non-viral delivery vectors (that are lipid-based) only have an efficiency of 1% due to their inability to escape the endolysosomal pathway[424]. In another study, approximately 70% of small interfering RNA (siRNA) delivered by a lipid vector was shown to be exocytosed via endosomal recycling[458]. Inducing endosomal escape carries the risk of impeding natural cellular processes that can have cytotoxic effects[459]. Moreover, the mechanism of escape itself is poorly understood, making it difficult to design delivery vectors that enable release into the cytosol.

In addition to endocytosis, some carriers have the ability to fuse directly with the plasma membrane and release their contents into the cytosol. These carriers are predominantly composed of viral proteins that fuse directly with the membrane, liposomes or cell-derived vesicles (exosomes) that are loaded with cargo[460, 461, 462]. Although

fusogenic carriers may have the potential to escape endocytosis, they are limited in terms of application to a wide range of target cell types, (as all cell types do not possess the same membrane properties to allow for fusion to occur) as well as genomic off-target effects from viral proteins and immunogens. The use of exosomes is a relatively new strategy for intracellular delivery and requires more robust characterisation of internalisation mechanisms.

4.1.2.2 Physical Methods

Physical methods of introducing payloads act by disrupting the continuity of the plasma membrane. Methods such as microinjection, various mechanical, optical or electrical poration techniques and the application of pore-forming carriers rely on rupturing the membrane. The resulting transient perforations in the membrane facilitate an almost immediate transfer of exogenous material into the cytosol. In some instances, even primary cell types can be transfected, which are otherwise impermeable to non-viral vectors[463]. These methods are promising through their application to a multitude of cell types, however do not come without challenges.

Microinjection was the first demonstration of a membrane disruption method for intracellular delivery[464]. Using glass micropipettes, injection of genetic material into a precise location within single cells has been possible for several decades. Moreover, this method allows for injection into the cytosol as well as directly into the nucleus, overcoming multiple membrane barriers[465]. The technique however is limited due to its low throughput, sample to sample variation, cytotoxicity issues from membrane damage, and high technical expertise required for its operation. Attempts to improve the scalability of the platform by developing a microfluidics device for injection, the numbers of cells compared to other methods still remain relatively low[466].

Membrane Poration approaches that use transient forces have been developed with the aim of reducing cytotoxic effects by precisely controlling the range and frequency of force applied. Electroporation being by far the most established field-disruption technique, is a method by which the application of an external electrical field results in an increased permeability of the cell membrane by the transient formation of pores[467]. Typically, the application of the field ranges from micro- to milli-seconds and between 0.2-1 V to induce reversible permeabilisation. However depending on the

cell type, permanent membrane disruption can be induced. Moreover, higher electrical fields may be required depending on the cell size, as well as for cargoes that must cross the nuclear membrane and specific intracellular targeting remains an issue, particularly for sensitive and difficult to transfect cell types[468]. In some instances, application of nanosecond pulses of higher magnitude have been shown to be more effective in crossing the nuclear membrane[469]. However, higher magnitudes of electrical field are shown to be associated with cargo degradation, particularly in the case of proteins[470].

Electroporation can be combined with delivery of non-viral carriers, with the hope that carriers protect the cargo from degradation[471]. Apart from cytotoxicity issues, electroporation results in extremely small pore sizes in the range of 10-100 nm. In comparison, optoporation (that involves the use of a laser to create a pore at a specific location on the cell surface) and sonoporation (a non-invasive technique that uses ultrasonic waves to create membrane disruptions) are methods that form larger pores (up to 10 times larger) enabling delivery of larger cargo[472, 473, 474]. However, these techniques run the risk of slow diffusion of large cargo that may not allow their localisation to their intracellular target site, and an inability to reseal large pores[470]. Although sonoporation has maintained the highest cell viability for delivery applications so far, endosomal entrapment and degradation has been suggested in trafficking of the delivered cargo, leading to their reduced efficiency[474].

Biochemical Agents such as detergents and pore-forming toxins have been used in other attempts to disrupt the membrane. Pore forming toxins such as Streptolysin O can bind to the membrane, oligomerise and insert a pore complex to create pores as large as 30 nm for allowing cargo to pass through[475]. Detergents such as digitonin and saponin sequester membrane cholesterol in a reversible manner, forming variable pore sizes through unknown mechanisms[476]. Following such membrane disruptions, the membrane must be able to recover by resealing, and restoring normal cell function. Due to large variations in pore sizes and numbers, the use of biochemical agents to porate the membrane are usually disruptive to cell function, particularly in case of sensitive cell types. Membrane repair itself is a complex process that creates changes in ion concentrations, metabolites, stress factors and reactive oxygen species, causing further damage to delivered biomolecules[477].

Overall, physical methods of intracellular delivery are faced with a different set of

challenges including cytotoxicity, lack of scalability and high variability. Moreover, the mechanisms that enable membrane disruption are only beginning to be uncovered. The finding that membrane deformation induced by a constriction through a flow device can trigger diffusion-based internalisation of cargo highlights that harsh disruption methods may not be necessary to overcome the barrier[478]. Although combining microfluidic platforms with membrane disruption techniques can improve throughput and cell viability substantially[479, 478, 480, 481], the heterogeneity in cell populations, results in a reduction in overall throughput due to different parameters required for each cell.

4.1.3 Nanoneedle Arrays for Biomolecule Delivery

The realisation that minimal disruptions in the membrane are required to maintain cell viability and function during intracellular delivery has fuelled the development of nanomaterial platforms that interface favourably with membrane components at the sub-cellular scale. Nanoinjection systems using single nanoneedles with radii of a few hundred nanometers and AFM operated tips provided proof-of-concept non-invasive cytocompatible delivery, even whilst being low throughput[482, 483, 484].

Recent advancements in nanofabrication techniques has assisted the production of precisely engineered surfaces with high-aspect ratio nanotopographies in a variety of shapes, sizes and geometries. Arrays of vertical nanoscale structures in the form of cones[315], wires[485], tubes[486], straws[487], and pillars[127] have been created in uniform or disordered patterns with controllable pitch spacing. Needles and wires are used to describe structures with higher aspect ratios, in contrast to rods, pillars and straws that normally refer to shorter cylindrical structures. While recognising the different shapes and geometries exist, for the sake of simplicity, substrates consisting of such nanostructures will now be referred to as nanoneedles.

Nanoneedle arrays enable tens to hundreds of nanoneedles to interface with a single cell simultaneously, increasing throughput of delivery substantially. Being surface bound nanostructures, they bypass potentially toxic cytosolic accumulation normally associated with nanoparticle-mediated delivery. Moreover, the small feature sizes help in maintaining viability of even the most sensitive cell types such as neurons[488], dendritic cells[489] and stem cells[490]. Meeting the requirements of general biocom-

patibility, nanoneedle arrays have been used as functionalised cell probes or hollow channels, for intracellular delivery. This has lead to a number of studies demonstrating highly efficient introduction of biologically relevant molecules such as peptides and proteins[485] and nucleic acids[491, 492, 485, 493, 494, 495, 315] into cells. Nanoneedles have also demonstrated potential to deliver membrane impermeable probes for metabolic labelling in mammalian cells[496]. Electron microscopy of the cell-nanoneedle interface has indicated that nanoneedles could also be used for efficient delivery of cell impermeable nanoparticles such as quantum dots into the cytosol of HeLa and Het-1a cells[254]. In some cases, nanoneedle-mediated delivery of DNA and siRNA has demonstrated desired changes in gene expression[485, 495, 315], and overall delivery efficiencies are estimated to range from 40-99%[497]. Although fewer attempts of delivery have been made in cell types that are difficult to transfect, one study has highlighted successful transfection of primary immune cells (over 40%) and the specific geometry of nanoneedles required to do so[489]. Moreover, intracellular delivery mediated by nanoneedles has also been shown to escape endolysosomal entrapment[495]. Continuous delivery has also been made possible using nanostraw devices, through which biomolecules can continuously be fed by their attachment to a reservoir[498, 493, 496, 499]. More recently, nanoneedle arrays functionalised with vascular endothelial growth factor plasmid stimulated neovascularisation by application of the device to the tissue surface *in-vivo*[315].

4.1.3.1 Nanoneedle Fabrication

Depending on the nanofabrication process, different sizes, geometries, porosities of nanoneedles can result (Fig. 4.5). Parameters such as height, radius, density, porosity, density, pitch and regularity of nanoneedles can be optimised, to suit the cell type and application. Nanowires and nanotubes can be produced by vapour-liquid-solid (VLS) growth, a highly controlled and reproducible process, usually resulting in the development of solid nanostructures[500]. For instance, in the development of silicon nanowires, silicon from in the vapour phase (eg. $SiCl_4$) is converted into a nanodrop of an alloy in the liquid phase (eg. Si-Au), after which Si nucleates beyond the eutectic point to form cylindrical structures in the solid phase. The VLS method can be combined with lithography techniques to produce extremely small nanostructures, with controllable

densities and arrangements[501].

Metal-assisted electrochemical etching (MACE) has been used to develop similar high-aspect ratio structures in the form of cones and tubes with the added advantage of introducing porosity[502]. In MACE, a noble metal (eg. $AgNO_3$) is deposited on a silicon surface behaves as a catalyst for the etching of silicon in the presence of hydrofluoric acid and oxidising agents. Again, when combined with lithography techniques, MACE can produced ordered arrays of nanoneedles reproducibly and at a lower cost than VLS[220].

Yet another etching method is deep reactive ion etching (DRIE), a process by which plasma containing ions (such as SF_6) are used to etch away silicon, followed by a protective phase (using C_4F_8) preventing the nanostructure from further etching[503]. Thus through this controllable cyclic process, DRIE can be used to etch down silicon to produce features down to 50 nm in diameter and up to 20 μm in height[503]. FIB etching using a Gallium ion source enables the production of single nanoneedles and AFM operated tips with nanometer precision based on the milling current[504]. However the process is time-consuming as each needle on the array is produced individually, and higher milling currents for quicker fabrication result in lower tip resolution. Replica moulding of nanofabricated surfaces with polymeric materials is an additional indirect method of producing arrays with transparent, compliant biomaterials, although feature sizes are generally in the range of hundreds of nanometers[505].

Nanoneedle arrays are typically manufactured from materials such as silicon[507], platinum[508], carbon[509], indium arsenide[510], gallium phosphide[234] or oxides of aluminium[493], zinc[511] or copper[512]. Of these, silicon, dominates the field, due to its use in the semiconducting industry. In addition, silicon can be made porous (using MACE for instance), which has considerable advantages for interfacing with biological components. Due to its biocompatibility[513], tuneable degradation properties[502], and high surface to volume ratio[514], porous silicon is an attractive option for applications that require both local and continuous release of biological cargoes. It is not surprising that porous silicon has found use in the production of drug delivery systems, small implantable devices and tissue engineering scaffolds, relying on its ability to interface biological tissues without inducing inflammatory responses[515].

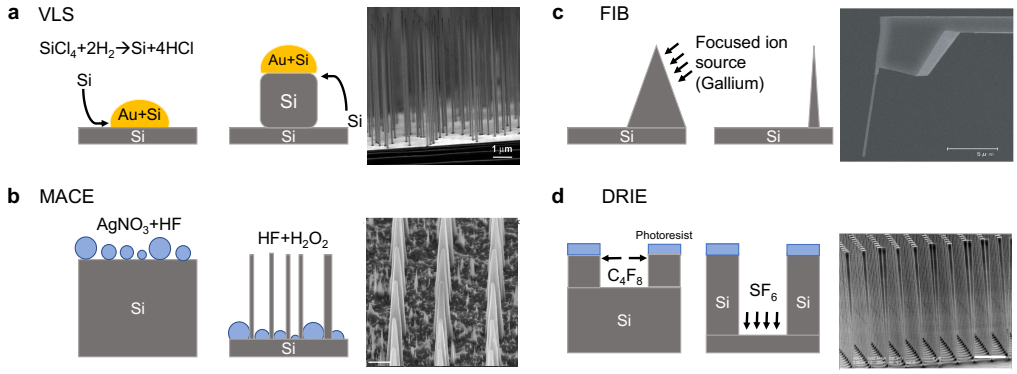


Figure 4.5: Methods of nanoneedle fabrication. a) In the VLS technique, a constant supply of Si in gaseous form allows nucleation when its concentration overcomes the eutectic point resulting in the formation of long silicon nanowires in the solid phase. Image reproduced from [506] with permission from American Chemical Society, copyright 2005. Scale bar = 1 μm. b) In the MACE technique, a noble metal in the presence of HF is deposited on a silicon surface and acts as a catalyst as silicon is etched down in the presence of HF. Controlling the etching parameters and combining this with microfabrication techniques can result in the formation of porous silicon nanoneedles. Image reproduced from [315] with permission from Springer Nature, copyright 2015. Scale bar = 2 μm. c) FIB (Focused ion beam) etching can be used to make single nanoneedles of desired thickness from AFM tips. Images reproduced from [504] with permission from Elsevier, copyright 2005. Scale bar = 5 μm. d) Deep reactive ion etching (DRIE) is a process that can be used to fabricate nanowires of high aspect ratio. Silicon is etched down by cycles of plasma (SF_6) and passivation (C_4F_8). Image reproduced from [503] with permission from AIP Publishing, copyright 2009. Scale bar = 2 μm.

4.1.4 Nanoneedle Properties for Intracellular Delivery

4.1.4.1 Nanoneedle Toxicity

Regardless of the manufacturing process, it is imperative that nanoneedle arrays do not incorporate any compounds that induce cytotoxicity or possess geometries that negatively impact cell function. For instance, fibroblasts cultured on gallium phosphide nanoneedles of different heights exhibited DNA damage and elevated levels of reactive oxygen species, particularly when cultured on longer needles up to 6.7 μm in height[256]. In addition, the diameter of nanoneedles can also influence cell viability as another study reported that using smaller diameter nanoneedles (90 nm) maintained viability in mammalian cells better than those with larger ones (400 nm)[492]. Typically structures with diameters 300 nm and below do not impede cell function, even when forcibly interfaced[491]. Nanoneedles made of copper oxide, a cytotoxic material have been coated with inert silicon dioxide to improve cell viability[512]. While these considerations are important, for the large part nanoneedle arrays are manufactured within these dimensions and are able to maintain cell viability up from several days to

a few weeks[516, 517, 497, 518]. Additionally, to induce favourable cell attachment, the surface of nanoneedle arrays can be modified by adsorption of matrix proteins that aid in cell adhesion such as fibronection[519], laminin[520], polylysine[521] or collagen[522].

4.1.4.2 Nanoneedle Surface Functionalisation

Besides maintaining viability during interfacing, successful nanoneedle-mediated delivery of biomolecules is largely dependent on their ability to modulate cargo adsorption and release, which is in turn dependent on the material of the nanoneedles and tuning their surface chemistry. The broad range of properties of therapeutically relevant cargo, such as their size, charge and robustness has further added to the complexities surrounding the best way to administer them via nanoneedle arrays. The first observations of intracellular delivery of proteins and nucleic acids via nanoneedle arrays were conducted by simple physisorption of cargo onto the substrate surface[485, 483]. The nanoneedle surface itself, can be modified for improving physisorption and further functionalisation by treatment with oxygen plasma, making it negatively charged and hydrophilic[523]. Payload adsorption improves with opposing charges of the surface and the cargo, which has led to surface functionalisation of nanoneedles with charged molecules. For instance, positively charged amine-terminated silanes such as 3-(aminopropyl)triethoxysilane (APTES) functionalised nanoneedle arrays have been used to aid in the adsorption of negatively charged nucleic acids onto nanoneedles for intracellular delivery[485]. Although such charged molecules increase adsorption of the payload, release of the payload into cells is equally important. For instance, nanoneedles that were treated with a positively-charged polymer polyethylimine used to electrostatically bind negatively charged DNA, demonstrated only 1% transfection efficiency, while APTES treated nanoneedles triggered nucleic acid delivery in over 95% of cells and high efficiency of gene silencing, most likely through hydrolysis of the silane layer[492, 485]. In another study, although successful immobilization of DNA to nanoneedles through streptavidin-biotin linkage was demonstrated, most of the DNA was not released on intracellular injection[482]. To overcome this problem, functionalisation of AFM-operated nanoneedles with positively charged polylysine that was used to bind a large excess of DNA, preventing its rapid release into solution. 50% of DNA could then be released within three minutes of intracellular injection[483]. These stud-

ies highlight the possible issues and need for optimisation of cargo loading and release strategies in the case of using solid nanoneedles for intracellular delivery.

4.1.4.3 Nanoneedle Porosity

Using porous nanoneedles is an alternative straightforward strategy for controlled release of biological payloads. Porous structures possess higher surface area making them amenable to higher loading capacities, and can be modified to act as cargo reservoirs[524]. As mentioned previously, the discovery of favourable properties of porous silicon nanoparticles for biointerfacing and its development as a versatile drug delivery system have provided a wealth of knowledge of its loading and release patterns[525, 526]. Controlled release of payloads loaded within pores is achievable via biodegradation of the material itself, or capping the pores with molecules that enable release in low pH environments found intracellularly[527, 528]. MACE can be used to produce porous silicon nanoneedles, imparting the advantageous cargo release mechanisms of porous silicon nanoparticles, with the added benefit of controlled interfacing with cells[502, 254]. In addition, it was estimated that nanoneedles formed from mesoporous silicon have an increased surface area for adsorption compared to solid nanoneedles of the same size by 300-fold[315]. Although porous nanoneedles can stimulate delivery for longer periods of time, the release characteristics are eventually reliant on the maximum volume that can be loaded within these tiny structures, and their degradation time.

Yet another type of nanoneedle device incorporating 'pores' in a different context are hollow nanoneedles, those that have a single pore or channel running through them. Below the substrate base, a reservoir of cargo that can constantly flow through the conduits provided by the nanoneedles via passive diffusion, eventually entering cells[499, 498]. In this manner, flow of cargo is essentially unlimited, with the ability to administer cargo repeatedly[499]. Due to the nature of the etching processes involved, nanostraws are generally short structures, as smaller lumens (100 nm) would require more shallow etching resulting in shorter pillar structures. For instance, hollow nanoneedles with 250 nm lumens are a maximum 5 μm in height[499], while 100 nm lumen nanoneedles are only 1 μm high[498, 487]. Smaller lumens also run the risk of being blocked by proteins in solution that may impede continuous delivery of the payload.

4.1.5 Gaining Intracellular Access with Nanoneedles

Apart from their major application in intracellular delivery, nanoneedle arrays have been used to measure endogenous enzymatic activity and pH[529, 530], record neuronal activity[521, 488], sense mechanical forces exerted by cells[520], control cell division[145], perform metabolic labelling[496] and monitor signalling events by introducing gene silencing[489]. Nanoneedle arrays thereby have the potential to serve many of current needs in delivery and sensing applications, making their ability to gain intracellular access and traverse the cell membrane a feature of utmost importance (Fig. 4.1).

The observation that biological cargo is efficiently delivered to the cytosol may suggest that nanoneedle arrays can easily penetrate cells. Indeed, a study reporting highly efficient delivery of a wide range of biomolecules by simply culturing cells on functionalised nanoneedle arrays also claimed that there was membrane penetration in over 95% of cells[485]. Along with this an absence of membrane surrounding the tips of nanoneedles was claimed to be due to membrane penetration[489]. Delivery of biomolecules such as GFP and membrane impermeable fluorescent dyes via hollow nanoneedles 100 nm in diameter has also been suggested to take place through direct membrane penetration, although considered a stochastic event as high variation in fluorescence intensities was observed across cells[487]. Moreover, it is suggested that the overall efficiency of penetration remains high due to the high density of nanoneedles, thereby increasing the chance of penetration. Consistent with this is the observation of low transfection rates (1%) when using nanowire substrates with only 2-3 nanoneedles interfacing per cell[492]. Direct penetration of the membrane offers advantages in terms of bypassing endocytotic uptake and entrapment. A homogenous distribution of delivered molecules in the cytosol (as opposed to punctate distribution signifying endosomal entrapment), and a lack of co-localisation with endosomal compartments indicate that nanoneedle mediated delivery does not occur via endocytosis[487, 495]. Conflicting evidence indicates that the cell membrane penetration by nanoneedles is a rare event without the application of external force. Experimental evidence indicates that only 7% of nanoneedles were able to gain intracellular access[487]. Moreover, a mechanical model of cell membrane penetration for nanoneedles supports this finding as the force required to penetrate the cell membrane was found to be an order of magnitude higher

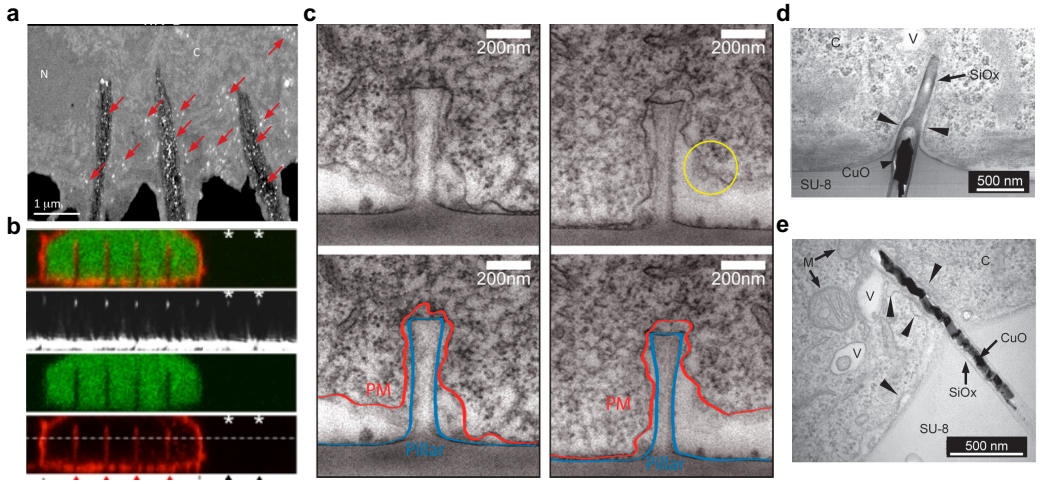


Figure 4.6: Microscopy of the cell-nanoneedle interface. The wide variety of high-aspect ratio nanoneedle arrays has led to few studies to investigate the membrane-nanoneedle interface. a) Electron microscopy image of porous silicon nanoneedles delivering quantum dots into the cytosol of HeLa cells. N = Nucleus, C = Cytosol. Image reproduced from [254] with permission from American Chemical Society, copyright 2015. b) Confocal microscopy of indium arsenide nanoneedle arrays deforming the cell membrane, while demonstrating lack of inserting into the cytosol. Image reproduced from [219] with permission from IOP publishing, copyright 2012. c) Series of transmission electron micrographs of nanopillar-cell interface indicating membrane wrapping around the nanopillars. Image reproduced from [246] with permission from American Chemical Society, copyright 2012. d), e) TEM images of the cell membrane wrapping around a silicon dioxide coated copper oxide nanowire. V = vesicle. Image reproduced from [512] with permission from John Wiley and Sons, copyright 2013.

than the force of gravity[531]. Further, a number of studies incorporating nanoneedle devices to obtain intracellular recordings of action potentials and enable high efficiency delivery was only possible in combination with electroporation or optoporation techniques[519, 532, 493, 533, 534]. The conformation of the membrane at the nanoneedle interface has been assessed in a few studies using microscopy techniques (Fig. 4.6). Electron microscopy of the cell membrane and nanoneedle interface have highlighted a tight association between the membrane and nanoneedles for a range of heights (500 nm to 2 μm) and diameters (50 nm - 500 nm)[512, 246, 252]. Image analysis of fluorescently tagged cell membranes interfaced with nanoneedles of varying lengths, spacing and surface functionalisations indicated that membranes wrapped around nanoneedles at the interface and that any absence of the membrane at the tip is due to high signal of fluorescence at the nanoneedle tip in comparison to the rest of the structures at the interface[219, 535]. In line with this observation, FIB-SEM data from a study using gold nanorods showed that penetration does not occur and engulfment itself varies spatially, as nanoneedles were engulfed only at the cell edges and not at the cell centre[536].

Finally, the initial presence of a membrane wrapping around SERS active nanoneedles, its disruption upon poration and its resealing process, that lead to changes in the membrane composition has been identified by Raman spectroscopy[486]. Other reports have provided insight on the ability of cells to actively deform their membranes around the nanostructures[184, 252, 127].

Overall, the variations in nanoneedle array geometry and surface functionalisation potentially contribute to conflicting observations in the literature surrounding their penetrability. While recognising that both outcomes are possible, the cell-nanoneedle interface warrants further characterisation to better explain the evolving concepts in achieving intracellular access with nanoneedles. Not only has this led to investigating the cell properties that may increase the changes of penetration but also nanoneedle properties that determine their ability to access the cytosol (Fig. 4.7).

4.1.6 Properties that Influence Nanoneedle Penetration

4.1.6.1 Cell Properties

Predictive models for cell settling on nanostructure arrays suggest that 2 μm pitch between nanoneedles may be the critical distance in determining whether cells remain suspended on top of the nanostructures or whether they settle to the bottom of the substrate[537]. This is an important parameter when considering how cells attach to nanoneedles as increasing the cell adhesion strength by coating nanoneedle arrays with adhesion molecule fibronectin can enhance intracellular access by 70%[487]. By increasing the adhesion force, the cell membrane is able to deform around the nanoneedles, resulting in a localised increase in membrane tension potentially leading to membrane penetration[538, 531]. A mechanical penetration model also suggests that cell stiffness is an influential factor in gaining access to the cytosol. Softer cells are less easily penetrated than stiff ones, requiring a longer indentation distance (5 μm as opposed to 1 μm) and smaller radii (<10 nm) to induce spontaneous penetration[531]. Experimental evidence indicating that only sharp and long nanoeedles and not thick and short ones were able to transfect less adherent primary immune cells is consistent with this idea[489]. Additionally, the insertion probability of single nanoneedles into cells is seen to increase with greater densities of actin cytoskeleton, suggesting that mechanical rigidity of cells may facilitate penetration[539]. In addition to the cytoskeleton, the cell membrane can

also provide a synergistic barrier to cytosolic access. Gaining intracellular access with nanoneedles was shown to be dependent on overcoming the actin cytoskeleton via Latrunculin A treatment and the cell membrane using dimethyl sulfoxide. Simultaneous treatment was shown to improve intracellular access compared to single treatments of one or the other[540]. In another study, transient chemical poration of the membrane using saponin, improved delivery of small molecules via nanoneedle arrays[499].

4.1.6.2 Application of External Force

Studies of AFM-operated nanoneedles have been instrumental in determining the quantity of force required to gain intracellular access. By visualising nanoneedle insertion via confocal microscopy alongside a corresponding drop in force-displacement curves by AFM, it was estimated that 0.5-20 nN of force, with an insertion speed of 3-10 μm/s was required to penetrate the membrane for a nanoneedle below 100 nm in radius in a number of different cell types[541, 504, 482, 483]. Arrays of nanoneedles exerting forces in the range of 2-6 nN applied via centrifugation on top of cultured cells was also shown to be sufficient for immediate delivery of plasmid DNA into primary neurons, co-delivery of DNA and siRNAs and intracellular sensing of enzymatic activity[542, 315, 530]. In a more complex system, arrays have been designed with a high-speed piezoelectric oscillator, that enable plasmid DNA delivery and expression with over 40% efficiency when in contact with cells[543].

It has been possible to gain intracellular access through electroporation at much lower potentials compared to standard electroporation, which is likely facilitated by the tight interaction at the membrane-nanoneedle interface[519, 532]. Experimental evidence suggest that electroporation enables intracellular access for one hour following stimulation, after which the membrane begins to reseal[532] and that access can be gained on multiple occasions in the same sample over several days[519, 532, 545]. In another study access by electroporation was facilitated in the remaining 50% of cells that were not spontaneously penetrated[521]. Plasmonic optoporation using nanoneedles made of plasmonic materials such as gold, porate the membrane with shock waves from laser light transduced by gold with the added advantage of spatial and temporal targeting[534].

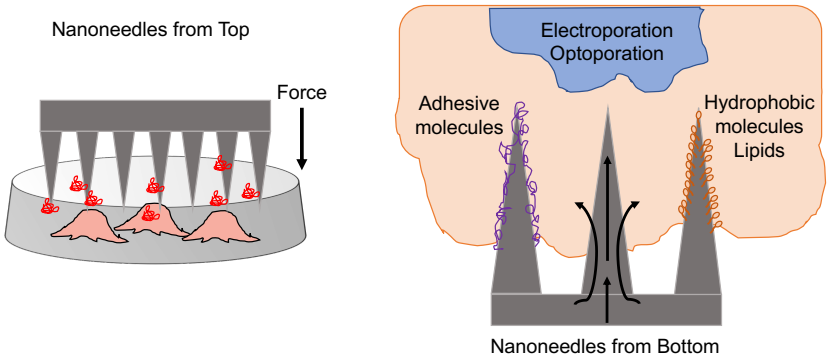


Figure 4.7: Schematic of methods to gain intracellular access using nanoneedles. Access to the cytosol can be triggered by application of external force. In the case of applying nanoneedle arrays from the top, centrifugation or application of force manually over cultured cells can be used to gain intracellular access[530]. The concept is similar to application of force via single AFM-operated nanoneedles[504]. In the case of culturing cells on nanoneedle arrays (nanoneedles from bottom), access can be improved by promoting cell adhesion through the use of cell-adhesive molecules such as fibronectin[487]. Electroporation and optoporation can be used in conjunction with nanoneedle arrays[519]. Coating nanoneedle arrays with 'stealth' molecules such as bilayers and hydrophobic silanes has also improved intracellular access[544].

4.1.6.3 Nanoneedle Surface Functionalisation

In addition to improving adsorption of cargo onto the nanoneedle surface (section 4.1.4.2), functionalisation of nanoneedles could also promote intracellular access without the application of external force. Coating extremely sharp nanoneedle probes with phospholipid bilayers and vesicles has enabled intracellular measurements of cardiac cell potential in a number of instances[544, 546, 484, 547]. Moreover, functionalising single nanoneedle tips with hydrophobic silanes enabled measurement of sub-threshold cell potentials as well as intracellular action potentials, while uncoated nanoneedles did not[548]. By mimicking the hydrophobic and hydrophilic arrangements present in the cell membrane, probes designed with hydrophobic cores designed to fuse with the cell membrane were efficient at inserting into a lipid bilayer, indicating that membrane access could be granted while using such stealth probes[549]. The fact that most transfection reagents including polyethylenimine (PEI) and poly-L-lysine (PLL) are developed on the basis of their high concentration of positively charged amine groups that can strongly bind negatively charged components such as DNA or the cell membrane, has fuelled attempts at functionalising amine groups on nanoneedles to increase interactions at the interface, enhancing the chances of membrane penetration. APTES functionalisation has been shown to improve adhesion of hMSCs on porous silicon sub-

strates by improving hydrophilicity that occurs through the addition of free amines at the surface[550]. APTES functionalisation of nanoneedle arrays has also been used in previous studies that showed high efficiencies of intracellular delivery[485, 315]. In other instances, relatively harsh strategies such as decorating nanoneedles with molecules of high positive charge such as cell penetrating peptides have been used to achieve 15% internalisation efficiency in primary neurons, with surprisingly little impact on cell viability[551].

Overall, the many parameters that influence intracellular access of nanoneedles demonstrates that a simple membrane penetration model does not fully describe the uniqueness and complexity of the cell-nanoneedle interface. The nature of interaction at the interface has a significant impact on events occurring across it, such as intracellular delivery, calling for more detailed investigations of the features of interaction and mechanism of delivery at the interface.

4.1.7 Potential Mechanisms of Nanoneedle-Mediated Delivery

Along with the aforementioned properties of nanoneedles and cells to facilitate cytosolic access, it is important to identify how the cell membrane responds to nanoneedle interfacing. As mentioned in section 1.3.2, the cell membrane is a highly complex and dynamic system that is sensitive to external forces, be it mechanical and biochemical. Mechanical deformation of the cell membrane can modulate the local composition of lipids and proteins[178], followed by crowding of intracellular scaffolding domains and potentially an induction of endocytosis[177, 173].

To this end, nanoneedle arrays can be recognised as topographical cues that induce nanoscale membrane deformation, and depending on the type and extent of curvature created, can influence accumulation of curvature sensing and endocytotic proteins. For instance, nanocones of 50 nm diameter have been used to study the recruitment of N-BAR domain proteins to sites of membrane deformation[183]. Moreover, nanopillars and nanobars induce curvature-dependent accumulation of proteins involved in CME[127]. Accumulation of CME proteins is initiated by positive curvatures within a radius of 200 nm, a finding supported by another study incorporating nanocolumns of 100 nm in diameter that induced clathrin protein accumulation[184]. A study modelling clathrin reorganisation during membrane invagination showed that over a certain degree

of indentation, there is disruption and 'fluidization' of the clathrin lattice around the indented area, initiating the binding and stabilisation of membrane curvature proteins and adaptors, leading to formation of clathrin coated pits[552].

Membrane tension is a key regulator of endo- and exocytosis, as the mechanical stress of the membrane is directly related to the cost of forming or losing vesicles[553]. The role of caveolae in membrane tension sensing, membrane resealing and endocytosis, highlights a potential role for their localisation to regions of high membrane tension and/or rupture during nanoneedle interfacing[435]. Although caveolae localisation was not found on nanopillars, caveolae have been observed on larger pillars of 5 μm diameter and height indicating an alternative role for their localisation[185].

High membrane curvature can influence stability of the membrane and also its permeability via changes in pore sizes[554]. This is indicative of the ambiguity in mechanism of delivery as small ruptures via membrane curvature may induce cytosolic entry, but cannot be resolved by current imaging techniques[512, 555]. It has been observed that for high-aspect ratio nanorods, intracellular access occurs only when tip of the rod is oriented perpendicular to the membrane surface, and uptake occurs as the cell initially perceives the nanostructure as a particle but eventually cannot engulf the entire length of the structure, causing frustrated phagocytosis and incomplete uptake[556, 557]. This is especially important since vertical nanoneedle arrays interface with cells perpendicularly. Additionally, the radius of the particle perceived by the cell is given by the tip radius of the nanostructure, usually between 50 and 100 nm, which is in the range for endocytotic uptake[430].

Although a number of studies have attempted to investigate membrane integrity and its contributions to nanoneedle-mediated delivery, the contribution of endocytosis towards cargo delivery via nanoneedles is a relatively new concept and remains to be investigated. Moreover, the ability to bypass the cell membrane barrier, the uptake response and fate of internalised cargo following nanoneedle-mediated delivery is cell type dependent and requires characterisation for clinically relevant cell types rather than transformed or immortalised cell lines studied in majority of nanoneedle literature.

4.1.8 Porous Silicon Nanoneedle Arrays for Biomolecule Delivery

Vertical arrays of biodegradable porous silicon nanoneedles used in this study have previously been shown to interface favourably with a number of cell types, with minimal impact on viability, while demonstrating proof-of-concept for delivery and sensing applications[507, 315, 530, 254, 558]. These nanoneedle arrays have enabled intracellular co-delivery of plasmid DNA and siRNA with over 90% efficiency, *in-vivo* delivery of plasmids for neovascularisation, and intracellular delivery of cell-impermeable quantum dots[315, 254].

Nanoneedle arrays used in this study are fabricated by Dr. Ciro Chiappini by combination of UV photolithography (that establishes position of the nanoneedles), MACE (that etches down the silicon and tailors porosity), and reactive ion etching (to introduce conical structure) (Fig. 4.8a). Porous silicon nanoneedle arrays are 4-5 μm in height, have a 2 μm pitch spacing, 50 nm tip diameter and 600 nm diameter at the base (Fig. 4.8b). The porosity allows these nanoneedles to be loaded with large concentrations of cargo, and their release profiles to be tailored to suit the application[254]. In spite of being porous, nanoneedles exhibit high failure and buckling loads around 260 nN, about 10-fold higher than force required to penetrate a cell membrane[482]. Additionally, porosity imparts tailorable degradation properties. In physiological conditions, these nanoneedles begin to lose their vertical structure by 8 hours, their complete shape by 15 hours and become shallow stumps by 24 hours (Fig. 4.8c)[315]. In this manner it is possible to inject payload overtime through an initial gain in intracellular access, while restoring original cell behaviour as the nanoneedles degrade (Fig. 4.8d).

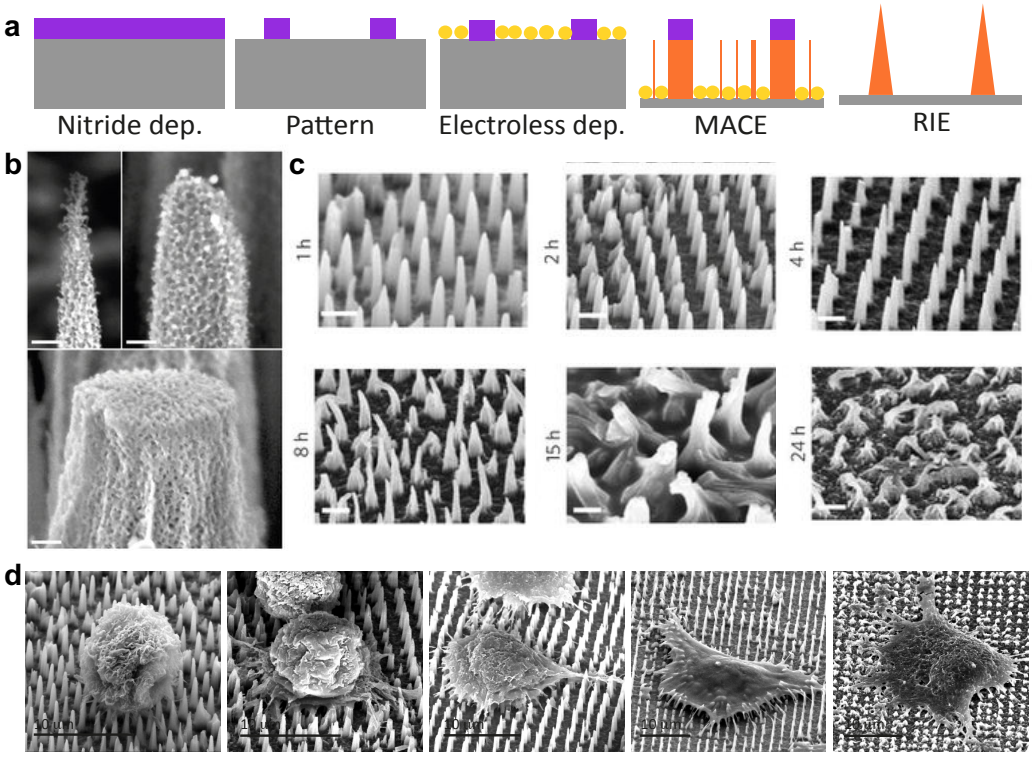


Figure 4.8: Fabrication, structure and degradation of vertical arrays of porous silicon nanoneedles. a) Fabrication process of porous silicon nanoneedles. Silicon nitride is deposited on a silicon wafer. Array of 600 nm dots with 2 μm pitch photoresist layer is deposited over the silicon nitride which is then etched down leaving silicon exposed. Silver nanoparticles are then deposited selectively on the silicon surface. MACE of silicon in HF yields porous silicon pillars. Reactive ion etching (RIE) of silicon in SF_6 results in conical shape of the nanoneedles. b) Scanning electron micrographs of porous nanoneedles of different tip diameters. Scale bar = 200 nm. c) Degradation of porous silicon nanoneedles over 24 hours at 37^{o}C with indicated times. Scale bar = 2 μm. a-c) Images reproduced from [315] with permission from Springer Nature, copyright 2015. d) SEM micrographs of cells cultured on nanoneedles over time, indicating initial attachment to complete spreading between 1 hour and 72 hours. Scale bar = 10 μm. Image reproduced from [254] with permission from American Chemical Society, copyright 2015.

4.2 Chapter Aims

Nanoneedle arrays have demonstrated high efficiencies of nucleic acid delivery[485, 489, 315]. However, the mechanisms by which cargo delivery occurs are unknown, while simple models of membrane penetration have not been able to describe the uniqueness of the membrane-nanoneedle interface. Direct evidence of membrane penetration while facilitating intracellular delivery is also lacking.

Given the complexity of the cell membrane and its ability to sense curvature, actively deform and initiate protein scaffolding, the involvement of membrane reshaping processes such as endocytosis during nanoneedle interfacing remains to be explored. Of parallel importance is the fate of the payload delivered by nanoneedles, as initiation of endocytosis can result in cargo degradation by endolysosomal entrapment.

In this chapter, the mechanism by which porous silicon nanoneedle arrays interact with the cell membrane to facilitate efficiency delivery of therapeutically relevant payloads, with a particular focus on the role of endocytosis, is investigated.

4.3 Materials and Methods

4.3.1 Antibodies and Reagents

6-Dodecanoyl-N,N-dimethyl-2-naphthylamine or Laurdan was purchased from Sigma-Aldrich. Anti-clathrin light chain (CLC, Rabbit) was purchased from Novus Biologicals (NBP2-14913), Anti-Caveolin-1 (Cav-1, Rabbit) was purchased from Abcam (ab2910), Anti-Early Endosome Antigen-1 (EEA1, Rabbit, C45B10), Anti-Lysosome Associated Membrane Protein-1 (Lamp1, Mouse, D4O1S) were purchased from Cell Signaling Technologies. Goat anti-Rabbit Fab' fragment was purchased from Jackson Immunolabs. Cy3-siRNA for GAPDH (Cy3-siRNA), Transferrin-Alexa488 (Tfn-488), Cholera Toxin B subunit-Alexa488 (CTxB-488), Albumin-Alexafluor488 (Alb-488) and Dextran-TexasRed (Dex-10kDa, Dex-40kDa and Dex-70kDa) and were purchased from ThermoFisher Scientific.

4.3.2 Preparation of Nanoneedle Arrays

Porous silicon nanoneedle arrays (nN) were fabricated by Dr. Ciro Chiappini and as previously described in [315, 502]. Flat silicon wafers (FSW) of the same size were used as controls. Nanoneedle arrays and FSW were cleaned using oxygen plasma for 15 minutes (PlasmaPrep II, Gala Instrumente, Germany). For experiments with 3-Aminopropyltriethoxysilane (APTES) functionalisation, nanoneedles and FSW were incubated with 2% (v/v) APTES (Sigma-Aldrich, A3648) in ethanol for 2.5 hours, after which they were extensively washed in 100% ethanol. Nanoneedle and FSW were dried under nitrogen gas. Prior to cell seeding functionalised and non-functionalised substrates were placed under a UV lamp for 20 minutes for further sterilisation. Cell seeding on nanoneedles and FSW took place immediately after plasma treatment in the case of non-functionalised substrates or within 24 hours of APTES functionalisation.

4.3.3 Cell Culture

HMSCs obtained from Lonza were expanded in chemically defined mesenchymal stem cell growth medium (MSCGM-CD, Lonza) or in MSCGM basal media (Lonza) with supplements added according the manufacturer's instructions until passage 3. HMSCs

were detached from culture flasks after rinsing with phosphate buffered saline (Invitrogen) using 0.05% (v/v) trypsin-EDTA and seeded on prepared nanoneedle or FSW substrates between passage 4 and 6. HMSCs were seeded in Minimum Essential Media Alpha (α-MEM, Gibco) supplemented with 10% (v/v) MSC-grade foetal bovine serum (Gibco) and 1% (v/v) Penicillin/Streptomycin (Gibco). For experiments without cargo loading onto nanoneedles and FSW, hMSCs were seeded on substrates placed in 24-well plates at 20,000 cells/cm^2 for 6 hours. For intracellular delivery experiments, in order to assess only cells in contact with the substrates for cargo uptake and not the rest of the well, a 50 μl cell suspension containing 60,000-80,000 cells was 'dry seeded' by dropping it over the substrates and care was taken to ensure it did not spread into the well. Substrates with the cell suspension were incubated for 1.5 hours at 37^{o}C, during which time the cells were allowed to attach to substrates alone, after which the media in each well was gently filled to normal volume and allowed to incubate for 24 hours. This ensured that all cells to be analysed remained on the substrates and did not attach to the bottom of the wells.

4.3.4 SICM Operation

SICM images of hMSCs cells cultured on nanoneedle arrays and FSW were acquired in hopping probe scanning mode using a home-built microscope (Fig **??**)[291]. Pipettes were pulled from borosilicate glass (Outer diameter = 1 mm, inner diameter = 0.5 mm, length = 7.5 cm Intracel, Cambridge, UK) using a P-2000 laser puller (Sutter Instruments). Pulling parameters for temperature and velocity of pull were optimised for each experiment to yield pipettes of roughly 100 nm and ion currents of 1 nA. Axopatch 200B amplifiers (Molecular Devices) were used to determine ion current measurements and a bias potential of 200 mV was applied. Pipettes were filled with sterile filtered PBS and attached to the piezo device. Ion current traces were tracked using pClamp10 (Molecular Devices).

Cells cultured on APTES and non-APTES treated nanoneedles and FSW for 6 hours were fixed in 4% (v/v) methanol-free paraformaldehyde solution (PFA, EM Sciences) for 15 minutes, washed with phosphate buffered saline (PBS) and placed in a 35 mm petri dish in PBS. After the pipette was immersed, a current of approximately 1 nA was detected, and the piezo controller was used to approach the sample. The pipette

approached the sample until there was a 0.3%-0.6% drop in current due to proximity to the sample surface. Cells were located by sudden increases in z-position of the pipette as shown by the current trace (See chapter 2, methods). SICM Image viewer, a home-written software was used for image presentation. Gwyiddion software for scanning probe microscopy data visualisation and analysis (www.gwyddion.net) was used for surface roughness measurements.

4.3.5 Electron Microscopy Sample Preparation

For scanning electron microscopy, hMSCs cultured on nanoneedles or FSW were fixed in 2.5% (v/v) GA in PBS or 0.1 M sodium cacodylate buffer for 30 minutes at room temperature. Samples fixed in GA-PBS were transferred to 0.1 M sodium cacodylate buffer. Samples were then treated with 1% (v/v) OsO_4 for 1 hour in 0.1M sodium cacodylate buffer. Samples were washed extensively in Milli-Q water twice for 5 minutes after which they were dehydrated in a series of graded ethanol concentrations in Milli-Q water twice for 5 minutes at 20%, 30%, 50%, 70%, 80% and 90%. Finally, samples were treated with 100% ethanol 4 times for 5 minutes each. Dehydrated samples were treated with hexamethyldisilazane (HMDS, Sigma) for 5 minutes and air dried.

For FIB-SEM and TEM, samples were prepared as above until the osmium fixation and wash step. Samples were treated with 1% (w/v) tannic acid (Sigma-Aldrich) in Milli-Q water for 1 hour and washed twice with Milli-Q water for 5 minutes. Samples were treated with 1% (w/v) UA in water for a minimum of 2.5 hours in the dark. Samples were washed in water twice for 5 minutes after which they went through a series of ethanol dehydrations as above. Dehydrated samples were infiltrated with epoxy resin as described previously. Excess resin was washed off with ethanol twice, with air drying the sample between washes, until some roughness of the sample surface was observed indicating that enough resin was washed off. Infiltrated samples were left to polymerise in an oven for 48 hours at 60^oC. For SEM and FIB-SEM, samples were mounted on aluminium stubs using carbon tape and sputtered with 10 nm of chromium or gold.

4.3.6 Electron Microscopy Imaging

4.3.6.1 SEM Imaging

For SEM, samples were visualised using a Sigma300 (Zeiss, Oberkochen, Germany) or Auriga Cross Beam SEM (Zeiss, Oberkochen, Germany) at an accelerating voltage of 5 kV and a working distance of 5 mm and secondary ion detector. The stage was tilted to 54^o for SEM imaging.

4.3.6.2 FIB-SEM Imaging

FIB-SEM imaging was conducted using Zeiss Auriga CrossBeam Workstation. Cells on nanoneedles were located using the SEM and the stage was tilted to 54^o. The same cell was located at the eucentric point using the FIB beam at a working distance of 5 mm. SEM images were obtained with an accelerating voltage of 1.6 kV using an electron back scatter detector. An imaging interval of 1 was used for 3D reconstructions yielding 30 nm sections using 1 nA:30 kV milling current. For vesicle number analysis, the sample was milled at 1 nA:30 kV until a row of nanoneedles appeared and a single image obtained at the estimated tallest part of the nanoneedles-membrane interface. Non-nanoneedles locations imaged in the same cell served as control.

4.3.6.3 FIB-Lift Out and TEM Imaging

FIB-milled lift-outs were prepared and imaged by Jelle Penders (Department of Materials, Imperial College London). Lamellas of hMSCs seeded on nanoneedles were prepared for TEM/STEM imaging by FIB-SEM lift-out using a Helios Nanolab 600 (FEI, Eindhoven, The Netherlands) equipped with a Gallium ion beam and a micromanipulator (Omniprobe, Oxford Instruments plc, Oxfordshire, United Kingdom). SEM imaging was performed at 2 kV and 0.17 nA and FIB milling at 30 kV with currents ranging from 28 pA to 2.8 nA. FIB polishing was performed down to 5 kV and 8 pA. A cell of interest was located by SEM imaging, showing normal morphology and proper preservation (Fig. 4.9a). The sample was oriented to have the nanoneedles rows perpendicular to the FIB direction. First a rough trench was milled in the front of the cell at 2.8 nA, then the region of interest was approached by milling at 0.92 nA while simultaneously imaging in SEM mode. After ensuring the cell staining and ultrastructure preservation

was adequate, milling was continued until the row of nanoneedles appeared (Fig. 4.9b). Platinum was deposited on top (1-1.5 μm wide) by Gallium assisted injection system at 93 pA-0.28 nA, up to a thickness of 1-2 μm. Further trenches were milled behind the region of interest and on the sides, freeing the lamella except for attachment to the base (Fig. 4.9c). The lamella was approached with the micromanipulator needle and attached by platinum deposition. The base of the lamella was milled loose and for structural stability of the lamella, up to 4 μm of silicon substrate was included in the lift-out (Fig. 4.9d). The middle post of a 3-post copper lift-out grid (Omniprobe, EM Sciences, Hatfield, PA, USA) was approached with the micromanipulator and the lamella was attached to the post by further platinum deposition, after which the micromanipulator was cut loose (Fig. 4.9e). The lamella was thinned to electron transparency, 100-120 nm, by FIB milling equally on both front and back of the lamella ensuring the apex of the nanoneedles is in the centre of the lamella (pre-thinning Fig. 4.9f, post-thinning Fig. 4.9g side view, Fig.h front view). The lift-outs were imaged by TEM with a JEOL JEM-2100F TEM at 200 kV or at 200 kV with a dark field detector in STEM mode.

4.3.7 Laurdan Staining, Multiphoton Imaging and Analysis

Thirty minutes prior to PFA fixation, media was aspirated and replaced with serum-free MSCGM containing a final concentration of 50 μM Laurdan. HMSCs on nanoneedle arrays and FSW were incubated with Laurdan containing media at 37^{o}C for 30 minutes. Media was aspirated, samples were washed with PBS and fixed in 4% (v/v) PFA.

Imaging of Laurdan stained samples was conducted using a Leica SP5 upright confocal microscope equipped with a Spectraphysics Mai-Tai 690-1020 multiphoton laser and a 63x oil immersion objective. Multiphoton imaging was set up according to [216]. Laurdan was excited at 800 nm and intensity images were detected by photomultiplier tubes (PMT) at 400-460 nm and 470-530 nm.

Generalised polarisation values (GP) were obtained according to:

$$GP = \frac{I_{400-460} - GI_{470-530}}{I_{400-460} + GI_{470-530}}$$

where the G value was calibrated for each experiment to allow cross comparison between different experiments due to the use of different PMT gains and I represents

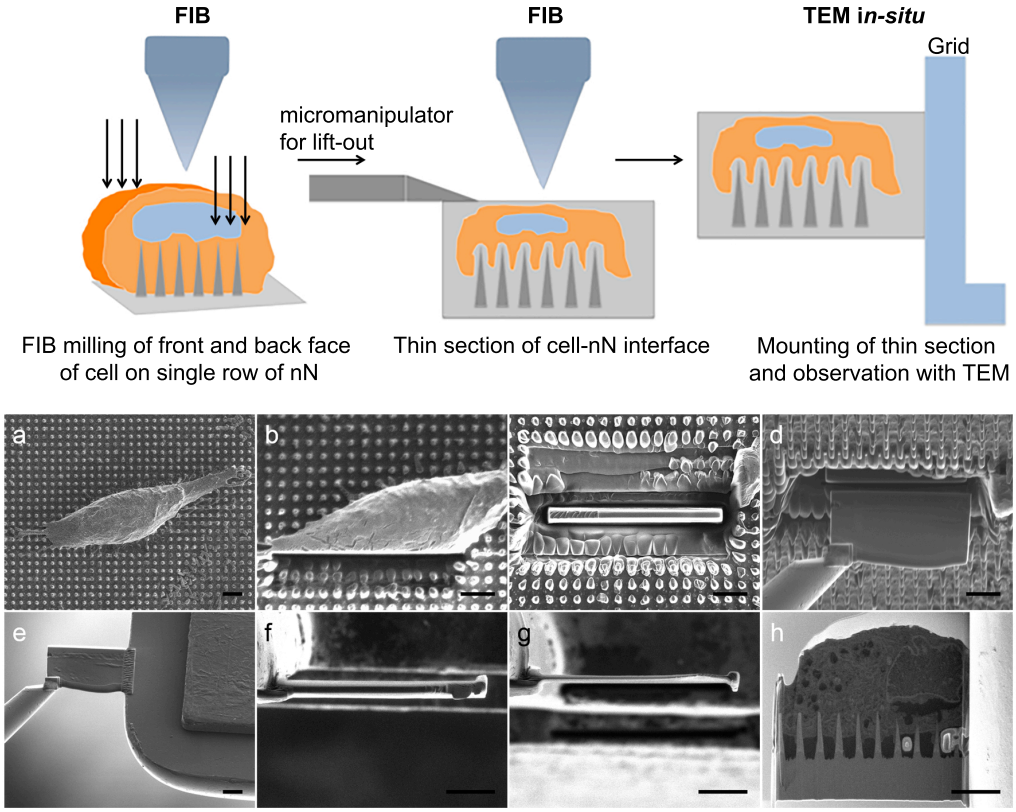


Figure 4.9: Schematic and process flow of FIB-SEM lift-out sample preparation for TEM. Top panel schematic summarises the process of FIB-SEM lift out for TEM. Bottom panel indicates actual process of lift-out of cell-nanoneedle thin-section. a) Location of cell of interest. b) Milling of first trench and observation of interior cell structure, mill until start of nanoneedle row. c) Platinum deposition on region of interest (1-1.5 μm wide), milling of trenches on the back and sides forming a free standing lamella. d) Approach and attachment of micromanipulator needle, milling of bottom and freeing of the lamella, retraction and lift-out of lamella. e) Approach and attachment of lamella to a lift-out grid by platinum deposition. f) Side view of the lamella prior to thinning. g) Thinning of the lamella equally on both sides to 100-120 nm thickness ensuring the apex of the nanoneedles is in the centre of the lamella. h) Front view of the lamella post thinning. Scale bars = 5 μm. Images obtained by Jelle Penders.

the intensity of pixels in the ordered channel (400-460) and the disordered channel (470-530)[216]. The G value was measured for each experiment and calculated from a calibration image G_{mes}, the intensity image of Laurdan at 50 μM concentration in dimethyl sulphoxide (DMSO) (i.e. the same concentration and the same PMT gains as in each experiment) and a G_{ref} value from the literature = 0.207[559] according to:

$$G = \frac{GP_{ref} + GP_{ref}GP_{mes} - GP_{mes} - 1}{GP_{mes} + GP_{ref}GP_{mes} - GP_{ref} - 1}$$

Laurdan images of confocal sections of hMSCs just above the tips of the nanoneedles and at the basal surface of FSW were obtained for analysis of GP values. A minimum

of 20 cells from 3 independent experiments were used for analysis.

4.3.8 Immunolabelling, confocal fluorescence imaging and analysis

HMSCs on nanoneedles and FSW were fixed with 4% PFA for 15 minutes in PBS. Samples were washed twice for 5 minutes in PBS and treated with 0.25% (v/v) Triton X-100 in PBS for 5 minutes. Samples were washed with PBS and incubated with 5% normal serum in PBS (v/v) of the same species as the secondary antibody for 1 hour at room temperature. Primary antibodies to Cav-1 (1:300, v/v), CLC (1:300, v/v), were allowed to incubate overnight at 4^oC in 0.1% (v/v) Bovine serum albumin (BSA) in PBS. For Lamp1 staining, PFA fixed samples were treated with methanol for 5 minutes at -20^oC and washed twice in PBS for 5 minutes. For immunofluorescence staining with multiple primary antibodies of the same species, primary antibodies to Cav-1 or CLC were applied as mentioned and samples were washed in 0.1% (v/v) BSA-PBS three times for 5 minutes. Samples were probed with goat anti-rabbit Fab' fragment (1:30, v/v) in 0.1% BSA-PBS was for 1.5 hours and washed three times for 5 minutes in 0.1% BSA-PBS. Secondary Alexafluor anti-goat antibodies (ThermoFisher Scientific) were applied to detect Cav-1 or CLC for 1 hour in 0.1% BSA-PBS in the dark (Fig. 4.10). Samples were probed with both EEA1 (1:100, v/v) and Lamp1 (1:200, v/v) antibodies in 0.1% BSA-PBS overnight at 4^oC. Samples were washed three times for 5 minutes in 0.1% BSA-PBS and probed with secondary Alexafluor antibodies for EEA1 and Lamp1. Samples were washed 3 times for 5 minutes in PBS, stained with DAPI (1:1000, v/v), washed and flipped upside down into chamber slides (Ibidi) containing Vectashield (Vector Labs) for imaging by confocal microscopy. Images were obtained using a Leica SP5 inverted microscope using a 63X oil immersion lens and optical zoom (Leica Microsystems, Wetzler, Germany). For co-localisation analysis, single planes of multi-channel images were imported into Volocity Software (6.3, Perkin-Elmer) and automatically thresholded using Costes' method. Mander's coefficient of overlap of channel 1 (siRNA) over channel 2 (CLC, Cav-1, EEA1 or Lamp1) was selected and converted to a percentage for statistical analysis. For endolysosomal pathway co-localisation analysis, multi-channel images of CLC or Cav-1 with EEA1 and Lamp1 were overlaid in a single channel and analysed for co-localisation with delivered payload as mentioned above.

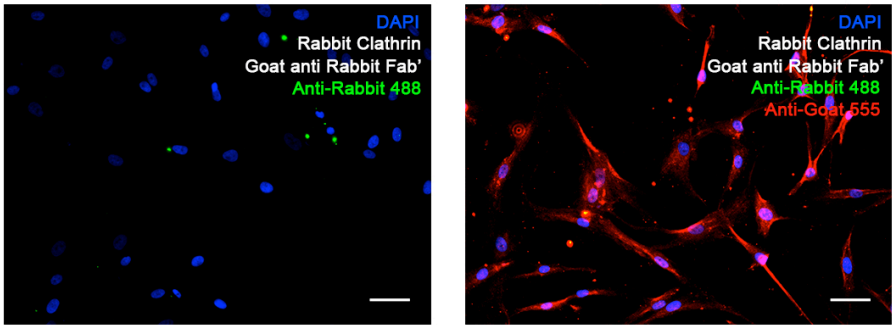


Figure 4.10: Fluorescence microscopy images of hMSCs immunolabeled with rabbit anti-clathrin antibody, incubated with goat-anti rabbit Fab' fragment followed by (left) donkey anti-rabbit secondary AlexaFluor488 or (right) anti-rabbit secondary AlexaFluor488 and anti-goat AlexaFluor555 indicating that the primary rabbit immunolabel is converted to goat by goat anti-rabbit Fab' fragment. Scale bar = 20 μm.

4.3.9 Nanoneedle-Mediated Biomolecule Loading and Delivery

Tfn-488 (25 μg/ml), Alb-488 (40 μg/ml), CTxB-488 (5 μg/ml), and Dex-TexasRed (10 kDa, 40 kDa and 70 kDa, 1 mg/ml) were each reconstituted in a previously optimised buffer containing 0.25 M glycine and 400 mM KCl, pH adjusted to 5.0 (Buffer 1). A volume of 10 μl of cargo solutions were physisorbed onto nanoneedles and FSW for 45 minutes in a humidified chamber at room temperature in the dark. Cargo loaded FSW substrates were rinsed briefly in Buffer 1 after which cells were dry seeded onto the substrates for 24 hours.

For Cy3-siRNA delivery, substrates were pre-treated with 2 M HCl for 10 minutes after plasma and UV treatment followed by rinsing in distilled water and air drying. 10 μl of Cy3-siRNA (1 μM) solution in Buffer 1 was adsorbed for 45 minutes in a humidified chamber in the dark. Substrates were washed once with Buffer 1 and air-dried. Substrates loaded with Cy3-siRNA were washed further with Buffer RPE (Qiagen) and air-dried. Cells were dry seeded on loaded substrates for 24 hours. For Cy3-siRNA delivery experiments, it was important that hMSCs were thawed from frozen, cultured to 70% confluence at passage 4 and seeded at passage 5 in all experiments.

4.3.10 Flow Cytometry

After 24 hours of culture on cargo loaded nanoneedle and FSW substrates, media was aspirated and substrates were transferred to a new well plate and washed with

ice cold PBS. Cells were detached from substrates using 0.05% (v/v) Trypsin-EDTA, collected and centrifuged at 300 x g for 7 minutes at 4^{o}C. Cells were resuspended in PBS and centrifuged once again, after which the pellet was resuspended in 200 μl of flow cytometry staining buffer (BioLegend). Flow cytometry data was acquired by Vincent Leonardo (Department of Materials, Imperial College London). Samples were measured with a LSR FORTESSA (BD) equipped with 488 nm and 561 nm laser and 530/30, 582/15 and 610/20 filters. Raw data were analysed with FlowJo and equal population gates were applied in order to allow direct comparison between experimental groups.

4.3.11 Quantitative Real Time Polymerase Chain Reaction (qRT-PCR)

qRT-PCR and analysis was performed by Dr. Hyejeong Seong (Department of Materials, Imperial College London). Cells on nanoneedle and FSW substrates were treated with Trizol reagent (Life Technologies), mixed with chloroform (1:5, v/v, Chloroform:Trizol) and separated by centrifugation for 15 min at 4^{o}C at 12,000 x g. RNA was isolated from the aqueous phase after the centrifugation using Direct-zol RNA MiniPrep Kit (Zymo Research) based on the manufacturer's instructions. cDNA was synthesised using High Capacity cDNA Reverse Transcription Kits (Applied Bioscience) according to the manufacturer's instructions. qRT-PCR was performed with the PowerUP SYBR Green Master Mix (Applied Biosystems), with 2.5 ng cDNA and 500 nM forward and reverse primers, using a StepOne Plus machine (Applied Biosystems). The StepOne Plus protocol ran as 95^{o}C for 2 minutes followed by 40 cycles of denaturation at 95^{o}C for 3 seconds and annealing at a temperature 60^{o}C for 30 seconds. Cycles-to-threshold (Ct) values were automatically obtained from the StepOne software v2.3. These values were exported to the Excel file and manually processed to generate fold change expression values. The expression of each gene of interest was normalized to the geometric mean of the expression of at least two housekeeping genes PPIA and RPL13A, generating the δC(t) value, and expression of 2^{-d}C(t) relative to the control. Primers were purchased from Invitrogen and sequences are listed below in Table 4.2.

Gene Name	Accession No.	Forward Primer 5'-3'/ Reverse Primer 5'-3'	Amplicon (bp)	Total Primer Conc.
GAPDH	NM002046.4	GCACCGTCAAGGCTGAGAAC TGGTGAAGACGCCAGTGGA	138	500 nM
PPIA	NM021130	CTTCACACGCCATAATGGC GTGATCTTCTTGCTGGTCTTG	273	500 nM
RPL13A	NM012423	AAGTACCAGGCAGTGACAG CCTGTTTCCGTAGCCTCATG	100	500 nM

Table 4.2: qRT-PCR Primer Sequences

4.3.12 Statistical Analysis

Statistical analysis was performed using GraphPad Prism 6.0. In the case where data of two groups were normally distributed, the Student's unpaired t-test was used. When the data was not normally distributed the non-parametric Wilcoxon-Mann-Whitney test was used. Significant differences were reported for p-values <0.05.

4.4 Results

4.4.1 Cell Viability

A key feature of nanoneedles is their ability to maintain cell viability during cell interfacing. This has been demonstrated in a number of cell types as well as nanoneedle arrays made of different materials[489, 560, 492]. Porous silicon nanoneedle arrays have also been applied to cancer cell lines such as HeLa[315] and OE33[530, 254], epithelial cell line Het-1A[530, 254]. Moreover, HeLa cells have been shown to survive for over five days on porous silicon nanoneedles, without any negative impact on their metabolism[315]. More recently, the viability and proliferation of primary cells such as hMSCs and human umbilical vein endothelial cells (HUVECs) on APTES functionalised porous silicon nanoneedles were tested up to 48 hours, showing no impact on cell viability (unpublished data).

In order to assess whether APTES functionalisation is necessary for maintenance of cell viability, hMSCs were cultured on porous silicon nanoneedles after treatment with oxygen plasma and UV sterilization. After 6 hours of culture, the viability of hMSCs on plasma treated nanoneedle arrays and FSW substrates was assessed using a LIVE/DEAD^{TM} cytotoxicity kit for mammalian cells (ThermoFisher Scientific) containing Calcein-AM (live, green) and Ethidium homodimer-1 (dead, red). Calcein-AM indicates esterase activity within cells, while ethidium homodimer-1 indicates a loss of cell membrane integrity. A time point of 6 hours was selected due to the degradation profile of nanoneedles, where in 6 hours the nanoneedles are still presented as sharp structures and their specific interactions with cells can be studied, while by 24 hours they remain as blunt stumps (Fig. 4.8c,d). LIVE/DEAD^{TM} labelling of hMSCs cultured on nanoneedle and FSW substrates indicated that cells were viable on both surfaces, with very few observed dead cells (Fig. 4.11).

4.4.2 Membrane Morphology on Nanoneedle Arrays

4.4.2.1 Nanoneedle Interfacing Induces Apical Membrane Ruffling

After ascertaining that nanoneedles do not impact hMSC viability, the morphology of the membrane on the nanoneedles was studied in more detail. Label free topographical

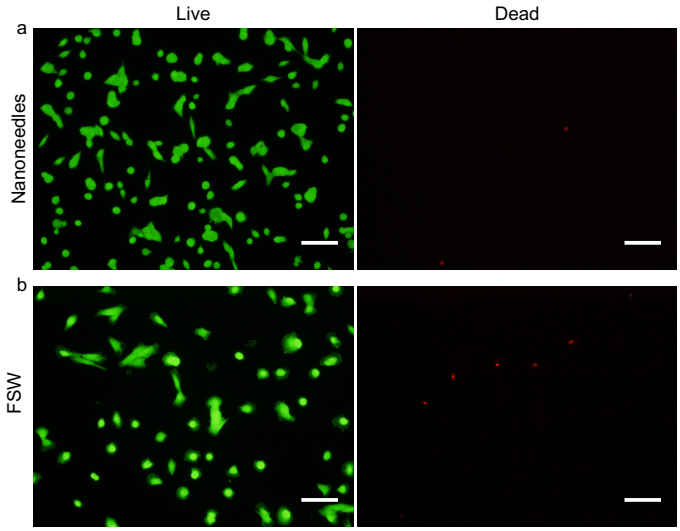


Figure 4.11: LIVE/DEAD^{TM} labelling of hMSCs cultured on a) nanoneedle arrays and b) FSW substrates for 6 hours. hMSC viability is maintained during interfacing with plasma treated nanoneedle arrays. Scale bar = 50 μm.

imaging of apical membrane of hMSCs cultured on nanoneedle arrays and FSW for 6 hours was performed through SICM. SICM was did not require sample dehydration or extensive fixation, and cells were imaged in their native, hydrated state. Nanoneedle arrays stimulated the formation of numerous membrane protrusions in hMSCs as observed by topographical maps of the membrane surface imaged by SICM (Fig. 4.12a). The membrane of hMSCs on nanoneedle arrays appeared ruffled, similar to dorsal membrane ruffles seen in cells treated with growth factors that stimulate macropinocytosis[561]. Moreover, membrane ruffling in hMSCs on nanoneedle arrays contributed to a 1.5-2-fold increase in apical membrane roughness compared to cells cultured on FSW (Fig. 4.12b,c).

This appearance of the membrane was further confirmed by SEM imaging. In addition to apical membrane ruffling, SEM imaging of tilted samples showed cells on nanoneedle arrays extending their filopodia, and pulling individual nanoneedles towards them (Fig. 4.12d). As a result, many bent nanoneedles were observed around the cell periphery, indicating that cells exert a considerable amount of force on these nanostructures[236]. Filopodia have previously been recognised as important cell processes responsible for topography sensing[145].

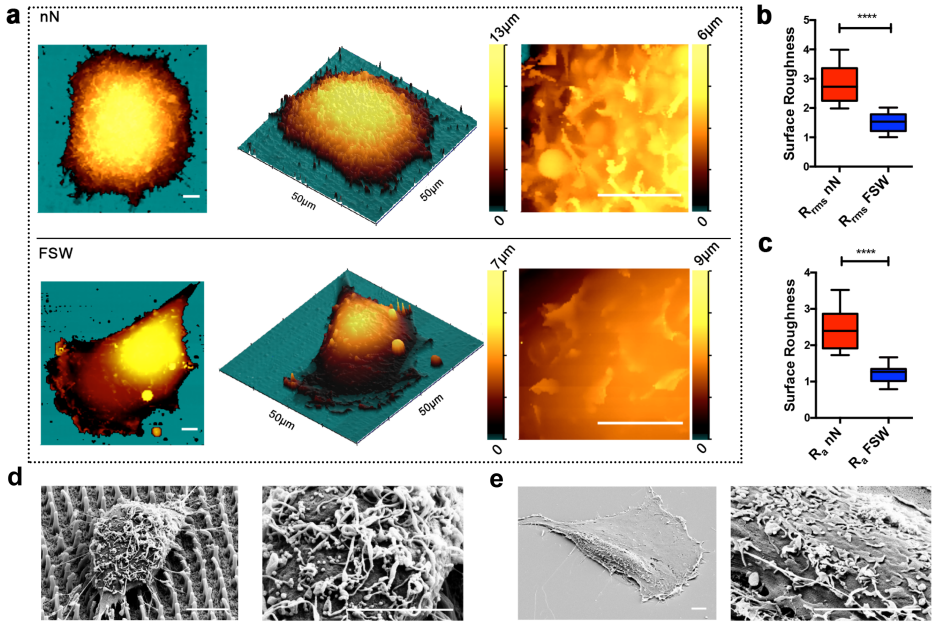


Figure 4.12: The membrane response to nanoneedle interfacing. a) Top panel: 2D, 3D and a zoomed-in 2D 20 μm x 20 μm SICM topographical scan of a hMSC cultured on nanoneedles after 6 hours. Bottom panel: 2D, 3D and a zoomed-in 2D 20 μm x 20 μm topographical SICM scan of a hMSC cultured on FSW after 6 hours. Scale bar = 10 μm. b) Surface roughness (R_{RMS}) of apical membrane of hMSCs on nanoneedles compared to FSW measured by SICM. c) Surface roughness (R_a) of apical membrane of hMSCs on nanoneedles compared to FSW measured by SICM. n = 8 for nN and n = 11 for FSW. Data represented as box and whisker plots with median, interquartile range, minimum and maximum values. ****p<0.0001 between indicated groups. d) Tilted SEM image of hMSC on nanoneedles and zoomed-in SEM image of its apical membrane. e) Tilted SEM image of hMSC on FSW and zoomed-in SEM image of its apical membrane. Scale bar = 5μm.

4.4.2.2 Nanoneedle Interfacing Stimulates Changes in Membrane Lipid Order

In order to elucidate whether nanoneedle interfacing induced changes in microdomain membrane ordering, particularly at the interface, Laurdan, a lipophilic membrane dye was used as a reporter for membrane order[559, 216]. For Laurdan, an increase in spectral shift of 50 nm takes place when it incorporates into more disordered fluid portions of the membrane (between 470-530 nm), while its binding to ordered phases of the membrane results in fluorescence at lower wavelengths (between 400-460 nm)(Fig. 4.13a). The spectral shift can then be used to determine both spatially and quantitatively, the proportions of the membrane in lipid ordered and disordered phases by calculating generalised polarisation (GP) values from the intensity at each pixel in the spectrally separated images (See methods).

Laurdan images were collected at confocal depths between the top of the apical membrane to the confocal plane above the nanoneedles. For FSW control, complete Z-stacks were obtained. For analysis, the confocal slice above the region of the nanoneedle arrays was selected and compared against the basal surface of cells on FSW (Fig. 4.13b). Analysed GP values for hMSCs on nanoneedle arrays compared to cells on FSW, indicated a mean positive shift of 0.07 in GP (Mean ± s.d. were 0.51 ± 0.04 for cells on nanoneedles versus 0.43 ± 0.06 for FSW)(Fig. 4.13c). This corresponded to a significant increase in membrane lipid ordering (Fig. 4.13d). Increased GP values in cells on nanoneedles were seen at the cell edges and in membrane protrusions which is consistent with other studies indicating increase in GP values in filopodia[562]. Moreover, the increase in GP was seen particularly in the confocal planes just above the nanoneedles, where the nanoneedle tips were estimated to interact with the cell membrane. However, the areas of increased GP values for hMSCs on nanoneedle arrays did not present any spatial correlation or co-localization with the nanoneedles themselves, perhaps due to the complexity of the interface considering the 3D structure of the nanoneedles and resolution limit of the microscope.

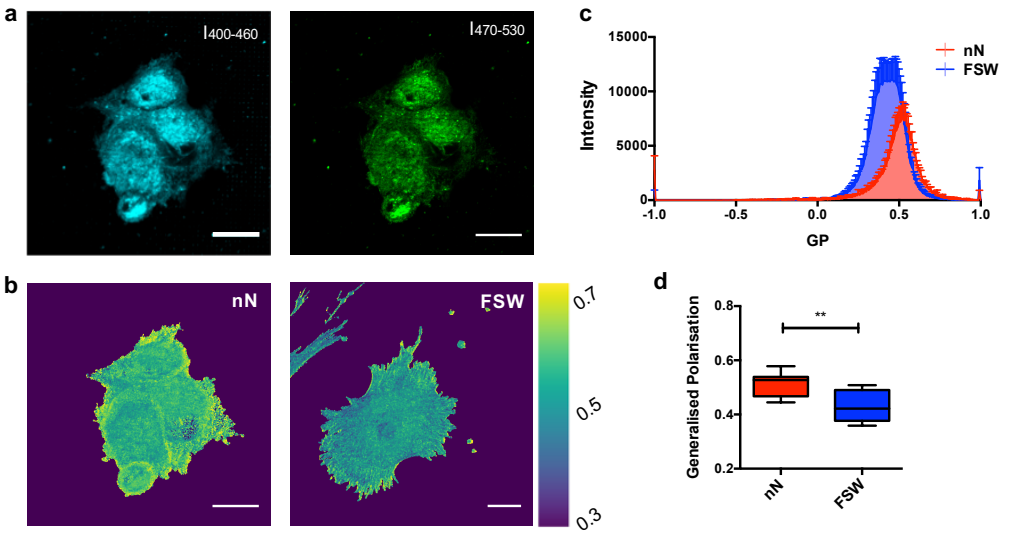


Figure 4.13: Nanoneedle stimulate changes in membrane order in hMSCs. False coloured intensity images of a single plane of hMSCs on nanoneedles after 6 hours of culture at depicting Laurdan images of 400-460 nm ($I_{400-460}$) and 470-530 nm ($I_{470-530}$). b) Representative psuedo-coloured GP images of hMSCs on nanoneedles (left) and FSW (right). All scale bars = 20 μm. c) Distribution of GP values depicting relative membrane order for hMSCs on nanoneedles and on FSW. d) Mean GP values for hMSCs on nanoneedles compared to FSW. Data are represented as box and whisker plots of mean GP values from N = 3 experiments and at least 20 cells for each condition. **p<0.01 between indicated groups.

4.4.3 Membrane Integrity at the Cell-Nanoneedle Interface

To better characterise the biointerface, a recently developed focused ion beam scanning electron microscopy (FIB-SEM) approach was used for *in-situ* slice-and-view, that permits visualisation of the interface at the nanoscale, at any selected location in the sample. A sample is sequentially milled by a focused ion beam generally comprised of gallium ions, while the newly milled face is imaged by an SEM detector (Fig. 4.14a, Schematic). Milling depths are determined by the magnitude of milling current, where lower milling currents enable greater control over milling, and lower slice thickness (down to 10 nm), but longer milling times. In order to observe different cellular components, samples were prepared according to the protocol optimised in Chapter 2. This allowed cells on the substrate to be imaged effectively (Fig. 4.14b).

After 6 hours of culture, the interface between hMSCs and nanoneedles was assessed with FIB-SEM. The samples were milled until the highest point of a row of nanoneedles was visible underneath the cells (Fig. 4.14c). At higher magnifications, FIB-SEM showed the basal membrane of hMSCs deforming and wrapping around individual nanoneedles without discontinuities in the membrane evident at 30 nm resolution, indicating that the membrane was not traversed in this situation. The membrane was in tight association for most of the length and tip of each nanoneedle similar to the portion of the membrane in contact with non-nanoneedle locations. There was an occasional appearance of a cleft at the side of the nanoneedles similar to what has been observed for cells on nanopillar structures (Fig. 4.14d,e)[252]. Although the samples were prepared with standard chemical fixation and dehydration techniques for EM, it is worth noting that chemical fixation of samples can be more damaging to intracellular tubular structures including cytoskeletal filaments, rather than the plasma membrane[563, 564].

Alongside FIB-SEM studies, analysis of resin-embedded sections was performed by transmission electron microscopy (TEM) or scanning TEM (STEM). Since it was necessary to observe cells on nanoneedles *in-situ*, thin sections of hMSCs on nanoneedles were prepared by the FIB lift out method (Fig. 4.9, methods). Thin-sections were prepared and imaged by Jelle Penders. Higher resolution STEM/TEM micrographs of FIB-milled sections showed extreme vicinity (in the order of nanometers) between

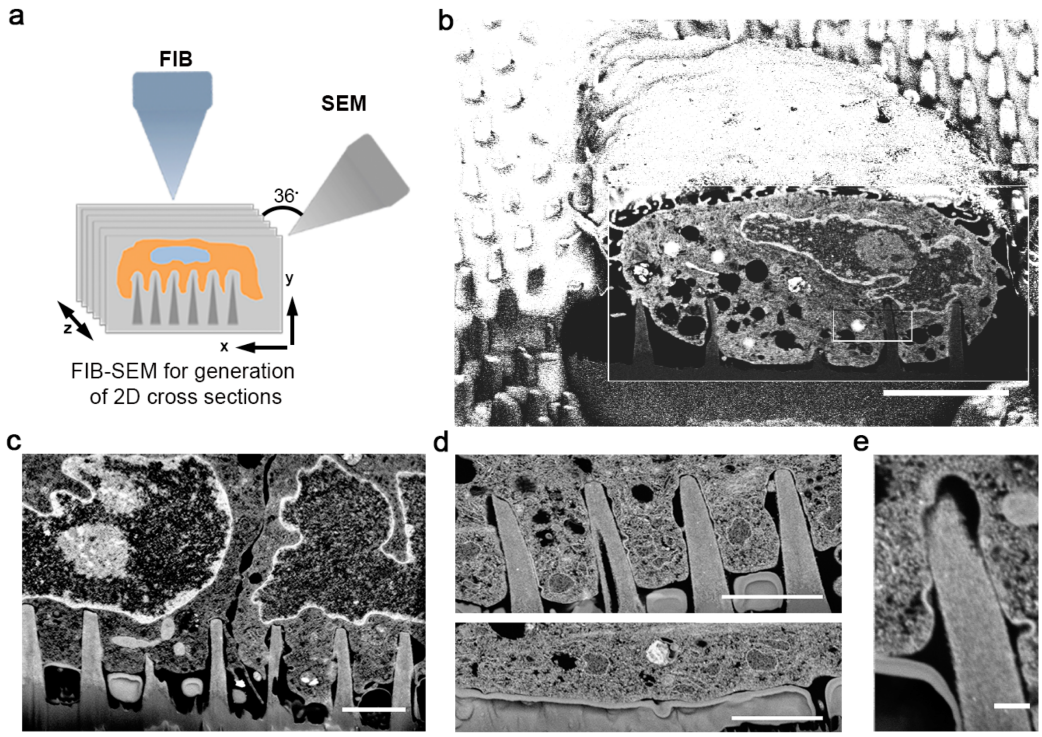


Figure 4.14: a) Schematic of FIB-SEM set up. 2D cross sections of the cell-nanoneedle interface at 30 nm sections as the focused ion (gallium) beam mills through the sample. Samples are milled orthogonally and newly milled face is imaged using an SEM backscatter detector at the coincidence point (where the beams meet). b) Zoomed-out SEM cross-section of an resin-embedded hMSC located on the nanoneedle sample. Scale bar = 6 μm. c) SEM images of a milled cross-section indicating two cells in contact while interfacing with nanoneedles. Scale bar = 2 μm. d) SEM images of milled cross sections of nanoneedle (top) and non-nanoneedle (bottom) regions indicating intact membranes. Scale bar = 2 μm. e) Zoomed-in view of membrane-nanoneedle interface indicating membrane-wrapping and clathrin-like vesicles. Scale bar = 200 nm.

nanoneedles and the membrane at the interface. The darkly stained 4-6 nm plasma membrane bilayer could be seen wrapping around the nanoneedles in multiple instances (Fig. 4.15a). Since the thickness of the section was approximately 100 nm, the membrane did not appear uniformly thick or defined across the nanoneedles as the membrane is present within different planes within the thin section itself. Nevertheless, the membrane was observed at the tip and over the side of the nanoneedles, along with some cases of inwardly budding vesicular structures (Fig. 4.15b).

4.4.4 Nanoneedle Interfacing Triggers Endocytosis

Given the lack of discontinuities in the plasma membrane, the absence of observed membrane penetration, increased membrane ruffling and membrane order, endocytosis could contribute to payload delivery via nanoneedle arrays. To investigate whether

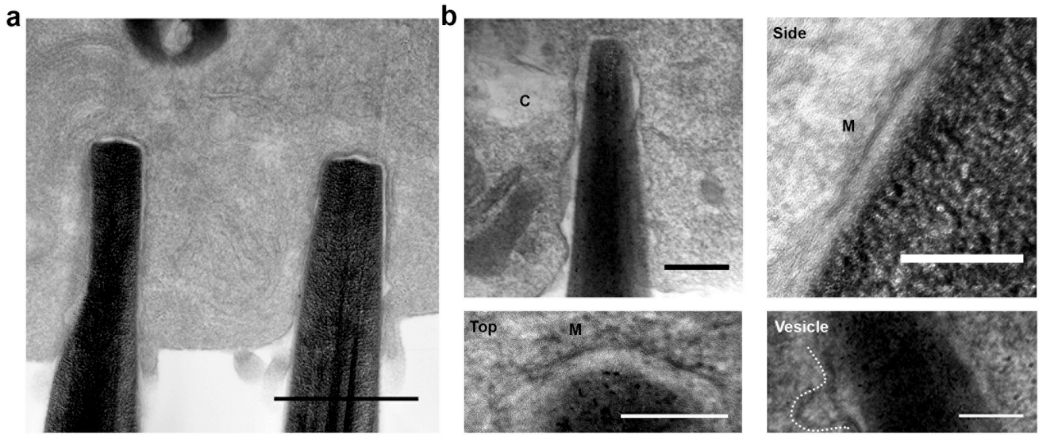


Figure 4.15: STEM and TEM of the cell-membrane nanoneedle interface. a) Zoomed-out STEM image of the hMSC-nanoneedle interface indicating two nanoneedles being wrapped by the cell membrane with close association and extreme vicinity between the membrane and nanoneedles. Scale bar = 1 μm. b) Left to right: TEM of a FIB lift-out thin section of the hMSC-nanoneedle interface. TEM image of the side of the nanoneedle. TEM image of the top of the nanoneedle interface. TEM image of the side of the interface indicating a vesicle at the side of the nanoneedle. C= cytosol M = membrane, scale bar = 200 nm. STEM/TEM imaging was conducted with Jelle Penders

endocytotic proteins are associated with membrane-nanoneedle interfacing, immunolabelling and fluorescence microscopy of proteins that modulate the formation of key endocytotic vesicles, namely clathrin light chain (CLC) for clathrin-mediated endocytosis (CME) and caveolin-1 (Cav-1) for caveolae-mediated endocytosis (CavME) was conducted for hMSCs cultured on nanoneedle arrays and FSW substrates. Immunofluorescence analysis highlighted that both CLC and Cav-1 were localised to nanoneedle locations, as the basal membrane of hMSCs was clustered with periodic intensity of these proteins (Fig. 4.16). Fourier transform analysis confirmed that the period (1.967 $\pm$ 0.05 μm) matched the nanoneedle spacing of 2 μm (Fig. 4.16d, h). The same proteins were unaffected both at the apical membrane, as well as basally or apically for hMSCs on FSW as no periodicity was observed (Fig. 4.16a, c, e, g).

In order to validate that the localisation of CLC and Cav-1 to sites of nanoneedle interfacing results in the formation of functional endocytotic vesicles, FIB-SEM was used to detect the presence of clathrin coated pits (CCP) and caveolae at the interface. Imaging the interface with nanoscale resolution of FIB-SEM, membrane invaginations in the size range and shape of CCPs and caveolae were found budding into the cell around the nanoneedles (Fig. 4.17a). CCPs, spherical 'coated' structures in the size range of 150-200 nm, and caveolae, smaller flask shaped structures were found invaginating

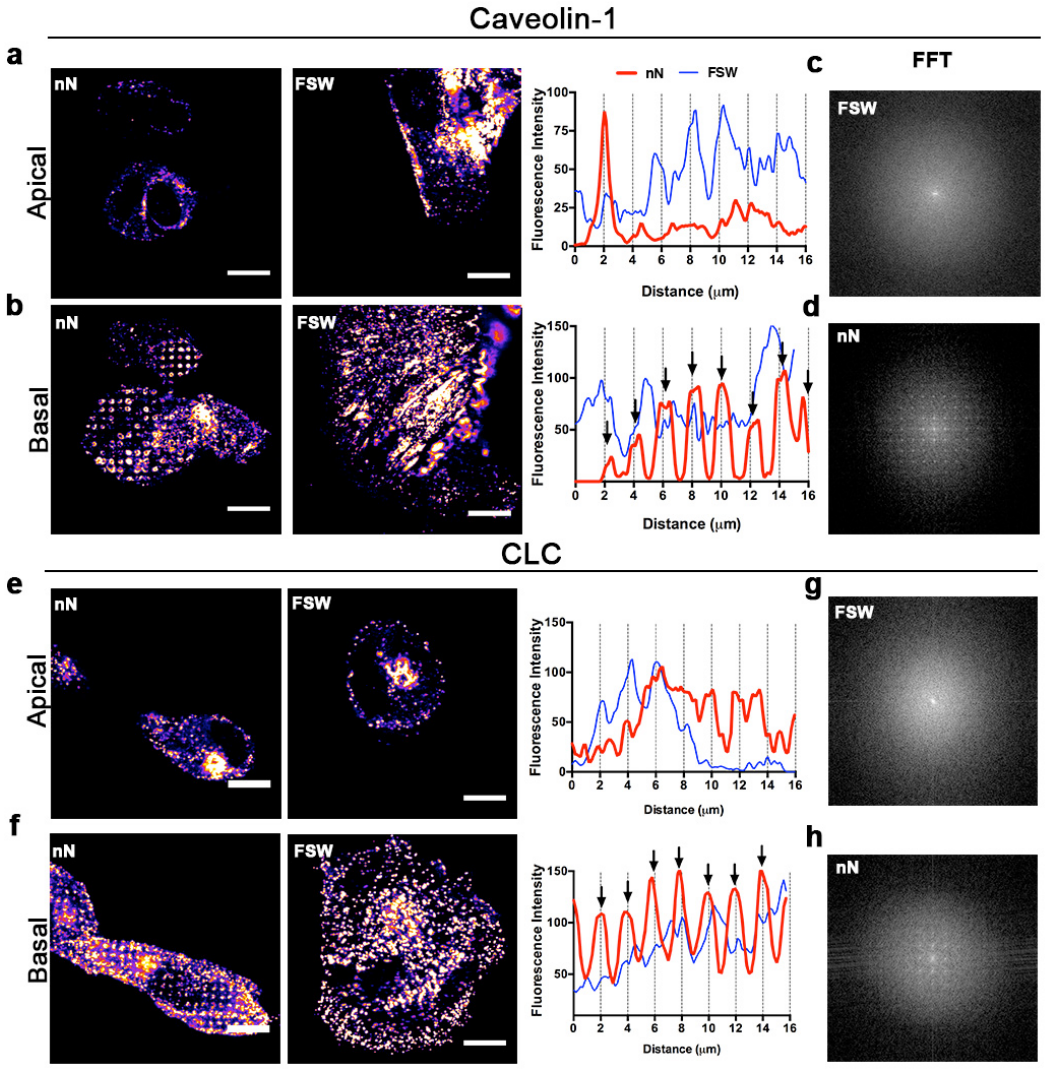


Figure 4.16: Endocytosis is triggered at sites of nanoneedle interfacing. Confocal fluorescence images of caveolin-1 in the a) apical membrane of hMSCs cultured on nanoneedles or FSW b) basal membrane of hMSCs cultured on nanoneedles or FSW and their respective intensity profiles across the apical or basal surface. Fourier transform analysis of basal surface of hMSCs on c) FSW and d) nanoneedles. Confocal fluorescence images of clathrin light chain (CLC) in the e) apical membrane of hMSCs cultured on nanoneedles or FSW and f) basal membrane of hMSCs cultured on nanoneedles or FSW and their respective intensity profiles across the apical and basal cell surfaces. Fourier transform analysis of basal surface of hMSCs on g) FSW and h) nanoneedles. Scale bars = 20 μm.

inwards into the cells around the tips and sides of nanoneedles.

By performing sequential imaging over two rows of four nanoneedles with 30 nm section thickness, a 3D reconstruction of this region with segmentation of vesicular structures was obtained (Fig. 4.17b). This was investigated further, by segmenting vesicles found at nanoneedle, and non-nanoneedle locations (Fig. 4.17c). The localisation of endocytotic vesicles was not found to accumulate to any specific regions around

the nanoneedles, as roughly equal distributions could be found along the entire length of the nanoneedles.

In order to ascertain that there was a re-distribution of endocytotic vesicles to nanoneedle locations, and not merely an accumulation of these structures due to the greater proportion of plasma membrane surrounding these regions, the number of endocytotic vesicles at nanoneedle locations versus non-nanoneedle locations were quantified (Fig. 4.17d). Cross-sectional images of rows of nanoneedles at their highest point were compared against regions of non-nanoneedle locations with the same magnification, for numbers of endocytotic vesicles normalised to the length of membrane analysed. For this analysis, a row of four nanoneedles was imaged in each instance for sufficient magnification to detect endocytotic vesicles. Numbers of vesicles for nanoneedle locations were seen to be significantly higher than for control regions with no nanoneedles, indicating that nanoneedle interfacing actively promotes the redistribution of CCP and caveolae to these locations.

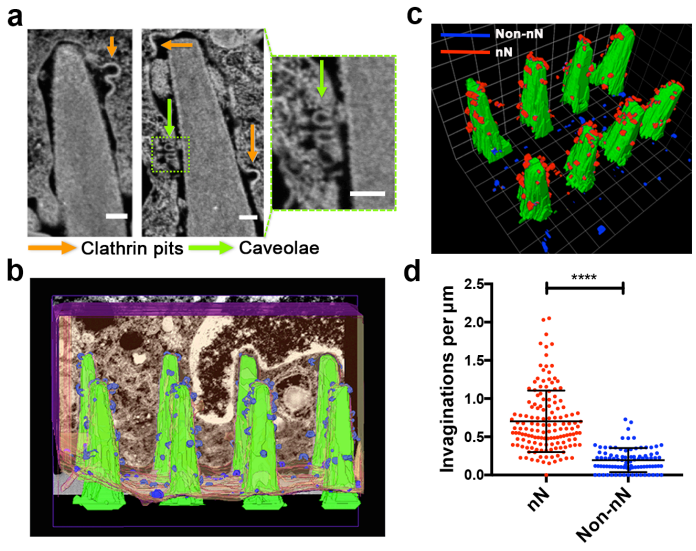


Figure 4.17: a) High-resolution FIB-SEM image of the hMSC-nanoneedle interface indicating the presence of endocytotic vesicles in the form of clathrin pits (orange arrows) and caveolae (green arrows). Scale bars = 100 nm. b) 3D reconstruction of two consecutive rows of nanoneedles with segmented cytoplasm, nanoneedles and vesicular structures present in the hMSC membrane across the interface. c) Segmentation of vesicles at nanoneedle and non-nanoneedle locations indicating distribution of vesicles around the nanoneedles, and non-nanoneedle locations. d) Quantification of vesicular invaginations in the membrane from FIB-SEM data at nanoneedle and non-nanoneedle locations. Data represented as scatter plots with lines indicating mean ± s.d. N = 4, from n = 10 (cells), ****$p<0.0001$ between the indicated groups.

4.4.5 Pathway-Specific Endocytosis Accounts for Cytosolic Delivery

The presence of endocytotic machinery at the membrane-nanoneedle interface, along with the lack of evidence for nanoneedles traversing the membrane, calls into question as to whether and to what extent specific endocytotic pathways are stimulated by nanoneedles. In order to assess this, cargo that are known to enter specifically through CME, CavME and macropinocytosis were delivered via nanoneedle arrays. CME was assessed by Transferrin (Tfn) uptake, CavME was assessed by internalization of cholera toxin B-subunit (CTxB) and albumin, while macropinocytosis was assessed by uptake of various Dextrans (10 kDa, 40 kDa and 70 kDa).

First, the adsorption efficiency of Tfn, Dex and CTxB on nanoneedle arrays and FSW was measured in order to ascertain that enhanced delivery of endocytosis-specific cargo via nanoneedles was not merely a result of increased payload adsorption due to nanoneedle surface area. The adsorption efficiencies of fluorescently labelled Tfn, Dex 10 kDa and CTxB on nanoneedle arrays and FSW were not found to be significantly different (Fig. 4.18.) However a considerable amount of variation in adsorption of Dex 10 kDa on nanoneedle and FSW was observed (Fig. 4.18d).

After ascertaining that nanoneedle did not adsorb significantly higher concentrations of payload, efficiencies of delivery of endocytosis-specific cargo into hMSCs via nanoneedles was assessed and compared with FSW. After 24 hours of culture, nanoneedles were able to deliver a number of endocytosis-specific cargo including Tfn, Albumin, CTxB and Dextrans of different sizes with significantly higher efficiency compared to FSW. For Tfn, primarily internalised by CME, although there was considerable variation (27%), nanoneedles were able to deliver Tfn close to 80% efficiency compared to FSW that only managed to deliver Tfn into 3% of cells (Fig. 4.19).

Similarly, cargo that have been reported to be specific for CavME such as albumin and CTxB were delivered via nanoneedles and FSW into hMSCs. After 24 hours of culture, hMSCs positive for fluorescently labelled albumin and CTxB were found to be internalised with higher efficiencies in the presence of nanoneedle arrays. Albumin, was internalised by almost 100% of the cells on nanoneedles, a 2-fold increase compared to FSW (Fig 4.20c). In addition, fluorescence intensities within cells were higher for cells cultured on nanoneedle arrays (Fig 4.20b). Similar to Tfn, the delivery of CTxB was

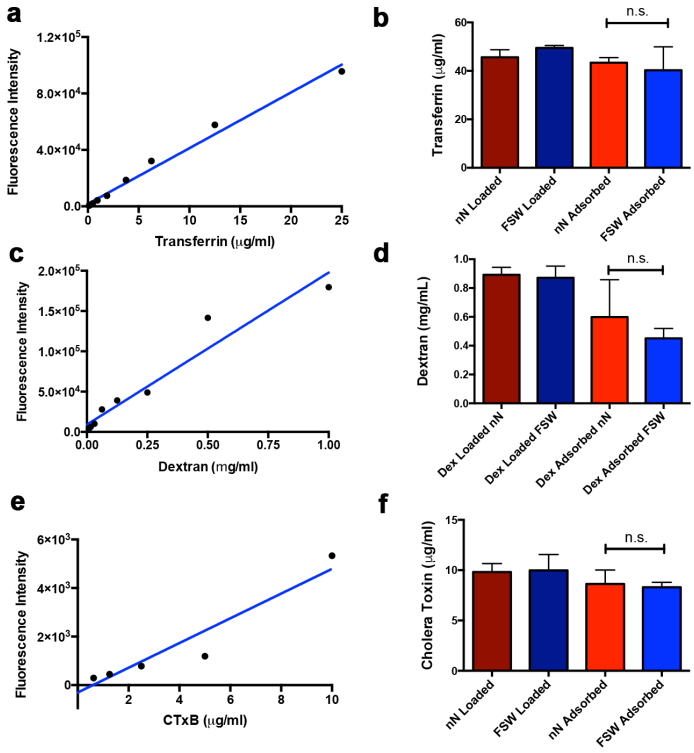


Figure 4.18: a) Standard curve of Tfn-Alexa488. b) Quantities of Tfn-488 initially loaded on nanoneedles and FSW, and finally adsorbed on nanoneedle and FSW after 45 minutes of incubation. c) Standard curve of Dextran 10kDa TexasRed. d) Quantities of Dextran 10kDa TexasRed initially loaded on nanoneedle and FSW, and finally adsorbed on nanoneedle and FSW after 45 minutes of incubation. e) Standard curve of CTxB-Alexa488. f) Quantities of CTxB-488 initially loaded on nanoneedle and FSW, and finally adsorbed on nanoneedle and FSW after 45 minutes of incubation. Loaded and adsorbed values presented as mean ± s.d. of N = 3 experiments for Tfn, CTxB and N = 2 for Dex, $p > 0.05$, not significant (n.s.) between indicated groups.

variable, although demonstrated higher internalisation by hMSCs on nanoneedle arrays in all instances, with a mean and s.d. of 30 ± 20% for nanoneedles compared to 4 ± 3% for FSW (Fig. 4.20f). Intensity of mean fluorescence was also seen to be great for cells on nanoneedle arrays (Fig 4.20e).

Next, the delivery of different sizes of Dextrans via nanoneedle arrays was investigated. Dextrans have been previously shown to be taken up via MP[422]. Dextran delivery via nanoneedle arrays demonstrated some unique characteristics. While Dextran of 10 kDa and 70 kDa were delivered in 46 ± 30% and 66 ± 30% of cells respectively via nanoneedle arrays, Dextran of 40 kDa was delivered with consistently low efficiency of 2.7 ± 1.8% (Fig. 4.21). Nevertheless, nanoneedle arrays outperformed FSW in delivering dextrans of different sizes in all instances.

In order to assess the fate of endocytosis specific cargo that enters during nanoneedle-

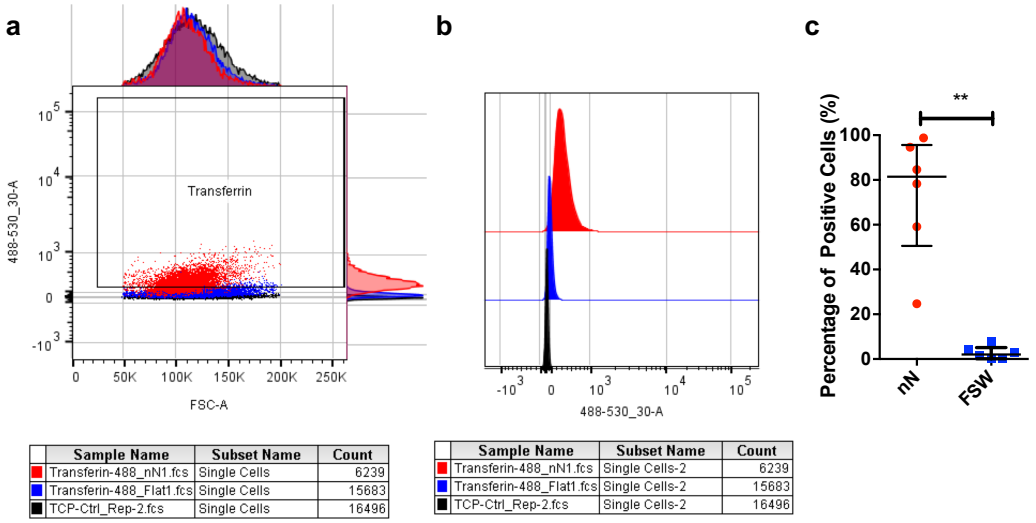


Figure 4.19: Delivery of CME specific Tfn (Tfn-Alexa488) mediated by nanoneedles. a) Representative scatter plots of flow cytometry data indicating Tfn uptake on nanoneedles (red) compared to FSW (blue) and control (black). b) Representative mean fluorescence intensity plots of flow cytometry data indicating an increase in Tfn-Alexa488 fluorescence in hMSCs cultured on nanoneedle arrays. c) Flow cytometry plots of Tfn uptake mediated by nanoneedles or FSW. Data represented as scatter plot distributions with bars indicating median and interquartile range. N = 3, n = 2 (biological replicates), **p<0.01 between indicated groups.

mediated delivery, the co-localisation of one cargo from each pathway was selected and assessed against their respective carrier markers (CLC or Cav-1 if applicable), endosomes and lysosomes. For instance, being a CME specific cargo, the intracellular localisation of Tfn was assessed against CLC, EEA1 and Lamp1. It was found that Tfn co-localised to the greatest extent with CLC (46 ± 16%) and Lamp1 (49 ± 20%) followed by EEA1 (33 ± 12%) in most cases (Fig. 4.22a).

The extent of co-localisation of CTxB with Cav-1 and EEA1 was variable. For instance, the co-localisation of CTxB with its carrier Cav-1 and with EEA1 ranged from below 20% in some cases to above 90% in others. CTxB was however seen to co-localise consistently with Lamp1 (82 ± 14%), suggesting that CavME stimulated by nanoneedles inevitably leads to lysosomal accumulation (Fig. 4.22b).

Unsurprisingly, Dex, showed highly consistent degrees of co-localisation with endosomes and lysosomes (20-30%), possibly owing to the fact that MP occurs from the apical cell surface, and relies on release of fluid phase markers into the surrounding media for internalisation rather than from the basal cell surface in contact with the nanoneedles (Fig. 4.22c).

In summary, when combining carriers markers, early endosomes and lysosomes,

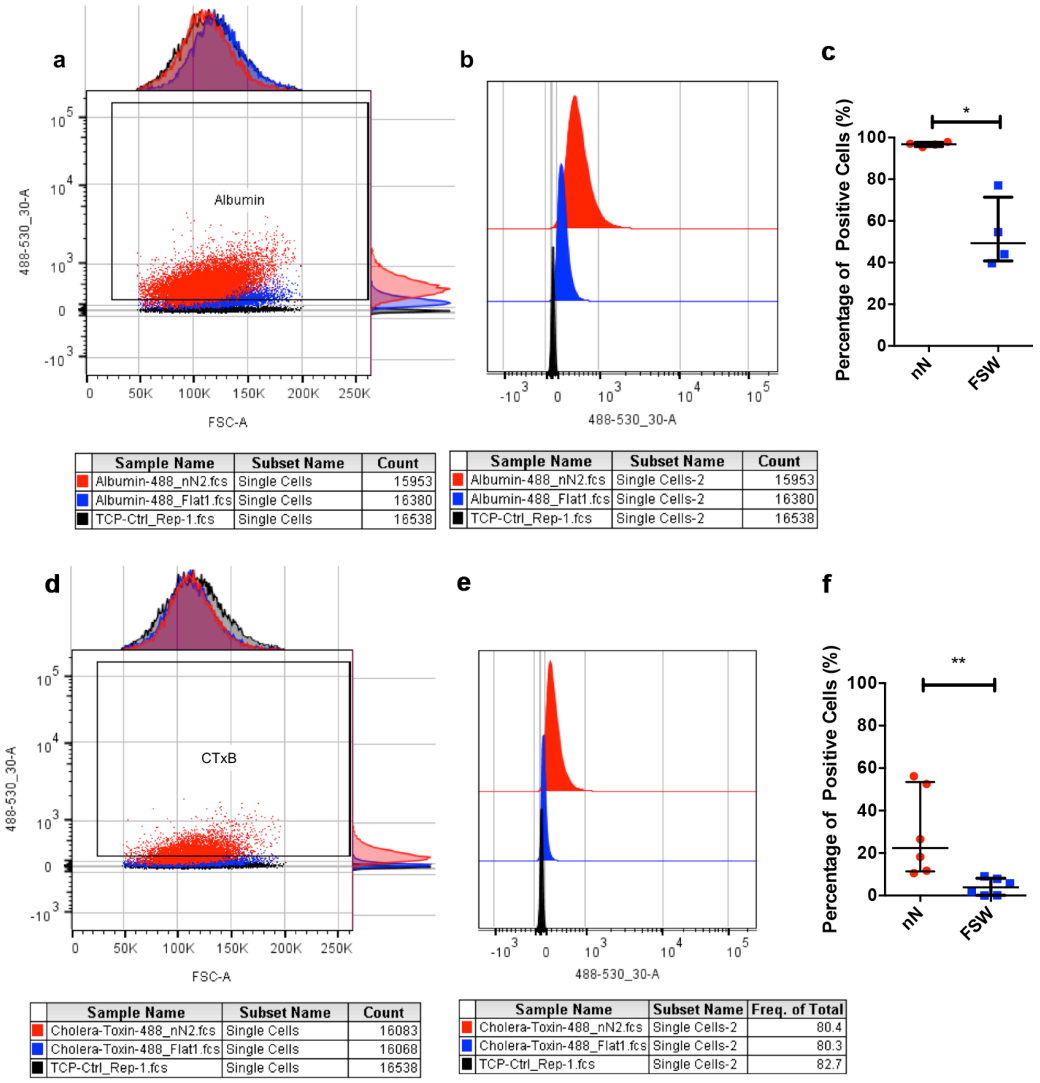


Figure 4.20: Delivery of CavME specific albumin and CTxB (Albumin-Alexa488 and CTxB-Alexa488 respectively) mediated by nanoneedles. a) Representative scatter plots of flow cytometry data indicating albumin uptake on nanoneedles (red) compared to FSW (blue) and control (black). b) Representative mean fluorescence intensity plots of flow cytometry data indicating an increase in Alb-Alexa488 fluorescence in hMSCs cultured on nanoneedle arrays. c) Flow cytometry plots of albumin uptake mediated by nanoneedles or FSW. Data represented as scatter plot distributions with bars indicating median and interquartile range. N = 2, n = 2, *p<0.05 between indicated groups. d) Representative scatter plots of flow cytometry data indicating CTxB uptake on nanoneedles (red) compared to FSW (blue) and control (black). e) Representative mean fluorescence intensity plots of flow cytometry data indicating an increase in CTxB-Alexa488 fluorescence in hMSCs cultured on nanoneedle arrays. f) Flow cytometry plots of CTxB uptake mediated by nanoneedles or FSW. Data represented as scatter plot distributions with bars indicating median and interquartile range. N = 3, n = 2 (biological replicates) *p<0.05 **p<0.01 between indicated groups.

it was confirmed that endocytosis by CavME were trafficked into the endolysomal system to the greatest extent (65 ± 20%) perhaps owing to their high accumulation particularly within lysosomes (Fig. 4.22d). This was followed by CME where 45 ± 17%

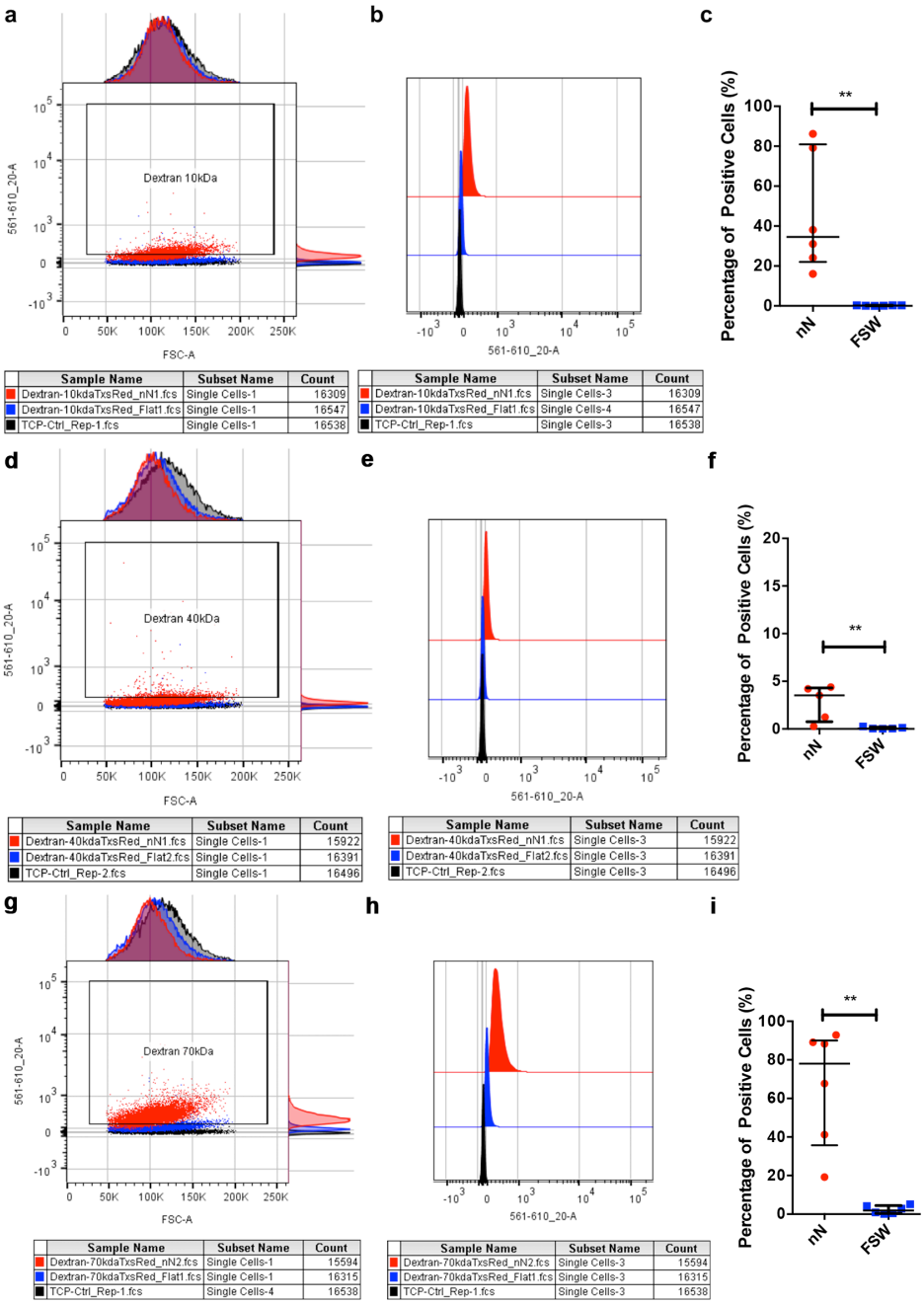


Figure 4.21: Delivery of dextrans (specific to MP) of different sizes labelled with TexasRed (Dex 10kDa, Dex 40kDa and Dex 70kDa) mediated by nanoneedles. Representative scatter plots of flow cytometry data indicating uptake of TexasRed labelled a) Dex 10 kDa d) Dex 40 kDa g) Dex 70 kDa uptake on nanoneedles (red) compared to FSW (blue) and control (black). Representative mean fluorescence intensity plots of flow cytometry data indicating an increase in intensity of TexasRed labelled b) Dex 10 kDa e) Dex 40kDa h) Dex 70kDa fluorescence in hMSCs cultured on nanoneedle arrays. Flow cytometry plots of c) Dex 10 kDa f) Dex 40 kDa i) Dex 70 kDa uptake mediated by nanoneedles or FSW. Data represented as scatter plot distributions with bars indicating median and interquartile range. N = 3, n = 2 (biological replicates) **p<0.01 between indicated groups.

of delivered Tfn was found in the endolysosomal system. MP stimulated in the presence of nanoneedles accounted for 38 ± 11% of accumulation of the Dextran payload within the endolysosomal pathway.

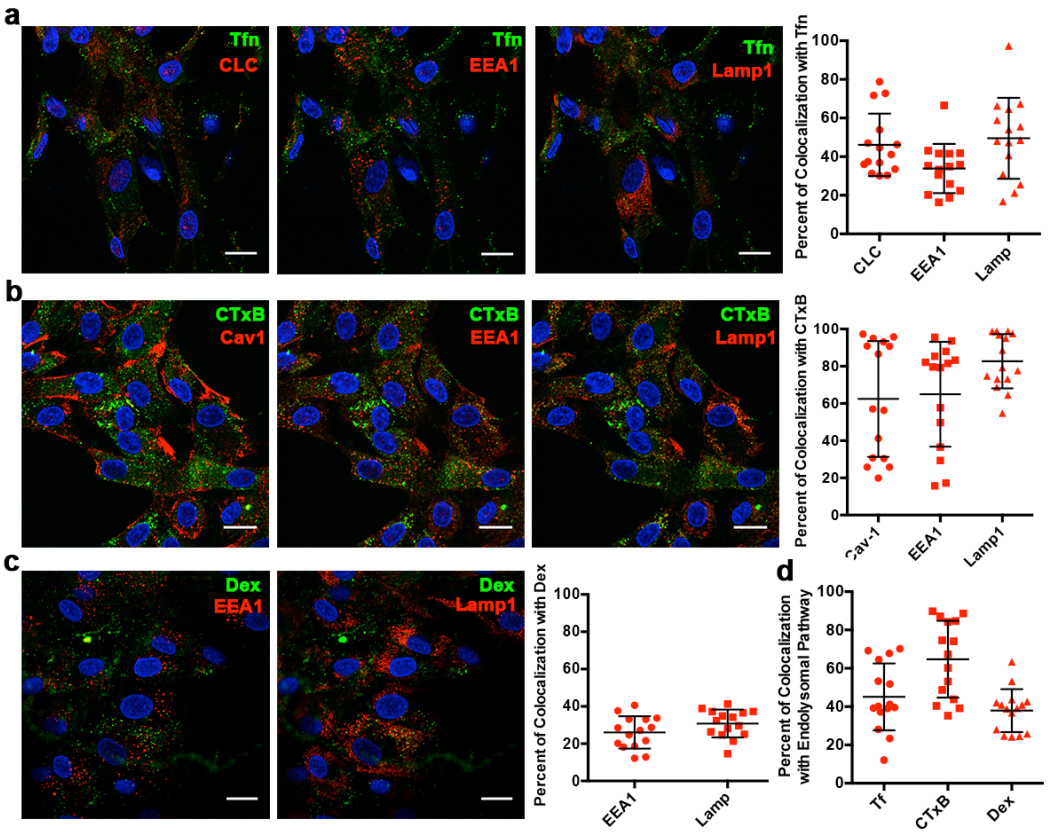


Figure 4.22: a) (L-R) Representative confocal plane images (above the region of nanoneedles) and quantification of Tfn co-localization with CLC, EEA1 and Lamp1 in hMSCs after 24 hours of delivery. b) (L-R) Representative confocal plane images (above the region of nanoneedles) and quantification of CTxB co-localisation with Cav-1, EEA1 and Lamp1 in hMSCs after 24 hours of delivery. c) (L-R) Representative confocal plane images (above the region of nanoneedles) and quantification of Dex 10 kDa co-localisation with EEA1 and Lamp1 in hMSCs after 24 hours of delivery. Quantified data represented as min-to-max box plots. N = 1, n = 3 (biological replicates), at least 5 images per n. d) Quantification of co-localisation of Tfn, CTxB and Dex 10 kDa with the endolysosomal pathway. Quantified data presented as min-to-max plots, N = 1, n = 3 (biological replicates), at least 5 images per n.

4.4.6 Nucleic Acid Fate Following Nanoneedle-Mediated Delivery

If endocytosis and its trafficking mechanisms are key contributors to nanoneedle-mediated delivery, the entrapment of therapeutically relevant payloads in endosomes and lysosomes may hamper their functionality. In order to assess this, the delivery of cyanine-3 (Cy3) labelled siRNA (Cy3-siRNA) targeting the silencing of glyceraldehyde 3-phosphate dehydrogenase (GAPDH) that relies on the co-localisation with the RISC complex in

the cytosol[565] was delivered via nanoneedle arrays.

Cy3-siRNA was physisorbed onto nanoneedle and FSW substrates in a previously optimised buffer for nucleic acid delivery (unpublished data, see methods). HMSCs cultured on Cy3-siRNA loaded nanoneedles and FSW were interfaced for 24 hours and assessed for Cy3-siRNA uptake by flow cytometry and confocal fluorescence microscopy. After 24 hours, Cy3-siRNA was clearly visible in the cytosol of hMSCs cultured on nanoneedle arrays, with a considerable amount of punctate signal present in the perinuclear region (Fig. 4.23a). Moreover, nanoneedles facilitated significantly higher levels of Cy3-siRNA delivery into hMSCs compared to FSW substrates as indicated by a 3-fold increase in percentage of Cy3-positive cells by flow cytometry (Fig. 4.23b, c).

Although efficienct intracellular delivery of nucleic acids into hMSCs was demonstrated, in order for nucleic acids such as siRNAs to express their function of altering gene expression, they must reach their target site within the cell (i.e. protein complexes within the cytoplasm). If endocytosis represents the primary mechanism of uptake from nanoneedle arrays, endocytosis of nucleic acids could lead to endosomal entrapment and lysosomal degradation or recycling, reducing the efficiency of the nanoneedle-delivery platform.

To assess the fate of delivered siRNA, immunostaining of components of the endolysosomal pathway was carried out in cells interfaced with Cy3-siRNA loaded nanoneedles after 24 hours (Fig. 4.23d). Co-localisation analysis of Cy3-siRNA with CLC, Cav-1, EEA1, Lamp1, and a combination of all these components constituting the majority of the endolysosomal pathway was conducted (Fig. 4.23e). The finding that an average of 45 $\pm$ 13% of siRNAs were co-localised with Cav-1, 34 $\pm$ 9% of siRNAs were co-localised with CLC, 44 $\pm$ 14% of siRNA with EEA1 positive endosomes and 40 $\pm$ 13% of the siRNAs were entrapped within lysosomes by their co-localisation with Lamp1, indicates that a substantial percentage of nucleic acids enter the endolysosomal pathway. Moreover, the average percentage of siRNA trafficked into the endolysosomal pathway as a whole was estimated to be approximately 60% (Fig. 4.23e). Thus although intracellular delivery via nanoneedles may be efficient, their entrapment within the endolysosomal system may account for any reduced efficiency of siRNAs in down-regulating gene expression. The functionality of siRNA-GAPDH delivered into hMSCs via nanoneedles was then assessed by PCR (Fig. 4.23f). Although siRNA-GAPDH

delivered into hMSCs via nanoneedles did not significantly reduce GADPH gene expression, there was an average reduction of expression by 42%, indicating that some proportion of siRNAs are available in the cytosol.

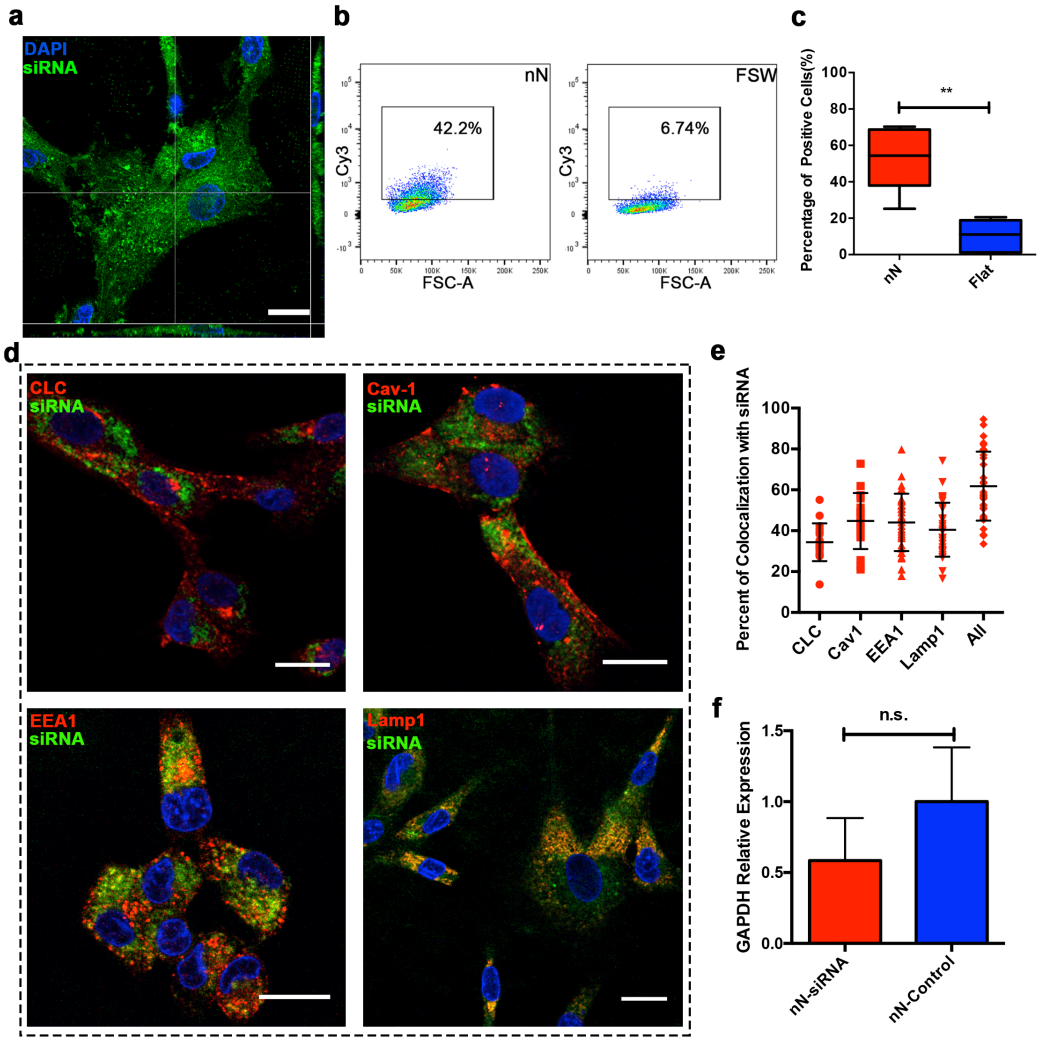


Figure 4.23: Fate of nucleic acids delivered via nanoneedles. a) Z-stack projection of confocal sections of hMSCs above the nanoneedles indicating delivery of fluorescently labelled Cy3-siRNA-GAPDH (green) in the cytosol after 24 hours of interfacing. b) Representative flow cytometry scatter plot of Cy3-siRNA uptake in hMSCs mediated by nanoneedles (left) and FSW (right) after 24 hours. c) Flow cytometry plots of Cy3-siRNA uptake in hMSCs mediated by nanoneedles compared to FSW after 24 hours. N = 4, n = 2 Data represented as min-to-max box and whisker plots with median and interquartile range **p<0.01 between indicated groups. d) Representative confocal fluorescence images for quantitative analysis of Cy3-siRNA co-localisation with CLC, Cav-1, EEA1 and Lamp1 as indicated in the images. Scale bars = 20 μm. e) Quantification of co-localisation of endocytotic carrier proteins (CLC, Cav-1), endosomes (EEA1) and late endosomes/lysosomes (Lamp1) and the combination of all these components (All) with Cy3-siRNA. Values reported as aligned scatter plot of percentages of Cy3-siRNA pixels overlapping with indicated components of the endolysosomal system (Mander's coefficient). Lines represent Mean ± s.d. N = 4, n = 2 for Lamp1, EEA1. N = 3, n = 1 for CLC, Cav-1. 5-10 images per sample. f) PCR indicating GAPDH relative expression in hMSCs after 24 hours of interfacing with or without siRNA-GAPDH loaded on nanoneedle substrates. N = 3, n = 3, Data represented as mean ± s.d. p = 0.2, not significant (n.s.).

4.4.7 Effect of Changing Surface Chemistry on Cell-Nanoneedle Interfacing

In order to investigate whether changing the surface chemistry of nanoneedles by addition of positively charged amines alters nanoneedle-membrane interactions, nanoneedles were functionalised with APTES by liquid phase conjugation. First, the viability of hMSCs on APTES functionalised nanoneedles (AP-nanoneedles) was tested. After 6 hours of culture, AP-nanoneedle arrays had negligible impact on viability (Fig. 4.24a, b). Cells were also able to spread over the arrays by this time. AP-nanoneedles were shown to stimulate formation of apical membrane ruffles to a significantly greater extent compared to AP-FSW, as indicated by SICM and SEM micrographs (Fig. 4.24c, d). Interestingly, the degree of apical membrane ruffling in cells cultured on AP-nanoneedles was significantly lower than previously observed on non-functionalised nanoneedle arrays (Fig. 4.12e).

Since some evidence indicates that increasing nanoneedle-membrane interactions can aid in overcoming the membrane barrier[540, 531], the basal membrane of hMSCs in contact with the nanoneedles was studied using FIB-SEM after 6 hours of interfacing. Initial observations showed that the basal membrane of hMSCs appeared highly invaginated by the nanoneedles, to visibly greater extents than observed previously on non-treated nanoneedles (Fig. 4.25a). A uniformly tight interface, with very few clefts between membrane and nanoneedle was observed. This was particularly the case when cells were more spread. Sequential milling of the interface indicated that along with the cell membrane, the nanoneedles heavily deformed the nuclear membrane, as it was clearly curtained over the nanoneedle tips (Fig. 4.25a). On closer examination, the cross sections just after milling a row of nanoneedles showed a gap indicating where the nanoneedle was, and the membrane deforming around this region (Fig 4.25b). This curtaining effect of the membrane was further confirmed by 3D reconstruction of the membrane-nanoneedle interface (Fig. 4.25c). Gaps between the membrane and nanoneedle could be clearly visualised, while the basal membrane itself appeared rough with nanoscale negative (inward) invaginations in the sections interacting with nanoneedles (Fig. 4.25d, e).

In order to ascertain whether the AP-nanoneedles stimulated endocytosis at regions

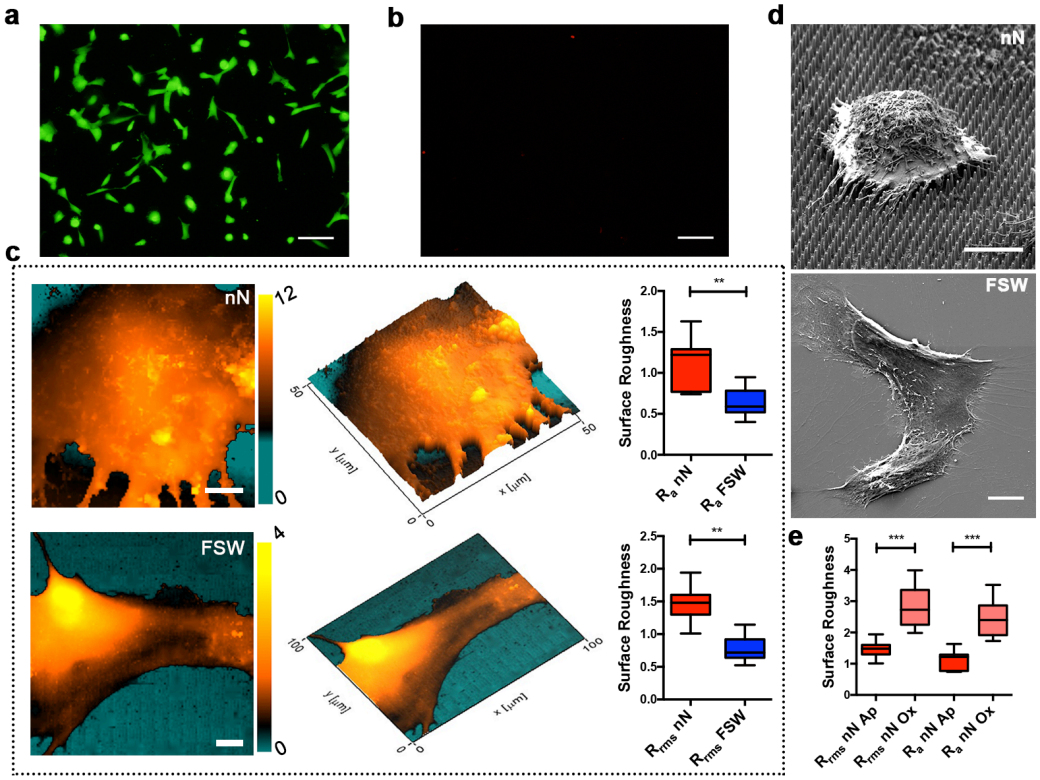


Figure 4.24: Effect of APTES functionalisation of nanoneedles on the membrane morphology. a) Live and b) dead staining of hMSCs on APTES functionalised nanoneedles after 6 hours. Scale bar = 50 μm using the LIVE/DEAD^{TM} assay kit. c) SICM micrographs and roughness measurements of hMSCs on APTES-nanoneedle arrays. L-R SICM 2D and 3D micrographs of hMSC on APTES treated nanoneedle arrays (nN, top panel) and on FSW (bottom panel) and corresponding apical membrane roughness measurements R_a (top) and R_{rms} (bottom). Scale bars = 20 μm. Data represented as min-to-max box and whisker plots with bars representing median and interquartile range, n = 7 for nanoneedles and n = 6 for FSW. **p<0.01 between indicated groups. d) SEM micrographs of hMSCs on nanoneedle arrays (nN) and FSW after 6 hours of interfacing. Scale bars = 10 μm. e) Surface roughness measurements of cells on AP-nanoneedles (nN Ap) and non-functionalised plasma oxidised nanoneedle arrays (nN Ox). Data represented as min-to-max box and whisker plots with bars representing median and interquartile range. ***p<0.001 between indicated groups.

of membrane deformation, the localisation of Cav-1 and CLC in hMSCs was studied by immunofluorescence. Much like hMSCs on non-functionalised nanoneedle arrays, after 6 hours of interfacing, both Cav-1 and CLC were localised to regions of the nanoneedles as FFT analysis of immunofluorescence intensity clearly displayed 2 μm periodicity for both proteins (Fig. 4.26a). In order to understand the time frame for Cav-1 and CLC to localise to these sites, immunofluorescence was conducted after 1 hour and 3 hours of interfacing with AP-nanoneedles. Interestingly, no localisation of either protein was found after 1 hour of interfacing (Fig. 4.26e, f). After 3 hours however, Cav-1 was co-localised with nanoneedles, whilst CLC was not (Fig. 4.26c, d).

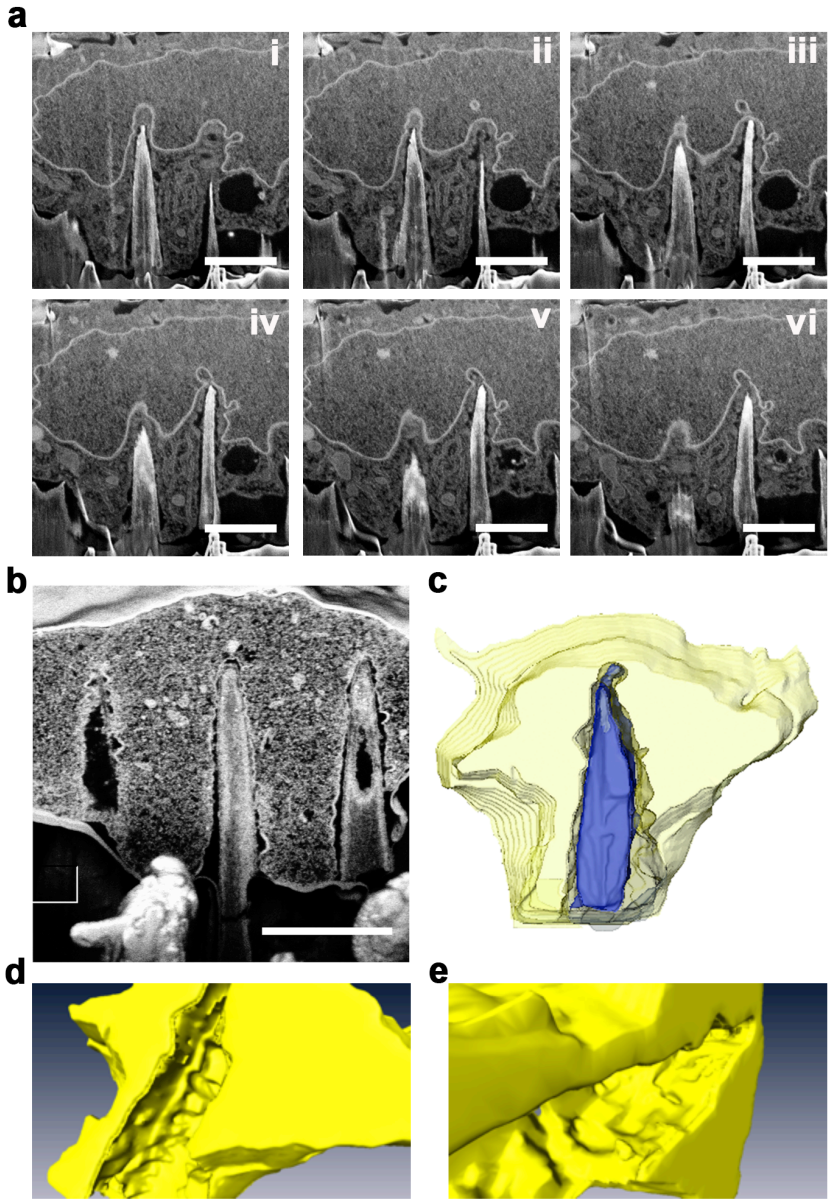


Figure 4.25: Basal membrane morphology at the AP-nanoneedle-membrane interface. a) (i-vi) Serial cross-section SEM images of the membrane-AP-nanoneedle interface indicating high degree of cell membrane and nuclear membrane invaginations. Scale bar = 2 μm. b) High-magnification SEM image of a row of nanoneedles. Left most nanoneedle has disappeared after milling indicated a gap left behind as the membrane deformed around its shape. Scale bar = 2 μm. c) 3D reconstruction of a AP-nanoneedle under a hMSC membrane indicating spaces between the nanoneedle and membrane. d), e) 3D reconstruction from c) without the nanoneedle indicating the conformation of the membrane around the nanoneedle.

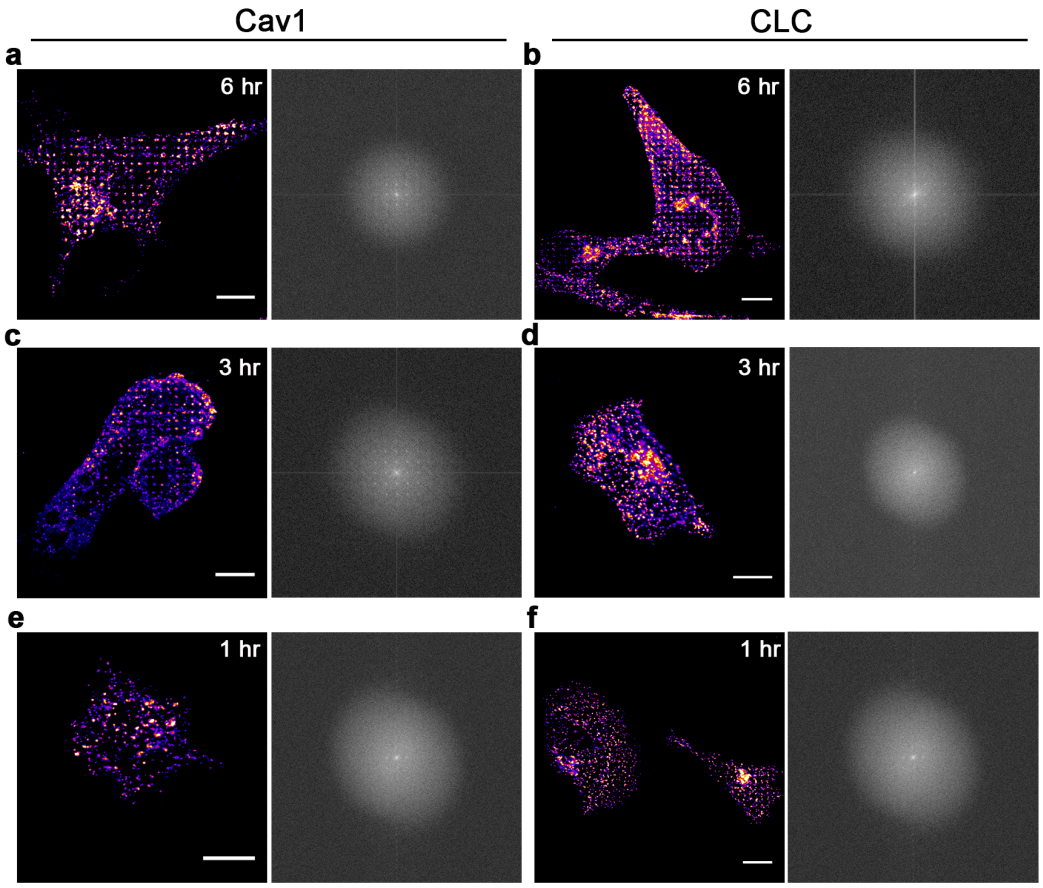


Figure 4.26: Effect of APTES surface functionalisation of nanoneedles on endocytotic protein localisation. Representative confocal fluorescence intensity micrographs and FFT images of Cav-1 (a, c, e) and CLC (b, d, f) in hMSCs on AP-nanoneedle arrays after a, b) 6 hours c, d) 3 hours and e, f) 1 hour of interfacing. Scale bars = 10 μm.

4.5 Discussion

The success of the nanoneedle platform as a membrane disruption tool that facilitates intracellular delivery relies on robust identification of cell membrane properties and characterisation of the interface. Additionally, a thorough investigation of the mechanism of payload transfer across the interface is necessary to validate its true efficiency.

Given their nanoscale feature sizes, porous silicon nanoneedle arrays are able to interface with cells, while maintaining cell viability and metabolism during interfacing[315]. The versatility of using these nanoneedle arrays is further demonstrated in this chapter, as they were able to interface favourably with hMSCs without surface functionalisation or adhesion promoting molecules, while introducing negligible cell death (Fig. 4.11). Although maintaining cell viability is not a new finding, it constitutes a considerable advantage of nanoneedle arrays in general as primary cell types are able to stay viable without surface manipulation of the arrays. This allows the platform to be characterised in isolation rather than having to decouple the effects of surface chemistry in the presence of topography.

The apical membrane of hMSCs cultured on nanoneedle arrays was visibly altered when visualised in the hydrated (SICM) and dehydrated state (SEM) (Fig. 4.12). There was a striking increase in dorsal membrane ruffles, membrane protrusions usually stimulated by growth factors and known to be hot spots for macropinocytosis[561]. This finding was consistent with another study that reported the presence of membrane protrusions on 90 and 40 nm high nanotubes by SEM[566]. MP can be enhanced with ruffles due to the action of membrane protrusions to fold back on the membrane, creating a macropinosome[421]. Moreover, apical membrane ruffles can assemble actin-related protein 2/3 (ARP2/3) complexes, that are responsible for recruiting vesicle scission proteins, dynamins, that scission off the macropinosomes[567]. In line with this, another study that reported an increase in MP through uptake of dextran from the media in hMSCs on micropillars also showed a concomitant increase in actin rich rings at the apical surface of the cells[568]. Actin rich rings in hMSCs on porous silicon nanoneedle arrays have also been shown by our group in a recent (yet unpublished) study.

Analysis of membrane order provides clues to the nature of the interface, the in-

tegrity and response of the membrane as it experiences high degrees of deformation by nanoneedles. It is unknown how nanotopographies or microtopographies influence membrane order across the interface. Membrane order depends on curvature as well as mechanical properties of the membrane such as lateral tension. For instance, it has been shown in vesicles that higher membrane curvature and increased lateral tension promote more fluidity, and therefore lower membrane order[569]. Disordered phases of membrane are thus likely to be present in regions of high lateral tension, where the energy to overcome the membrane barrier and traverse the membrane is also reduced [569, 531, 570]. In this study, hMSCs on nanoneedle arrays displayed higher membrane order near the membrane-nanoneedle interface, indicating an active response to the surface topography (Fig 4.13). Additionally, hMSCs on nanoneedles appear more rounded and less spread compared to flat controls (Fig. 4.11) and are unable to form large focal adhesions (unpublished data from our group and[571]), suggesting that they do not possess high lateral tension, perhaps leading to the finding of higher lipid order on nanoneedle arrays. Moreover, compressive forces on the membrane can lead to asymmetrical increases in lipid density, packing and ordering[318]. The invasion of Shiga Toxin has been shown to proceed with increasing negative curvature and compressive stress on the outer layer of the membrane, creating increased lipid density and order in these regions resulting in highly ordered 100 nm tubular membrane invaginations. It can be speculated that nanoneedle arrays stress the membrane in a similar fashion, due to the low lateral tension, which would otherwise prevent invaginations to be formed (Fig. 4.27).

The cell membrane and the cytoskeleton impart mechanical properties to the cell, and constitute the primary barriers to intracellular entry[540, 539]. For membrane penetration to take place, nanoneedles must overcome the tension of the membrane first in order to gain intracellular access[531]. This in turn depends upon parameters of the system such as stiffness of the membrane, strength of adhesion, nanoneedle pitch spacing and sharpness[537, 570]. Although mechanical models have provided great insight into these parameters, ultimately they only present guidelines for what might occur. Imaging the cell-nanoneedle interface with sufficient resolution is hence critical to determining the route of entry via nanoneedles.

To resolve the question of whether nanoneedles can traverse the membrane, both

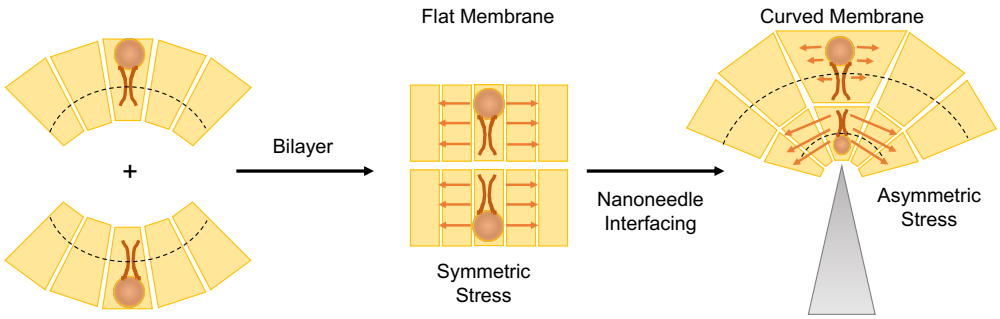


Figure 4.27: Schematic of possible mechanism of increasing membrane lipid order by nanoneedle interfacing. A bilayer is formed by two phospholipid monolayers that have no preference for curvature and form a symmetrical bilayer, equal amounts of lateral tension on the inner and outer layers. Nanoneedle interfacing results in increased compressive stress on the outer lipid membrane, with compressive stress on the lipid head region and tensile stress in the tail region, and lipid density can increase on one side as the membrane binds to the nanoneedle[572]. Increased membrane thickness and order can result from the increase in lipid density at these regions[318]. Figure adapted from [318].

fluorescence and electron microscopy have previously been used to investigate basal membrane continuity. While fluorescence microscopy allows the possibility of imaging cells live in their hydrated state, it lacks sufficient resolution to study the interface with nanometre precision[219]. Electron microscopy provides sufficient resolution to investigate the interface, however previous TEM studies have relied on substrate removal prior to microtome sectioning that may introduce artefacts[246]. Thus in this study, imaging of the membrane-nanoneedle interface was conducted *in-situ* using FIB-SEM and TEM of FIB lift-out thin sections. By incorporating a sample preparation protocol that adequately stains lipids and proteins, the membrane could be clearly distinguished at the interface (Fig. 4.14). Moreover, by creating thin-sections using FIB milling, damage induced by mechanical sectioning particularly at the interface was avoided (Fig. 4.9). The finding from this study were consistent with another recent report incorporating FIB-SEM to study the cell-nanopillar interface, although the aspect ratio of these structures were much lower[252]. Although the result cannot prove that the membrane is not impaled on initial contact with the nanoneedles, even if this does occur the membrane is able to reseal, preventing long-term access to the cytosol[519].

Endocytosis represents the primary mechanism for cells to uptake cargo from their external environment. Previous indications for topographical stimulation of endocytosis have emerged from studies reporting local accumulation of endocytotic proteins at cell-substrate interface[127, 184, 185]. The finding that porous silicon nanoneedle

arrays stimulated the localisation of clathrin coat and caveolae specific proteins is likely a result of their propensity to accumulate to sites of high membrane curvature[127] or tension[573] respectively (Fig. 4.16). In the case of caveolae, which were not previously shown to accumulate to highly curved regions of nanopillars[127], but only on larger micropillar arrays[185], their localisation could be a result of adaptations to membrane stress[435]. Moreover, caveolae are normally present in highly ordered membrane regions, which is consistent with increased lipid ordering seen in hMSCs on nanoneedle arrays (Fig 4.13). As in studies using nanopillar arrays, which confirmed an increase in number of CME events at the interface by assessing the appearance and dynamics of dynamin[127, 184], porous silicon nanoneedle arrays also stimulated an increase in endocytotic vesicle localisation at sites of nanoneedle invaginations compared to non-nanoneedle locations (Fig. 4.17).

Since indications for enhanced MP, CavME and CME were present from imaging data, an investigation into which endocytotic pathway contributes to cargo internalisation was conducted, to find that all three pathways promoted highly efficient biomolecule delivery of their respective cargo. Previously, only one study has investigated delivery of endocytotic payloads, where they highlighted increased macropinocytic uptake from the media while culturing cells on 2 μm micropillars[568]. In their study, dextran internalisation by hMSCs was saturated for cells cultured on flat or patterned substrates by 18 hours, while in this study, significant internalisation of dextran was seen by 24 hours. The differences could be due to release kinetics and the method of delivery as they delivered payload through the media, while in this study the payload was loaded within the porous needles. Consistent with their findings, was that internalisation of dextran was found to be independent of the surface area of cells in contact with the substrate (Fig. 4.21).

CME is considered a fast endocytotic process and cargo recycling is estimated to take place within 7 minutes[574]. The fact that Tfn is delivered with high efficiency and can be observed within cells after 24 hours indicates that CME occurs continuously, due to payload availability at the interface as nanoneedles degrade, establishing the system for sustained delivery over long periods of time (Fig. 4.19).

Following uptake, the trafficking modalities of each of these cargo showed that payload that entered via CavME accumulated within lysosomes to the greatest extent

compared to macropinocytosis and CME (Fig. 4.22). This potentially indicates that delivery via macropinocytosis or CME allows a greater proportion of payload to leak into the cytosol as greater percentages of Tfn and Dex did not co-localise with the endolysosomal system.

In the absence of membrane penetration, initiation of endocytotic processes, and uptake of endocytosis specific cargo, the fate and delivery of nucleic acids via nanoneedles was studied. Nanoneedles have previously been used to facilitate high efficiency delivery of nucleic acids, however their mechanism of uptake and fate after uptake have not been investigated[485, 315]. Delivery of plasmid DNA and siRNA by porous silicon nanoneedle arrays has previously been shown in a number of cell lines[315, 254], but not in primary cell types that are considerably more challenging candidates. Thus in this study, nanoneedle-mediated delivery of siRNA into hMSCs was attempted validate that the platform is applicable to primary cells. Although siRNA successfully entered hMSCs after 24 hours, the finding that approximately 60% of siRNA entered the endolysosomal system (Fig. 4.23), may potentially limit their co-localisation with their target site, the RISC complex[565] within the cytosol (Fig. 4.28). Although previous studies have indicated that delivery mediated by nanoneedles can bypass endocytosis entirely, this conclusion was reached by assessing the lack of punctate appearance of delivered cargo in many instances, rather than direct analysis of co-localisation data[487]. Nanoneedle-assisted delivery of nucleic acids conjugated to nanocages into HeLa has also been shown to escape endosomal entrapment[495], however the use of carriers as well as moving from cell line to primary cell type can widely modify the uptake mechanism or change whether uptake occurs at all[568]. From our study, over 45% of siRNA co-localised with Cav-1 indicating that CavME may be responsible for a substantial proportion of siRNA delivery.

Despite co-localisation of siRNA-GAPDH with the endolysosomal system, GAPDH expression was silenced by 42% indicating that siRNA does reach its target site. Thus, although endocytosis may represent a key mechanism of cargo internalisation via nanoneedles, it is possible that alternative delivery mechanisms could occur across the interface. For instance, it has been reported from patch clamp experiments that polished, smooth pipette tips create better seals and allow less leakage than rough ones[575, 576]. Since nanoneedles used in this study are porous and rough, a leaky interface may be created,

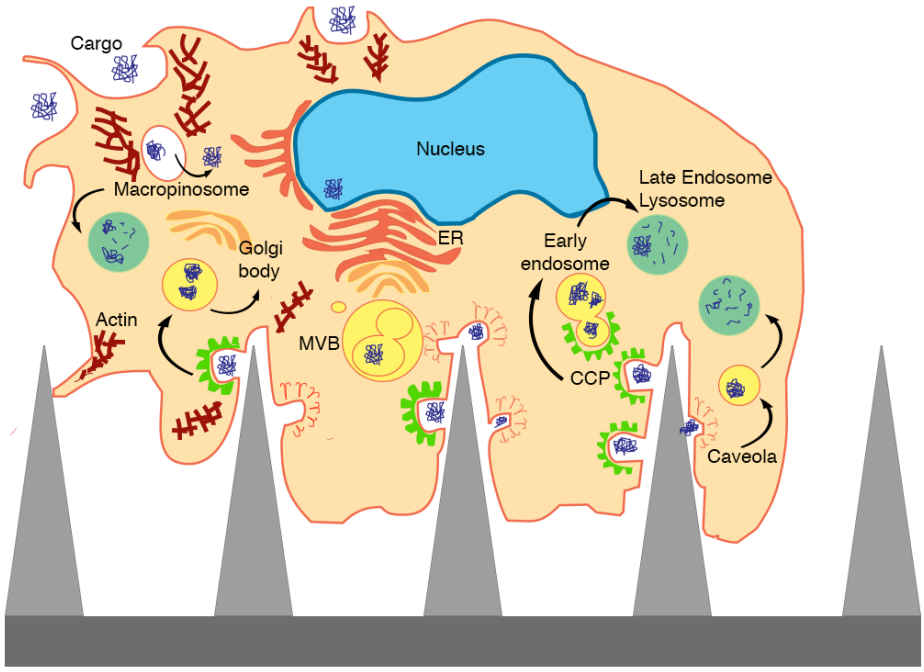


Figure 4.28: Schematic of mechanisms of nanoneedle-mediated delivery related to endocytosis. Macropinocytosis, CME and CavME are triggered by nanoneedle interfacing. Macropinocytosis at the apical cell surface occurs as dorsal ruffles fold back on the cell membrane, while caveolae and clathrin coated pits (CCP) are localised to the basal membrane at the nanoneedle interface. Macropinosomes, CCP and caveolae are eventually trafficked through the endosomes, multivesicular bodies, later endosomes and lysosomes.

allowing some amount of diffusion into the cytosol.

A variety of surface modifications including the functionalisation of silanes as well as cell adhesion promoting molecules have been used to increase the probability of membrane penetration by nanoneedles. Xu et al showed improvements in penetration from 6% to 12% when nanostraws with the ectopic coating of fibronectin[487]. Treating nanoneedle arrays with aminosilanes resulted in apical membrane ruffling (Fig. 4.24c, d), although to a visibly lower extent than non-treated substrates (Fig. 4.24e). This could be due to the fact that aminosilanes promote membrane nanoneedle contact via the positively charged amine resulting in better adhesion, possibly stimulating actin re-localisation, which changing the extent of ruffling in the cell[568]. Although cell spreading was generally improved and the basal membrane as well as the nucleus at the nanoneedle interface appeared heavily deformed, while assessing the ability of AP-nanoneedles to penetrate the membrane, it was found that despite the presence of the positively charged amine group on the nanoneedle surface, fusion and penetration of

the negatively charged membrane by the nanoneedles was not achieved (Fig. 4.25). The results from this study are consistent with another fluorescence microscopy study of the cell-nanowire interface, that indicated surface coatings of nanowires with aminosilanes or polyethylimine resulted in encapsulation by the membrane. Only 4 out of 54 11-μm long aminosilane coated nanowires did not show an apparent membrane, indicating that longer nanowires may promote access, albeit at low probability[219].

The case for activation of endocytosis in aminosilane treated nanoneedles was supported by the finding that that endocytotic proteins caveolin-1 and clathrin light chain were localised to nanoneedle indentation sites (Fig. 4.26). Interestingly, while accumulation of caveolae and clathrin coat proteins were seen after 6 hours of interfacing, only caveolin-1 was localised to nanoneedles at 3 hours, indicating that caveolin-1 respond to nanoneedle topography sooner than clathrin proteins. One potential reason for this difference may be due to the fact that caveolae are present within the plasma membrane and therefore provide a first order response as soon as the cell attaches to the nanoneedles, while clathrin is localised only after sequential accumulation of curvature sensing proteins, actin and adaptors[428]. Moreover, clathrin vesicles are unlikely to modulate plasma membrane tension being rich in protein, small and spherical[553]. This is in line with the idea that membrane tension is governed firstly by in-plane tension of the lipid bilayer that is buffered by caveolae, and followed by cytoskeletal tension produced by actin remodelling, that CME is dependent on for stabilising clathrin pits[553, 577].

4.6 Conclusion

In summary, the mechanism of interaction between porous silicon nanoneedle arrays and hMSCs to facilitate delivery of biomolecules was investigated to find that endocytosis plays an important role in intracellular delivery (Fig. 4.28). Nanoneedles were able to interface favourably with primary cells, that was independent of surface functionalisation. As nanoneedle arrays interface with the hMSCs, they trigger a series of membrane responses, including the stimulation of membrane ruffling and increased membrane order. This was accompanied by the cell membrane wrapping tightly around the nanoneedles in all instances observed, indicating that nanoneedles cannot gain long-term cytosolic access. The presence of the lipid bilayer at the cell-nanoneedle interface likely affects the mechanism of payload transfer across the interface. The presence of endocytotic proteins at sites of nanoneedle interfacing highlighted that these processes are localised to and active at the interface.

Endocytosis was confirmed to be a key contributor to biomolecule internalisation across the nanoneedle interface, likely stimulated by the act of deforming the cell membrane, increasing curvature and inducing local accumulation of vesicles. SiRNAs, and endocytosis pathway specific cargoes were delivered with high efficiencies into hMSCs, and establish the nanoneedle system as a high efficiency biomolecule delivery platform. The peculiar interface created by nanoneedles does however promote endocytosis and subsequently endolysosomal entrapment of the cargo, but not without permitting a percentage the payload to diffuse into the cytosol, either by diffusion or endosomal escape.

Overall, the study provides insight into how nanotopography in the form of nanoneedles can promote efficient delivery of therapeutically relevant cargo into primary cells. These findings have implications for using such devices that require intracellular access including nucleic acid delivery and biomolecule sensing applications.

4.7 Future Work

The findings of this study indicate that nanoneedle interfacing facilitates a substantial proportion of payload delivery via endocytosis. In addition, the absence of direct membrane penetration would indicate that the membrane is not traversed or is able to reseal following interfacing. Thus, in order to increase the probability of membrane penetration, changing the surface chemistry of the nanoneedles using other adhesive molecules and surface functionalisations should be tested. Moreover, the interface could be studied at earlier time points to assess whether membrane penetration can occur during cell attachment and spreading. In addition, the leakiness of the membrane-nanoneedle interface should be studied, potentially by measuring resistance[519] in order to understand whether the payload can diffuse across the interface.

Along with co-localisation analysis with the endolysosomal pathways, presented in 4.22, it would be useful to conduct other biochemical analysis such as a proximity ligation assay or co-immunoprecipitation to support the data reported in the co-localisation analysis. Moreover, in order to assess which pathway contributes to payload uptake most significantly, endocytotic pathways would have to be disrupted via genetic knockdowns where possible. For instance, knocking down Rac1 or RhoGTPases could identify whether actin remodelling affects uptake via macropinocytosis. SiRNA for caveolin could be used to assess the uptake dependency on CavME.

Since nanoneedles were loaded with payload, it would also be important to assess the quantity of payload that is internalised from solution, which can be assessed by quantifying the fluorescence of the payload in the media after 24 hours. In addition, a direct comparison of siRNA delivery by nanoneedles compared to Lipofectamine would further highlight the efficiency of the platform.

4.8 Limitations of the Study

In this chapter, the mechanisms of interaction between nanoneedle arrays and hMSCs was investigated to find for the first time that endocytosis plays an significant role in payload internalisation. In this study however, different endocytosis pathways could not be inhibited due to a number of reasons - i) inhibitors are highly non-specific particularly beyond very short time points and ii) since chemical inhibitors would need to be loaded into the nanoneedle arrays for the same time as the cargo, these would be toxic and non-specific. Other methods such as genetic knockdowns to inhibit specific pathways were not investigated in this study as hMSCs are difficult candidates for transfection. This could however be achieved with other cell types but the mechanism of interaction between immortalised cell lines and non-primary cell types may differ. In addition, due to the lack of negative or positive controls available for co-localisation analysis, it was not possible to distinguish true co-localisation because of the lack of measurement of background fluroescence co-localisation of endolysosomal pathway components and payload using such controls.

5. Concluding Remarks and Future Directions

In recent years, the increasing evidence that suggests that biophysical cues can probe and control stem cell behaviour has led to great advancements in the development of biomaterials. These materials are selected and engineered based on the extracellular microenvironment that stem cells experience while carrying out cell fate transitions. By providing physical cues that work synergistically with soluble factors the efficiency with which stem cells differentiate can be increased substantially, via supplementing them with cues of the microenvironment that facilitate desired changes in behaviour. However, the complexity of the microenvironment based on the interplay between biochemical and physical cues, has made the design of materials a challenging task. Moreover, the high sensitivity of stem cells to external cues and the many unknowns of their precise interactions have a direct impact on their fate and behaviour, which ultimately affects their use as a cell source in the clinic. It is thus imperative to investigate features of the stem cell response to physical material cues for the continued development of biomaterials that can precisely and reproducibly control stem cell behaviour.

Physical and chemical cues presented on the surface of materials greatly affect cell fate. Physical cues such as topography and stiffness, as well as patterning of chemical groups on a surface can trigger intracellular signalling pathways, that is based on the specific features of ligand binding, cell adhesion and subsequent forces transduced. The forces transduced via the cytoskeleton translate into genetic changes that ultimately control fate transitions. Thus, through the addition of well-designed material cues while utilising the feature of direct contact between cell and material, the ability to manipulate gene expression and achieve directed stem cell guidance is made possible.

In order to design specific material cues, it is necessary to obtain information about the features of cell interaction when in direct contact with the material. Indeed, how

cells respond to single material cues for biomaterial design is becoming an important topic, as cell behaviour has been shown to change dramatically based on stiffness, spatial positioning or chemical composition of the material at the nanoscale. In addition, recognising the response occurring from cell adhesion, as well as its transduction through the cytosol and eventual impact on the nucleus under the governance of material cues determines how to better design physical cues for cell manipulation strategies.

The question then arises as to how to one monitors and observes such interactions. Robust methods for studying such biointerfaces are equally important in providing directionality for future development of materials as well as highlighting the role of biological components in facilitating a response. Since such interactions occur on the nanoscale in a localised manner, the ability to visualise cellular and subcellular features along with the material in question, with high spatial and temporal resolution is a critical aspect for obtaining information about key cell components involved in a response.

With a focus on developing and applying new techniques to achieve the above, the effect of material cues in the form of substrate topography on cell behaviour was investigated in two ways:

(i) First, at the level of the nucleus by providing new tools to study nuclear remodelling and the epigenetic response to microgrooved topography

(ii) Second, at the level of the cell membrane by attempts to introduce external cargo intracellularly through the use of high-aspect ratio nanotopographical cues.

In both these studies, the cell-to-material interface was characterised high resolution microscopy techniques, while highlighting the development and application of visualisation techniques and analysis to these complex interfaces. It is hoped that methods of investigation developed and applied in this body of work will be applicable to not only study the interactions of cells with material topography, but also other biophysical cues such as substrate stiffness, chemical patterning and external forces that have the potential to exert control over stem cell function.

5.1 Optimisation of Visualisation Methods to Study Cell-Material Interactions

In order to study the complex interplay between cells and materials, existing methods were optimised and validated for use on material substrates. The state-of-the-art technique of FIB-SEM that has only made recent contributions in biology was optimised and validated for the purpose of visualising intracellular architecture of cells *in-situ*. The cell staining protocol for FIB-SEM had a dramatic effect on the ability to display intracellular structures, highlighting the various considerations in sample preparation. Using a combination of heavy metal stains provided sufficient ultrastructural detail.

Although the protocol for FIB-SEM optimised in this chapter was shown to be adequate in gaining sufficient ultrastructural detail, different concentrations and incubation times for each of the staining reagents were not optimised for each case, rather selected based on protocols previously published. In order to optimise the protocol further, these parameters should be tested to make the protocol more efficient as it has a lengthy preparation time of five days at present.

In contrast, SICM which did not require extensive sample preparation, required optimisation of the approach parameters and microscope operation. Using angled and upright approaches to scan cells on opaque nanoneedle arrays, proved how SICM could image cell membrane in its native state, without the need for labelling, dehydration or even fixation. Since the membrane itself is a highly dynamic structure that responds to surface topography, it was interesting to study the membrane organisation using polarity sensitive probes such as Laurdan, that fluoresce at different wavelengths based on lipid packing. In order to study this phenomenon, the application of Laurdan dye to the membrane of cells cultured on opaque biomaterial substrates such as nanoneedle arrays and flat silicon wafers was tested, as it has previously not been optimised for cells on biomaterial substrates, to find that dye concentrations and incubation times did not affect its intracellular uptake, or staining distribution, but only staining intensity.

The findings of this optimisation study informed decisions for the investigations that followed, as these techniques were incorporated for visualisation and analysis of the stem cell response to material topography.

5.2 New Microscopy Methods to Study the Influence of Microgrooved Substrates on Nuclear Remodelling

Material topography has previously been used to modulate a variety of cellular processes including differentiation, proliferation and migration. These processes are initiated through changes in cell shape and the reorganisation of the cytoskeleton, that manifest at the level of the genome via its direct link with the nucleus. In chapter 3, the conformational, epigenetic and mechanical changes that occur in the nucleus in response to microgrooved topography were investigated through the development and application of state-of-the-art microscopy techniques.

FIB-SEM as a standalone technique provided unprecedented detail of the physical conformation of the nuclei in response to microtopography. Novel findings from this chapter indicate that grooved topography significantly induce the formation of deep nuclear invaginations, across substantial lengths of the nuclear surface. In addition, a novel method for the observation of immunogold labels with FIB-SEM was successfully developed, which permitted the visualisation of epigenetic modifications and their movement in response to microtopography. Moreover, the relocation of silencing epigenetic modifications to the nuclear periphery was shown to correlate with increased mechanical stiffness of the nucleus, highlighting the ability to microgrooved topography to modulate chromatin architecture.

Overall, this study demonstrated the ability to visualise the localisation of single antigens of interest alongside cell ultrastructure in 3D with nanometre resolution, in cells in direct contact with biomaterial substrates. This is a new method that has the ability to clarify many of the structure-function relationships in studying biointerfaces that currently cannot be solved with other high-resolution microscopy techniques.

5.2.1 Future Directions

While the focus of this chapter was to develop and validate immunogold labelling method with FIB-SEM for studying cell-material interactions, it enables the technique to be used to study other cell-material interactions wherein the nature of the sample (in terms of its physical dimensions, opacity or thickness) limits it being studied by other powerful techniques such as super resolution microscopy or CLEM. The findings

of this study demonstrate the utility and novelty of FIB-SEM imaging in combination with immunogold labelling to identify the location of relevant targets in relation to their association with the ultrastructural components of the cell. Here, the localisation of H3K9me3 is studied, however immunolabelling of any protein of interest could be conducted. The method is therefore limited by the quality of the primary antibody and its penetrability rather than the sample preparation process. Moreover, the method is not limited to 2D materials as block sectioning of 3D matrices can be conducted with FIB-SEM. Thus it would be interesting to apply immunolabelling FIB-SEM method to those biomaterial culture systems wherein CLEM cannot be conducted, typically thick or opaque samples. Additionally, immunolabelling with FIB-SEM has offers particular novelty in studying specific antigens of interest that are hypothesised to associate with structural components of the cell recognisable by EM.

Although TEM has been instrumental in our understanding of the different types of NRs and their formation[210], FIB-SEM offers a complete 3D view of the nucleoplasmic reticulum (NR) as well as *in-situ* slice-and-view to then investigate the NR's functional involvement during nuclear remodelling under topographical cues. In this study, microgrooves stimulated formation of type II NRs as well as an increase in peripheral distribution of H3K9me3. However, since no direct correlation between type II NRs and epigenetic marks were observed in nuclei on microgrooves, it would be interesting to identify proteins involved at the NR-nucleoplasm interface, as these targets could be directly visualised with the invaginating nuclear membrane with unparalleled z-resolution of the FIB-SEM. For instance, it has been shown that NPCs localise to type II NRs[210], and that specific NPC proteins are expressed during cell differentiation[213]. To this end, immunogold FIB-SEM could be used to study specific NPC proteins that may co-localise with type II NRs to facilitate transcriptional processes and intranuclear-cytoplasmic cross-talk[214]. In addition, immunogold FIB-SEM using domain specific antibodies can potentially resolve the orientation of NPC proteins within the nuclear pore basket that may lead to it being open or closed in conformation[578].

In this study, a material that triggers nuclear membrane deformation was used to assess the relationship with epigenetic marks, however the method can be applied to any biological question i.e. irrespective or whether a material is involved or not. For instance, since specific segments (such as C- or N-terminal) of proteins can be tagged

using antibodies, immunogold FIB-SEM could be used to visualise how some endoplasmic reticulum (ER) proteins can flip across a membrane to influence ER function[579].

Since SICM was demonstrated the ability to map the nuclear stiffness of cells on microgrooved substrates, this method of assessing cell mechanics could be extended to studying cells on other material topographies. Moreover, higher resolution stiffness maps of single cells can be obtained for more in-detail analysis and correlation of the cell membrane topography with mechanical properties.

5.3 Investigating the Cell Membrane Response to Nanoneedle Arrays for Delivering Biological Payloads

For most part, the use of material cues in stimulating desired changes in cell behaviour is based on using materials that only provide external cues and do not interface with its intracellular content. With advancements in nanofabrication technologies, this concept has changed in recent years through the use of materials designed to probe the intracellular environment of cells. Attempts to gain intracellular access for biomolecule delivery applications have thus led to investigations of material systems that can facilitate or enhance payload transfer across the interface through negotiating the cell membrane barrier. In particular, because material topography can stimulate a response from the cell membrane and its constitutive components, it is necessary to assess the nature of its interactions at the biointerface. In chapter 4, the use of nanoneedle arrays as a tool to facilitate biomolecule delivery was investigated. Through their intimate interaction with the cell membrane, nanoneedle arrays were shown to modulate key processes of cell membrane remodelling, resulting in the activation of endocytotic pathways at the membrane-nanoneedle interface.

Novel findings from this chapter indicate that nanoneedle arrays significantly improve the delivery of endocytotic specific payloads as well as nucleic acids in hMSCs. This feature that is partly mediated by the endocytotic processes, that are selectively enhanced at the cell-nanoneedle interface demonstrates that the substrate topography is a key stimulator of membrane remodelling through the induction of membrane curvature and its recognition, that results in a cascade of protein binding events to facilitate intracellular uptake. Previously, nanotopographies in the form of nanoposts[184] and nanopillars[127] have been shown to stimulate endocytosis at the interface, however for the first time, this study reports that the enhancement of endocyotosis at the interface is also a major contributor to payload transfer and its subsequent trafficking mechanism within the cell.

Despite payload uptake via endocytosis and endosomal trafficking, additional novel findings highlight that a significant fraction of delivered nucleic acids remain active

in the cytosol. In previous work, reports of nanoneedle-mediated biomolecule delivery are highly variable ranging from 0% to over 90%, depending on the cell type as well as nanoneedle properties[516, 485, 492, 489, 315, 512]. The results from this study indicate that in addition to these factors, endocytosis pathway engagement and the trafficking mechanism also plays in a significant role in the efficiency of the nanoneedle delivery platform. Thus, this study highlights that these aspects of cytosolic entry must be considered for the continued optimisation and development of nanoneedle arrays for biomolecule delivery.

5.3.1 Future Directions

The best established pathways of endocytosis were investigated in this study. It is possible that clathrin and caveolae independent pathways may be activated at the interface. Since relatively little is known about these pathways and their trafficking, it is possible that some of these pathways may be responsible for payload internalisation, especially since many of them do not possess coat proteins and are linked to the invaginating membrane. Moreover, the trafficking routes of each of these pathways may also be different to CME, CavME and MP. It would therefore be important to investigate the dependencies on such pathways.

Live-cell imaging was not conducted in this study, however with advances in microscopy techniques and set-ups, it would be possible to image cargo release, uptake and trafficking. Inhibitors were not used in this study due to their non-specific effects especially after long incubation times (24 hours in this case). Knocking down endocytosis specific genes such as clathrin, caveolin-1 or Rac1 for MP, although difficult to achieve in hMSCs could be conducted in order to confirm the findings in relation to siRNA uptake and trafficking. Although co-localisation analysis enabled the assessment of cargo entering the endosomes and lysosomes, cytosolic accumulation was not directly observed. By conjugating the surface of a gold nanoparticle with the cargo, cytosolic delivery can be studied using FIB-SEM. Not only would this provide an understanding of payload transfer across the interface, but also a direct view of payload within the cytosol, lysosomes or endosomes simultaneously.

Currently, the major hurdle in intracellular delivery platforms is endosomal entrapment. However, endosomal trafficking is important for incoming cargo to reach their

target site (eg. the perinuclear region or the nucleus), that is mostly facilitated by microtubule transport within the cytosol. Thus, although nanoneedle interfacing results in a proportion of uptake of cargo by endocytosis, this might be an advantage in terms of proximity of the nanoinjected molecules to their active sites. Endosomal escape itself is a highly investigated field and the combination of the nanoneedle delivery system with endosomal escape probes could be a potential approach for successful delivery as well as cytosolic release of the payload.

5.4 Conclusion

The success of regenerative medicine and tissue engineering relies on robust strategies to faithfully recapitulate aspects of the microenvironment that supports the intended cell lineage transitions. Creating environments that are conducive to controlling cell behaviour requires a fundamental understanding of physical cues that translate into biological changes, which has fuelled the development of biomaterial platforms for individualised investigations of cell-material interactions.

Studies such as in this body of work have been conducted with the aim to provide an understanding of the stem cell response to material topography, with implications for controlling cell function and fate. By providing avenues for incorporation of new methods to visualise and assess cell behaviour on engineered substrates, unanswered biological questions with regards to the cell-material interface have been addressed. The use of immunogold labels within FIB-SEM as a tool to study nuclear remodelling in response to microgrooved topography was demonstrated as a robust technique in elucidating the relationship between cell structure and function, which is currently a challenge for cell-material systems. The study of the ability of material topography to enhance the intracellular delivery of therapeutic payload has provided novel insights into the unique nature and features of the cell-material interface, as well as the cellular components that modulate these interactions with great attention to detail.

It is hoped that providing new ways to probe and monitor the response of cells to engineered material cues will lead to improvements in relevant complexity of biomaterials in the near future as well as in our understanding of fundamental biology that is so elegantly designed.

References

[1] Irving L. Weissman. "Translating Stem and Progenitor Cell Biology to the Clinic: Barriers and Opportunities". en. In: *Science* 287.5457 (Feb. 2000), pp. 1442–1446. ISSN: 0036-8075, 1095-9203. DOI: 10.1126/science.287.5457.1442.

[2] James A. Thomson et al. "Embryonic Stem Cell Lines Derived from Human Blastocysts". en. In: *Science* 282.5391 (Nov. 1998), pp. 1145–1147. ISSN: 0036-8075, 1095-9203. DOI: 10.1126/science.282.5391.1145.

[3] Kazutoshi Takahashi et al. "Induction of Pluripotent Stem Cells from Adult Human Fibroblasts by Defined Factors". eng. In: *Cell* 131.5 (Nov. 2007), pp. 861–872. ISSN: 0092-8674. DOI: 10.1016/j.cell.2007.11.019.

[4] Andrew S. Lee et al. "Tumorigenicity as a Clinical Hurdle for Pluripotent Stem Cell Therapies". En. In: *Nature Medicine* 19.8 (Aug. 2013), p. 998. ISSN: 1546-170X. DOI: 10.1038/nm.3267.

[5] Erin A. Kimbrel and Robert Lanza. "Current Status of Pluripotent Stem Cells: Moving the First Therapies to the Clinic". En. In: *Nature Reviews Drug Discovery* 14.10 (Oct. 2015), p. 681. ISSN: 1474-1784. DOI: 10.1038/nrd4738.

[6] Hoang Nguyen, Margaret A. Goodell, and Noah Shroyer. "Somatic Stem Cell Heterogeneity: Diversity in the Blood, Skin and Intestinal Stem Cell Compartments". En. In: *Nature Reviews Molecular Cell Biology* 16.5 (May 2015), p. 299. ISSN: 1471-0080. DOI: 10.1038/nrm3980.

[7] Ulrich Lindner et al. "Mesenchymal Stem or Stromal Cells: Toward a Better Understanding of Their Biology?" In: *Transfusion Medicine and Hemotherapy* 37.2 (Apr. 2010), pp. 75–83. ISSN: 1660-3796. DOI: 10.1159/000290897.

[8] Paolo Bianco, Pamela Gehron Robey, and Paul J. Simmons. "Mesenchymal Stem Cells: Revisiting History, Concepts, and Assays". In: *Cell Stem Cell* 2.4 (Apr. 2008), pp. 313–319. ISSN: 1934-5909. DOI: 10.1016/j.stem.2008.03.002.

[9] Mihaela Chivu-Economescu and Martin Rubach. "Hematopoietic Stem Cells Therapies". eng. In: *Current Stem Cell Research & Therapy* 12.2 (2017), pp. 124–133. ISSN: 2212-3946. DOI: 10.2174/1574888X10666151026114241.

[10] Alessandro Aiuti et al. "Correction of ADA-SCID by Stem Cell Gene Therapy Combined with Nonmyeloablative Conditioning". en. In: *Science* 296.5577 (June 2002), pp. 2410–2413. ISSN: 0036-8075, 1095-9203. DOI: 10.1126/science.1070104.

[11] Matthew M. Hsieh et al. "Nonmyeloablative HLA-Matched Sibling Allogeneic Hematopoietic Stem Cell Transplantation for Severe Sickle Cell Phenotype". eng. In: *JAMA* 312.1 (July 2014), pp. 48–56. ISSN: 1538-3598. DOI: 10.1001/jama.2014.7192.

[12] Alan Trounson and Courtney McDonald. “Stem Cell Therapies in Clinical Trials: Progress and Challenges”. eng. In: *Cell Stem Cell* 17.1 (July 2015), pp. 11–22. ISSN: 1875-9777. DOI: 10.1016/j.stem.2015.06.007.

[13] Deepak Srivastava and Natalie DeWitt. “In Vivo Cellular Reprogramming: The Next Generation”. English. In: *Cell* 166.6 (Sept. 2016), pp. 1386–1396. ISSN: 0092-8674, 1097-4172. DOI: 10.1016/j.cell.2016.08.055.

[14] Xiulan Yang, Lil Pabon, and Charles E. Murry. “Engineering Adolescence: Maturation of Human Pluripotent Stem Cell-Derived Cardiomyocytes”. In: *Circulation research* 114.3 (Jan. 2014), pp. 511–523. ISSN: 0009-7330. DOI: 10.1161/CIRCRESAHA.114.300558.

[15] Christopher N. Mayhew and James M. Wells. “Converting Human Pluripotent Stem Cells to Beta Cells: Recent Advances and Future Challenges”. In: *Current opinion in organ transplantation* 15.1 (Feb. 2010), pp. 54–60. ISSN: 1087-2418. DOI: 10.1097/MOT.0b013e3283337e1c.

[16] Francesca Gattazzo, Anna Urciuolo, and Paolo Bonaldo. “Extracellular Matrix: A Dynamic Microenvironment for Stem Cell Niche”. In: *Biochimica et Biophysica Acta (BBA) - General Subjects*. Matrix-mediated cell behaviour and properties 1840.8 (Aug. 2014), pp. 2506–2519. ISSN: 0304-4165. DOI: 10.1016/j.bbagen.2014.01.010.

[17] Christian Frantz, Kathleen M. Stewart, and Valerie M. Weaver. “The Extracellular Matrix at a Glance”. In: *Journal of Cell Science* 123.24 (Dec. 2010), pp. 4195–4200. ISSN: 0021-9533. DOI: 10.1242/jcs.023820.

[18] Bruce Alberts et al. “The Extracellular Matrix of Animals”. en. In: (2002).

[19] Harvey Lodish et al. “Cell-Matrix Adhesion”. en. In: (2000).

[20] Isaac A. Janson and Andrew J. Putnam. “Extracellular Matrix Elasticity and Topography: Material-Based Cues That Affect Cell Function via Conserved Mechanisms”. en. In: *Journal of Biomedical Materials Research Part A* 103.3 (Mar. 2015), pp. 1246–1258. ISSN: 1552-4965. DOI: 10.1002/jbm.a.35254.

[21] Nicholas D. Evans and Eileen Gentleman. “The Role of Material Structure and Mechanical Properties in Cell–Matrix Interactions”. en. In: *Journal of Materials Chemistry B* 2.17 (2014), pp. 2345–2356. DOI: 10.1039/C3TB21604G.

[22] Caroline Bonnans, Jonathan Chou, and Zena Werb. “Remodelling the Extracellular Matrix in Development and Disease”. In: *Nature reviews. Molecular cell biology* 15.12 (Dec. 2014), pp. 786–801. ISSN: 1471-0072. DOI: 10.1038/nrm3904.

[23] Mito Kanatsu-Shinohara et al. “Homing of Mouse Spermatogonial Stem Cells to Germline Niche Depends on Beta1-Integrin”. eng. In: *Cell Stem Cell* 3.5 (Nov. 2008), pp. 533–542. ISSN: 1875-9777. DOI: 10.1016/j.stem.2008.08.002.

[24] A. J. Potocnik, C. Brakebusch, and R. Fässler. “Fetal and Adult Hematopoietic Stem Cells Require Beta1 Integrin Function for Colonizing Fetal Liver, Spleen, and Bone Marrow”. eng. In: *Immunity* 12.6 (June 2000), pp. 653–663. ISSN: 1074-7613.

[25] Shihuan Kuang, Mark A. Gillespie, and Michael A. Rudnicki. “Niche Regulation of Muscle Satellite Cell Self-Renewal and Differentiation”. eng. In: *Cell Stem Cell* 2.1 (Jan. 2008), pp. 22–31. ISSN: 1875-9777. DOI: 10.1016/j.stem.2007.12.012.

[26] Yukiko M. Yamashita. “Cell Adhesion in Regulation of Asymmetric Stem Cell Division”. In: *Current opinion in cell biology* 22.5 (Oct. 2010), pp. 605–610. ISSN: 0955-0674. DOI: 10.1016/j.ceb.2010.07.009.

[27] Andrew B. J. Prowse et al. “Stem Cell Integrins: Implications for Ex-Vivo Culture and Cellular Therapies”. eng. In: *Stem Cell Research* 6.1 (Jan. 2011), pp. 1–12. ISSN: 1876-7753. DOI: 10.1016/j.scr.2010.09.005.

[28] Richard O. Hynes. “Integrins: Bidirectional, Allosteric Signaling Machines”. In: *Cell* 110.6 (Sept. 2002), pp. 673–687. ISSN: 0092-8674. DOI: 10.1016/S0092-8674(02)00971-6.

[29] Shawdee Eshghi and David V. Schaffer. “Engineering Microenvironments to Control Stem Cell Fate and Function”. eng. In: *StemBook*. Cambridge (MA): Harvard Stem Cell Institute, 2008.

[30] Isaac Brownell et al. “Nerve-Derived Sonic Hedgehog Defines a Niche for Hair Follicle Stem Cells Capable of Becoming Epidermal Stem Cells”. English. In: *Cell Stem Cell* 8.5 (May 2011), pp. 552–565. ISSN: 1934-5909, 1875-9777. DOI: 10.1016/j.stem.2011.02.021.

[31] Amir Schajnovitz et al. “CXCL12 Secretion by Bone Marrow Stromal Cells Is Dependent on Cell Contact and Mediated by Connexin-43 and Connexin-45 Gap Junctions”. eng. In: *Nature Immunology* 12.5 (May 2011), pp. 391–398. ISSN: 1529-2916. DOI: 10.1038/ni.2017.

[32] Ellen J. Ward et al. “Stem Cells Signal to the Niche through the Notch Pathway in the Drosophila Ovary”. In: *Current Biology* 16.23 (Dec. 2006), pp. 2352–2358. ISSN: 0960-9822. DOI: 10.1016/j.cub.2006.10.022.

[33] Russell C. Addis and Jonathan A. Epstein. “Induced Regeneration–the Progress and Promise of Direct Reprogramming for Heart Repair”. eng. In: *Nature Medicine* 19.7 (July 2013), pp. 829–836. ISSN: 1546-170X. DOI: 10.1038/nm.3225.

[34] J. C. Adams and F. M. Watt. “Regulation of Development and Differentiation by the Extracellular Matrix”. eng. In: *Development (Cambridge, England)* 117.4 (Apr. 1993), pp. 1183–1198. ISSN: 0950-1991.

[35] R Langer and J P Vacanti. “Tissue Engineering”. eng. In: *Science (New York, N.Y.)* 260.5110 (May 1993), pp. 920–926. ISSN: 0036-8075.

[36] Juliana Lott Carvalho et al. “Innovative Strategies for Tissue Engineering”. en. In: *Advances in Biomaterials Science and Biomedical Applications* (2013). DOI: 10.5772/53337.

[37] Ning Wang. “Review of Cellular Mechanotransduction”. en. In: *Journal of Physics D: Applied Physics* 50.23 (2017), p. 233002. ISSN: 0022-3727. DOI: 10.1088/1361-6463/aa6e18.

[38] Benjamin Geiger, Joachim P. Spatz, and Alexander D. Bershadsky. “Environmental Sensing through Focal Adhesions”. En. In: *Nature Reviews Molecular Cell Biology* 10.1 (Jan. 2009), p. 21. ISSN: 1471-0080. DOI: 10.1038/nrm2593.

[39] Geoffrey M. Cooper. “Signal Transduction and the Cytoskeleton”. en. In: (2000).

[40] Thomas D. Pollard and John A. Cooper. “Actin, a Central Player in Cell Shape and Movement”. en. In: *Science* 326.5957 (Nov. 2009), pp. 1208–1212. ISSN: 0036-8075, 1095-9203. DOI: 10.1126/science.1175862.

[41] Thomas D Pollard and Gary G Borisy. “Cellular Motility Driven by Assembly and Disassembly of Actin Filaments”. In: *Cell* 112.4 (Feb. 2003), pp. 453–465. ISSN: 0092-8674. DOI: 10.1016/S0092-8674(03)00120-X.

[42] Paolo P. Provenzano and Patricia J. Keely. “Mechanical Signaling through the Cytoskeleton Regulates Cell Proliferation by Coordinated Focal Adhesion and Rho GTPase Signaling”. In: *Journal of Cell Science* 124.8 (Apr. 2011), pp. 1195–1205. ISSN: 0021-9533. DOI: 10.1242/jcs.067009.

[43] Olivia L. Mooren, Brian J. Galletta, and John A. Cooper. “Roles for Actin Assembly in Endocytosis”. In: *Annual Review of Biochemistry* 81.1 (2012), pp. 661–686. DOI: 10.1146/annurev-biochem-060910-094416.

[44] David A. Calderwood, Sanford J. Shattil, and Mark H. Ginsberg. “Integrins and Actin Filaments: Reciprocal Regulation of Cell Adhesion and Signaling”. en. In: *Journal of Biological Chemistry* 275.30 (July 2000), pp. 22607–22610. ISSN: 0021-9258, 1083-351X. DOI: 10.1074/jbc.R900037199.

[45] Christian Frantz, Kathleen M. Stewart, and Valerie M. Weaver. “The Extracellular Matrix at a Glance”. In: *Journal of Cell Science* 123.24 (Dec. 2010), pp. 4195–4200. ISSN: 0021-9533. DOI: 10.1242/jcs.023820.

[46] Marion K. Gordon and Rita A. Hahn. “Collagens”. eng. In: *Cell and Tissue Research* 339.1 (Jan. 2010), pp. 247–257. ISSN: 1432-0878. DOI: 10.1007/s00441-009-0844-4.

[47] I. R. Chambers et al. “The Measurement of Brain Tissue Stiffness In-Vivo”. eng. In: *Acta Neurochirurgica. Supplement* 102 (2008), pp. 287–289. ISSN: 0065-1419.

[48] T. Franz et al. “In Situ Compressive Stiffness, Biochemical Composition, and Structural Integrity of Articular Cartilage of the Human Knee Joint”. eng. In: *Osteoarthritis and Cartilage* 9.6 (Aug. 2001), pp. 582–592. ISSN: 1063-4584. DOI: 10.1053/joca.2001.0418.

[49] Penelope C. Georges et al. “Increased Stiffness of the Rat Liver Precedes Matrix Deposition: Implications for Fibrosis”. eng. In: *American Journal of Physiology. Gastrointestinal and Liver Physiology* 293.6 (Dec. 2007), G1147–1154. ISSN: 0193-1857. DOI: 10.1152/ajpgi.00032.2007.

[50] Penelope C. Georges and Paul A. Janmey. “Cell Type-Specific Response to Growth on Soft Materials”. eng. In: *Journal of Applied Physiology (Bethesda, Md.: 1985)* 98.4 (Apr. 2005), pp. 1547–1553. ISSN: 8750-7587. DOI: 10.1152/japplphysiol.01121.2004.

[51] Jérôme Solon et al. “Fibroblast Adaptation and Stiffness Matching to Soft Elastic Substrates”. In: *Biophysical Journal* 93.12 (Dec. 2007), pp. 4453–4461. ISSN: 0006-3495. DOI: 10.1529/biophysj.106.101386.

[52] Yue Ding, Guang-Kui Xu, and Gang-Feng Wang. “On the Determination of Elastic Moduli of Cells by AFM Based Indentation”. en. In: *Scientific Reports* 7 (Apr. 2017), p. 45575. ISSN: 2045-2322. DOI: 10.1038/srep45575.

[53] John M. Maloney et al. “Mesenchymal Stem Cell Mechanics from the Attached to the Suspended State”. eng. In: *Biophysical Journal* 99.8 (Oct. 2010), pp. 2479–2487. ISSN: 1542-0086. DOI: 10.1016/j.bpj.2010.08.052.

[54] M. Puig-De-Morales et al. “Measurement of Cell Microrheology by Magnetic Twisting Cytometry with Frequency Domain Demodulation”. eng. In: *Journal of Applied Physiology (Bethesda, Md.: 1985)* 91.3 (Sept. 2001), pp. 1152–1159. ISSN: 8750-7587. DOI: 10.1152/jappl.2001.91.3.1152.

[55] T. Ohashi et al. “Intracellular Mechanics and Mechanotransduction Associated with Chondrocyte Deformation during Pipette Aspiration”. eng. In: *Biorheology* 43.3,4 (2006), pp. 201–214. ISSN: 0006-355X.

[56] Adam J. Engler et al. “Matrix Elasticity Directs Stem Cell Lineage Specification”. In: *Cell* 126.4 (Aug. 2006), pp. 677–689. ISSN: 0092-8674. DOI: 10.1016/j.cell.2006.06.044.

[57] Britta Trappmann et al. “Extracellular-Matrix Tethering Regulates Stem-Cell Fate”. En. In: *Nature Materials* 11.7 (July 2012), p. 642. ISSN: 1476-4660. DOI: 10.1038/nmat3339.

[58] Jessica H. Wen et al. “Interplay of Matrix Stiffness and Protein Tethering in Stem Cell Differentiation”. En. In: *Nature Materials* 13.10 (Oct. 2014), p. 979. ISSN: 1476-4660. DOI: 10.1038/nmat4051.

[59] Krishanu Saha et al. “Substrate Modulus Directs Neural Stem Cell Behavior”. In: *Biophysical Journal* 95.9 (Nov. 2008), pp. 4426–4438. ISSN: 0006-3495. DOI: 10.1529/biophysj.108.132217.

[60] Murat Guvendiren and Jason A. Burdick. “Stiffening Hydrogels to Probe Short- and Long-Term Cellular Responses to Dynamic Mechanics”. En. In: *Nature Communications* 3 (Apr. 2012), p. 792. ISSN: 2041-1723. DOI: 10.1038/ncomms1792.

[61] Hyun Joon Kong et al. “Non-Viral Gene Delivery Regulated by Stiffness of Cell Adhesion Substrates”. En. In: *Nature Materials* 4.6 (June 2005), p. 460. ISSN: 1476-4660. DOI: 10.1038/nmat1392.

[62] Brendon M. Baker et al. “Cell-Mediated Fibre Recruitment Drives Extracellular Matrix Mechanosensing in Engineered Fibrillar Microenvironments”. En. In: *Nature Materials* 14.12 (Dec. 2015), p. 1262. ISSN: 1476-4660. DOI: 10.1038/nmat4444.

[63] Nathaniel Huebsch et al. “Matrix Elasticity of Void-Forming Hydrogels Controls Transplanted-Stem-Cell-Mediated Bone Formation”. En. In: *Nature Materials* 14.12 (Dec. 2015), p. 1269. ISSN: 1476-4660. DOI: 10.1038/nmat4407.

[64] Max Darnell et al. “Substrate Stress-Relaxation Regulates Scaffold Remodeling and Bone Formation In Vivo”. en. In: *Advanced Healthcare Materials* 6.1 (Jan. 2017), n/a–n/a. ISSN: 2192-2659. DOI: 10.1002/adhm.201601185.

[65] Shigenori Nonaka et al. “Determination of Left–Right Patterning of the Mouse Embryo by Artificial Nodal Flow”. En. In: *Nature* 418.6893 (July 2002), p. 96. ISSN: 1476-4687. DOI: 10.1038/nature00849.

[66] Kameswara Rao Badri, Yuanxiang Zhou, and Lucia Schuger. “Embryological Origin of Airway Smooth Muscle”. In: *Proceedings of the American Thoracic*

Society 5.1 (Jan. 2008), pp. 4–10. ISSN: 1546-3222. DOI: 10.1513/pats.200704-049VS.

[67] Jay R. Hove et al. "Intracardiac Fluid Forces Are an Essential Epigenetic Factor for Embryonic Cardiogenesis". En. In: *Nature* 421.6919 (Jan. 2003), p. 172. ISSN: 1476-4687. DOI: 10.1038/nature01282.

[68] Cornelia Hahn and Martin A. Schwartz. "Mechanotransduction in Vascular Physiology and Atherogenesis". En. In: *Nature Reviews Molecular Cell Biology* 10.1 (Jan. 2009), p. 53. ISSN: 1471-0080. DOI: 10.1038/nrm2596.

[69] J. Klein-Nulend et al. "Microgravity and Bone Cell Mechanosensitivity". In: *Advances in Space Research*. Space Life Sciences: Gravitational Biology: 2002 32.8 (Oct. 2003), pp. 1551–1559. ISSN: 0273-1177. DOI: 10.1016/S0273-1177(03)90395-4.

[70] Eleni Tzima et al. "A Mechanosensory Complex That Mediates the Endothelial Cell Response to Fluid Shear Stress". En. In: *Nature* 437.7057 (Sept. 2005), p. 426. ISSN: 1476-4687. DOI: 10.1038/nature03952.

[71] W. Madej et al. "Physiological and Excessive Mechanical Compression of Articular Cartilage Activates Smad2/3P Signaling". In: *Osteoarthritis and Cartilage* 22.7 (July 2014), pp. 1018–1025. ISSN: 1063-4584. DOI: 10.1016/j.joca.2014.04.024.

[72] Shuichi Mizuno. "A Novel Method for Assessing Effects of Hydrostatic Fluid Pressure on Intracellular Calcium: A Study with Bovine Articular Chondrocytes". eng. In: *American Journal of Physiology. Cell Physiology* 288.2 (Feb. 2005), pp. C329–337. ISSN: 0363-6143. DOI: 10.1152/ajpcell.00131.2004.

[73] P. F. Davies, A. Robotewskyj, and M. L. Griem. "Quantitative Studies of Endothelial Cell Adhesion. Directional Remodeling of Focal Adhesion Sites in Response to Flow Forces". eng. In: *The Journal of Clinical Investigation* 93.5 (May 1994), pp. 2031–2038. ISSN: 0021-9738. DOI: 10.1172/JCI117197.

[74] M. M. Knight et al. "Mechanical Compression and Hydrostatic Pressure Induce Reversible Changes in Actin Cytoskeletal Organisation in Chondrocytes in Agarose". eng. In: *Journal of Biomechanics* 39.8 (2006), pp. 1547–1551. ISSN: 0021-9290. DOI: 10.1016/j.jbiomech.2005.04.006.

[75] Sandra B. Lemke and Frank Schnorrer. "Mechanical Forces during Muscle Development". In: *Mechanisms of Development*. Roles of physical forces in development 144 (Apr. 2017), pp. 92–101. ISSN: 0925-4773. DOI: 10.1016/j.mod.2016.11.003.

[76] Stéphanie Pellegrin and Harry Mellor. "Actin Stress Fibres". en. In: *Journal of Cell Science* 120.20 (Oct. 2007), pp. 3491–3499. ISSN: 0021-9533, 1477-9137. DOI: 10.1242/jcs.018473.

[77] Jennifer S. Park et al. "Differential Effects of Equiaxial and Uniaxial Strain on Mesenchymal Stem Cells". en. In: *Biotechnology and Bioengineering* 88.3 (Nov. 2004), pp. 359–368. ISSN: 1097-0290. DOI: 10.1002/bit.20250.

[78] Stephen D. Thorpe et al. "The Response of Bone Marrow-Derived Mesenchymal Stem Cells to Dynamic Compression Following TGF-Beta3 Induced Chondro-

genic Differentiation". eng. In: *Annals of Biomedical Engineering* 38.9 (Sept. 2010), pp. 2896–2909. ISSN: 1573-9686. DOI: 10.1007/s10439-010-0059-6.

[79] Ji-Yeon Jang et al. "Combined Effects of Surface Morphology and Mechanical Straining Magnitudes on the Differentiation of Mesenchymal Stem Cells without Using Biochemical Reagents". eng. In: *Journal of Biomedicine & Biotechnology* 2011 (2011), p. 860652. ISSN: 1110-7251. DOI: 10.1155/2011/860652.

[80] Kimiko Yamamoto et al. "Fluid Shear Stress Induces Differentiation of Flk-1-Positive Embryonic Stem Cells into Vascular Endothelial Cells in Vitro". In: *American Journal of Physiology-Heart and Circulatory Physiology* 288.4 (Apr. 2005), H1915–H1924. ISSN: 0363-6135. DOI: 10.1152/ajpheart.00956.2004.

[81] Barbara Illi et al. "Epigenetic Histone Modification and Cardiovascular Lineage Programming in Mouse Embryonic Stem Cells Exposed to Laminar Shear Stress". en. In: *Circulation Research* 96.5 (Mar. 2005), pp. 501–508. ISSN: 0009-7330, 1524-4571. DOI: 10.1161/01.RES.0000159181.06379.63.

[82] Feng Guo et al. "Controlling Cell–Cell Interactions Using Surface Acoustic Waves". In: *Proceedings of the National Academy of Sciences of the United States of America* 112.1 (Jan. 2015), pp. 43–48. ISSN: 0027-8424. DOI: 10.1073/pnas.1422068112.

[83] Vicard Du et al. "A 3D Magnetic Tissue Stretcher for Remote Mechanical Control of Embryonic Stem Cell Differentiation". En. In: *Nature Communications* 8.1 (Sept. 2017), p. 400. ISSN: 2041-1723. DOI: 10.1038/s41467-017-00543-2.

[84] J Taipale and J Keski-Oja. "Growth Factors in the Extracellular Matrix." In: *The FASEB Journal* 11.1 (Jan. 1997), pp. 51–59. ISSN: 0892-6638. DOI: 10.1096/fasebj.11.1.9034166.

[85] Erkki Ruoslahti and Michael D. Pierschbacher. "New Perspectives in Cell Adhesion: RGD and Integrins". In: *Science* 238.4826 (1987), pp. 491–497. ISSN: 0036-8075.

[86] Danielle S. W. Benoit and Kristi S. Anseth. "The Effect on Osteoblast Function of Colocalized RGD and PHSRN Epitopes on PEG Surfaces". In: *Biomaterials* 26.25 (Sept. 2005), pp. 5209–5220. ISSN: 0142-9612. DOI: 10.1016/j.biomaterials.2005.01.045.

[87] Christopher J. Flaim, Shu Chien, and Sangeeta N. Bhatia. "An Extracellular Matrix Microarray for Probing Cellular Differentiation". En. In: *Nature Methods* 2.2 (Jan. 2005), p. 119. ISSN: 1548-7105. DOI: 10.1038/nmeth736.

[88] Mark A. LaBarge et al. "Human Mammary Progenitor Cell Fate Decisions Are Products of Interactions with Combinatorial Microenvironments". en. In: *Integrative Biology* 1.1 (Jan. 2009), pp. 70–79. ISSN: 1757-9708. DOI: 10.1039/B816472J.

[89] Yoav Soen et al. "Exploring the Regulation of Human Neural Precursor Cell Differentiation Using Arrays of Signaling Microenvironments". In: *Molecular Systems Biology* 2 (July 2006), p. 37. ISSN: 1744-4292. DOI: 10.1038/msb4100076.

[90] Rowena McBeath et al. "Cell Shape, Cytoskeletal Tension, and RhoA Regulate Stem Cell Lineage Commitment". In: *Developmental Cell* 6.4 (Apr. 2004), pp. 483–495. ISSN: 1534-5807. DOI: 10.1016/S1534-5807(04)00075-9.

[91] Benjamin L. Beckstead, Daniel M. Santosa, and Cecilia M. Giachelli. "Mimicking Cell–Cell Interactions at the Biomaterial–Cell Interface for Control of Stem Cell Differentiation". en. In: *Journal of Biomedical Materials Research Part A* 79A.1 (Oct. 2006), pp. 94–103. ISSN: 1552-4965. DOI: 10.1002/jbm.a.30760.

[92] Matthew J. Dalby et al. "The Control of Human Mesenchymal Cell Differentiation Using Nanoscale Symmetry and Disorder". En. In: *Nature Materials* 6.12 (Dec. 2007), p. 997. ISSN: 1476-4660. DOI: 10.1038/nmat2013.

[93] Lingyin Li et al. "Spatial Control of Cell Fate Using Synthetic Surfaces to Potentiate TGF-β Signaling". en. In: *Proceedings of the National Academy of Sciences* 108.29 (July 2011), pp. 11745–11750. ISSN: 0027-8424, 1091-6490. DOI: 10.1073/pnas.1101454108.

[94] Matthias P. Lutolf et al. "Perturbation of Single Hematopoietic Stem Cell Fates in Artificial Niches". In: *Integrative biology : quantitative biosciences from nano to macro* 1.1 (Jan. 2009), pp. 59–69. ISSN: 1757-9694. DOI: 10.1039/b815718a.

[95] Danielle S. W. Benoit et al. "Small Functional Groups for Controlled Differentiation of Hydrogel-Encapsulated Human Mesenchymal Stem Cells". En. In: *Nature Materials* 7.10 (Oct. 2008), p. 816. ISSN: 1476-4660. DOI: 10.1038/nmat2269.

[96] Celeste M. Nelson et al. "Change in Cell Shape Is Required for Matrix Metalloproteinase-Induced Epithelial-Mesenchymal Transition of Mammary Epithelial Cells". eng. In: *Journal of Cellular Biochemistry* 105.1 (Sept. 2008), pp. 25–33. ISSN: 1097-4644. DOI: 10.1002/jcb.21821.

[97] Rowena McBeath et al. "Cell Shape, Cytoskeletal Tension, and RhoA Regulate Stem Cell Lineage Commitment". eng. In: *Developmental Cell* 6.4 (Apr. 2004), pp. 483–495. ISSN: 1534-5807.

[98] Raheem Peerani et al. "Niche-Mediated Control of Human Embryonic Stem Cell Self-Renewal and Differentiation". In: *The EMBO Journal* 26.22 (Nov. 2007), pp. 4744–4755. ISSN: 0261-4189. DOI: 10.1038/sj.emboj.7601896.

[99] Anne C. von Philipsborn et al. "Microcontact Printing of Axon Guidance Molecules for Generation of Graded Patterns". En. In: *Nature Protocols* 1.3 (Oct. 2006), p. 1322. ISSN: 1750-2799. DOI: 10.1038/nprot.2006.251.

[100] Rebecca J. McMurray et al. "Nanoscale Surfaces for the Long-Term Maintenance of Mesenchymal Stem Cell Phenotype and Multipotency". En. In: *Nature Materials* 10.8 (Aug. 2011), p. 637. ISSN: 1476-4660. DOI: 10.1038/nmat3058.

[101] Deok-Ho Kim et al. "Nanoscale Cues Regulate the Structure and Function of Macroscopic Cardiac Tissue Constructs". en. In: *Proceedings of the National Academy of Sciences* 107.2 (Jan. 2010), pp. 565–570. ISSN: 0027-8424, 1091-6490. DOI: 10.1073/pnas.0906504107.

[102] Gileade P. Freitas et al. "Effect of Surface Nanotopography on Bone Response to Titanium Implant". eng. In: *The Journal of Oral Implantology* 42.3 (June 2016), pp. 240–247. ISSN: 1548-1336. DOI: 10.1563/aaid-joi-D-14-00254.

[103] Marc J. Madou. *Fundamentals of Microfabrication: The Science of Miniaturization, Second Edition*. en. CRC Press, Mar. 2002. ISBN: 978-0-8493-0826-0.

[104] N. Gadegaard et al. "Arrays of Nano-Dots for Cellular Engineering". In: *Microelectronic Engineering*. Proceedings of the 28th International Conference on

Micro- and Nano-Engineering 67-68 (June 2003), pp. 162–168. ISSN: 0167-9317. DOI: 10.1016/S0167-9317(03)00067-4.

[105] Jinquan Huang et al. "Fabrication of Silicon Nanowires with Precise Diameter Control Using Metal Nanodot Arrays as a Hard Mask Blocking Material in Chemical Etching". In: *Chemistry of Materials* 22.13 (July 2010), pp. 4111–4116. ISSN: 0897-4756. DOI: 10.1021/cm101121c.

[106] Younan Xia et al. "Replica Molding Using Polymeric Materials: A Practical Step toward Nanomanufacturing". In: *Advanced Materials* 9.2 (Feb. 1997), pp. 147–149. ISSN: 1521-4095. DOI: 10.1002/adma.19970090211.

[107] David Lu et al. "Microgrooved Surface Modulates Neuron Differentiation in Human Embryonic Stem Cells". en. In: *Human Embryonic Stem Cell Protocols*. Methods in Molecular Biology. Humana Press, New York, NY, 2014, pp. 281–287. ISBN: 978-1-4939-2667-1 978-1-4939-2668-8. DOI: 10.1007/7651_2014_81.

[108] Jennifer B. Recknor, Donald S. Sakaguchi, and Surya K. Mallapragada. "Directed Growth and Selective Differentiation of Neural Progenitor Cells on Micropatterned Polymer Substrates". eng. In: *Biomaterials* 27.22 (Aug. 2006), pp. 4098–4108. ISSN: 0142-9612. DOI: 10.1016/j.biomaterials.2006.03.029.

[109] Natalia Gomez, Shaochen Chen, and Christine E. Schmidt. "Polarization of Hippocampal Neurons with Competitive Surface Stimuli: Contact Guidance Cues Are Preferred over Chemical Ligands". eng. In: *Journal of the Royal Society, Interface* 4.13 (Apr. 2007), pp. 223–233. ISSN: 1742-5689. DOI: 10.1098/rsif.2006.0171.

[110] Man Ryul Lee et al. "Direct Differentiation of Human Embryonic Stem Cells into Selective Neurons on Nanoscale Ridge/Groove Pattern Arrays". eng. In: *Biomaterials* 31.15 (May 2010), pp. 4360–4366. ISSN: 1878-5905. DOI: 10.1016/j.biomaterials.2010.02.012.

[111] Gregory T. Christopherson, Hongjun Song, and Hai-Quan Mao. "The Influence of Fiber Diameter of Electrospun Substrates on Neural Stem Cell Differentiation and Proliferation". eng. In: *Biomaterials* 30.4 (Feb. 2009), pp. 556–564. ISSN: 1878-5905. DOI: 10.1016/j.biomaterials.2008.10.004.

[112] Seunghan Oh et al. "Stem Cell Fate Dictated Solely by Altered Nanotube Dimension". en. In: *Proceedings of the National Academy of Sciences* 106.7 (Feb. 2009), pp. 2130–2135. ISSN: 0027-8424, 1091-6490. DOI: 10.1073/pnas.0813200106.

[113] Peter Newman et al. "Relationship between Nanotopographical Alignment and Stem Cell Fate with Live Imaging and Shape Analysis". En. In: *Scientific Reports* 6 (Dec. 2016), p. 37909. ISSN: 2045-2322. DOI: 10.1038/srep37909.

[114] Rajat K. Das et al. "Influence of Nanohelical Shape and Periodicity on Stem Cell Fate". In: *ACS Nano* 7.4 (Apr. 2013), pp. 3351–3361. ISSN: 1936-0851. DOI: 10.1021/nn4001325.

[115] Giulio Abagnale et al. "Surface Topography Guides Morphology and Spatial Patterning of Induced Pluripotent Stem Cell Colonies". English. In: *Stem Cell Reports* 9.2 (Aug. 2017), pp. 654–666. ISSN: 2213-6711. DOI: 10.1016/j.stemcr.2017.06.016.

[116] Sharon Gerecht et al. “The Effect of Actin Disrupting Agents on Contact Guidance of Human Embryonic Stem Cells”. In: *Biomaterials* 28.28 (Oct. 2007), pp. 4068–4077. ISSN: 0142-9612. DOI: 10.1016/j.biomaterials.2007.05.027.

[117] Laura A. Smith et al. “The Influence of Three-Dimensional Nanofibrous Scaffolds on the Osteogenic Differentiation of Embryonic Stem Cells”. eng. In: *Biomaterials* 30.13 (May 2009), pp. 2516–2522. ISSN: 1878-5905. DOI: 10.1016/j.biomaterials.2009.01.009.

[118] Louisa C.Y. Lee et al. “Nanotopography Controls Cell Cycle Changes Involved with Skeletal Stem Cell Self-Renewal and Multipotency”. In: *Biomaterials* 116 (Feb. 2017), pp. 10–20. ISSN: 0142-9612. DOI: 10.1016/j.biomaterials.2016.11.032.

[119] Terje Sjöström et al. “Fabrication of Pillar-like Titania Nanostructures on Titanium and Their Interactions with Human Skeletal Stem Cells”. In: *Acta Biomaterialia* 5.5 (June 2009), pp. 1433–1441. ISSN: 1742-7061. DOI: 10.1016/j.actbio.2009.01.007.

[120] Weiqiang Chen et al. “Nanotopography Influences Adhesion, Spreading, and Self-Renewal of Human Embryonic Stem Cells”. In: *ACS Nano* 6.5 (May 2012), pp. 4094–4103. ISSN: 1936-0851. DOI: 10.1021/nn3004923.

[121] Yen P. Kong et al. “Expression of Oct4 in Human Embryonic Stem Cells Is Dependent on Nanotopographical Configuration”. In: *Acta Biomaterialia* 9.5 (May 2013), pp. 6369–6380. ISSN: 1742-7061. DOI: 10.1016/j.actbio.2013.01.036.

[122] Timothy L. Downing et al. “Biophysical Regulation of Epigenetic State and Cell Reprogramming”. En. In: *Nature Materials* 12.12 (Dec. 2013), p. 1154. ISSN: 1476-4660. DOI: 10.1038/nmat3777.

[123] Karina Kulangara et al. “The Effect of Substrate Topography on Direct Reprogramming of Fibroblasts to Induced Neurons”. In: *Biomaterials* 35.20 (July 2014), pp. 5327–5336. ISSN: 0142-9612. DOI: 10.1016/j.biomaterials.2014.03.034.

[124] Constant Morez et al. “Enhanced Efficiency of Genetic Programming toward Cardiomyocyte Creation through Topographical Cues”. In: *Biomaterials* 70 (Nov. 2015), pp. 94–104. ISSN: 0142-9612. DOI: 10.1016/j.biomaterials.2015.07.063.

[125] Junren Sia et al. “Effect of Biophysical Cues on Reprogramming to Cardiomyocytes”. In: *Biomaterials* 103 (Oct. 2016), pp. 1–11. ISSN: 0142-9612. DOI: 10.1016/j.biomaterials.2016.06.034.

[126] Ross G. Harrison. “On the Stereotropism of Embryonic Cells”. en. In: *Science* 34.870 (Sept. 1911), pp. 279–281. ISSN: 0036-8075, 1095-9203. DOI: 10.1126/science.34.870.279.

[127] Wenting Zhao et al. “Nanoscale Manipulation of Membrane Curvature for Probing Endocytosis in Live Cells”. en. In: *Nature Nanotechnology* 12.8 (Aug. 2017), pp. 750–756. ISSN: 1748-3387. DOI: 10.1038/nnano.2017.98.

[128] Lindsey Hanson et al. “Vertical Nanopillars for in Situ Probing of Nuclear Mechanics in Adherent Cells”. en. In: *Nature Nanotechnology* 10.6 (June 2015), pp. 554–562. ISSN: 1748-3387. DOI: 10.1038/nnano.2015.88.

[129] Elisabetta Ada Cavalcanti-Adam et al. “Cell Spreading and Focal Adhesion Dynamics Are Regulated by Spacing of Integrin Ligands”. In: *Biophysical Journal* 92.8 (Apr. 2007), pp. 2964–2974. ISSN: 0006-3495. DOI: 10.1529/biophysj.106.089730.

[130] Elisabetta Ada Cavalcanti-Adam et al. “Cell Adhesion and Response to Synthetic Nanopatterned Environments by Steering Receptor Clustering and Spatial Location”. In: *HFSP Journal* 2.5 (Oct. 2008), pp. 276–285. ISSN: 1955-2068. DOI: 10.2976/1.2976662.

[131] Françoise Coussen et al. “Trimers of the Fibronectin Cell Adhesion Domain Localize to Actin Filament Bundles and Undergo Rearward Translocation”. en. In: *Journal of Cell Science* 115.12 (June 2002), pp. 2581–2590. ISSN: 0021-9533, 1477-9137.

[132] Sarah A. Fraser et al. “Sub-Micron and Nanoscale Feature Depth Modulates Alignment of Stromal Fibroblasts and Corneal Epithelial Cells in Serum-Rich and Serum-Free Media”. In: *Journal of biomedical materials research. Part A* 86.3 (Sept. 2008), pp. 725–735. ISSN: 1549-3296. DOI: 10.1002/jbm.a.31519.

[133] Andrew Hart et al. “Osteoprogenitor Response to Low-Adhesion Nanotopographies Originally Fabricated by Electron Beam Lithography”. en. In: *Journal of Materials Science: Materials in Medicine* 18.6 (June 2007), pp. 1211–1218. ISSN: 0957-4530, 1573-4838. DOI: 10.1007/s10856-007-0157-7.

[134] Matthew J. Dalby, Nikolaj Gadegaard, and Chris D.W. Wilkinson. “The Response of Fibroblasts to Hexagonal Nanotopography Fabricated by Electron Beam Lithography”. en. In: *Journal of Biomedical Materials Research Part A* 84A.4 (Mar. 2008), pp. 973–979. ISSN: 1552-4965. DOI: 10.1002/jbm.a.31409.

[135] Joseph L. Charest et al. “Hot Embossing for Micropatterned Cell Substrates”. In: *Biomaterials* 25.19 (Aug. 2004), pp. 4767–4775. ISSN: 0142-9612. DOI: 10.1016/j.biomaterials.2003.12.011.

[136] Ann M. Rajnicek, Louise E. Foubister, and Colin D. McCaig. “Alignment of Corneal and Lens Epithelial Cells by Co-Operative Effects of Substratum Topography and DC Electric Fields”. In: *Biomaterials* 29.13 (May 2008), pp. 2082–2095. ISSN: 0142-9612. DOI: 10.1016/j.biomaterials.2008.01.015.

[137] Chang Ho Seo et al. “The Effect of Substrate Microtopography on Focal Adhesion Maturation and Actin Organization via the RhoA/ROCK Pathway”. In: *Biomaterials* 32.36 (Dec. 2011), pp. 9568–9575. ISSN: 0142-9612. DOI: 10.1016/j.biomaterials.2011.08.077.

[138] Jesse K. Biehl et al. “Proliferation of Mouse Embryonic Stem Cell Progeny and the Spontaneous Contractile Activity of Cardiomyocytes Are Affected by Microtopography”. en. In: *Developmental Dynamics* 238.8 (Aug. 2009), pp. 1964–1973. ISSN: 1097-0177. DOI: 10.1002/dvdy.22030.

[139] Bibhu Ranjan Sarangi et al. “Coordination between Intra- and Extracellular Forces Regulates Focal Adhesion Dynamics”. In: *Nano Letters* 17.1 (Jan. 2017), pp. 399–406. ISSN: 1530-6984. DOI: 10.1021/acs.nanolett.6b04364.

[140] Matthew John Dalby et al. “Osteoprogenitor Response to Semi-Ordered and Random Nanotopographies”. In: *Biomaterials* 27.15 (May 2006), pp. 2980–2987. ISSN: 0142-9612. DOI: 10.1016/j.biomaterials.2006.01.010.

[141] W. A. Loesberg et al. “The Threshold at Which Substrate Nanogroove Dimensions May Influence Fibroblast Alignment and Adhesion”. In: *Biomaterials* 28.27 (Sept. 2007), pp. 3944–3951. ISSN: 0142-9612. DOI: 10.1016/j.biomaterials.2007.05.030.

[142] Chiung Wen Kuo, Di-Yen Chueh, and Peilin Chen. “Investigation of Size–Dependent Cell Adhesion on Nanostructured Interfaces”. In: *Journal of Nanobiotechnology* 12 (Dec. 2014). ISSN: 1477-3155. DOI: 10.1186/s12951-014-0054-4.

[143] Ha-Rim Seo et al. “Nanopillar Surface Topology Promotes Cardiomyocyte Differentiation through Cofilin-Mediated Cytoskeleton Rearrangement”. In: *ACS Applied Materials & Interfaces* 9.20 (May 2017), pp. 16803–16812. ISSN: 1944-8244. DOI: 10.1021/acsami.7b01555.

[144] Satoshi Fujita, Masahiro Ohshima, and Hiroo Iwata. “Time-Lapse Observation of Cell Alignment on Nanogrooved Patterns”. In: *Journal of the Royal Society Interface* 6.Suppl 3 (June 2009), S269–S277. ISSN: 1742-5689. DOI: 10.1098/rsif.2008.0428.focus.

[145] Jörg Albuschies and Viola Vogel. “The Role of Filopodia in the Recognition of Nanotopographies”. eng. In: *Scientific Reports* 3 (2013), p. 1658. ISSN: 2045-2322. DOI: 10.1038/srep01658.

[146] Laura E McNamara et al. “Investigation of the Limits of Nanoscale Filopodial Interactions”. In: *Journal of Tissue Engineering* 5 (May 2014). ISSN: 2041-7314. DOI: 10.1177/2041731414536177.

[147] Geoffrey M. Cooper. “Structure of the Plasma Membrane”. en. In: (2000).

[148] S. J. Singer and Garth L. Nicolson. “The Fluid Mosaic Model of the Structure of Cell Membranes”. en. In: *Science* 175.4023 (Feb. 1972), pp. 720–731. ISSN: 0036-8075, 1095-9203. DOI: 10.1126/science.175.4023.720.

[149] Donald M. Engelman. “Membranes Are More Mosaic than Fluid”. eng. In: *Nature* 438.7068 (Dec. 2005), pp. 578–580. ISSN: 1476-4687. DOI: 10.1038/nature04394.

[150] Gunnar von Heijne. “Membrane-Protein Topology”. en. In: *Nature Reviews Molecular Cell Biology* 7.12 (Dec. 2006), pp. 909–918. ISSN: 1471-0080. DOI: 10.1038/nrm2063.

[151] Sushmita Mukherjee and Frederick R. Maxfield. “Membrane Domains”. In: *Annual Review of Cell and Developmental Biology* 20.1 (Oct. 2004), pp. 839–866. ISSN: 1081-0706. DOI: 10.1146/annurev.cellbio.20.010403.095451.

[152] Kai Simons and Derek Toomre. “Lipid Rafts and Signal Transduction”. en. In: *Nature Reviews Molecular Cell Biology* 1.1 (Oct. 2000), pp. 31–39. ISSN: 1471-0080. DOI: 10.1038/35036052.

[153] D. A. Brown and E. London. “Functions of Lipid Rafts in Biological Membranes”. In: *Annual Review of Cell and Developmental Biology* 14.1 (Nov. 1998), pp. 111–136. ISSN: 1081-0706. DOI: 10.1146/annurev.cellbio.14.1.111.

[154] Garth L. Nicolson. “The Fluid—Mosaic Model of Membrane Structure: Still Relevant to Understanding the Structure, Function and Dynamics of Biological Membranes after More than 40years”. In: *Biochimica et Biophysica Acta (BBA) - Biomembranes*. Membrane Structure and Function: Relevance in the Cell’s Physiology, Pathology and Therapy 1838.6 (June 2014), pp. 1451–1466. ISSN: 0005-2736. DOI: 10.1016/j.bbamem.2013.10.019.

[155] Bodil Ramstedt and J. Peter Slotte. “Sphingolipids and the Formation of Sterol-Enriched Ordered Membrane Domains”. In: *Biochimica et Biophysica Acta (BBA) - Biomembranes*. Sphingolipids, Apoptosis and Disease 1758.12 (Dec. 2006), pp. 1945–1956. ISSN: 0005-2736. DOI: 10.1016/j.bbamem.2006.05.020.

[156] Thomas Harder et al. “Lipid Domain Structure of the Plasma Membrane Revealed by Patching of Membrane Components”. en. In: *The Journal of Cell Biology* 141.4 (May 1998), pp. 929–942. ISSN: 0021-9525, 1540-8140. DOI: 10.1083/jcb.141.4.929.

[157] Roxann J. Schroeder et al. “Cholesterol and Sphingolipid Enhance the Triton X-100 Insolubility of Glycosylphosphatidylinositol-Anchored Proteins by Promoting the Formation of Detergent-Insoluble Ordered Membrane Domains”. en. In: *Journal of Biological Chemistry* 273.2 (Sept. 1998), pp. 1150–1157. ISSN: 0021-9258, 1083-351X. DOI: 10.1074/jbc.273.2.1150.

[158] Kai Simons and Derek Toomre. “Lipid Rafts and Signal Transduction”. en. In: *Nature Reviews Molecular Cell Biology* 1.1 (Oct. 2000), pp. 31–39. ISSN: 1471-0080. DOI: 10.1038/35036052.

[159] Daniel Lingwood and Kai Simons. “Lipid Rafts As a Membrane-Organizing Principle”. en. In: *Science* 327.5961 (Jan. 2010), pp. 46–50. ISSN: 0036-8075, 1095-9203. DOI: 10.1126/science.1174621.

[160] Takeshi Harayama and Howard Riezman. “Understanding the Diversity of Membrane Lipid Composition”. en. In: *Nature Reviews Molecular Cell Biology* (Feb. 2018). ISSN: 1471-0080. DOI: 10.1038/nrm.2017.138.

[161] Harvey T. McMahon and Emmanuel Boucrot. “Membrane Curvature at a Glance”. en. In: *J Cell Sci* 128.6 (Mar. 2015), pp. 1065–1070. ISSN: 0021-9533, 1477-9137. DOI: 10.1242/jcs.114454.

[162] Harvey T. McMahon and Jennifer L. Gallop. “Membrane Curvature and Mechanisms of Dynamic Cell Membrane Remodelling”. eng. In: *Nature* 438.7068 (Dec. 2005), pp. 590–596. ISSN: 1476-4687. DOI: 10.1038/nature04396.

[163] Sina Sadeghi, Marcus Müller, and Richard L.C. Vink. “Raft Formation in Lipid Bilayers Coupled to Curvature”. In: *Biophysical Journal* 107.7 (Oct. 2014), pp. 1591–1600. ISSN: 0006-3495. DOI: 10.1016/j.bpj.2014.07.072.

[164] Raghuveer Parthasarathy, Cheng-han Yu, and Jay T. Groves. “Curvature-Modulated Phase Separation in Lipid Bilayer Membranes”. In: *Langmuir* 22.11 (May 2006), pp. 5095–5099. ISSN: 0743-7463. DOI: 10.1021/la060390o.

[165] Raghuveer Parthasarathy and Jay T. Groves. “Curvature and Spatial Organization in Biological Membranes”. en. In: *Soft Matter* 3.1 (Dec. 2006), pp. 24–33. ISSN: 1744-6848. DOI: 10.1039/B608631D.

[166] Shimrit Katz and Sefi Givli. *Curvature-Induced Spatial Ordering of Composition in Lipid Membranes*. en. https://www.hindawi.com/journals/cmmm/2017/7275131/. Research Article. 2017. DOI: 10.1155/2017/7275131.

[167] Arun Yethiraj and James C. Weisshaar. "Why Are Lipid Rafts Not Observed In Vivo?" In: *Biophysical Journal* 93.9 (Nov. 2007), pp. 3113–3119. ISSN: 0006-3495. DOI: 10.1529/biophysj.106.101931.

[168] Erdinc Sezgin et al. "The Mystery of Membrane Organization: Composition, Regulation and Roles of Lipid Rafts". en. In: *Nature Reviews Molecular Cell Biology* 18.6 (June 2017), pp. 361–374. ISSN: 1471-0080. DOI: 10.1038/nrm.2017.16.

[169] Guillaume Drin and Bruno Antonny. "Amphipathic Helices and Membrane Curvature". In: *FEBS Letters*. Frontiers in Membrane Biochemistry 584.9 (May 2010), pp. 1840–1847. ISSN: 0014-5793. DOI: 10.1016/j.febslet.2009.10.022.

[170] Felix Campelo, Harvey T. McMahon, and Michael M. Kozlov. "The Hydrophobic Insertion Mechanism of Membrane Curvature Generation by Proteins". In: *Biophysical Journal* 95.5 (Sept. 2008), pp. 2325–2339. ISSN: 0006-3495. DOI: 10.1529/biophysj.108.133173.

[171] Piers J. Walser et al. "Constitutive Formation of Caveolae in a Bacterium". In: *Cell* 150.4 (Aug. 2012), pp. 752–763. ISSN: 0092-8674. DOI: 10.1016/j.cell.2012.06.042.

[172] Mathieu Pinot et al. "Polyunsaturated Phospholipids Facilitate Membrane Deformation and Fission by Endocytic Proteins". en. In: *Science* 345.6197 (Aug. 2014), pp. 693–697. ISSN: 0036-8075, 1095-9203. DOI: 10.1126/science.1255288.

[173] Iris K. Jarsch, Frederic Daste, and Jennifer L. Gallop. "Membrane Curvature in Cell Biology: An Integration of Molecular Mechanisms". en. In: *J Cell Biol* 214.4 (Aug. 2016), pp. 375–387. ISSN: 0021-9525, 1540-8140. DOI: 10.1083/jcb.201604003.

[174] Kaspar D. Mossman et al. "Altered TCR Signaling from Geometrically Repatterned Immunological Synapses". en. In: *Science* 310.5751 (Nov. 2005), pp. 1191–1193. ISSN: 0036-8075, 1095-9203. DOI: 10.1126/science.1119238.

[175] Matthew J. Dalby et al. "Use of Nanotopography to Study Mechanotransduction in Fibroblasts – Methods and Perspectives". In: *European Journal of Cell Biology* 83.4 (Jan. 2004), pp. 159–169. ISSN: 0171-9335. DOI: 10.1078/0171-9335-00369.

[176] E. Martines et al. "A Parallel-Plate Flow Chamber to Study Initial Cell Adhesion on a Nanofeatured Surface". In: *IEEE Transactions on NanoBioscience* 3.2 (June 2004), pp. 90–95. ISSN: 1536-1241. DOI: 10.1109/TNB.2004.828268.

[177] Yijian Rao and Volker Haucke. "Membrane Shaping by the Bin/Amphiphysin/Rvs (BAR) Domain Protein Superfamily". en. In: *Cellular and Molecular Life Sciences* 68.24 (Dec. 2011), pp. 3983–3993. ISSN: 1420-682X, 1420-9071. DOI: 10.1007/s00018-011-0768-5.

[178] Mijo Simunovic et al. "When Physics Takes over: BAR Proteins and Membrane Curvature". In: *Trends in cell biology* 25.12 (Dec. 2015), pp. 780–792. ISSN: 0962-8924. DOI: 10.1016/j.tcb.2015.09.005.

[179] Kohji Takei et al. “Functional Partnership between Amphiphysin and Dynamin in Clathrin-Mediated Endocytosis”. en. In: *Nature Cell Biology* 1.1 (May 1999), pp. 33–39. ISSN: 1476-4679. DOI: 10.1038/9004.

[180] Emmanuel Boucrot et al. “Endophilin Marks and Controls a Clathrin-Independent Endocytic Pathway”. en. In: *Nature* 517.7535 (Jan. 2015), pp. 460–465. ISSN: 1476-4687. DOI: 10.1038/nature14067.

[181] William Mike Henne et al. “FCHo Proteins Are Nucleators of Clathrin-Mediated Endocytosis”. In: *Science (New York, N.Y.)* 328.5983 (June 2010), pp. 1281–1284. ISSN: 0036-8075. DOI: 10.1126/science.1188462.

[182] Sohail Ahmed, Wah Ing Goh, and Wenyu Bu. “I-BAR Domains, IRSp53 and Filopodium Formation”. In: *Seminars in Cell & Developmental Biology*. Membrane Curvature 21.4 (June 2010), pp. 350–356. ISSN: 1084-9521. DOI: 10.1016/j.semcdb.2009.11.008.

[183] Milos Galic et al. “External Push and Internal Pull Forces Recruit Curvature-Sensing N-BAR Domain Proteins to the Plasma Membrane”. en. In: *Nature Cell Biology* 14.8 (Aug. 2012), pp. 874–881. ISSN: 1476-4679. DOI: 10.1038/ncb2533.

[184] Matthew J Dalby et al. “Attempted Endocytosis of Nano-Environment Produced by Colloidal Lithography by Human Fibroblasts”. In: *Experimental Cell Research* 295.2 (May 2004), pp. 387–394. ISSN: 0014-4827. DOI: 10.1016/j.yexcr.2004.02.004.

[185] Caroline Moerke, Petra Mueller, and Barbara Nebe. “Attempted Caveolae-Mediated Phagocytosis of Surface-Fixed Micro-Pillars by Human Osteoblasts”. eng. In: *Biomaterials* 76 (Jan. 2016), pp. 102–114. ISSN: 1878-5905. DOI: 10.1016/j.biomaterials.2015.10.030.

[186] Changjin Huang et al. “The Role of Substrate Topography on the Cellular Uptake of Nanoparticles”. en. In: *Journal of Biomedical Materials Research Part B: Applied Biomaterials* 104.3 (Apr. 2016), pp. 488–495. ISSN: 1552-4981. DOI: 10.1002/jbm.b.33397.

[187] Melissa Crisp et al. “Coupling of the Nucleus and Cytoplasm: Role of the LINC Complex”. en. In: *J Cell Biol* 172.1 (Jan. 2006), pp. 41–53. ISSN: 0021-9525, 1540-8140. DOI: 10.1083/jcb.200509124.

[188] S. W. French et al. “Interaction of Intermediate Filaments with Nuclear Lamina and Cell Periphery”. In: *Electron Microscopy Reviews* 2.1 (Jan. 1989), pp. 17–51. ISSN: 0892-0354. DOI: 10.1016/0892-0354(89)90009-9.

[189] Martin W. Goldberg. “Nuclear Pore Complex Tethers to the Cytoskeleton”. In: *Seminars in Cell & Developmental Biology*. Nuclear pores 68 (Aug. 2017), pp. 52–58. ISSN: 1084-9521. DOI: 10.1016/j.semcdb.2017.06.017.

[190] Dipen Rajgor and Catherine M. Shanahan. “Nesprins: From the Nuclear Envelope and Beyond”. In: *Expert Reviews in Molecular Medicine* 15 (2013). ISSN: 1462-3994. DOI: 10.1017/erm.2013.6.

[191] Caterina Strambio-De-Castillia, Mario Niepel, and Michael P. Rout. “The Nuclear Pore Complex: Bridging Nuclear Transport and Gene Regulation”. en. In: *Nature Reviews Molecular Cell Biology* 11.7 (July 2010), pp. 490–501. ISSN: 1471-0080. DOI: 10.1038/nrm2928.

[192] Christian Lanctôt et al. “Dynamic Genome Architecture in the Nuclear Space: Regulation of Gene Expression in Three Dimensions”. en. In: *Nature Reviews Genetics* 8.2 (Feb. 2007), pp. 104–115. ISSN: 1471-0064. DOI: 10.1038/nrg2041.

[193] Karine Anselme et al. “Role of the Nucleus as a Sensor of Cell Environment Topography”. en. In: *Advanced Healthcare Materials* (), n/a–n/a. ISSN: 2192-2659. DOI: 10.1002/adhm.201701154.

[194] Spencer W. Crowder et al. “Material Cues as Potent Regulators of Epigenetics and Stem Cell Function”. English. In: *Cell Stem Cell* 18.1 (Jan. 2016), pp. 39–52. ISSN: 1934-5909, 1875-9777. DOI: 10.1016/j.stem.2015.12.012.

[195] Mark Fricker et al. “Interphase Nuclei of Many Mammalian Cell Types Contain Deep, Dynamic, Tubular Membrane-Bound Invaginations of the Nuclear Envelope”. In: *The Journal of Cell Biology* 136.3 (Feb. 1997), pp. 531–544. ISSN: 0021-9525.

[196] Karsten Gehrig, Rosemary B. Cornell, and Neale D. Ridgway. “Expansion of the Nucleoplasmic Reticulum Requires the Coordinated Activity of Lamins and CTP:Phosphocholine Cytidylyltransferase α”. en. In: *Molecular Biology of the Cell* 19.1 (Jan. 2008), pp. 237–247. ISSN: 1059-1524, 1939-4586. DOI: 10.1091/mbc.E07-02-0179.

[197] Selma Osmanagic-Myers, Thomas Dechat, and Roland Foisner. “Lamins at the Crossroads of Mechanosignaling”. en. In: *Genes & Development* 29.3 (Jan. 2015), pp. 225–237. ISSN: 0890-9369, 1549-5477. DOI: 10.1101/gad.255968.114.

[198] Yosef Gruenbaum et al. “The Nuclear Lamina Comes of Age”. eng. In: *Nature reviews. Molecular cell biology* 6.1 (Jan. 2005), pp. 21–31. ISSN: 1471-0072. DOI: 10.1038/nrm1550.

[199] Maria Polychronidou, Andrea Hellwig, and Jörg Grosshans. “Farnesylated Nuclear Proteins Kugelkern and Lamin Dm0 Affect Nuclear Morphology by Directly Interacting with the Nuclear Membrane”. In: *Molecular Biology of the Cell* 21.19 (Oct. 2010), pp. 3409–3420. ISSN: 1059-1524. DOI: 10.1091/mbc.E10-03-0230.

[200] Kin-Hoe Chow, Rachel E. Factor, and Katharine S. Ullman. “The Nuclear Envelope Environment and Its Cancer Connections”. en. In: *Nature Reviews Cancer* 12.3 (Mar. 2012), pp. 196–209. ISSN: 1474-1768. DOI: 10.1038/nrc3219.

[201] Patricia M. Davidson and Jan Lammerding. “Broken Nuclei – Lamins, Nuclear Mechanics, and Disease”. English. In: *Trends in Cell Biology* 24.4 (Apr. 2014), pp. 247–256. ISSN: 0962-8924, 1879-3088. DOI: 10.1016/j.tcb.2013.11.004.

[202] Ada L. Olins et al. “The LINC-Less Granulocyte Nucleus”. In: *European Journal of Cell Biology* 88.4 (Apr. 2009), pp. 203–214. ISSN: 0171-9335. DOI: 10.1016/j.ejcb.2008.10.001.

[203] J. David Pajerowski et al. “Physical Plasticity of the Nucleus in Stem Cell Differentiation”. en. In: *Proceedings of the National Academy of Sciences* 104.40 (Oct. 2007), pp. 15619–15624. ISSN: 0027-8424, 1091-6490. DOI: 10.1073/pnas.0702576104.

[204] Joe Swift et al. “Nuclear Lamin-A Scales with Tissue Stiffness and Enhances Matrix-Directed Differentiation”. en. In: *Science* 341.6149 (Aug. 2013), p. 1240104. ISSN: 0036-8075, 1095-9203. DOI: 10.1126/science.1240104.

[205] Laura E McNamara et al. “The Role of Microtopography in Cellular Mechanotransduction”. eng. In: *Biomaterials* 33.10 (Apr. 2012), pp. 2835–2847. ISSN: 1878-5905. DOI: 10.1016/j.biomaterials.2011.11.047.

[206] Guillaume Drin et al. “A General Amphipathic α-Helical Motif for Sensing Membrane Curvature”. en. In: *Nature Structural & Molecular Biology* 14.2 (Feb. 2007), pp. 138–146. ISSN: 1545-9985. DOI: 10.1038/nsmb1194.

[207] Frank Alber et al. “The Molecular Architecture of the Nuclear Pore Complex”. en. In: *Nature* 450.7170 (Nov. 2007), pp. 695–701. ISSN: 1476-4687. DOI: 10.1038/nature06405.

[208] Noémi Mészáros et al. “Nuclear Pore Basket Proteins Are Tethered to the Nuclear Envelope and Can Regulate Membrane Curvature”. In: *Developmental Cell* 33.3 (May 2015), pp. 285–298. ISSN: 1534-5807. DOI: 10.1016/j.devcel.2015.02.017.

[209] Benjamin Vollmer et al. “Dimerization and Direct Membrane Interaction of Nup53 Contribute to Nuclear Pore Complex Assembly”. en. In: *The EMBO Journal* 31.20 (Oct. 2012), pp. 4072–4084. ISSN: 0261-4189, 1460-2075. DOI: 10.1038/emboj.2012.256.

[210] Chris N. Goulbourne, Ashraf N. Malhas, and David J. Vaux. “The Induction of a Nucleoplasmic Reticulum by Prelamin A Accumulation Requires CTP:Phosphocholine Cytidylyltransferase-α”. eng. In: *Journal of Cell Science* 124.Pt 24 (Dec. 2011), pp. 4253–4266. ISSN: 1477-9137. DOI: 10.1242/jcs.091009.

[211] Marek M. Drozdz et al. “Formation of a Nucleoplasmic Reticulum Requires de Novo Assembly of Nascent Phospholipids and Shows Preferential Incorporation of Nascent Lamins”. En. In: *Scientific Reports* 7.1 (Aug. 2017), p. 7454. ISSN: 2045-2322. DOI: 10.1038/s41598-017-07614-w.

[212] Yuan Li et al. “Biophysical Regulation of Histone Acetylation in Mesenchymal Stem Cells”. In: *Biophysical Journal* 100.8 (Apr. 2011), pp. 1902–1909. ISSN: 0006-3495. DOI: 10.1016/j.bpj.2011.03.008.

[213] Maximiliano A. D’Angelo et al. “A Change In Nuclear Pore Complex Composition Regulates Cell Differentiation”. In: *Developmental Cell* 22.2 (Feb. 2012), pp. 446–458. ISSN: 1534-5807. DOI: 10.1016/j.devcel.2011.11.021.

[214] Maximiliano A. D’Angelo. “Nuclear Pore Complexes as Hubs for Gene Regulation”. In: *Nucleus* 9.1 (Jan. 2018), pp. 142–148. ISSN: 1949-1034. DOI: 10.1080/19491034.2017.1395542.

[215] Maya Capelson and Martin W Hetzer. “The Role of Nuclear Pores in Gene Regulation, Development and Disease”. In: *EMBO Reports* 10.7 (July 2009), pp. 697–705. ISSN: 1469-221X. DOI: 10.1038/embor.2009.147.

[216] Dylan M. Owen et al. “Quantitative Imaging of Membrane Lipid Order in Cells and Organisms”. en. In: *Nature Protocols* 7.1 (Jan. 2012), pp. 24–35. ISSN: 1750-2799. DOI: 10.1038/nprot.2011.419.

[217] Steve Paddock. “Confocal Reflection Microscopy: The "Other" Confocal Mode”. eng. In: *BioTechniques* 32.2 (Feb. 2002), pp. 274, 276–278. ISSN: 0736-6205.

[218] Claudia Müller and Kay Scheffler. “Five Advantages of Inverted Over Upright Microscopes in Industrial Applications”. en. In: (Mar. 2015).

[219] Trine Berthing et al. “Cell Membrane Conformation at Vertical Nanowire Array Interface Revealed by Fluorescence Imaging”. en. In: *Nanotechnology* 23.41 (Oct. 2012), p. 415102. ISSN: 0957-4484. DOI: 10.1088/0957-4484/23/41/415102.

[220] Bo Huang et al. “Three-Dimensional Super-Resolution Imaging by Stochastic Optical Reconstruction Microscopy”. en. In: *Science* 319.5864 (Aug. 2008), pp. 810–813. ISSN: 0036-8075, 1095-9203. DOI: 10.1126/science.1153529.

[221] Andrew M. Sydor et al. “Super-Resolution Microscopy: From Single Molecules to Supramolecular Assemblies”. In: *Trends in Cell Biology*. Special Issue: Quantitative Cell Biology 25.12 (Dec. 2015), pp. 730–748. ISSN: 0962-8924. DOI: 10.1016/j.tcb.2015.10.004.

[222] Samuel T. Hess et al. “Dynamic Clustered Distribution of Hemagglutinin Resolved at 40 Nm in Living Cell Membranes Discriminates between Raft Theories”. en. In: *Proceedings of the National Academy of Sciences* 104.44 (Oct. 2007), pp. 17370–17375. ISSN: 0027-8424, 1091-6490. DOI: 10.1073/pnas.0708066104.

[223] Anna Löschberger et al. “Super-Resolution Imaging Visualizes the Eightfold Symmetry of Gp210 Proteins around the Nuclear Pore Complex and Resolves the Central Channel with Nanometer Resolution”. en. In: *J Cell Sci* 125.3 (Feb. 2012), pp. 570–575. ISSN: 0021-9533, 1477-9137. DOI: 10.1242/jcs.098822.

[224] Stefan Bretschneider, Christian Eggeling, and Stefan W. Hell. “Breaking the Diffraction Barrier in Fluorescence Microscopy by Optical Shelving”. eng. In: *Physical Review Letters* 98.21 (May 2007), p. 218103. ISSN: 0031-9007. DOI: 10.1103/PhysRevLett.98.218103.

[225] Sara A. Jones et al. “Fast Three-Dimensional Super-Resolution Imaging of Live Cells”. In: *Nature methods* 8.6 (June 2011), pp. 499–508. ISSN: 1548-7091. DOI: 10.1038/nmeth.1605.

[226] Eric Betzig et al. “Imaging Intracellular Fluorescent Proteins at Nanometer Resolution”. en. In: *Science* 313.5793 (Sept. 2006), pp. 1642–1645. ISSN: 0036-8075, 1095-9203. DOI: 10.1126/science.1127344.

[227] Marie Versaevel et al. “Super-Resolution Microscopy Reveals LINC Complex Recruitment at Nuclear Indentation Sites”. en. In: *Scientific Reports* 4 (Dec. 2014), p. 7362. ISSN: 2045-2322. DOI: 10.1038/srep07362.

[228] Fan-Ching Chien et al. “Exploring the Formation of Focal Adhesions on Patterned Surfaces Using Super-Resolution Imaging”. en. In: *Small* 7.20 (Oct. 2011), pp. 2906–2913. ISSN: 1613-6829. DOI: 10.1002/smll.201100753.

[229] Yolanda Markaki et al. “The Potential of 3D-FISH and Super-Resolution Structured Illumination Microscopy for Studies of 3D Nuclear Architecture”. en. In: *BioEssays* 34.5 (May 2012), pp. 412–426. ISSN: 1521-1878. DOI: 10.1002/bies.201100176.

[230] Sina Wäldchen et al. “Light-Induced Cell Damage in Live-Cell Super-Resolution Microscopy”. In: *Scientific Reports* 5 (Oct. 2015), p. 15348. DOI: 10.1038/srep15348.

[231] Johnny Tam and David Merino. “Stochastic Optical Reconstruction Microscopy (STORM) in Comparison with Stimulated Emission Depletion (STED) and Other Imaging Methods”. eng. In: *Journal of Neurochemistry* 135.4 (Nov. 2015), pp. 643–658. ISSN: 1471-4159. DOI: 10.1111/jnc.13257.

[232] Fischer Joachim and Wegener Martin. “Three-dimensional Optical Laser Lithography beyond the Diffraction Limit”. In: *Laser & Photonics Reviews* 7.1 (Jan. 2013), pp. 22–44. ISSN: 1863-8880. DOI: 10.1002/lpor.201100046.

[233] Wolfgang Baumeister, Rudo Grimm, and Jochen Walz. “Electron Tomography of Molecules and Cells”. In: *Trends in Cell Biology* 9.2 (Feb. 1999), pp. 81–85. ISSN: 0962-8924. DOI: 10.1016/S0962-8924(98)01423-8.

[234] Waldemar Hällström et al. “Gallium Phosphide Nanowires as a Substrate for Cultured Neurons”. In: *Nano Letters* 7.10 (Oct. 2007), pp. 2960–2965. ISSN: 1530-6984. DOI: 10.1021/nl070728e.

[235] Joanna M. Łopacińska et al. “Cell Motility, Morphology, Viability and Proliferation in Response to Nanotopography on Silicon Black”. en. In: *Nanoscale* 4.12 (2012), pp. 3739–3745. DOI: 10.1039/C2NR11455K.

[236] Zhou Li et al. “Quantifying the Traction Force of a Single Cell by Aligned Silicon Nanowire Array”. In: *Nano Letters* 9.10 (Oct. 2009), pp. 3575–3580. ISSN: 1530-6984. DOI: 10.1021/nl901774m.

[237] G. E. Palade. “A Study of Fixation for Electron Microscopy”. eng. In: *The Journal of Experimental Medicine* 95.3 (Mar. 1952), pp. 285–298. ISSN: 0022-1007.

[238] J. G. Hirsch and M. E. Fedorko. “Ultrastructure of Human Leukocytes after Simultaneous Fixation with Glutaraldehyde and Osmium Tetroxide and "Post-fixation" in Uranyl Acetate”. eng. In: *The Journal of Cell Biology* 38.3 (Sept. 1968), pp. 615–627. ISSN: 0021-9525.

[239] B. A. Afzelius. “Section Staining for Electron Microscopy Using Tannic Acid as a Mordant: A Simple Method for Visualization of Glycogen and Collagen”. eng. In: *Microscopy Research and Technique* 21.1 (Mar. 1992), pp. 65–72. ISSN: 1059-910X. DOI: 10.1002/jemt.1070210110.

[240] P. K. Rivlin and P. A. Raymond. “Use of Osmium Tetroxide-Potassium Ferricyanide in Reconstructing Cells from Serial Ultrathin Sections”. eng. In: *Journal of Neuroscience Methods* 20.1 (May 1987), pp. 23–33. ISSN: 0165-0270.

[241] P. Böck and K. Gorgas. “Alkaline Lead Citrate: A Selective Stain for Glutaraldehyde Precipitates of Indolamines and Primary Catecholamines in Electron Microscopy”. eng. In: *Histochemistry* 47.1 (Apr. 1976), pp. 59–62. ISSN: 0301-5564.

[242] Mohammed Yusuf et al. “Staining and Embedding of Human Chromosomes for 3-d Serial Block-Face Scanning Electron Microscopy”. eng. In: *BioTechniques* 57.6 (Dec. 2014), pp. 302–307. ISSN: 1940-9818. DOI: 10.2144/000114236.

[243] Aldo Leal-Egaña et al. “Determination of Pore Size Distribution at the Cell-Hydrogel Interface”. In: *Journal of Nanobiotechnology* 9 (May 2011), p. 24. ISSN: 1477-3155. DOI: 10.1186/1477-3155-9-24.

[244] B. Baharloo, M. Textor, and D. M. Brunette. “Substratum Roughness Alters the Growth, Area, and Focal Adhesions of Epithelial Cells, and Their Proximity to Titanium Surfaces”. en. In: *Journal of Biomedical Materials Research Part A* 74A.1 (July 2005), pp. 12–22. ISSN: 1552-4965. DOI: 10.1002/jbm.a.30321.

[245] Günter Wrobel et al. “Transmission Electron Microscopy Study of the Cell–Sensor Interface”. en. In: *Journal of The Royal Society Interface* 5.19 (Feb. 2008), pp. 213–222. ISSN: 1742-5689, 1742-5662. DOI: 10.1098/rsif.2007.1094.

[246] Lindsey Hanson et al. “Characterization of the Cell–Nanopillar Interface by Transmission Electron Microscopy”. In: *Nano Letters* 12.11 (Nov. 2012), pp. 5815–5820. ISSN: 1530-6984. DOI: 10.1021/nl303163y.

[247] Anna Fendyur et al. “Formation of Essential Ultrastructural Interface between Cultured Hippocampal Cells and Gold Mushroom-Shaped MEA- Toward “IN-CELL” Recordings from Vertebrate Neurons”. English. In: *Frontiers in Neuroengineering* 4 (2011). ISSN: 1662-6443. DOI: 10.3389/fneng.2011.00014.

[248] Andreas Hoenger and J Richard McIntosh. “Probing the Macromolecular Organization of Cells by Electron Tomography”. In: *Current Opinion in Cell Biology.* Cell structure and dynamics 21.1 (Feb. 2009), pp. 89–96. ISSN: 0955-0674. DOI: 10.1016/j.ceb.2008.12.003.

[249] Martin F. Hohmann-Marriott et al. “Nanoscale 3D Cellular Imaging by Axial Scanning Transmission Electron Tomography”. en. In: *Nature Methods* 6.10 (Oct. 2009), pp. 729–731. ISSN: 1548-7105. DOI: 10.1038/nmeth.1367.

[250] Christopher J. Peddie and Lucy M. Collinson. “Exploring the Third Dimension: Volume Electron Microscopy Comes of Age”. eng. In: *Micron (Oxford, England: 1993)* 61 (June 2014), pp. 9–19. ISSN: 1878-4291. DOI: 10.1016/j.micron.2014.01.009.

[251] Clarissa Villinger et al. “FIB/SEM Tomography with TEM-like Resolution for 3D Imaging of High-Pressure Frozen Cells”. en. In: *Histochemistry and Cell Biology* 138.4 (Aug. 2012), pp. 549–556. ISSN: 0948-6143, 1432-119X. DOI: 10.1007/s00418-012-1020-6.

[252] Francesca Santoro et al. “Revealing the Cell–Material Interface with Nanometer Resolution by Focused Ion Beam/Scanning Electron Microscopy”. In: *ACS Nano* 11.8 (Aug. 2017), pp. 8320–8328. ISSN: 1936-0851. DOI: 10.1021/acsnano.7b03494.

[253] Rafał Wierzbicki et al. “Mapping the Complex Morphology of Cell Interactions with Nanowire Substrates Using FIB-SEM”. In: *PLoS ONE* 8.1 (Jan. 2013), e53307. DOI: 10.1371/journal.pone.0053307.

[254] Ciro Chiappini et al. “Biodegradable Nanoneedles for Localized Delivery of Nanoparticles in Vivo: Exploring the Biointerface”. ENG. In: *ACS nano* (Apr. 2015). ISSN: 1936-086X. DOI: 10.1021/acsnano.5b01490.

[255] Magnus Ø Olderøy et al. “Biochemical and Structural Characterization of Neocartilage Formed by Mesenchymal Stem Cells in Alginate Hydrogels”. en. In:

PLOS ONE 9.3 (Mar. 2014), e91662. ISSN: 1932-6203. DOI: 10.1371/journal.pone.0091662.

[256] Henrik Persson et al. "Fibroblasts Cultured on Nanowires Exhibit Low Motility, Impaired Cell Division, and DNA Damage". In: *Small (Weinheim an Der Bergstrasse, Germany)* 9.23 (Dec. 2013), pp. 4006–4016. ISSN: 1613-6810. DOI: 10.1002/smll.201300644.

[257] Yury S. Bykov et al. "Correlative Light and Electron Microscopy Methods for the Study of Virus-Cell Interactions". eng. In: *FEBS letters* 590.13 (July 2016), pp. 1877–1895. ISSN: 1873-3468. DOI: 10.1002/1873-3468.12153.

[258] Matthew R. G. Russell et al. "3D Correlative Light and Electron Microscopy of Cultured Cells Using Serial Blockface Scanning Electron Microscopy". en. In: *J Cell Sci* 130.1 (Jan. 2017), pp. 278–291. ISSN: 0021-9533, 1477-9137. DOI: 10.1242/jcs.188433.

[259] Anna Löschberger et al. "Correlative Super-Resolution Fluorescence and Electron Microscopy of the Nuclear Pore Complex with Molecular Resolution". en. In: *J Cell Sci* 127.20 (Oct. 2014), pp. 4351–4355. ISSN: 0021-9533, 1477-9137. DOI: 10.1242/jcs.156620.

[260] Kem A. Sochacki et al. "Endocytic Proteins Are Partitioned at the Edge of the Clathrin Lattice in Mammalian Cells". en. In: *Nature Cell Biology* 19.4 (Apr. 2017), pp. 352–361. ISSN: 1476-4679. DOI: 10.1038/ncb3498.

[261] Abraham J. Koster and Judith Klumperman. "Electron Microscopy in Cell Biology: Integrating Structure and Function". eng. In: *Nature Reviews. Molecular Cell Biology* Suppl (Sept. 2003), SS6–10. ISSN: 1471-0072.

[262] Rossana C. N. Melo et al. "Pre-Embedding Immunogold Labeling to Optimize Protein Localization at Subcellular Compartments and Membrane Microdomains of Leukocytes". en. In: *Nature Protocols* 9.10 (Oct. 2014), pp. 2382–2394. ISSN: 1750-2799. DOI: 10.1038/nprot.2014.163.

[263] Emma Evergren et al. "A Pre-Embedding Immunogold Approach for Detection of Synaptic Endocytic Proteins in Situ". eng. In: *Journal of Neuroscience Methods* 135.1-2 (May 2004), pp. 169–174. ISSN: 0165-0270. DOI: 10.1016/j.jneumeth.2003.12.010.

[264] Bruno M. Humbel et al. "Pre-embedding Immunolabeling for Electron Microscopy: An Evaluation of Permeabilization Methods and Markers". en. In: *Microscopy Research and Technique* 42.1 (July 1998), pp. 43–58. ISSN: 1097-0029. DOI: 10.1002/(SICI)1097-0029(19980701)42:1<43::AID-JEMT6>3.0.CO;2-S.

[265] Hong Yi et al. "A Novel Procedure for Pre-Embedding Double Immunogold–Silver Labeling at the Ultrastructural Level". en. In: *Journal of Histochemistry & Cytochemistry* 49.3 (Mar. 2001), pp. 279–283. ISSN: 0022-1554. DOI: 10.1177/002215540104900301.

[266] Mark H. Ellisman et al. "Picking Faces out of a Crowd: Genetic Labels for Identification of Proteins in Correlated Light and Electron Microscopy Imaging". eng. In: *Methods in Cell Biology* 111 (2012), pp. 139–155. ISSN: 0091-679X. DOI: 10.1016/B978-0-12-416026-2.00008-X.

[267] C. Hopkins et al. “Chimeric Molecules Employing Horseradish Peroxidase as Reporter Enzyme for Protein Localization in the Electron Microscope”. eng. In: *Methods in Enzymology* 327 (2000), pp. 35–45. ISSN: 0076-6879.

[268] Xiaokun Shu et al. “A Genetically Encoded Tag for Correlated Light and Electron Microscopy of Intact Cells, Tissues, and Organisms”. en. In: *PLOS Biology* 9.4 (Apr. 2011), e1001041. ISSN: 1545-7885. DOI: 10.1371/journal.pbio.1001041.

[269] Jeffrey D. Martell et al. “Engineered Ascorbate Peroxidase as a Genetically Encoded Reporter for Electron Microscopy”. en. In: *Nature Biotechnology* 30.11 (Nov. 2012), pp. 1143–1148. ISSN: 1546-1696. DOI: 10.1038/nbt.2375.

[270] Jeffrey D. Martell et al. “Electron Microscopy Using the Genetically Encoded APEX2 Tag in Cultured Mammalian Cells”. en. In: *Nature Protocols* 12.9 (Sept. 2017), pp. 1792–1816. ISSN: 1750-2799. DOI: 10.1038/nprot.2017.065.

[271] Eileen Gentleman et al. “Comparative Materials Differences Revealed in Engineered Bone as a Function of Cell-Specific Differentiation”. en. In: *Nature Materials* 8.9 (Sept. 2009), pp. 763–770. ISSN: 1476-4660. DOI: 10.1038/nmat2505.

[272] Sajanlal R. Panikkanvalappil et al. “Unraveling the Biomolecular Snapshots of Mitosis in Healthy and Cancer Cells Using Plasmonically-Enhanced Raman Spectroscopy”. In: *Journal of the American Chemical Society* 136.45 (Nov. 2014), pp. 15961–15968. ISSN: 0002-7863. DOI: 10.1021/ja506289u.

[273] James W. Chan et al. “Label-Free Separation of Human Embryonic Stem Cells and Their Cardiac Derivatives Using Raman Spectroscopy”. In: *Analytical Chemistry* 81.4 (Feb. 2009), pp. 1324–1331. ISSN: 0003-2700. DOI: 10.1021/ac801665m.

[274] Katherine J. I. Ember et al. “Raman Spectroscopy and Regenerative Medicine: A Review”. en. In: *npj Regenerative Medicine* 2.1 (May 2017), p. 12. ISSN: 2057-3995. DOI: 10.1038/s41536-017-0014-3.

[275] Charalambos Kallepitis et al. “Quantitative Volumetric Raman Imaging of Three Dimensional Cell Cultures”. en. In: *Nature Communications* 8 (Mar. 2017), p. 14843. ISSN: 2041-1723. DOI: 10.1038/ncomms14843.

[276] Holly J. Butler et al. “Using Raman Spectroscopy to Characterize Biological Materials”. eng. In: *Nature Protocols* 11.4 (Apr. 2016), pp. 664–687. ISSN: 1750-2799. DOI: 10.1038/nprot.2016.036.

[277] Richard J Colton et al. “Scanning Probe Microscopy”. In: *Current Opinion in Chemical Biology* 1.3 (Oct. 1997), pp. 370–377. ISSN: 1367-5931. DOI: 10.1016/S1367-5931(97)80076-2.

[278] David Alsteens et al. “Atomic Force Microscopy-Based Characterization and Design of Biointerfaces”. en. In: *Nature Reviews Materials* 2.5 (May 2017), p. 17008. ISSN: 2058-8437. DOI: 10.1038/natrevmats.2017.8.

[279] Jens Friedrichs, Jonne Helenius, and Daniel J. Muller. “Quantifying Cellular Adhesion to Extracellular Matrix Components by Single-Cell Force Spectroscopy”. en. In: *Nature Protocols* 5.7 (July 2010), pp. 1353–1361. ISSN: 1750-2799. DOI: 10.1038/nprot.2010.89.

[280] Clemens M. Franz and Daniel J. Müller. "Analyzing Focal Adhesion Structure by Atomic Force Microscopy". en. In: *Journal of Cell Science* 118.22 (Nov. 2005), pp. 5315–5323. ISSN: 0021-9533, 1477-9137. DOI: 10.1242/jcs.02653.

[281] Batirtze Prats-Mateu and Notburga Gierlinger. "Tip in–Light on: Advantages, Challenges, and Applications of Combining AFM and Raman Microscopy on Biological Samples". In: *Microscopy Research and Technique* 80.1 (Jan. 2017), pp. 30–40. ISSN: 1059-910X. DOI: 10.1002/jemt.22744.

[282] H. X. You et al. "Atomic Force Microscopy Imaging of Living Cells: A Preliminary Study of the Disruptive Effect of the Cantilever Tip on Cell Morphology". eng. In: *Ultramicroscopy* 82.1-4 (Feb. 2000), pp. 297–305. ISSN: 0304-3991.

[283] E. Henderson, P. G. Haydon, and D. S. Sakaguchi. "Actin Filament Dynamics in Living Glial Cells Imaged by Atomic Force Microscopy". eng. In: *Science (New York, N.Y.)* 257.5078 (Sept. 1992), pp. 1944–1946. ISSN: 0036-8075.

[284] Jan Seifert et al. "Comparison of Atomic Force Microscopy and Scanning Ion Conductance Microscopy for Live Cell Imaging". In: *Langmuir* (May 2015). ISSN: 0743-7463. DOI: 10.1021/acs.langmuir.5b01124.

[285] Johannes Rheinlaender et al. "Comparison of Scanning Ion Conductance Microscopy with Atomic Force Microscopy for Cell Imaging". In: *Langmuir* 27.2 (Jan. 2011), pp. 697–704. ISSN: 0743-7463. DOI: 10.1021/la103275y.

[286] André Meister et al. "FluidFM: Combining Atomic Force Microscopy and Nanofluidics in a Universal Liquid Delivery System for Single Cell Applications and Beyond". eng. In: *Nano Letters* 9.6 (June 2009), pp. 2501–2507. ISSN: 1530-6992. DOI: 10.1021/nl901384x.

[287] Orane Guillaume-Gentil et al. "Force-Controlled Manipulation of Single Cells: From AFM to FluidFM". eng. In: *Trends in Biotechnology* 32.7 (July 2014), pp. 381–388. ISSN: 1879-3096. DOI: 10.1016/j.tibtech.2014.04.008.

[288] Orane Guillaume-Gentil, Tomaso Zambelli, and Julia A. Vorholt. "Isolation of Single Mammalian Cells from Adherent Cultures by Fluidic Force Microscopy". eng. In: *Lab on a Chip* 14.2 (Jan. 2014), pp. 402–414. ISSN: 1473-0189. DOI: 10.1039/c3lc51174j.

[289] P. K. Hansma et al. "The Scanning Ion-Conductance Microscope". eng. In: *Science (New York, N.Y.)* 243.4891 (Feb. 1989), pp. 641–643. ISSN: 0036-8075.

[290] Y. E. Korchev et al. "Scanning Ion Conductance Microscopy of Living Cells". eng. In: *Biophysical Journal* 73.2 (Aug. 1997), pp. 653–658. ISSN: 0006-3495. DOI: 10.1016/S0006-3495(97)78100-1.

[291] Pavel Novak et al. "Nanoscale Live-Cell Imaging Using Hopping Probe Ion Conductance Microscopy". en. In: *Nature Methods* 6.4 (Apr. 2009), pp. 279–281. ISSN: 1548-7091. DOI: 10.1038/nmeth.1306.

[292] Andrew I. Shevchuk et al. "Imaging Proteins in Membranes of Living Cells by High-Resolution Scanning Ion Conductance Microscopy". en. In: *Angewandte Chemie International Edition* 45.14 (Mar. 2006), pp. 2212–2216. ISSN: 1521-3773. DOI: 10.1002/anie.200503915.

[293] Johannes Rheinlaender and Tilman E. Schäffer. "Image Formation, Resolution, and Height Measurement in Scanning Ion Conductance Microscopy". In: *Journal*

of Applied Physics 105.9 (May 2009), p. 094905. ISSN: 0021-8979. DOI: 10.1063/1.3122007.

[294] Nicolas Schierbaum et al. "Macro-SICM: A Scanning Ion Conductance Microscope for Large-Range Imaging". In: *Analytical Chemistry* 90.8 (Apr. 2018), pp. 5048–5054. ISSN: 0003-2700. DOI: 10.1021/acs.analchem.7b04764.

[295] Andrew I. Shevchuk et al. "An Alternative Mechanism of Clathrin-Coated Pit Closure Revealed by Ion Conductance Microscopy". In: *The Journal of Cell Biology* 197.4 (May 2012), pp. 499–508. ISSN: 0021-9525. DOI: 10.1083/jcb.201109130.

[296] Andrew Shevchuk et al. "Angular Approach Scanning Ion Conductance Microscopy". eng. In: *Biophysical Journal* 110.10 (May 2016), pp. 2252–2265. ISSN: 1542-0086. DOI: 10.1016/j.bpj.2016.04.017.

[297] Julia Gorelik et al. "Dynamic Assembly of Surface Structures in Living Cells". en. In: *Proceedings of the National Academy of Sciences* 100.10 (May 2003), pp. 5819–5822. ISSN: 0027-8424, 1091-6490. DOI: 10.1073/pnas.1030502100.

[298] Yuri E. Korchev et al. "Functional Localization of Single Active Ion Channels on the Surface of a Living Cell". en. In: *Nature Cell Biology* 2.9 (Sept. 2000), pp. 616–619. ISSN: 1465-7392. DOI: 10.1038/35023563.

[299] Julia Gorelik et al. "Ion Channels in Small Cells and Subcellular Structures Can Be Studied with a Smart Patch-Clamp System." In: *Biophysical Journal* 83.6 (Dec. 2002), pp. 3296–3303. ISSN: 0006-3495.

[300] Pavel Novak et al. "Nanoscale-Targeted Patch-Clamp Recordings of Functional Presynaptic Ion Channels". English. In: *Neuron* 79.6 (Sept. 2013), pp. 1067–1077. ISSN: 0896-6273. DOI: 10.1016/j.neuron.2013.07.012.

[301] Alexander R. Lyon et al. "Loss of T-Tubules and Other Changes to Surface Topography in Ventricular Myocytes from Failing Human and Rat Heart". en. In: *Proceedings of the National Academy of Sciences* 106.16 (Apr. 2009), pp. 6854–6859. ISSN: 0027-8424, 1091-6490. DOI: 10.1073/pnas.0809777106.

[302] Anamika Bhargava et al. "Super-Resolution Scanning Patch Clamp Reveals Clustering of Functional Ion Channels in Adult Ventricular MyocyteNovelty and Significance". en. In: *Circulation Research* 112.8 (Apr. 2013), pp. 1112–1120. ISSN: 0009-7330, 1524-4571. DOI: 10.1161/CIRCRESAHA.111.300445.

[303] Wim J. J. M. Scheenen and Tansu Celikel. "Nanophysiology: Bridging Synapse Ultrastructure, Biology, and Physiology Using Scanning Ion Conductance Microscopy". eng. In: *Synapse (New York, N.Y.)* 69.5 (May 2015), pp. 233–241. ISSN: 1098-2396. DOI: 10.1002/syn.21807.

[304] Yuji Nashimoto et al. "Nanoscale Imaging of an Unlabeled Secretory Protein in Living Cells Using Scanning Ion Conductance Microscopy". In: *Analytical Chemistry* 87.5 (Mar. 2015), pp. 2542–2545. ISSN: 0003-2700. DOI: 10.1021/ac5046388.

[305] Yanjun Zhang et al. "Spearhead Nanometric Field-Effect Transistor Sensors for Single-Cell Analysis". In: *ACS Nano* 10.3 (Mar. 2016), pp. 3214–3221. ISSN: 1936-0851. DOI: 10.1021/acsnano.5b05211.

[306] R. Proksch et al. “Imaging the Internal and External Pore Structure of Membranes in Fluid: TappingMode Scanning Ion Conductance Microscopy”. English. In: *Biophysical Journal* 71.4 (Oct. 1996), pp. 2155–2157. ISSN: 0006-3495. DOI: 10.1016/S0006-3495(96)79416-X.

[307] Matthias Böcker et al. “Scanning Ion Conductance Microscopy with Distance-Modulated Shear Force Control”. en. In: *Nanotechnology* 18.14 (2007), p. 145505. ISSN: 0957-4484. DOI: 10.1088/0957-4484/18/14/145505.

[308] J. Gorelik et al. “Scanning Surface Confocal Microscopy for Simultaneous Topographical and Fluorescence Imaging: Application to Single Virus-like Particle Entry into a Cell”. en. In: *Proceedings of the National Academy of Sciences* 99.25 (Oct. 2002), pp. 16018–16023. ISSN: 0027-8424, 1091-6490. DOI: 10.1073/pnas.252458399.

[309] Daniel Sánchez et al. “Noncontact Measurement of the Local Mechanical Properties of Living Cells Using Pressure Applied via a Pipette”. In: *Biophysical Journal* 95.6 (Sept. 2008), pp. 3017–3027. ISSN: 0006-3495. DOI: 10.1529/biophysj.108.129551.

[310] Johannes Rheinlaender and Tilman E. Schäffer. “Mapping the Mechanical Stiffness of Live Cells with the Scanning Ion Conductance Microscope”. en. In: *Soft Matter* 9.12 (Feb. 2013), pp. 3230–3236. ISSN: 1744-6848. DOI: 10.1039/C2SM27412D.

[311] Richard W. Clarke et al. “Low Stress Ion Conductance Microscopy of Sub-Cellular Stiffness †Electronic Supplementary Information (ESI) Available: Supplementary Methods and Expanded Data Presentations of Approach Curves, Stiffness Maps, and Nanopipet Stresses and Forces. See DOI: 10.1039/C6sm01106c Click Here for Additional Data File. Click Here for Additional Data File.” In: *Soft Matter* 12.38 (Oct. 2016), pp. 7953–7958. ISSN: 1744-683X. DOI: 10.1039/c6sm01106c.

[312] Richard W. Clarke et al. “Pipette–Surface Interaction: Current Enhancement and Intrinsic Force”. In: *Journal of the American Chemical Society* 135.1 (Jan. 2013), pp. 322–329. ISSN: 0002-7863. DOI: 10.1021/ja3094586.

[313] A. Belu et al. “Ultra-Thin Resin Embedding Method for Scanning Electron Microscopy of Individual Cells on High and Low Aspect Ratio 3D Nanostructures”. eng. In: *Journal of Microscopy* 263.1 (July 2016), pp. 78–86. ISSN: 1365-2818. DOI: 10.1111/jmi.12378.

[314] Elizabeth Schroeder-Reiter et al. “Focused Ion Beam (FIB) Combined with High Resolution Scanning Electron Microscopy: A Promising Tool for 3D Analysis of Chromosome Architecture”. eng. In: *Journal of Structural Biology* 165.2 (Feb. 2009), pp. 97–106. ISSN: 1095-8657. DOI: 10.1016/j.jsb.2008.10.002.

[315] C. Chiappini et al. “Biodegradable Silicon Nanoneedles Delivering Nucleic Acids Intracellularly Induce Localized in Vivo Neovascularization”. en. In: *Nature Materials* 14.5 (May 2015), pp. 532–539. ISSN: 1476-1122. DOI: 10.1038/nmat4249.

[316] T. Parasassi et al. “Phase Fluctuation in Phospholipid Membranes Revealed by Laurdan Fluorescence.” en. In: *Biophysical Journal* 57.6 (June 1990), p. 1179. DOI: 10.1016/S0006-3495(90)82637-0.

[317] Serge Mazeres, Farzad Fereidouni, and Etienne Joly. “Using Spectral Decomposition of the Signals from Laurdan-Derived Probes to Evaluate the Physical State of Membranes in Live Cells”. In: *F1000Research* 6 (Aug. 2017). ISSN: 2046-1402. DOI: 10.12688/f1000research.11577.2.

[318] Winfried Römer et al. “Shiga Toxin Induces Tubular Membrane Invaginations for Its Uptake into Cells”. en. In: *Nature* 450.7170 (Nov. 2007), pp. 670–675. ISSN: 1476-4687. DOI: 10.1038/nature05996.

[319] Katharina Gaus et al. “Integrin-Mediated Adhesion Regulates Membrane Order”. In: *The Journal of Cell Biology* 174.5 (Aug. 2006), pp. 725–734. ISSN: 0021-9525. DOI: 10.1083/jcb.200603034.

[320] Marie Versaevel, Thomas Grevesse, and Sylvain Gabriele. “Spatial Coordination between Cell and Nuclear Shape within Micropatterned Endothelial Cells”. en. In: *Nature Communications* 3 (Feb. 2012), p. 671. DOI: 10.1038/ncomms1668.

[321] Angus I. Lamond and William C. Earnshaw. “Structure and Function in the Nucleus”. en. In: *Science* 280.5363 (Apr. 1998), pp. 547–553. ISSN: 0036-8075, 1095-9203. DOI: 10.1126/science.280.5363.547.

[322] Emily Hatch and Martin Hetzer. “Breaching the Nuclear Envelope in Development and Disease”. In: *The Journal of Cell Biology* 205.2 (Apr. 2014), pp. 133–141. ISSN: 0021-9525. DOI: 10.1083/jcb.201402003.

[323] Tom Misteli. “Concepts in Nuclear Architecture”. en. In: *BioEssays* 27.5 (May 2005), pp. 477–487. ISSN: 1521-1878. DOI: 10.1002/bies.20226.

[324] Susan M. Gasser. “Visualizing Chromatin Dynamics in Interphase Nuclei”. eng. In: *Science (New York, N.Y.)* 296.5572 (May 2002), pp. 1412–1416. ISSN: 1095-9203. DOI: 10.1126/science.1067703.

[325] Thomas Cremer and Marion Cremer. “Chromosome Territories”. In: *Cold Spring Harbor Perspectives in Biology* 2.3 (Mar. 2010). ISSN: 1943-0264. DOI: 10.1101/cshperspect.a003889.

[326] Séverine Chambeyron and Wendy A. Bickmore. “Does Looping and Clustering in the Nucleus Regulate Gene Expression?” eng. In: *Current Opinion in Cell Biology* 16.3 (June 2004), pp. 256–262. ISSN: 0955-0674. DOI: 10.1016/j.ceb.2004.03.004.

[327] Thomas Cremer et al. “Chromosome Territories–a Functional Nuclear Landscape”. eng. In: *Current Opinion in Cell Biology* 18.3 (June 2006), pp. 307–316. ISSN: 0955-0674. DOI: 10.1016/j.ceb.2006.04.007.

[328] K. Laurence Jost, Bianca Bertulat, and M. Cristina Cardoso. “Heterochromatin and Gene Positioning: Inside, Outside, Any Side?” In: *Chromosoma* 121.6 (Dec. 2012), pp. 555–563. ISSN: 0009-5915. DOI: 10.1007/s00412-012-0389-2.

[329] Séverine Chambeyron and Wendy A. Bickmore. “Chromatin Decondensation and Nuclear Reorganization of the HoxB Locus upon Induction of Transcription”. eng. In: *Genes & Development* 18.10 (May 2004), pp. 1119–1130. ISSN: 0890-9369. DOI: 10.1101/gad.292104.

[330] Steven T. Kosak and Mark Groudine. “Form Follows Function: The Genomic Organization of Cellular Differentiation”. eng. In: *Genes & Development* 18.12 (June 2004), pp. 1371–1384. ISSN: 0890-9369. DOI: 10.1101/gad.1209304.

[331] Sung-Hye Park et al. “Ultrastructure of Human Embryonic Stem Cells and Spontaneous and Retinoic Acid-Induced Differentiating Cells”. In: *Ultrastructural Pathology* 28.4 (Jan. 2004), pp. 229–238. ISSN: 0191-3123. DOI: 10.1080/01913120490515595.

[332] Nick Gilbert et al. “Chromatin Architecture of the Human Genome: Gene-Rich Domains Are Enriched in Open Chromatin Fibers”. eng. In: *Cell* 118.5 (Sept. 2004), pp. 555–566. ISSN: 0092-8674. DOI: 10.1016/j.cell.2004.08.011.

[333] Robert Schneider and Rudolf Grosschedl. “Dynamics and Interplay of Nuclear Architecture, Genome Organization, and Gene Expression”. en. In: *Genes & Development* 21.23 (Jan. 2007), pp. 3027–3043. ISSN: 0890-9369, 1549-5477. DOI: 10.1101/gad.1604607.

[334] Claire Francastel et al. “Nuclear Compartmentalization and Gene Activity”. en. In: *Nature Reviews Molecular Cell Biology* 1.2 (Nov. 2000), pp. 137–143. ISSN: 1471-0080. DOI: 10.1038/35040083.

[335] Predrag Jevtić et al. “Sizing and Shaping the Nucleus: Mechanisms and Significance”. In: *Current opinion in cell biology* 0 (June 2014), pp. 16–27. ISSN: 0955-0674. DOI: 10.1016/j.ceb.2014.01.003.

[336] Dong-Hwee Kim et al. “Volume Regulation and Shape Bifurcation in the Cell Nucleus”. eng. In: *Journal of Cell Science* 128.18 (Sept. 2015), pp. 3375–3385. ISSN: 1477-9137. DOI: 10.1242/jcs.166330.

[337] Oswaldo A. Lozoya, Christopher L. Gilchrist, and Farshid Guilak. “Universally Conserved Relationships between Nuclear Shape and Cytoplasmic Mechanical Properties in Human Stem Cells”. en. In: *Scientific Reports* 6 (Mar. 2016), p. 23047. ISSN: 2045-2322. DOI: 10.1038/srep23047.

[338] Michael C. Keeling et al. “Actomyosin and Vimentin Cytoskeletal Networks Regulate Nuclear Shape, Mechanics and Chromatin Organization”. en. In: *Scientific Reports* 7.1 (July 2017), p. 5219. ISSN: 2045-2322. DOI: 10.1038/s41598-017-05467-x.

[339] Ashraf Malhas, Chris Goulbourne, and David J. Vaux. “The Nucleoplasmic Reticulum: Form and Function”. eng. In: *Trends in Cell Biology* 21.6 (June 2011), pp. 362–373. ISSN: 1879-3088. DOI: 10.1016/j.tcb.2011.03.008.

[340] Marek Mateusz Drozdz and David John Vaux. “Shared Mechanisms in Physiological and Pathological Nucleoplasmic Reticulum Formation”. In: *Nucleus* 8.1 (Oct. 2016), pp. 34–45. ISSN: 1949-1034. DOI: 10.1080/19491034.2016.1252893.

[341] Danielle M. Jorgens et al. “Deep Nuclear Invaginations Are Linked to Cytoskeletal Filaments – Integrated Bioimaging of Epithelial Cells in 3D Culture”. In: *Journal of Cell Science* 130.1 (Jan. 2017), pp. 177–189. ISSN: 0021-9533. DOI: 10.1242/jcs.190967.

[342] Wihelma Echevarría et al. “Regulation of Calcium Signals in the Nucleus by a Nucleoplasmic Reticulum”. eng. In: *Nature Cell Biology* 5.5 (May 2003), pp. 440–446. ISSN: 1465-7392. DOI: 10.1038/ncb980.

[343] Soňa Legartová et al. “Nuclear Structures Surrounding Internal Lamin Invaginations”. en. In: *Journal of Cellular Biochemistry* 115.3 (Mar. 2014), pp. 476–487. ISSN: 1097-4644. DOI: 10.1002/jcb.24681.

[344] J. Espada and M. Esteller. “Epigenetic Control of Nuclear Architecture”. In: *Cellular and Molecular Life Sciences* 64.4 (Feb. 2007), pp. 449–457. ISSN: 1420-682X. DOI: 10.1007/s00018-007-6358-x.

[345] Bilian Jin, Yajun Li, and Keith D. Robertson. “DNA Methylation: Superior or Subordinate in the Epigenetic Hierarchy?” eng. In: *Genes & Cancer* 2.6 (June 2011), pp. 607–617. ISSN: 1947-6027. DOI: 10.1177/1947601910393957.

[346] Thomas Clouaire and Irina Stancheva. “Methyl-CpG Binding Proteins: Specialized Transcriptional Repressors or Structural Components of Chromatin?” In: *Cellular and molecular life sciences : CMLS* 65.10 (May 2008), pp. 1509–1522. ISSN: 1420-682X. DOI: 10.1007/s00018-008-7324-y.

[347] Jesus Espada et al. “Human DNA Methyltransferase 1 Is Required for Maintenance of the Histone H3 Modification Pattern”. eng. In: *The Journal of Biological Chemistry* 279.35 (Aug. 2004), pp. 37175–37184. ISSN: 0021-9258. DOI: 10.1074/jbc.M404842200.

[348] John S. Choy et al. “DNA Methylation Increases Nucleosome Compaction and Rigidity”. In: *Journal of the American Chemical Society* 132.6 (Feb. 2010), pp. 1782–1783. ISSN: 0002-7863. DOI: 10.1021/ja910264z.

[349] Nick Gilbert et al. “DNA Methylation Affects Nuclear Organization, Histone Modifications, and Linker Histone Binding but Not Chromatin Compaction”. en. In: *J Cell Biol* 177.3 (May 2007), pp. 401–411. ISSN: 0021-9525, 1540-8140. DOI: 10.1083/jcb.200607133.

[350] Robert K. McGinty and Song Tan. “Nucleosome Structure and Function”. In: *Chemical Reviews* 115.6 (Mar. 2015), pp. 2255–2273. ISSN: 0009-2665. DOI: 10.1021/cr500373h.

[351] Philip J. J. Robinson and Daniela Rhodes. “Structure of the ’30 Nm’ Chromatin Fibre: A Key Role for the Linker Histone”. eng. In: *Current Opinion in Structural Biology* 16.3 (June 2006), pp. 336–343. ISSN: 0959-440X. DOI: 10.1016/j.sbi.2006.05.007.

[352] Andrew J. Bannister and Tony Kouzarides. “Regulation of Chromatin by Histone Modifications”. en. In: *Cell Research* 21.3 (Mar. 2011), pp. 381–395. ISSN: 1001-0602. DOI: 10.1038/cr.2011.22.

[353] Hisashi Tamaru et al. “Trimethylated Lysine 9 of Histone H3 Is a Mark for DNA Methylation in Neurospora Crassa”. eng. In: *Nature Genetics* 34.1 (May 2003), pp. 75–79. ISSN: 1061-4036. DOI: 10.1038/ng1143.

[354] T. R. Hebbes, A. W. Thorne, and C. Crane-Robinson. “A Direct Link between Core Histone Acetylation and Transcriptionally Active Chromatin”. eng. In: *The EMBO journal* 7.5 (May 1988), pp. 1395–1402. ISSN: 0261-4189.

[355] Kevin A. Janssen, Simone Sidoli, and Benjamin A. Garcia. “Recent Achievements in Characterizing the Histone Code and Approaches to Integrating Epigenomics and Systems Biology”. In: *Methods in enzymology* 586 (2017), pp. 359–378. ISSN: 0076-6879. DOI: 10.1016/bs.mie.2016.10.021.

[356] Raphaël Margueron and Danny Reinberg. “Chromatin Structure and the Inheritance of Epigenetic Information”. en. In: *Nature Reviews Genetics* 11.4 (Apr. 2010), pp. 285–296. ISSN: 1471-0064. DOI: 10.1038/nrg2752.

[357] Adrian Bird. “DNA Methylation Patterns and Epigenetic Memory”. en. In: *Genes & Development* 16.1 (Jan. 2002), pp. 6–21. ISSN: 0890-9369, 1549-5477. DOI: 10.1101/gad.947102.

[358] François Fuks. “DNA Methylation and Histone Modifications: Teaming up to Silence Genes”. eng. In: *Current Opinion in Genetics & Development* 15.5 (Oct. 2005), pp. 490–495. ISSN: 0959-437X. DOI: 10.1016/j.gde.2005.08.002.

[359] Shelley L Berger. “Histone Modifications in Transcriptional Regulation”. In: *Current Opinion in Genetics & Development* 12.2 (Apr. 2002), pp. 142–148. ISSN: 0959-437X. DOI: 10.1016/S0959-437X(02)00279-4.

[360] B. D. Strahl and C. D. Allis. “The Language of Covalent Histone Modifications”. eng. In: *Nature* 403.6765 (Jan. 2000), pp. 41–45. ISSN: 0028-0836. DOI: 10.1038/47412.

[361] T. Jenuwein and C. D. Allis. “Translating the Histone Code”. eng. In: *Science (New York, N.Y.)* 293.5532 (Aug. 2001), pp. 1074–1080. ISSN: 0036-8075. DOI: 10.1126/science.1063127.

[362] Bharat Burman et al. “Histone Modifications Predispose Genome Regions to Breakage and Translocation”. In: *Genes & Development* 29.13 (July 2015), pp. 1393–1402. ISSN: 0890-9369. DOI: 10.1101/gad.262170.115.

[363] Justin S. Becker, Dario Nicetto, and Kenneth S. Zaret. “H3K9me3-Dependent Heterochromatin: Barrier to Cell Fate Changes”. eng. In: *Trends in genetics: TIG* 32.1 (Jan. 2016), pp. 29–41. ISSN: 0168-9525. DOI: 10.1016/j.tig.2015.11.001.

[364] Daniele Canzio et al. “Chromodomain-Mediated Oligomerization of HP1 Suggests a Nucleosome Bridging Mechanism for Heterochromatin Assembly”. In: *Molecular cell* 41.1 (Jan. 2011), pp. 67–81. ISSN: 1097-2765. DOI: 10.1016/j.molcel.2010.12.016.

[365] A. H. Peters et al. “Loss of the Suv39h Histone Methyltransferases Impairs Mammalian Heterochromatin and Genome Stability”. eng. In: *Cell* 107.3 (Nov. 2001), pp. 323–337. ISSN: 0092-8674.

[366] Christopher R. Vakoc et al. “Histone H3 Lysine 9 Methylation and HP1γ Are Associated with Transcription Elongation through Mammalian Chromatin”. In: *Molecular Cell* 19.3 (Aug. 2005), pp. 381–391. ISSN: 1097-2765. DOI: 10.1016/j.molcel.2005.06.011.

[367] A. Taddei et al. “Reversible Disruption of Pericentric Heterochromatin and Centromere Function by Inhibiting Deacetylases”. eng. In: *Nature Cell Biology* 3.2 (Feb. 2001), pp. 114–120. ISSN: 1465-7392. DOI: 10.1038/35055010.

[368] Daniele Zink et al. “Transcription-Dependent Spatial Arrangements of CFTR and Adjacent Genes in Human Cell Nuclei”. en. In: *J Cell Biol* 166.6 (Sept. 2004), pp. 815–825. ISSN: 0021-9525, 1540-8140. DOI: 10.1083/jcb.200404107.

[369] Karen E. Brown et al. “Expression of α- and β-Globin Genes Occurs within Different Nuclear Domains in Haemopoietic Cells”. en. In: *Nature Cell Biology* 3.6 (June 2001), pp. 602–606. ISSN: 1476-4679. DOI: 10.1038/35078577.

[370] Erin M. Bank and Yosef Gruenbaum. “The Nuclear Lamina and Heterochromatin: A Complex Relationship”. eng. In: *Biochemical Society Transactions* 39.6 (Dec. 2011), pp. 1705–1709. ISSN: 1470-8752. DOI: 10.1042/BST20110603.

[371] Sarah M. Schreiner et al. “The Tethering of Chromatin to the Nuclear Envelope Supports Nuclear Mechanics”. en. In: *Nature Communications* 6 (June 2015), p. 7159. ISSN: 2041-1723. DOI: 10.1038/ncomms8159.

[372] Irina Solovei et al. “LBR and Lamin A/C Sequentially Tether Peripheral Heterochromatin and Inversely Regulate Differentiation”. In: *Cell* 152.3 (Jan. 2013), pp. 584–598. ISSN: 0092-8674. DOI: 10.1016/j.cell.2013.01.009.

[373] Andrey Poleshko and Richard A Katz. “Specifying Peripheral Heterochromatin during Nuclear Lamina Reassembly”. In: *Nucleus* 5.1 (Jan. 2014), pp. 32–39. ISSN: 1949-1034. DOI: 10.4161/nucl.28167.

[374] Justin Demmerle, Adam J. Koch, and James M. Holaska. “Emerin and Histone Deacetylase 3 (HDAC3) Cooperatively Regulate Expression and Nuclear Positions of MyoD, Myf5, and Pax7 Genes during Myogenesis”. In: *Chromosome research : an international journal on the molecular, supramolecular and evolutionary aspects of chromosome biology* 21.8 (Dec. 2013), pp. 765–779. ISSN: 0967-3849. DOI: 10.1007/s10577-013-9381-9.

[375] Raz Somech et al. “The Nuclear-Envelope Protein and Transcriptional Repressor LAP2β Interacts with HDAC3 at the Nuclear Periphery, and Induces Histone H4 Deacetylation”. en. In: *Journal of Cell Science* 118.17 (Sept. 2005), pp. 4017–4025. ISSN: 0021-9533, 1477-9137. DOI: 10.1242/jcs.02521.

[376] Eran Meshorer and Tom Misteli. “Chromatin in Pluripotent Embryonic Stem Cells and Differentiation”. en. In: *Nature Reviews Molecular Cell Biology* 7.7 (July 2006), pp. 540–546. ISSN: 1471-0072. DOI: 10.1038/nrm1938.

[377] Sol Efroni et al. “Global Transcription in Pluripotent Embryonic Stem Cells”. In: *Cell Stem Cell* 2.5 (May 2008), pp. 437–447. ISSN: 1934-5909. DOI: 10.1016/j.stem.2008.03.021.

[378] Shai Melcer et al. “Histone Modifications and Lamin A Regulate Chromatin Protein Dynamics in Early Embryonic Stem Cell Differentiation”. en. In: *Nature Communications* 3 (June 2012), p. 910. DOI: 10.1038/ncomms1915.

[379] Carol B. Ware et al. “Histone Deacetylase Inhibition Elicits an Evolutionarily Conserved Self-Renewal Program in Embryonic Stem Cells”. eng. In: *Cell Stem Cell* 4.4 (Apr. 2009), pp. 359–369. ISSN: 1875-9777. DOI: 10.1016/j.stem.2009.03.001.

[380] Amnon Buxboim et al. “Coordinated Increase of Nuclear Tension and Lamin-A with Matrix Stiffness Outcompetes Lamin-B Receptor That Favors Soft Tissue Phenotypes”. eng. In: *Molecular Biology of the Cell* 28.23 (Nov. 2017), pp. 3333–3348. ISSN: 1939-4586. DOI: 10.1091/mbc.E17-06-0393.

[381] Stephen D. Thorpe and David A. Lee. “Dynamic Regulation of Nuclear Architecture and Mechanics—a Rheostatic Role for the Nucleus in Tailoring Cellular

Mechanosensitivity". In: *Nucleus* 8.3 (Feb. 2017), pp. 287–300. ISSN: 1949-1034. DOI: 10.1080/19491034.2017.1285988.

[382] Matthew J. Dalby et al. "Nanomechanotransduction and Interphase Nuclear Organization Influence on Genomic Control". en. In: *Journal of Cellular Biochemistry* 102.5 (Dec. 2007), pp. 1234–1244. ISSN: 1097-4644. DOI: 10.1002/jcb.21354.

[383] Johanne Le Beyec et al. "Cell Shape Regulates Global Histone Acetylation in Human Mammary Epithelial Cells". In: *Experimental cell research* 313.14 (Aug. 2007), pp. 3066–3075. ISSN: 0014-4827. DOI: 10.1016/j.yexcr.2007.04.022.

[384] Li Luo et al. "The Nuclear Periphery of Embryonic Stem Cells Is a Transcriptionally Permissive and Repressive Compartment". en. In: *Journal of Cell Science* 122.20 (Oct. 2009), pp. 3729–3737. ISSN: 0021-9533, 1477-9137. DOI: 10.1242/jcs.052555.

[385] Karen N. Thatcher and Janine M. LaSalle. "Dynamic Changes in Histone H3 Lysine 9 Acetylation Localization Patterns during Neuronal Maturation Require MeCP2". In: *Epigenetics : official journal of the DNA Methylation Society* 1.1 (2006), pp. 24–31. ISSN: 1559-2294.

[386] J.M. Bridger et al. "Internal Lamin Structures within G1 Nuclei of Human Dermal Fibroblasts". In: *Journal of Cell Science* 104.2 (1993), pp. 297–306.

[387] Clayton T. McKee et al. "Topographic Modulation of the Orientation and Shape of Cell Nuclei and Their Influence on the Measured Elastic Modulus of Epithelial Cells". In: *Biophysical Journal* 101.9 (Nov. 2011), pp. 2139–2146. ISSN: 0006-3495. DOI: 10.1016/j.bpj.2011.09.042.

[388] Ekta Makhija, D. S. Jokhun, and G. V. Shivashankar. "Nuclear Deformability and Telomere Dynamics Are Regulated by Cell Geometric Constraints". en. In: *Proceedings of the National Academy of Sciences* 113.1 (Jan. 2016), E32–E40. ISSN: 0027-8424, 1091-6490. DOI: 10.1073/pnas.1513189113.

[389] Florent Badique et al. "Directing Nuclear Deformation on Micropillared Surfaces by Substrate Geometry and Cytoskeleton Organization". eng. In: *Biomaterials* 34.12 (Apr. 2013), pp. 2991–3001. ISSN: 1878-5905. DOI: 10.1016/j.biomaterials.2013.01.018.

[390] Yuan Li et al. "Biophysical Regulation of Histone Acetylation in Mesenchymal Stem Cells". In: *Biophysical Journal* 100.8 (Apr. 2011), pp. 1902–1909. ISSN: 0006-3495. DOI: 10.1016/j.bpj.2011.03.008.

[391] K. L. Goldenthal et al. "Postfixation Detergent Treatment for Immunofluorescence Suppresses Localization of Some Integral Membrane Proteins". eng. In: *The Journal of Histochemistry and Cytochemistry: Official Journal of the Histochemistry Society* 33.8 (Aug. 1985), pp. 813–820. ISSN: 0022-1554. DOI: 10.1177/33.8.3894499.

[392] Ulrike Schnell et al. "Immunolabeling Artifacts and the Need for Live-Cell Imaging". en. In: *Nature Methods* 9.2 (Feb. 2012), pp. 152–158. ISSN: 1548-7105. DOI: 10.1038/nmeth.1855.

[393] Amélie Béduer et al. “Engineering of Adult Human Neural Stem Cells Differentiation through Surface Micropatterning”. eng. In: *Biomaterials* 33.2 (Jan. 2012), pp. 504–514. ISSN: 1878-5905. DOI: 10.1016/j.biomaterials.2011.09.073.

[394] Huy Quang Le et al. “Mechanical Regulation of Transcription Controls Polycomb-Mediated Gene Silencing during Lineage Commitment”. en. In: *Nature Cell Biology* 18.8 (Aug. 2016), pp. 864–875. ISSN: 1476-4679. DOI: 10.1038/ncb3387.

[395] Arash Tajik et al. “Transcription Upregulation via Force-Induced Direct Stretching of Chromatin”. en. In: *Nature Materials* 15.12 (Dec. 2016), pp. 1287–1296. ISSN: 1476-4660. DOI: 10.1038/nmat4729.

[396] Stephen T. Spagnol and Kris Noel Dahl. “Spatially Resolved Quantification of Chromatin Condensation through Differential Local Rheology in Cell Nuclei Fluorescence Lifetime Imaging”. en. In: *PLOS ONE* 11.1 (Jan. 2016), e0146244. ISSN: 1932-6203. DOI: 10.1371/journal.pone.0146244.

[397] Gabriela Galiová et al. “Chromatin Changes Induced by Lamin A/C Deficiency and the Histone Deacetylase Inhibitor Trichostatin A”. eng. In: *European Journal of Cell Biology* 87.5 (May 2008), pp. 291–303. ISSN: 0171-9335. DOI: 10.1016/j.ejcb.2008.01.013.

[398] Le Cong et al. “Multiplex Genome Engineering Using CRISPR/Cas Systems”. en. In: *Science* (Jan. 2013), p. 1231143. ISSN: 0036-8075, 1095-9203. DOI: 10.1126/science.1231143.

[399] George A. Calin and Carlo M. Croce. “MicroRNA Signatures in Human Cancers”. en. In: *Nature Reviews Cancer* 6.11 (Nov. 2006), pp. 857–866. ISSN: 1474-1768. DOI: 10.1038/nrc1997.

[400] Daniela Karra and Ralf Dahm. “Transfection Techniques for Neuronal Cells”. en. In: *Journal of Neuroscience* 30.18 (May 2010), pp. 6171–6177. ISSN: 0270-6474, 1529-2401. DOI: 10.1523/JNEUROSCI.0183-10.2010.

[401] A. Rughetti et al. “Transfected Human Dendritic Cells to Induce Antitumor Immunity”. en. In: *Gene Therapy* 7.17 (Sept. 2000), pp. 1458–1466. ISSN: 1476-5462. DOI: 10.1038/sj.gt.3301266.

[402] Luis G. Villa-Diaz, Jose L. Garcia-Perez, and Paul H. Krebsbach. “Enhanced Transfection Efficiency of Human Embryonic Stem Cells by the Incorporation of DNA Liposomes in Extracellular Matrix”. In: *Stem Cells and Development* 19.12 (Dec. 2010), pp. 1949–1957. ISSN: 1547-3287. DOI: 10.1089/scd.2009.0505.

[403] David Benjamin Turitz Cox, Randall Jeffrey Platt, and Feng Zhang. “Therapeutic Genome Editing: Prospects and Challenges”. en. In: *Nature Medicine* 21.2 (Feb. 2015), pp. 121–131. ISSN: 1546-170X. DOI: 10.1038/nm.3793.

[404] Luigi Warren et al. “Highly Efficient Reprogramming to Pluripotency and Directed Differentiation of Human Cells with Synthetic Modified mRNA”. eng. In: *Cell Stem Cell* 7.5 (Nov. 2010), pp. 618–630. ISSN: 1875-9777. DOI: 10.1016/j.stem.2010.08.012.

[405] Frederick Anokye-Danso et al. “Highly Efficient miRNA-Mediated Reprogramming of Mouse and Human Somatic Cells to Pluripotency”. In: *Cell stem cell* 8.4 (Apr. 2011), pp. 376–388. ISSN: 1934-5909. DOI: 10.1016/j.stem.2011.03.001.

[406] Dohoon Kim et al. “Generation of Human Induced Pluripotent Stem Cells by Direct Delivery of Reprogramming Proteins”. eng. In: *Cell Stem Cell* 4.6 (June 2009), pp. 472–476. ISSN: 1875-9777. DOI: 10.1016/j.stem.2009.05.005.

[407] Martin P. Stewart et al. “*In Vitro* and *Ex Vivo* Strategies for Intracellular Delivery”. en. In: *Nature* 538.7624 (Oct. 2016), pp. 183–192. ISSN: 1476-4687. DOI: 10.1038/nature19764.

[408] William S. Trimble and Sergio Grinstein. “Barriers to the Free Diffusion of Proteins and Lipids in the Plasma Membrane”. In: *The Journal of Cell Biology* 208.3 (Feb. 2015), pp. 259–271. ISSN: 0021-9525. DOI: 10.1083/jcb.201410071.

[409] Bruce Alberts et al. “Transport into the Cell from the Plasma Membrane: Endocytosis”. en. In: (2002).

[410] Mark A. Kay. “State-of-the-Art Gene-Based Therapies: The Road Ahead”. eng. In: *Nature Reviews. Genetics* 12.5 (May 2011), pp. 316–328. ISSN: 1471-0064. DOI: 10.1038/nrg2971.

[411] Clare E. Thomas, Anja Ehrhardt, and Mark A. Kay. “Progress and Problems with the Use of Viral Vectors for Gene Therapy”. In: *Nature Reviews Genetics* 4.5 (May 2003), pp. 346–358. ISSN: 14710056, 14710064. DOI: 10.1038/nrg1066.

[412] Hao Yin et al. “Non-Viral Vectors for Gene-Based Therapy”. en. In: *Nature Reviews Genetics* 15.8 (Aug. 2014), pp. 541–555. ISSN: 1471-0064. DOI: 10.1038/nrg3763.

[413] Corey J. Bishop, Jayoung Kim, and Jordan J. Green. “Biomolecule Delivery to Engineer the Cellular Microenvironment for Regenerative Medicine”. In: *Annals of biomedical engineering* 42.7 (July 2014), pp. 1557–1572. ISSN: 0090-6964. DOI: 10.1007/s10439-013-0932-1.

[414] C. W. Pouton and L. W. Seymour. “Key Issues in Non-Viral Gene Delivery”. eng. In: *Advanced Drug Delivery Reviews* 46.1-3 (Mar. 2001), pp. 187–203. ISSN: 0169-409X.

[415] Moumita Ray et al. “Intracellular Delivery of Proteins by Nanocarriers”. eng. In: *Nanomedicine (London, England)* 12.8 (Apr. 2017), pp. 941–952. ISSN: 1748-6963. DOI: 10.2217/nnm-2016-0393.

[416] Andrew F. Adler and Kam W. Leong. “Emerging Links between Surface Nanotechnology and Endocytosis: Impact on Nonviral Gene Delivery”. In: *Nano today* 5.6 (Dec. 2010), pp. 553–569. ISSN: 1748-0132. DOI: 10.1016/j.nantod.2010.10.007.

[417] Irene Canton and Giuseppe Battaglia. “Endocytosis at the Nanoscale”. eng. In: *Chemical Society Reviews* 41.7 (Apr. 2012), pp. 2718–2739. ISSN: 1460-4744. DOI: 10.1039/c2cs15309b.

[418] Akin Akinc and Giuseppe Battaglia. “Exploiting Endocytosis for Nanomedicines”. In: *Cold Spring Harbor Perspectives in Biology* 5.11 (Nov. 2013). ISSN: 1943-0264. DOI: 10.1101/cshperspect.a016980.

[419] Cicily Chapman-Andresen. “The Early Days of Pinocytosis”. en. In: *Carlsberg Research Communications* 49.2 (Jan. 1984), pp. 179–186. ISSN: 0105-1938. DOI: 10.1007/BF02913945.

[420] Jet Phey Lim and Paul A. Gleeson. “Macropinocytosis: An Endocytic Pathway for Internalising Large Gulps”. en. In: *Immunology and Cell Biology* 89.8 (Nov. 2011), pp. 836–843. ISSN: 1440-1711. DOI: 10.1038/icb.2011.20.

[421] Gareth Bloomfield and Robert R. Kay. “Uses and Abuses of Macropinocytosis”. en. In: *J Cell Sci* 129.14 (July 2016), pp. 2697–2705. ISSN: 0021-9533, 1477-9137. DOI: 10.1242/jcs.176149.

[422] Arwyn Tomos Jones. “Macropinocytosis: Searching for an Endocytic Identity and Role in the Uptake of Cell Penetrating Peptides”. en. In: *Journal of Cellular and Molecular Medicine* 11.4 (July 2007), pp. 670–684. ISSN: 1582-4934. DOI: 10.1111/j.1582-4934.2007.00062.x.

[423] Sean D. Conner and Sandra L. Schmid. “Regulated Portals of Entry into the Cell”. en. In: *Nature* 422.6927 (Mar. 2003), pp. 37–44. ISSN: 1476-4687. DOI: 10.1038/nature01451.

[424] Jerome Gilleron et al. “Image-Based Analysis of Lipid Nanoparticle–Mediated siRNA Delivery, Intracellular Trafficking and Endosomal Escape”. En. In: *Nature Biotechnology* 31.7 (July 2013), p. 638. ISSN: 1546-1696. DOI: 10.1038/nbt.2612.

[425] Yizhou Dong et al. “Lipopeptide Nanoparticles for Potent and Selective siRNA Delivery in Rodents and Nonhuman Primates”. en. In: *Proceedings of the National Academy of Sciences* 111.11 (Mar. 2014), pp. 3955–3960. ISSN: 0027-8424, 1091-6490. DOI: 10.1073/pnas.1322937111.

[426] E. L. Racoosin and J. A. Swanson. “Macropinosome Maturation and Fusion with Tubular Lysosomes in Macrophages”. eng. In: *The Journal of Cell Biology* 121.5 (June 1993), pp. 1011–1020. ISSN: 0021-9525.

[427] L. J. Hewlett, A. R. Prescott, and C. Watts. “The Coated Pit and Macropinocytic Pathways Serve Distinct Endosome Populations”. en. In: *The Journal of Cell Biology* 124.5 (Mar. 1994), pp. 689–703. ISSN: 0021-9525, 1540-8140. DOI: 10.1083/jcb.124.5.689.

[428] Harvey T. McMahon and Emmanuel Boucrot. “Molecular Mechanism and Physiological Functions of Clathrin-Mediated Endocytosis”. en. In: *Nature Reviews Molecular Cell Biology* 12.8 (Aug. 2011), pp. 517–533. ISSN: 1471-0080. DOI: 10.1038/nrm3151.

[429] Mark Marsh and Ari Helenius. “Virus Entry: Open Sesame”. eng. In: *Cell* 124.4 (Feb. 2006), pp. 729–740. ISSN: 0092-8674. DOI: 10.1016/j.cell.2006.02.007.

[430] Joanna Rejman et al. “Size-Dependent Internalization of Particles via the Pathways of Clathrin- and Caveolae-Mediated Endocytosis.” In: *Biochemical Journal* 377.Pt 1 (Jan. 2004), pp. 159–169. ISSN: 0264-6021. DOI: 10.1042/BJ20031253.

[431] Marcelo Ehrlich et al. “Endocytosis by Random Initiation and Stabilization of Clathrin-Coated Pits”. eng. In: *Cell* 118.5 (Sept. 2004), pp. 591–605. ISSN: 0092-8674. DOI: 10.1016/j.cell.2004.08.017.

[432] Marko Kaksonen and Aurélien Roux. “Mechanisms of Clathrin-Mediated Endocytosis”. en. In: *Nature Reviews Molecular Cell Biology* (Feb. 2018). ISSN: 1471-0080. DOI: 10.1038/nrm.2017.132.

[433] Robert G. Parton and Kai Simons. “The Multiple Faces of Caveolae”. en. In: *Nature Reviews Molecular Cell Biology* 8.3 (Mar. 2007), pp. 185–194. ISSN: 1471-0080. DOI: 10.1038/nrm2122.

[434] Carsten Gram Hansen, Gillian Howard, and Benjamin J. Nichols. “Pacsin 2 Is Recruited to Caveolae and Functions in Caveolar Biogenesis”. eng. In: *Journal of Cell Science* 124.Pt 16 (Aug. 2011), pp. 2777–2785. ISSN: 1477-9137. DOI: 10.1242/jcs.084319.

[435] Robert G. Parton and Miguel A. del Pozo. “Caveolae as Plasma Membrane Sensors, Protectors and Organizers”. en. In: *Nature Reviews Molecular Cell Biology* 14.2 (Feb. 2013), pp. 98–112. ISSN: 1471-0072. DOI: 10.1038/nrm3512.

[436] Zhenjie Zhuang et al. “Is Caveolin Involved in Normal Proximal Tubule Function? Presence in Model PT Systems but Absence in Situ”. eng. In: *American Journal of Physiology. Renal Physiology* 300.1 (Jan. 2011), F199–206. ISSN: 1522-1466. DOI: 10.1152/ajprenal.00513.2010.

[437] Victor Rizzo et al. “Recruitment of Endothelial Caveolae into Mechanotransduction Pathways by Flow Conditioning in Vitro”. In: *American Journal of Physiology-Heart and Circulatory Physiology* 285.4 (Oct. 2003), H1720–H1729. ISSN: 0363-6135. DOI: 10.1152/ajpheart.00344.2002.

[438] Pierre Sens and Matthew S. Turner. “Budded Membrane Microdomains as Tension Regulators”. eng. In: *Physical Review. E, Statistical, Nonlinear, and Soft Matter Physics* 73.3 Pt 1 (Mar. 2006), p. 031918. ISSN: 1539-3755. DOI: 10.1103/PhysRevE.73.031918.

[439] Deepak K. Sharma et al. “The Glycosphingolipid, Lactosylceramide, Regulates Beta1-Integrin Clustering and Endocytosis”. eng. In: *Cancer Research* 65.18 (Sept. 2005), pp. 8233–8241. ISSN: 0008-5472. DOI: 10.1158/0008-5472.CAN-05-0803.

[440] Jane Sottile and Jennifer Chandler. “Fibronectin Matrix Turnover Occurs through a Caveolin-1-Dependent Process”. eng. In: *Molecular Biology of the Cell* 16.2 (Feb. 2005), pp. 757–768. ISSN: 1059-1524. DOI: 10.1091/mbc.E04-08-0672.

[441] Christine Hoffmann et al. “Caveolin Limits Membrane Microdomain Mobility and Integrin-Mediated Uptake of Fibronectin-Binding Pathogens”. eng. In: *Journal of Cell Science* 123.Pt 24 (Dec. 2010), pp. 4280–4291. ISSN: 1477-9137. DOI: 10.1242/jcs.064006.

[442] Eva-Maria Damm et al. “Clathrin- and Caveolin-1–Independent Endocytosis: Entry of Simian Virus 40 into Cells Devoid of Caveolae”. en. In: *The Journal of Cell Biology* 168.3 (Jan. 2005), pp. 477–488. ISSN: 0021-9525, 1540-8140. DOI: 10.1083/jcb.200407113.

[443] John R. Henley et al. “Dynamin-Mediated Internalization of Caveolae”. en. In: *The Journal of Cell Biology* 141.1 (Apr. 1998), pp. 85–99. ISSN: 0021-9525, 1540-8140. DOI: 10.1083/jcb.141.1.85.

[444] Satyajit Mayor and Richard E. Pagano. “Pathways of Clathrin-Independent Endocytosis”. en. In: *Nature Reviews Molecular Cell Biology* 8.8 (Aug. 2007), pp. 603–612. ISSN: 1471-0080. DOI: 10.1038/nrm2216.

[445] C. Lamaze et al. “Interleukin 2 Receptors and Detergent-Resistant Membrane Domains Define a Clathrin-Independent Endocytic Pathway”. eng. In: *Molecular Cell* 7.3 (Mar. 2001), pp. 661–671. ISSN: 1097-2765.

[446] Zhi-Jie Cheng et al. “Distinct Mechanisms of Clathrin-Independent Endocytosis Have Unique Sphingolipid Requirements”. en. In: *Molecular Biology of the Cell* 17.7 (Jan. 2006), pp. 3197–3210. ISSN: 1059-1524, 1939-4586. DOI: 10.1091/mbc.E05-12-1101.

[447] Satyajit Mayor, Robert G. Parton, and Julie G. Donaldson. “Clathrin-Independent Pathways of Endocytosis”. en. In: *Cold Spring Harbor Perspectives in Biology* 6.6 (Jan. 2014), a016758. ISSN: , 1943-0264. DOI: 10.1101/cshperspect.a016758.

[448] Oleg O. Glebov, Nicholas A. Bright, and Benjamin J. Nichols. “Flotillin-1 Defines a Clathrin-Independent Endocytic Pathway in Mammalian Cells”. en. In: *Nature Cell Biology* 8.1 (Jan. 2006), pp. 46–54. ISSN: 1476-4679. DOI: 10.1038/ncb1342.

[449] Grant P. Otto and Benjamin J. Nichols. “The Roles of Flotillin Microdomains – Endocytosis and Beyond”. en. In: *J Cell Sci* 124.23 (Dec. 2011), pp. 3933–3940. ISSN: 0021-9533, 1477-9137. DOI: 10.1242/jcs.092015.

[450] Richard Lundmark et al. “The GTPase-Activating Protein GRAF1 Regulates the CLIC/GEEC Endocytic Pathway”. English. In: *Current Biology* 18.22 (Nov. 2008), pp. 1802–1808. ISSN: 0960-9822. DOI: 10.1016/j.cub.2008.10.044.

[451] Tounsia Aït-Slimane et al. “Basolateral Internalization of GPI-Anchored Proteins Occurs via a Clathrin-Independent Flotillin-Dependent Pathway in Polarized Hepatic Cells”. en. In: *Molecular Biology of the Cell* 20.17 (Jan. 2009), pp. 3792–3800. ISSN: 1059-1524, 1939-4586. DOI: 10.1091/mbc.E09-04-0275.

[452] Crislyn D’Souza-Schorey et al. “ARF6 Targets Recycling Vesicles to the Plasma Membrane: Insights from an Ultrastructural Investigation”. In: *The Journal of Cell Biology* 140.3 (Feb. 1998), pp. 603–616. ISSN: 0021-9525.

[453] Harish Radhakrishna and Julie G. Donaldson. “ADP-Ribosylation Factor 6 Regulates a Novel Plasma Membrane Recycling Pathway”. en. In: *The Journal of Cell Biology* 139.1 (Oct. 1997), pp. 49–61. ISSN: 0021-9525, 1540-8140. DOI: 10.1083/jcb.139.1.49.

[454] Paul Saftig and Judith Klumperman. “Lysosome Biogenesis and Lysosomal Membrane Proteins: Trafficking Meets Function”. en. In: *Nature Reviews Molecular Cell Biology* 10.9 (Sept. 2009), pp. 623–635. ISSN: 1471-0080. DOI: 10.1038/nrm2745.

[455] Juan S. Bonifacino and Raul Rojas. “Retrograde Transport from Endosomes to the Trans-Golgi Network”. eng. In: *Nature Reviews. Molecular Cell Biology* 7.8 (Aug. 2006), pp. 568–579. ISSN: 1471-0072. DOI: 10.1038/nrm1985.

[456] J. L. a. N. Murk et al. “Endosomal Compartmentalization in Three Dimensions: Implications for Membrane Fusion”. en. In: *Proceedings of the National Academy of Sciences* 100.23 (Nov. 2003), pp. 13332–13337. ISSN: 0027-8424, 1091-6490. DOI: 10.1073/pnas.2232379100.

[457] Camilla Raiborg and Harald Stenmark. “The ESCRT Machinery in Endosomal Sorting of Ubiquitylated Membrane Proteins”. eng. In: *Nature* 458.7237 (Mar. 2009), pp. 445–452. ISSN: 1476-4687. DOI: 10.1038/nature07961.

[458] Gaurav Sahay et al. “Efficiency of siRNA Delivery by Lipid Nanoparticles Is Limited by Endocytic Recycling”. eng. In: *Nature Biotechnology* 31.7 (July 2013), pp. 653–658. ISSN: 1546-1696. DOI: 10.1038/nbt.2614.

[459] Hongtao Lv et al. “Toxicity of Cationic Lipids and Cationic Polymers in Gene Delivery”. eng. In: *Journal of Controlled Release: Official Journal of the Controlled Release Society* 114.1 (Aug. 2006), pp. 100–109. ISSN: 0168-3659. DOI: 10.1016/j.jconrel.2006.04.014.

[460] Toos Daemen et al. “Virosomes for Antigen and DNA Delivery”. eng. In: *Advanced Drug Delivery Reviews* 57.3 (Jan. 2005), pp. 451–463. ISSN: 0169-409X. DOI: 10.1016/j.addr.2004.09.005.

[461] Sarah Kube et al. “Fusogenic Liposomes as Nanocarriers for the Delivery of Intracellular Proteins”. In: *Langmuir* 33.4 (Jan. 2017), pp. 1051–1059. ISSN: 0743-7463. DOI: 10.1021/acs.langmuir.6b04304.

[462] Yoosoo Yang et al. “Virus-Mimetic Fusogenic Exosomes for Direct Delivery of Integral Membrane Proteins to Target Cell Membranes”. eng. In: *Advanced Materials (Deerfield Beach, Fla.)* 29.13 (Apr. 2017). ISSN: 1521-4095. DOI: 10.1002/adma.201605604.

[463] Sonja Van Meirvenne et al. “Efficient Genetic Modification of Murine Dendritic Cells by Electroporation with mRNA”. en. In: *Cancer Gene Therapy* 9.9 (Sept. 2002), pp. 787–797. ISSN: 1476-5500. DOI: 10.1038/sj.cgt.7700499.

[464] M. A. Barber. “A Technic for the Inoculation of Bacteria and Other Substances Into Living Cells”. en. In: *The Journal of Infectious Diseases* 8.3 (Apr. 1911), pp. 348–360. ISSN: 0022-1899. DOI: 10.1093/infdis/8.3.348.

[465] Van B. Lu et al. “Intranuclear Microinjection of DNA into Dissociated Adult Mammalian Neurons”. In: *Journal of Visualized Experiments : JoVE* 34 (Dec. 2009). ISSN: 1940-087X. DOI: 10.3791/1614.

[466] A. Adamo et al. “Microfluidic Jet Injection for Delivering Macromolecules into Cells”. In: *Journal of micromechanics and microengineering : structures, devices, and systems* 23 (Mar. 2013). ISSN: 0960-1317. DOI: 10.1088/0960-1317/23/3/035026.

[467] C. Chen et al. “Membrane Electroporation Theories: A Review”. eng. In: *Medical & Biological Engineering & Computing* 44.1-2 (Mar. 2006), pp. 5–14. ISSN: 0140-0118. DOI: 10.1007/s11517-005-0020-2.

[468] Azam Bolhassani, Afshin Khavari, and Zahra Orafa. “Electroporation – Advantages and Drawbacks for Delivery of Drug, Gene and Vaccine”. en. In: *Application of Nanotechnology in Drug Delivery* (2014). DOI: 10.5772/58376.

[469] K. H. Schoenbachk et al. “Ultrashort Electrical Pulses Open a New Gateway into Biological Cells”. In: *Conference Record of the Twenty-Sixth International Power Modulator Symposium, 2004 and 2004 High-Voltage Workshop.* May 2004, pp. 205–209. DOI: 10.1109/MODSYM.2004.1433545.

[470] J. Mark Meacham et al. “Physical Methods for Intracellular Delivery: Practical Aspects from Laboratory Use to Industrial-Scale Processing”. In: *Journal of laboratory automation* 19.1 (Feb. 2014), pp. 1–18. ISSN: 2211-0682. DOI: 10.1177/2211068213494388.

[471] Pouyan E. Boukany et al. “Nonendocytic Delivery of Lipoplex Nanoparticles into Living Cells Using Nanochannel Electroporation”. eng. In: *Advanced Healthcare Materials* 3.5 (May 2014), pp. 682–689. ISSN: 2192-2659. DOI: 10.1002/adhm.201300213.

[472] M. Tsukakoshi et al. “A Novel Method of DNA Transfection by Laser Microbeam Cell Surgery”. en. In: *Applied Physics B* 35.3 (Nov. 1984), pp. 135–140. ISSN: 0946-2171, 1432-0649. DOI: 10.1007/BF00697702.

[473] Yi-Chien Wu et al. “Massively Parallel Delivery of Large Cargo into Mammalian Cells with Light Pulses”. en. In: *Nature Methods* 12.5 (May 2015), pp. 439–444. ISSN: 1548-7105. DOI: 10.1038/nmeth.3357.

[474] Anthony Delalande et al. “Sonoporation: Mechanistic Insights and Ongoing Challenges for Gene Transfer”. eng. In: *Gene* 525.2 (Aug. 2013), pp. 191–199. ISSN: 1879-0038. DOI: 10.1016/j.gene.2013.03.095.

[475] I. Walev et al. “Delivery of Proteins into Living Cells by Reversible Membrane Permeabilization with Streptolysin-O”. eng. In: *Proceedings of the National Academy of Sciences of the United States of America* 98.6 (Mar. 2001), pp. 3185–3190. ISSN: 0027-8424. DOI: 10.1073/pnas.051429498.

[476] I. Hapala. “Breaking the Barrier: Methods for Reversible Permeabilization of Cellular Membranes”. eng. In: *Critical Reviews in Biotechnology* 17.2 (1997), pp. 105–122. ISSN: 0738-8551. DOI: 10.3109/07388559709146609.

[477] Sandra T. Cooper and Paul L. McNeil. “Membrane Repair: Mechanisms and Pathophysiology”. eng. In: *Physiological Reviews* 95.4 (Oct. 2015), pp. 1205–1240. ISSN: 1522-1210. DOI: 10.1152/physrev.00037.2014.

[478] Armon Sharei et al. “A Vector-Free Microfluidic Platform for Intracellular Delivery”. en. In: *Proceedings of the National Academy of Sciences* 110.6 (Feb. 2013), pp. 2082–2087. ISSN: 0027-8424, 1091-6490. DOI: 10.1073/pnas.1218705110.

[479] Tao Geng et al. “Flow-through Electroporation Based on Constant Voltage for Large-Volume Transfection of Cells”. eng. In: *Journal of Controlled Release: Official Journal of the Controlled Release Society* 144.1 (May 2010), pp. 91–100. ISSN: 1873-4995. DOI: 10.1016/j.jconrel.2010.01.030.

[480] Pouyan E. Boukany et al. “Nanochannel Electroporation Delivers Precise Amounts of Biomolecules into Living Cells”. en. In: *Nature Nanotechnology* 6.11 (Nov. 2011), pp. 747–754. ISSN: 1748-3395. DOI: 10.1038/nnano.2011.164.

[481] Yanxiang Deng et al. “Intracellular Delivery of Nanomaterials via an Inertial Microfluidic Cell Hydroporator”. In: *Nano Letters* (Mar. 2018). ISSN: 1530-6984. DOI: 10.1021/acs.nanolett.8b00704.

[482] Sung Woong Han et al. “A Molecular Delivery System by Using AFM and Nanoneedle”. In: *Biosensors and Bioelectronics*. Selected Papers from the Eighth World Congress on Biosensors, Part II 20.10 (Apr. 2005), pp. 2120–2125. ISSN: 0956-5663. DOI: 10.1016/j.bios.2004.08.023.

[483] Sung-Woong Han et al. “High-Efficiency DNA Injection into a Single Human Mesenchymal Stem Cell Using a Nanoneedle and Atomic Force Microscopy”. In: *Nanomedicine: Nanotechnology, Biology and Medicine* 4.3 (Sept. 2008), pp. 215–225. ISSN: 1549-9634. DOI: 10.1016/j.nano.2008.03.005.

[484] Quan Qing et al. “Free-Standing Kinked Nanowire Transistor Probes for Targeted Intracellular Recording in Three Dimensions”. en. In: *Nature Nanotechnology* 9.2 (Feb. 2014), pp. 142–147. ISSN: 1748-3387. DOI: 10.1038/nnano.2013.273.

[485] Alex K. Shalek et al. “Vertical Silicon Nanowires as a Universal Platform for Delivering Biomolecules into Living Cells”. In: *Proceedings of the National Academy of Sciences of the United States of America* 107.5 (Feb. 2010), pp. 1870–1875. ISSN: 0027-8424. DOI: 10.1073/pnas.0909350107.

[486] Rosanna La Rocca et al. “Out-of-Plane Plasmonic Antennas for Raman Analysis in Living Cells”. en. In: *Small* 11.36 (Sept. 2015), pp. 4632–4637. ISSN: 1613-6829. DOI: 10.1002/smll.201500891.

[487] Alexander M. Xu et al. “Quantification of Nanowire Penetration into Living Cells”. en. In: *Nature Communications* 5 (Apr. 2014). DOI: 10.1038/ncomms4613.

[488] Ren Liu et al. “High Density Individually Addressable Nanowire Arrays Record Intracellular Activity from Primary Rodent and Human Stem Cell Derived Neurons”. eng. In: *Nano Letters* 17.5 (May 2017), pp. 2757–2764. ISSN: 1530-6992. DOI: 10.1021/acs.nanolett.6b04752.

[489] Alex K. Shalek et al. “Nanowire-Mediated Delivery Enables Functional Interrogation of Primary Immune Cells: Application to the Analysis of Chronic Lymphocytic Leukemia”. In: *Nano Letters* 12.12 (Dec. 2012), pp. 6498–6504. ISSN: 1530-6984. DOI: 10.1021/nl3042917.

[490] Jose E. Perez, Timothy Ravasi, and Jürgen Kosel. “Mesenchymal Stem Cells Cultured on Magnetic Nanowire Substrates”. en. In: *Nanotechnology* 28.5 (2017), p. 055703. ISSN: 0957-4484. DOI: 10.1088/1361-6528/aa52a3.

[491] Timothy E. McKnight et al. “Tracking Gene Expression after DNA Delivery Using Spatially Indexed Nanofiber Arrays”. In: *Nano Letters* 4.7 (July 2004), pp. 1213–1219. ISSN: 1530-6984. DOI: 10.1021/nl049504b.

[492] Woong Kim et al. “Interfacing Silicon Nanowires with Mammalian Cells”. In: *Journal of the American Chemical Society* 129.23 (June 2007), pp. 7228–7229. ISSN: 0002-7863. DOI: 10.1021/ja071456k.

[493] Xi Xie et al. “Nanostraw–Electroporation System for Highly Efficient Intracellular Delivery and Transfection”. In: *ACS Nano* 7.5 (May 2013), pp. 4351–4358. ISSN: 1936-0851. DOI: 10.1021/nn400874a.

[494] Jingjing Pan et al. “Stimulation of Gene Transfection by Silicon Nanowire Arrays Modified with Polyethylenimine”. eng. In: *ACS applied materials & interfaces* 6.16 (Aug. 2014), pp. 14391–14398. ISSN: 1944-8252. DOI: 10.1021/am5036626.

[495] Chan Miu Shan and Lo Pik Kwan. “Nanoneedle-Assisted Delivery of Site-Selective Peptide-Functionalized DNA Nanocages for Targeting Mitochondria and Nuclei”. In: *Small* 10.7 (Apr. 2014), pp. 1255–1260. ISSN: 1613-6810. DOI: 10.1002/smll.201302993.

[496] Alexander M. Xu et al. “Direct Intracellular Delivery of Cell-Impermeable Probes of Protein Glycosylation by Using Nanostraws”. en. In: *ChemBioChem* 18.7 (Apr. 2017), pp. 623–628. ISSN: 1439-7633. DOI: 10.1002/cbic.201600689.

[497] Sara Bonde et al. “Exploring Arrays of Vertical One-Dimensional Nanostructures for Cellular Investigations”. eng. In: *Nanotechnology* 25.36 (Sept. 2014), p. 362001. ISSN: 1361-6528. DOI: 10.1088/0957-4484/25/36/362001.

[498] Jules J. VanDersarl, Alexander M. Xu, and Nicholas A. Melosh. “Nanostraws for Direct Fluidic Intracellular Access”. In: *Nano Letters* 12.8 (Aug. 2012), pp. 3881–3886. ISSN: 1530-6984. DOI: 10.1021/nl204051v.

[499] Elad Peer et al. “Hollow Nanoneedle Array and Its Utilization for Repeated Administration of Biomolecules to the Same Cells”. In: *ACS Nano* 6.6 (June 2012), pp. 4940–4946. ISSN: 1936-0851. DOI: 10.1021/nn300443h.

[500] Heon Jin Choi. “Vapor-Liquid-Solid Growth of Semiconductor Nanowires”. English. In: *Semiconductor Nanostructures for Optoelectronic Devices: Processing, Characterization and Applications* (Oct. 2012). DOI: 10.1007/978-3-642-22480-5\%00201.

[501] Hong Jin Fan, Peter Werner, and Margit Zacharias. “Semiconductor Nanowires: From Self-Organization to Patterned Growth”. eng. In: *Small (Weinheim an Der Bergstrasse, Germany)* 2.6 (June 2006), pp. 700–717. ISSN: 1613-6829. DOI: 10.1002/smll.200500495.

[502] Ciro Chiappini et al. “Biodegradable Porous Silicon Barcode Nanowires with Defined Geometry”. en. In: *Advanced Functional Materials* 20.14 (July 2010), pp. 2231–2239. ISSN: 1616-3028. DOI: 10.1002/adfm.201000360.

[503] Y. Q. Fu et al. “Deep Reactive Ion Etching as a Tool for Nanostructure Fabrication”. In: *Journal of Vacuum Science & Technology B: Microelectronics and Nanometer Structures Processing, Measurement, and Phenomena* 27.3 (May 2009), pp. 1520–1526. ISSN: 1071-1023. DOI: 10.1116/1.3065991.

[504] SungWoong Han et al. “Gene Expression Using an Ultrathin Needle Enabling Accurate Displacement and Low Invasiveness”. In: *Biochemical and Biophysical Research Communications* 332.3 (July 2005), pp. 633–639. ISSN: 0006-291X. DOI: 10.1016/j.bbrc.2005.04.059.

[505] Ying Zhang et al. “Replica Molding of High-Aspect-Ratio Polymeric Nanopillar Arrays with High Fidelity”. In: *Langmuir* 22.20 (Sept. 2006), pp. 8595–8601. ISSN: 0743-7463. DOI: 10.1021/la061372+.

[506] Allon I. Hochbaum et al. “Controlled Growth of Si Nanowire Arrays for Device Integration”. In: *Nano Letters* 5.3 (Mar. 2005), pp. 457–460. ISSN: 1530-6984. DOI: 10.1021/nl047990x.

[507] C. Chiappini and C. Almeida. “8 - Silicon Nanoneedles for Drug Delivery”. In: *Semiconducting Silicon Nanowires for Biomedical Applications*. Ed. by Jeffery L. Coffer. Woodhead Publishing, 2014, pp. 144–167. ISBN: 978-0-85709-766-8. DOI: 10.1533/9780857097712.2.144.

[508] D. Choi et al. “In Vitro Detection of Neural Activity with Vertically Grown Single Platinum Nanowire”. In: *2009 IEEE 22nd International Conference on Mi-*

cro Electro Mechanical Systems. Jan. 2009, pp. 360–362. DOI: 10.1109/MEMSYS.2009.4805393.

[509] Yuan Yu, Liangzhuan Wu, and Jinfang Zhi. "Diamond Nanowires: Fabrication, Structure, Properties, and Applications". eng. In: *Angewandte Chemie (International Ed. in English)* 53.52 (Dec. 2014), pp. 14326–14351. ISSN: 1521-3773. DOI: 10.1002/anie.201310803.

[510] Trine Berthing et al. "Intact Mammalian Cell Function on Semiconductor Nanowire Arrays: New Perspectives for Cell-Based Biosensing". en. In: *Small* 7.5 (Mar. 2011), pp. 640–647. ISSN: 1613-6829. DOI: 10.1002/smll.201001642.

[511] Prashant Sharma et al. "Efficient Intracellular Delivery of Biomacromolecules Employing Clusters of Zinc Oxide Nanowires". en. In: *Nanoscale* 9.40 (2017), pp. 15371–15378. DOI: 10.1039/C7NR05219G.

[512] Florian Mumm et al. "A Transparent Nanowire-Based Cell Impalement Device Suitable for Detailed Cell–Nanowire Interaction Studies". en. In: *Small* 9.2 (Jan. 2013), pp. 263–272. ISSN: 1613-6829. DOI: 10.1002/smll.201201314.

[513] Suet P. Low and Nicolas H. Voelcker. "Biocompatibility of Porous Silicon". en. In: *Handbook of Porous Silicon*. Springer, Cham, 2014, pp. 1–13. ISBN: 978-3-319-04508-5. DOI: 10.1007/978-3-319-04508-5_38-1.

[514] R. Herino et al. "Porosity and Pore Size Distributions of Porous Silicon Layers". en. In: *Journal of The Electrochemical Society* 134.8 (Jan. 1987), pp. 1994–2000. ISSN: 0013-4651, 1945-7111. DOI: 10.1149/1.2100805.

[515] Emily J. Anglin et al. "Porous Silicon in Drug Delivery Devices and Materials". In: *Advanced drug delivery reviews* 60.11 (Aug. 2008), pp. 1266–1277. ISSN: 0169-409X. DOI: 10.1016/j.addr.2008.03.017.

[516] Timothy E. McKnight et al. "Intracellular Integration of Synthetic Nanostructures with Viable Cells for Controlled Biochemical Manipulation". en. In: *Nanotechnology* 14.5 (May 2003), p. 551. ISSN: 0957-4484. DOI: 10.1088/0957-4484/14/5/313.

[517] Sara Bonde et al. "Tuning InAs Nanowire Density for HEK293 Cell Viability, Adhesion, and Morphology: Perspectives for Nanowire-Based Biosensors". In: *ACS Applied Materials & Interfaces* 5.21 (Nov. 2013), pp. 10510–10519. ISSN: 1944-8244. DOI: 10.1021/am402070k.

[518] Moria Kwiat et al. "Highly Ordered Large-Scale Neuronal Networks of Individual Cells – Toward Single Cell to 3D Nanowire Intracellular Interfaces". In: *ACS Applied Materials & Interfaces* 4.7 (July 2012), pp. 3542–3549. ISSN: 1944-8244. DOI: 10.1021/am300602e.

[519] Chong Xie et al. "Intracellular Recording of Action Potentials by Nanopillar Electroporation". en. In: *Nature Nanotechnology* 7.3 (Mar. 2012), pp. 185–190. ISSN: 1748-3395. DOI: 10.1038/nnano.2012.8.

[520] Waldemar Hällström et al. "Fifteen-Piconewton Force Detection from Neural Growth Cones Using Nanowire Arrays". In: *Nano Letters* 10.3 (Mar. 2010), pp. 782–787. ISSN: 1530-6984. DOI: 10.1021/nl902675h.

[521] Jacob T. Robinson et al. "Vertical Nanowire Electrode Arrays as a Scalable Platform for Intracellular Interfacing to Neuronal Circuits". en. In: *Nature Nan-*

otechnology 7.3 (Mar. 2012), pp. 180–184. ISSN: 1748-3387. DOI: 10.1038/nnano.2011.249.

[522] Gianni Ciofani, Giada Graziana Genchi, and Virgilio Mattoli. "ZnO Nanowire Arrays as Substrates for Cell Proliferation and Differentiation". In: *Materials Science and Engineering: C* 32.2 (Mar. 2012), pp. 341–347. ISSN: 0928-4931. DOI: 10.1016/j.msec.2011.11.001.

[523] Kyoung Je Cha et al. "Enhanced Osteogenic Fate and Function of MC3T3-E1 Cells on Nanoengineered Polystyrene Surfaces with Nanopillar and Nanopore Arrays". en. In: *Biofabrication* 5.2 (2013), p. 025007. ISSN: 1758-5090. DOI: 10.1088/1758-5082/5/2/025007.

[524] J. Salonen et al. "Mesoporous Silicon Microparticles for Oral Drug Delivery: Loading and Release of Five Model Drugs". eng. In: *Journal of Controlled Release: Official Journal of the Controlled Release Society* 108.2-3 (Nov. 2005), pp. 362–374. ISSN: 0168-3659. DOI: 10.1016/j.jconrel.2005.08.017.

[525] Igor I. Slowing et al. "Mesoporous Silica Nanoparticles as Controlled Release Drug Delivery and Gene Transfection Carriers". eng. In: *Advanced Drug Delivery Reviews* 60.11 (Aug. 2008), pp. 1278–1288. ISSN: 0169-409X. DOI: 10.1016/j.addr.2008.03.012.

[526] Ennio Tasciotti et al. "Mesoporous Silicon Particles as a Multistage Delivery System for Imaging and Therapeutic Applications". en. In: *Nature Nanotechnology* 3.3 (Mar. 2008), pp. 151–157. ISSN: 1748-3395. DOI: 10.1038/nnano.2008.34.

[527] Yan-Li Zhao et al. "pH-Operated Nanopistons on the Surfaces of Mesoporous Silica Nanoparticles". In: *Journal of the American Chemical Society* 132.37 (Sept. 2010), pp. 13016–13025. ISSN: 0002-7863. DOI: 10.1021/ja105371u.

[528] Min Xue et al. "pH-Operated Mechanized Porous Silicon Nanoparticles". In: *Journal of the American Chemical Society* 133.23 (June 2011), pp. 8798–8801. ISSN: 0002-7863. DOI: 10.1021/ja201252e.

[529] Yu-Ran Na et al. "Probing Enzymatic Activity inside Living Cells Using a Nanowire–Cell "Sandwich" Assay". In: *Nano Letters* 13.1 (Jan. 2013), pp. 153–158. ISSN: 1530-6984. DOI: 10.1021/nl3037068.

[530] Ciro Chiappini et al. "Mapping Local Cytosolic Enzymatic Activity in Human Esophageal Mucosa with Porous Silicon Nanoneedles". en. In: *Advanced Materials* 27.35 (Sept. 2015), pp. 5147–5152. ISSN: 1521-4095. DOI: 10.1002/adma.201501304.

[531] Xi Xie et al. "Mechanical Model of Vertical Nanowire Cell Penetration". In: *Nano Letters* 13.12 (Dec. 2013), pp. 6002–6008. ISSN: 1530-6984. DOI: 10.1021/nl403201a.

[532] Ziliang Carter Lin et al. "Iridium Oxide Nanotube Electrodes for Sensitive and Prolonged Intracellular Measurement of Action Potentials". en. In: *Nature Communications* 5 (Feb. 2014), p. 3206. ISSN: 2041-1723. DOI: 10.1038/ncomms4206.

[533] Valeria Caprettini et al. "Soft Electroporation for Delivering Molecules into Tightly Adherent Mammalian Cells through 3D Hollow Nanoelectrodes". en. In: *Scientific Reports* 7.1 (Aug. 2017), p. 8524. ISSN: 2045-2322. DOI: 10.1038/s41598-017-08886-y.

[534] Messina Gabriele C. et al. “Spatially, Temporally, and Quantitatively Controlled Delivery of Broad Range of Molecules into Selected Cells through Plasmonic Nanotubes”. In: *Advanced Materials* 27.44 (Oct. 2015), pp. 7145–7149. ISSN: 0935-9648. DOI: 10.1002/adma.201503252.

[535] Rune S. Frederiksen et al. “Modulation of Fluorescence Signals from Biomolecules along Nanowires Due to Interaction of Light with Oriented Nanostructures”. In: *Nano Letters* 15.1 (Jan. 2015), pp. 176–181. ISSN: 1530-6984. DOI: 10.1021/nl503344y.

[536] Francesca Santoro et al. “Interfacing Electrogenic Cells with 3D Nanoelectrodes: Position, Shape, and Size Matter”. In: *ACS Nano* 8.7 (July 2014), pp. 6713–6723. ISSN: 1936-0851. DOI: 10.1021/nn500393p.

[537] Nina Buch-Månson et al. “Towards a Better Prediction of Cell Settling on Nanostructure Arrays—Simple Means to Complicated Ends”. en. In: *Advanced Functional Materials* 25.21 (June 2015), pp. 3246–3255. ISSN: 1616-3028. DOI: 10.1002/adfm.201500399.

[538] Suijian Qi et al. “Cell Adhesion and Spreading Behavior on Vertically Aligned Silicon Nanowire Arrays”. In: *ACS Applied Materials & Interfaces* 1.1 (Jan. 2009), pp. 30–34. ISSN: 1944-8244. DOI: 10.1021/am800027d.

[539] H. Kagiwada et al. “The Mechanical Properties of a Cell, as Determined by Its Actin Cytoskeleton, Are Important for Nanoneedle Insertion into a Living Cell”. English. In: *Cytoskeleton* 67.8 (2010), pp. 496–503. ISSN: 1949-3584. DOI: 10.1002/cm.20460.

[540] Amin Aalipour et al. “Plasma Membrane and Actin Cytoskeleton as Synergistic Barriers to Nanowire Cell Penetration”. In: *Langmuir* 30.41 (Oct. 2014), pp. 12362–12367. ISSN: 0743-7463. DOI: 10.1021/la502273f.

[541] Ikuo Obataya et al. “Nanoscale Operation of a Living Cell Using an Atomic Force Microscope with a Nanoneedle”. In: *Nano Letters* 5.1 (Jan. 2005), pp. 27–30. ISSN: 1530-6984. DOI: 10.1021/nl0485399.

[542] Ying Wang et al. “Poking Cells for Efficient Vector-Free Intracellular Delivery”. en. In: *Nature Communications* 5 (July 2014), p. 4466. ISSN: 2041-1723. DOI: 10.1038/ncomms5466.

[543] Daisuke Matsumoto et al. “Oscillating High-Aspect-Ratio Monolithic Silicon Nanoneedle Array Enables Efficient Delivery of Functional Bio-Macromolecules into Living Cells”. en. In: *Scientific Reports* 5 (Oct. 2015), p. 15325. ISSN: 2045-2322. DOI: 10.1038/srep15325.

[544] Bozhi Tian et al. “Three-Dimensional, Flexible Nanoscale Field-Effect Transistors as Localized Bioprobes”. en. In: *Science* 329.5993 (Aug. 2010), pp. 830–834. ISSN: 0036-8075, 1095-9203. DOI: 10.1126/science.1192033.

[545] Ziliang Carter Lin et al. “Accurate Nanoelectrode Recording of Human Pluripotent Stem Cell-Derived Cardiomyocytes for Assaying Drugs and Modeling Disease”. en. In: *Microsystems & Nanoengineering* 3 (Mar. 2017), p. 16080. ISSN: 2055-7434. DOI: 10.1038/micronano.2016.80.

[546] Xiaojie Duan et al. “Intracellular Recordings of Action Potentials by an Extracellular Nanoscale Field-Effect Transistor”. en. In: *Nature Nanotechnology* 7.3 (Mar. 2012), pp. 174–179. ISSN: 1748-3395. DOI: 10.1038/nnano.2011.223.

[547] Tian-Ming Fu et al. “Sub-10-Nm Intracellular Bioelectronic Probes from Nanowire–Nanotube Heterostructures”. en. In: *Proceedings of the National Academy of Sciences* 111.4 (Jan. 2014), pp. 1259–1264. ISSN: 0027-8424, 1091-6490. DOI: 10.1073/pnas.1323389111.

[548] Matthew R. Angle and Andreas T. Schaefer. “Neuronal Recordings with Solid-Conductor Intracellular Nanoelectrodes (SCINEs)”. en. In: *PLOS ONE* 7.8 (Aug. 2012), e43194. ISSN: 1932-6203. DOI: 10.1371/journal.pone.0043194.

[549] Benjamin D. Almquist and Nicholas A. Melosh. “Fusion of Biomimetic Stealth Probes into Lipid Bilayer Cores”. en. In: *Proceedings of the National Academy of Sciences* 107.13 (Mar. 2010), pp. 5815–5820. ISSN: 0027-8424, 1091-6490. DOI: 10.1073/pnas.0909250107.

[550] Peng-Yuan Wang et al. “Screening Mesenchymal Stem Cell Attachment and Differentiation on Porous Silicon Gradients”. en-au. In: 22.16 (2012), pp. 3414–3423.

[551] Jae-Hyun Lee et al. “Spontaneous Internalization of Cell Penetrating Peptide-Modified Nanowires into Primary Neurons”. In: *Nano Letters* 16.2 (Feb. 2016), pp. 1509–1513. ISSN: 1530-6984. DOI: 10.1021/acs.nanolett.6b00020.

[552] Nicholas Cordella et al. “Membrane Indentation Triggers Clathrin Lattice Reorganization and Fluidization”. en. In: *Soft Matter* 11.3 (Dec. 2014), pp. 439–448. ISSN: 1744-6848. DOI: 10.1039/C4SM01650E.

[553] Nils C. Gauthier, Thomas A. Masters, and Michael P. Sheetz. “Mechanical Feedback between Membrane Tension and Dynamics”. eng. In: *Trends in Cell Biology* 22.10 (Oct. 2012), pp. 527–535. ISSN: 1879-3088. DOI: 10.1016/j.tcb.2012.07.005.

[554] Seyed R. Tabaei et al. “Single Vesicle Analysis Reveals Nanoscale Membrane Curvature Selective Pore Formation in Lipid Membranes by an Antiviral α-Helical Peptide”. In: *Nano Letters* 12.11 (Nov. 2012), pp. 5719–5725. ISSN: 1530-6984. DOI: 10.1021/nl3029637.

[555] Miu Shan Chan and Pik Kwan Lo. “Nanoneedle-Assisted Delivery of Site-Selective Peptide-Functionalized DNA Nanocages for Targeting Mitochondria and Nuclei”. eng. In: *Small (Weinheim an Der Bergstrasse, Germany)* 10.7 (Apr. 2014), pp. 1255–1260. ISSN: 1613-6829. DOI: 10.1002/smll.201302993.

[556] Huajian Gao. “Probing Mechanical Principles of Cell–Nanomaterial Interactions”. In: *Journal of the Mechanics and Physics of Solids*. Sixtieth anniversary issue in honor of Professor Rodney Hill 62 (Jan. 2014), pp. 312–339. ISSN: 0022-5096. DOI: 10.1016/j.jmps.2013.08.018.

[557] Xinghua Shi et al. “Cell Entry of One-Dimensional Nanomaterials Occurs by Tip Recognition and Rotation”. en. In: *Nature Nanotechnology* 6.11 (Nov. 2011), pp. 714–719. ISSN: 1748-3387. DOI: 10.1038/nnano.2011.151.

[558] Ciro Chiappini et al. “Porous Silicon Nanoneedles By Metal Assisted Chemical Etch for Intracellular Sensing and Delivery”. en. In: *ECS Transactions* 69.2

(Sept. 2015), pp. 63–68. ISSN: 1938-6737, 1938-5862. DOI: 10.1149/06902.0063ecst.

[559] Katharina Gaus, Tobias Zech, and Thomas Harder. "Visualizing Membrane Microdomains by Laurdan 2-Photon Microscopy". eng. In: *Molecular Membrane Biology* 23.1 (2006 Jan-Feb), pp. 41–48. ISSN: 0968-7688. DOI: 10.1080/09687860500466857.

[560] Chong Xie et al. "Noninvasive Neuron Pinning with Nanopillar Arrays". In: *Nano Letters* 10.10 (Oct. 2010), pp. 4020–4024. ISSN: 1530-6984. DOI: 10.1021/nl101950x.

[561] Markus C. Kerr and Rohan D. Teasdale. "Defining Macropinocytosis". en. In: *Traffic* 10.4 (Apr. 2009), pp. 364–371. ISSN: 1600-0854. DOI: 10.1111/j.1600-0854.2009.00878.x.

[562] Katharina Gaus et al. "Visualizing Lipid Structure and Raft Domains in Living Cells with Two-Photon Microscopy". en. In: *Proceedings of the National Academy of Sciences* 100.26 (Dec. 2003), pp. 15554–15559. ISSN: 0027-8424, 1091-6490. DOI: 10.1073/pnas.2534386100.

[563] Jan R.T. van Weering et al. "Intracellular Membrane Traffic at High Resolution". In: *Methods in cell biology* 96 (2010), pp. 619–648. ISSN: 0091-679X. DOI: 10.1016/S0091-679X(10)96026-3.

[564] Edward Brown et al. "Studying Intracellular Transport Using High-Pressure Freezing and Correlative Light Electron Microscopy". eng. In: *Seminars in Cell & Developmental Biology* 20.8 (Oct. 2009), pp. 910–919. ISSN: 1096-3634. DOI: 10.1016/j.semcdb.2009.07.006.

[565] Ashley J. Pratt and Ian J. MacRae. "The RNA-Induced Silencing Complex: A Versatile Gene-Silencing Machine". In: *The Journal of Biological Chemistry* 284.27 (July 2009), pp. 17897–17901. ISSN: 0021-9258. DOI: 10.1074/jbc.R900012200.

[566] Catherine Cecilia Berry et al. "The Fibroblast Response to Tubes Exhibiting Internal Nanotopography". In: *Biomaterials* 26.24 (Aug. 2005), pp. 4985–4992. ISSN: 0142-9612. DOI: 10.1016/j.biomaterials.2005.01.046.

[567] James D. Orth et al. "The Large GTPase Dynamin Regulates Actin Comet Formation and Movement in Living Cells". en. In: *Proceedings of the National Academy of Sciences* 99.1 (Aug. 2002), pp. 167–172. ISSN: 0027-8424, 1091-6490. DOI: 10.1073/pnas.012607899.

[568] Benjamin K. K. Teo et al. "The Effect of Micro and Nanotopography on Endocytosis in Drug and Gene Delivery Systems". In: *Biomaterials* 32.36 (Dec. 2011), pp. 9866–9875. ISSN: 0142-9612. DOI: 10.1016/j.biomaterials.2011.08.088.

[569] Yan-Liang Zhang, John A. Frangos, and Mirianas Chachisvilis. "Laurdan Fluorescence Senses Mechanical Strain in the Lipid Bilayer Membrane". eng. In: *Biochemical and Biophysical Research Communications* 347.3 (Sept. 2006), pp. 838–841. ISSN: 0006-291X. DOI: 10.1016/j.bbrc.2006.06.152.

[570] Xi Xie et al. "Determining the Time Window for Dynamic Nanowire Cell Penetration Processes". In: *ACS Nano* 9.12 (Dec. 2015), pp. 11667–11677. ISSN: 1936-0851. DOI: 10.1021/acsnano.5b05498.

[571] So Yeon Kim and Eun Gyeong Yang. “Collective Behaviors of Mammalian Cells on Amine-Coated Silicon Nanowires”. en. In: *Nanotechnology* 24.45 (2013), p. 455704. ISSN: 0957-4484. DOI: 10.1088/0957-4484/24/45/455704.

[572] William M. Gelbart, Avinoam Ben-Shaul, and Didier Roux, eds. *Micelles, Membranes, Microemulsions, and Monolayers*. en. Partially Ordered Systems. New York: Springer-Verlag, 1994. ISBN: 978-1-4613-8391-8.

[573] Bidisha Sinha et al. “Cells Respond to Mechanical Stress by Rapid Disassembly of Caveolae”. eng. In: *Cell* 144.3 (Feb. 2011), pp. 402–413. ISSN: 1097-4172. DOI: 10.1016/j.cell.2010.12.031.

[574] R. N. Ghosh, D. L. Gelman, and F. R. Maxfield. “Quantification of Low Density Lipoprotein and Transferrin Endocytic Sorting HEp2 Cells Using Confocal Microscopy”. eng. In: *Journal of Cell Science* 107 (Pt 8) (Aug. 1994), pp. 2177–2189. ISSN: 0021-9533.

[575] M Malboubi et al. “Effects of the Surface Morphology of Pipette Tip on Giga-Seal Formation”. In: *Engineering Letters* 17 (Nov. 2009).

[576] Majid Malboubi, Yuchun Gu, and Kyle Jiang. “Surface Properties of Glass Micropipettes and Their Effect on Biological Studies”. In: *Nanoscale Research Letters* 6.1 (May 2011), p. 401. ISSN: 1931-7573. DOI: 10.1186/1556-276X-6-401.

[577] Mihaela Anitei and Bernard Hoflack. “Bridging Membrane and Cytoskeleton Dynamics in the Secretory and Endocytic Pathways”. en. In: *Nature Cell Biology* 14.1 (Jan. 2012), pp. 11–19. ISSN: 1476-4679. DOI: 10.1038/ncb2409.

[578] Nelly Panté and Birthe Fahrenkrog. “Exploring Nuclear Pore Complex Molecular Architecture by Immuno-Electron Microscopy Using Xenopus Oocytes”. eng. In: *Methods in Cell Biology* 122 (2014), pp. 81–98. ISSN: 0091-679X. DOI: 10.1016/B978-0-12-417160-2.00004-7.

[579] Hiroyuki Nakao et al. “Membrane-Spanning Sequences in Endoplasmic Reticulum Proteins Promote Phospholipid Flip-Flop”. In: *Biophysical Journal* 110.12 (June 2016), pp. 2689–2697. ISSN: 0006-3495. DOI: 10.1016/j.bpj.2016.05.023.

Appendix

List of Publications

Spearhead Nanometric Field-Effect Transistor Sensors for Single-Cell Analysis. Yanjun Zhang, Jan Clausmeyer, Babak Babakinejad, Ainara Lopez Cordoba, Tayyibah Ali, Andrew Shevchuk, Yasufumi Takahashi, Pavel Novak, Christopher Edwards, Max Lab, Sahana Gopal, Ciro Chiappini, Uma Anand, Luca Magnani, R. Charles Coombes, Julia Gorelik, Tomokazu Matsue, Wolfgang Schuhmann, David Klenerman, Elena V. Sviderskaya, and Yuri Korchev
ACS Nano 2016 10 (3), 3214-3221
DOI: 10.1021/acsnano.5b05211

Angular Approach Scanning Ion Conductance Microscopy.
Andrew Shevchuk, Sergiy Tokar, Sahana Gopal, Jose L. Sanchez-Alonso, Andrei I. Tarasov, A. Catalina Velez-Ortega, Ciro Chiappini, Patrik Rorsman, Molly M. Stevens, Julia Gorelik, Gregory I. Frolenkov, David Klenerman, Yuri Korchev.
Biophysical Journal, Volume 110, Issue 10, 2016, Pages 2252-2265
DOI: 10.1016/j.bpj.2016.04.017

Quantitative X-ray microradiography for high-throughput phenotyping of osteoarthritis in mice.
Julian A. Waung, Stephanie A. Maynard, Sahana Gopal, Apostolos Gogakos, John G. Logan, Graham R. Williams, J.H. Duncan Bassett
Osteoarthritis and Cartilage, Volume 22, Issue 10, 2014, Pages 1396-1400, ISSN 1063-4584, DOI: 10.1016/j.joca.2014.04.015.

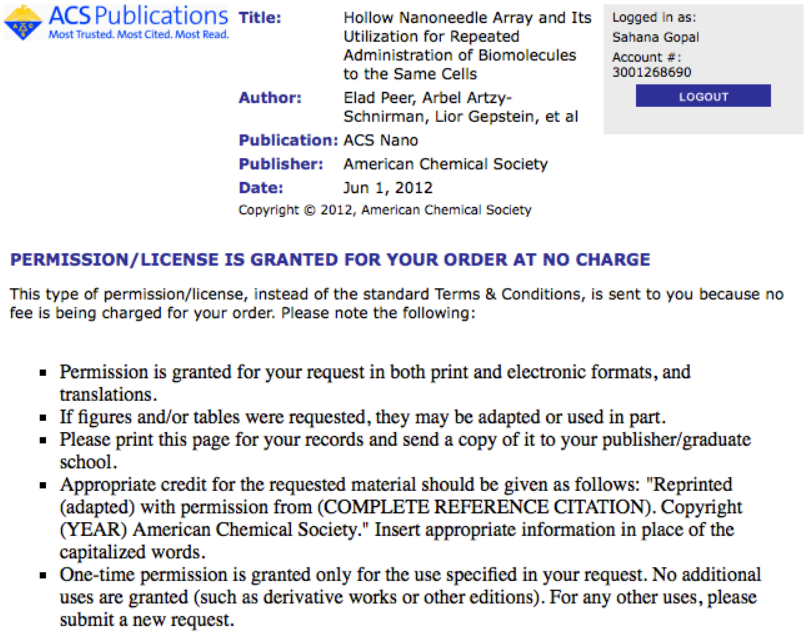
Nanoneedle-mediated Stimulation Reveals Non-canonical Regulation of Mechanoresponsive Cellular Components.
Catherine S. Hansel, Spencer W. Crowder, Samuel Cooper, Sahana Gopal, Maria Joao Pardelha da Cruz, Leonardo de Oliveira Martins, Debora Keller, Stephen Rothery, Michele Becce, Anthony E. G. Cass, Chris Bakal, Ciro Chiappini, Molly M. Stevens
Submitted to Nature Communications

Porous Silicon Nanoneedles Modulate Endocytosis to Deliver Biological Payloads.
Sahana Gopal, Ciro Chiappini, Jelle Penders, Vincent Leonardo, Hyejeong Seong, Stephen Rothery, Yuri Korchev, Andrew Shevchuk, Molly M. Stevens
Ready for Submission

Antigen labelling for visualisation under FIB-SEM: A new method for nanoscale 3D visualisation of cell-material interactions.
Sahana Gopal, Ciro Chiappini, Andrea Serio, Chia-Chen Hsu, James Armstrong, Qu Chen, Molly M. Stevens
In preparation

Rights and Permissions

Permission for Peer et al. 2012



ACS Publications
Most Trusted. Most Cited. Most Read.

Title: Hollow Nanoneedle Array and Its Utilization for Repeated Administration of Biomolecules to the Same Cells

Author: Elad Peer, Arbel Artzy-Schnirman, Lior Gepstein, et al

Publication: ACS Nano

Publisher: American Chemical Society

Date: Jun 1, 2012

Copyright © 2012, American Chemical Society

Logged in as:
Sahana Gopal
Account #:
3001268690
LOGOUT

PERMISSION/LICENSE IS GRANTED FOR YOUR ORDER AT NO CHARGE

This type of permission/license, instead of the standard Terms & Conditions, is sent to you because no fee is being charged for your order. Please note the following:

- Permission is granted for your request in both print and electronic formats, and translations.
- If figures and/or tables were requested, they may be adapted or used in part.
- Please print this page for your records and send a copy of it to your publisher/graduate school.
- Appropriate credit for the requested material should be given as follows: "Reprinted (adapted) with permission from (COMPLETE REFERENCE CITATION). Copyright (YEAR) American Chemical Society." Insert appropriate information in place of the capitalized words.
- One-time permission is granted only for the use specified in your request. No additional uses are granted (such as derivative works or other editions). For any other uses, please submit a new request.

Permission for Hanson et al. 2012

ACS Publications
Most Trusted. Most Cited. Most Read.

Title: Characterization of the Cell–Nanopillar Interface by Transmission Electron Microscopy

Author: Lindsey Hanson, Ziliang Carter Lin, Chong Xie, et al

Publication: Nano Letters

Publisher: American Chemical Society

Date: Nov 1, 2012

Copyright © 2012, American Chemical Society

LOGIN

If you're a copyright.com user, you can login to RightsLink using your copyright.com credentials.

Already **a RightsLink user** or want to learn more?

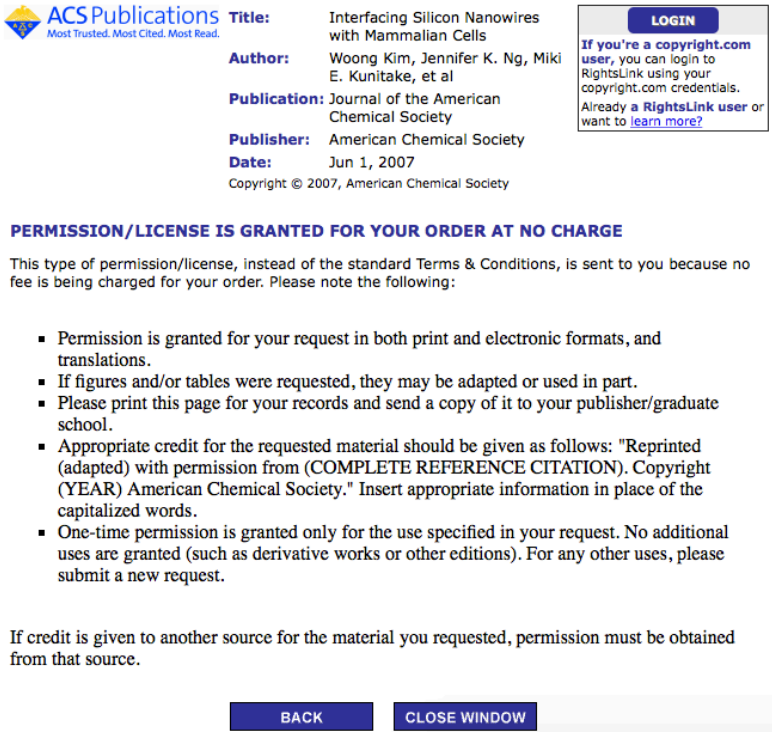
PERMISSION/LICENSE IS GRANTED FOR YOUR ORDER AT NO CHARGE

This type of permission/license, instead of the standard Terms & Conditions, is sent to you because no fee is being charged for your order. Please note the following:

- Permission is granted for your request in both print and electronic formats, and translations.
- If figures and/or tables were requested, they may be adapted or used in part.
- Please print this page for your records and send a copy of it to your publisher/graduate school.
- Appropriate credit for the requested material should be given as follows: "Reprinted (adapted) with permission from (COMPLETE REFERENCE CITATION). Copyright (YEAR) American Chemical Society." Insert appropriate information in place of the capitalized words.
- One-time permission is granted only for the use specified in your request. No additional uses are granted (such as derivative works or other editions). For any other uses, please submit a new request.

If credit is given to another source for the material you requested, permission must be obtained from that source.

Permission for Kim et al. 2007



ACS Publications
Most Trusted. Most Cited. Most Read.

Title: Interfacing Silicon Nanowires with Mammalian Cells
Author: Woong Kim, Jennifer K. Ng, Miki E. Kunitake, et al
Publication: Journal of the American Chemical Society
Publisher: American Chemical Society
Date: Jun 1, 2007

Copyright © 2007, American Chemical Society

LOGIN

If you're a copyright.com user, you can login to RightsLink using your copyright.com credentials.

Already a RightsLink user or want to learn more?

PERMISSION/LICENSE IS GRANTED FOR YOUR ORDER AT NO CHARGE

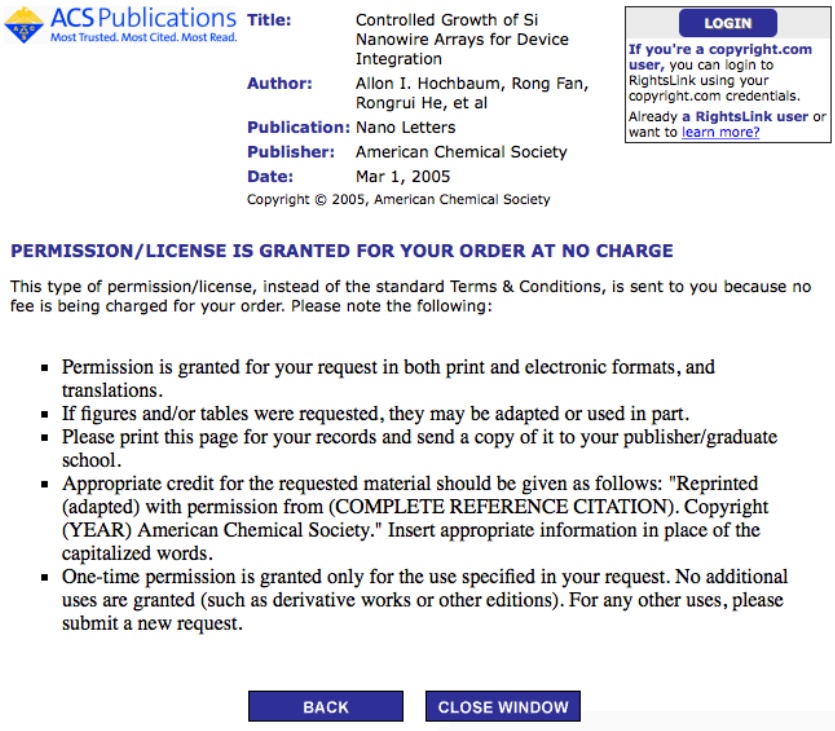
This type of permission/license, instead of the standard Terms & Conditions, is sent to you because no fee is being charged for your order. Please note the following:

- Permission is granted for your request in both print and electronic formats, and translations.
- If figures and/or tables were requested, they may be adapted or used in part.
- Please print this page for your records and send a copy of it to your publisher/graduate school.
- Appropriate credit for the requested material should be given as follows: "Reprinted (adapted) with permission from (COMPLETE REFERENCE CITATION). Copyright (YEAR) American Chemical Society." Insert appropriate information in place of the capitalized words.
- One-time permission is granted only for the use specified in your request. No additional uses are granted (such as derivative works or other editions). For any other uses, please submit a new request.

If credit is given to another source for the material you requested, permission must be obtained from that source.

BACK CLOSE WINDOW

Permission for Hochbaum et al. 2005



ACS Publications
Most Trusted. Most Cited. Most Read.

Title: Controlled Growth of Si Nanowire Arrays for Device Integration

Author: Allon I. Hochbaum, Rong Fan, Rongrui He, et al

Publication: Nano Letters

Publisher: American Chemical Society

Date: Mar 1, 2005

Copyright © 2005, American Chemical Society

LOGIN

If you're a copyright.com user, you can login to RightsLink using your copyright.com credentials.

Already **a RightsLink user** or want to learn more?

PERMISSION/LICENSE IS GRANTED FOR YOUR ORDER AT NO CHARGE

This type of permission/license, instead of the standard Terms & Conditions, is sent to you because no fee is being charged for your order. Please note the following:

- Permission is granted for your request in both print and electronic formats, and translations.
- If figures and/or tables were requested, they may be adapted or used in part.
- Please print this page for your records and send a copy of it to your publisher/graduate school.
- Appropriate credit for the requested material should be given as follows: "Reprinted (adapted) with permission from (COMPLETE REFERENCE CITATION). Copyright (YEAR) American Chemical Society." Insert appropriate information in place of the capitalized words.
- One-time permission is granted only for the use specified in your request. No additional uses are granted (such as derivative works or other editions). For any other uses, please submit a new request.

BACK CLOSE WINDOW

Permission for Chiappini et al. 2015 a

SPRINGER NATURE LICENSE
TERMS AND CONDITIONS

Apr 02, 2018

This Agreement between Miss. Sahana Gopal ("You") and Springer Nature ("Springer Nature") consists of your license details and the terms and conditions provided by Springer Nature and Copyright Clearance Center.

License Number	4320761387369
License date	Apr 02, 2018
Licensed Content Publisher	Springer Nature
Licensed Content Publication	Nature Materials
Licensed Content Title	Biodegradable silicon nanoneedles delivering nucleic acids intracellularly induce localized in vivo neovascularization
Licensed Content Author	C. Chiappini, E. De Rosa, J. O. Martinez, X. Liu, J. Steele et al.
Licensed Content Date	Mar 30, 2015
Licensed Content Volume	14
Licensed Content Issue	5
Type of Use	Thesis/Dissertation
Requestor type	academic/university or research institute
Format	print and electronic
Portion	figures/tables/illustrations
Number of figures/tables/illustrations	1
High-res required	no
Will you be translating?	no
Circulation/distribution	<501
Author of this Springer Nature content	no
Title	Cell material interactions
Instructor name	Sahana Gopal
Institution name	Imperial College London
Expected presentation date	May 2018
Portions	Figure 1
Requestor Location	Miss. Sahana Gopal flat 191 grove hall court london, nw89nx United Kingdom Attn: Miss. Sahana Gopal
Billing Type	Invoice

Permission for Chiappini et al. 2015 b



Logged in as:
Sahana Gopal
LOGOUT

Title: Biodegradable Nanoneedles for Localized Delivery of Nanoparticles in Vivo: Exploring the Biointerface

Author: Ciro Chiappini, Jonathan O. Martinez, Enrica De Rosa, et al

Publication: ACS Nano

Publisher: American Chemical Society

Date: May 1, 2015

Copyright © 2015, American Chemical Society

PERMISSION/LICENSE IS GRANTED FOR YOUR ORDER AT NO CHARGE

This type of permission/license, instead of the standard Terms & Conditions, is sent to you because no fee is being charged for your order. Please note the following:

- Permission is granted for your request in both print and electronic formats, and translations.
- If figures and/or tables were requested, they may be adapted or used in part.
- Please print this page for your records and send a copy of it to your publisher/graduate school.
- Appropriate credit for the requested material should be given as follows: "Reprinted (adapted) with permission from (COMPLETE REFERENCE CITATION). Copyright (YEAR) American Chemical Society." Insert appropriate information in place of the capitalized words.
- One-time permission is granted only for the use specified in your request. No additional uses are granted (such as derivative works or other editions). For any other uses, please submit a new request.

If credit is given to another source for the material you requested, permission must be obtained from that source.

Permission for Berthing et al. 2012

Order Details

Nanotechnology

Order detail ID: 71098547
Order License Id: 4320780220932
ISSN: 0957-4484
Publication Type: Journal
Volume:
Issue:
Start page:
Publisher: IOP Publishing
Author/Editor: Institute of Physics (Great Britain) ; American Institute of Physics

Permission Status: Granted
Permission type: Republish or display content
Type of use: Thesis/Dissertation
View details

Note: This item will be invoiced or charged separately through CCC's **RightsLink** service. More info **$ 0.00**

Permission for Han et al. 2005

ELSEVIER LICENSE TERMS AND CONDITIONS

Jun 12, 2018

This Agreement between Miss. Sahana Gopal ("You") and Elsevier ("Elsevier") consists of your license details and the terms and conditions provided by Elsevier and Copyright Clearance Center.

License Number	4320820982388
License date	Apr 02, 2018
Licensed Content Publisher	Elsevier
Licensed Content Publication	Biochemical and Biophysical Research Communications
Licensed Content Title	Gene expression using an ultrathin needle enabling accurate displacement and low invasiveness
Licensed Content Author	SungWoong Han,Chikashi Nakamura,Ikuo Obataya,Noriyuki Nakamura,Jun Miyake
Licensed Content Date	Jul 8, 2005
Licensed Content Volume	332
Licensed Content Issue	3
Licensed Content Pages	7
Start Page	633
End Page	639
Type of Use	reuse in a thesis/dissertation
Intended publisher of new work	other
Portion	figures/tables/illustrations
Number of figures/tables/illustrations	1
Format	both print and electronic

Permission for Mumm et al. 2012

JOHN WILEY AND SONS LICENSE TERMS AND CONDITIONS

Jun 12, 2018

This Agreement between Miss. Sahana Gopal ("You") and John Wiley and Sons ("John Wiley and Sons") consists of your license details and the terms and conditions provided by John Wiley and Sons and Copyright Clearance Center.

License Number	4320830724714
License date	Apr 02, 2018
Licensed Content Publisher	John Wiley and Sons
Licensed Content Publication	Small
Licensed Content Title	A Transparent Nanowire-Based Cell Impalement Device Suitable for Detailed Cell–Nanowire Interaction Studies
Licensed Content Author	Florian Mumm, Kai M. Beckwith, Sara Bonde, et al
Licensed Content Date	Oct 4, 2012
Licensed Content Volume	9
Licensed Content Issue	2
Licensed Content Pages	10
Type of use	Dissertation/Thesis
Requestor type	University/Academic
Format	Print and electronic
Portion	Figure/table
Number of figures/tables	3
Original Wiley figure/table number(s)	7b,c
Will you be translating?	No
Title of your thesis /	Cell material interactions

Permission for Novak et al. 2009

SPRINGER NATURE LICENSE
TERMS AND CONDITIONS

Jun 12, 2018

This Agreement between Miss. Sahana Gopal ("You") and Springer Nature ("Springer Nature") consists of your license details and the terms and conditions provided by Springer Nature and Copyright Clearance Center.

License Number	4321860785221
License date	Apr 04, 2018
Licensed Content Publisher	Springer Nature
Licensed Content Publication	Nature Methods
Licensed Content Title	Nanoscale live-cell imaging using hopping probe ion conductance microscopy
Licensed Content Author	Pavel Novak, Chao Li, Andrew I Shevchuk, Ruben Stepanyan, Matthew Caldwell et al.
Licensed Content Date	Mar 1, 2009
Licensed Content Volume	6
Licensed Content Issue	4
Type of Use	Thesis/Dissertation
Requestor type	academic/university or research institute
Format	print and electronic
Portion	figures/tables/illustrations
Number of figures/tables/illustrations	1
High-res required	no
Will you be translating?	no
Circulation/distribution	<501

Permission for Margueron et al. 2010

SPRINGER NATURE LICENSE
TERMS AND CONDITIONS

Jun 12, 2018

This Agreement between Miss. Sahana Gopal ("You") and Springer Nature ("Springer Nature") consists of your license details and the terms and conditions provided by Springer Nature and Copyright Clearance Center.

License Number	4345370385219
License date	May 10, 2018
Licensed Content Publisher	Springer Nature
Licensed Content Publication	Nature Reviews Genetics
Licensed Content Title	Chromatin structure and the inheritance of epigenetic information
Licensed Content Author	Raphaël Margueron, Danny Reinberg
Licensed Content Date	Apr 1, 2010
Licensed Content Volume	11
Licensed Content Issue	4
Type of Use	Thesis/Dissertation
Requestor type	academic/university or research institute
Format	print and electronic
Portion	figures/tables/illustrations
Number of figures/tables/illustrations	1
High-res required	no
Will you be translating?	no
Circulation/distribution	<501
Author of this Springer Nature content	no